Interfacing ultracold atoms with nanomagnetic domain walls

WEST, ADAM,DANIEL

WEST, ADAM,DANIEL (2012) *Interfacing ultracold atoms with nanomagnetic domain walls*, Durham theses, Durham University. Available at Durham E-Theses Online: http://etheses.dur.ac.uk/3588/

Interfacing Ultracold Atoms with Nanomagnetic Domain Walls

Adam West

A thesis submitted in partial fulfilment
of the requirements for the degree of
Doctor of Philosophy

Department of Physics
Durham University

May 21, 2012

Interfacing Ultracold Atoms with Nanomagnetic Domain Walls

Adam West

Abstract

This thesis presents the first realisation of a new type of hybrid quantum device based on spintronic technology. We demonstrate an interaction between the magnetic fringing fields produced by domain walls within planar permalloy nanowires and a cloud of ultracold ^{87}Rb atoms. This interaction is manifested through the realisation of a magnetic atom mirror produced by a two-dimensional domain wall array. The interaction is tuned through the reconfiguration of the micromagnetic structure.

Analytic modelling of the fringing fields is developed and shows good agreement with calculations based on micromagnetically simulated structures. The accurate and rapid calculation of the fringing fields permits simulation of the resulting atom dynamics, which agrees well with data. In turn, we use the atom dynamics as a probe of the micromagnetic reconfiguration processes that take place and observe a collective behaviour which is both reliably reproducible and in agreement with alternative, conventional magnetometry. We also observe evidence of stochastic behaviour, characteristic of superparamagnetic systems.

We consider the development of a more advanced spintronics-based atom chip which will allow for the creation of extremely tight mobile atom traps. We consider the problems associated with ensuring that the trapping potential is adiabatic, sufficiently deep, and technically feasible. In particular we examine techniques to circumvent losses due to Majorana spin-flip transitions. As a result of this study we propose a novel scheme for creating time-averaged potentials via the piezoelectric actuation of magnetic field sources. We show that this technique presents significant fundamental and technical advantages over conventional time-averaging schemes.

Declaration

I confirm that no part of the material offered has previously been submitted by myself for a degree in this or any other University. Where material has been generated through joint work, the work of others has been indicated.

Adam West
Durham, May 21, 2012

Acknowledgements

I would like to thank first of all you, the reader, for perusing this thesis, unless of course you're simply browsing the acknowledgments in search of a mention! I sincerely hope it is of some use.

Huge thanks must of course go to the rest of 'team nano': Ifan and Kev. I am sure that without them this project would not have reaped the fruits it has. Their help, support and criticism have been invaluable through the last three and a half years. In particular I would like to thank them for a remarkable open door policy, always being willing to discuss matters in the midst of their own commitments.

I would also like to thank of course our colleagues in Sheffield. Their patience and ability to work with me, despite my relative ignorance of their field, is certainly laudable. They too have always been on hand when I have had questions, and I would like to say it has been a pleasure to collaborate with them.

The nanowire project has been lucky to have a huge amount of support from the staff at Durham. In particular I must express my gratitude to the technicians in the workshops, whose understanding and level of service are a credit to the department. I am especially grateful to John, who has been extremely supportive in what I find the frustrating world of electronics.

My time at Durham has been made an enjoyable one by a huge number of people. I would like to thank each and every one of them for the support, fun and friendship they have provided. The AtMol group at Durham is an environment that I will certainly miss when I leave, and is one that truly surpasses all other groups I have visited in nurturing a climate where discussion, collaboration, criticism and sociability all thrive together. The support I have received on both a personal and professional level from my friends in AtMol has been invaluable.

Outside of physics I have been fortunate enough to make friends with a large number of people at Durham during my extended stay in what is a wonderful city. More wonderful still are the times I have shared and the people with whom I have spent my time. I would like to say thank you to them for a truly fantastic time.

Finally I give all my thanks to my parents and family for their love and support through all I do, for giving me all that I could want or need, and for their patience, understanding and of course all the offers of proof-reading!

To my parents,
for all their love.

Contents

List of Figures

Chapter 1

Introduction

1.1 Hybrid quantum systems

The field of atom optics has experienced enormous growth that has produced a vast array of experiments which have transformed the typically tumultuous quantum world into a tractable and fecund environment for research [1, 2, 3]. The continuing development of microfabrication techniques such as lithography [4] has filliped a shift within atom optics towards miniaturisation which has resulted in the birth of a new type of 'lab on a chip' for ultracold quantum particles [5]. This has permitted the production of a wide variety of arenas for study which boast an unrivalled combination of freedom of design, robustness and compactness, allowing very precise control over the external and internal degrees of freedom of quantum particles. Whilst the advent of ultracold physics paved the way towards the paradigm of an isolated quantum system, the development of hybrid devices has allowed the interfacing of quantum particles with solid-state architectures through a range of novel methods, giving rise to many new regimes of study and applications.

Through the use of such hybrid devices we are able to not only study the building blocks of quantum matter, but also to use quantum objects as tools with which to study other systems. The use of ultracold atoms as a probe has been demonstrated in a number of applications, for example through the imaging of nanoscale structures [6] or as a precise and sensitive measure of magnetic fields [7]. There have also been numerous demonstrations of the coupling of quantum particles to macroscopic objects [8, 9, 10, 11, 12].

Perhaps the most exciting aspect of the use of hybrid devices is that they are often inherently scalable, allowing for the simultaneous control and manipulation of large numbers of quantum objects. The notion of a quantum computer remains the quintessential embodiment of such quantum control and has fuelled many of the developments of hybrid interfaces which combine microscopic particles with macroscopic objects. Such devices also allow the user to combine the varying benefits of different physical objects. For example, the creation of an array of atom-photon junctions has been realised [13], combining the fundamental mobility of photons with the strong interactions of atoms within a scalable architecture that bears the hallmarks of a quantum information processing scheme [14].

We can roughly divide hybrid quantum devices according to the type of field which is employed. Electric fields have found greatest utility in the manipulation of ions, leading to exceptionally strong confinement and the individual shuttling of single particles [15]. This exquisite control has provided some of the best demonstrations of quantum gates to date [16, 17].

The use of optical fields has always played an extremely important role within atom optics, ever since the advent of laser cooling. Optical dipole traps have helped to realise routes to achieving Bose-Einstein condensation [18] and the extension to optical lattices has permitted the development of scalable systems of ultracold atoms through which the optical confinement, detection and manipulation of single atoms has been achieved [19].

One of the most ubiquitous developments within atom optics is the magneto-optical trap. A magnetic quadrupole field is used to provide a spatially dependent dissipative optical force to cool and confine atoms [20, 21] — a technique which has been adopted by thousands of researchers. The magnetic quadrupole is also used on its own to trap atoms in a conservative potential. Magnetic trapping was the culmination of years of experiments that utilise magnetic fields to manipulate microscopic particles [22] that began with the experiments of Stern and Gerlach in 1922 [23]. Their eponymous force arises from applying a spatially varying magnetic field, $\vec{B}$, to a permanent magnetic dipole, $\vec{\mu}$:

$$\vec{F}_{\mathrm{SG}} = \vec{\nabla}\left(-\vec{\mu}.\vec{B}\right). \tag{1.1}$$

The Stern-Gerlach force underpins all magnetic atom optics, and in this work we shall focus on magnetic devices throughout.

Magnetic atom optics can be roughly divided into two types of device: those which are based on current-carrying wires, and those which are based on permanent magnetic material. Some of the first realisations of magnetic atom optics were based on current-carrying wires. Their flexibility allows for easy production of a range of magnetic field geometries, as prescribed by the Biot-Savart law:

$$\vec{B}(\vec{r}) = \frac{\mu_0 I}{4\pi} \int \frac{\mathrm{d}\vec{l} \times \vec{r}}{|\vec{r}|^3}, \tag{1.2}$$

which describes the field at a position r produced by a current I flowing along a path made of elements dl. The guiding of thermal atoms was first demonstrated using current-carrying wires [24] and has since been replicated with ultracold atoms [25]. The first magnetic traps were also realised using current-carrying wires in the form of the aforementioned quadrupole trap [26] — the simplest possible geometry that will provide 3D confinement. Since then, similar technology has been used to create a variety of traps, including Z- or U-traps which are often incorporated into atom chips to act as stepping-stones to more complicated experiments [27, 28, 29].

An advantage of using current-carrying wires to trap atoms is that they can be switched on and off, allowing for a degree of dynamic control. The same technology has also allowed for the creation of more complex trapping geometries via the technique of RF-dressing, e.g. [30]. However, there is also a clear disadvantage when using current-carrying wires in that they are inherently noisy objects [31]. Imperfections in the fabrication of the wires can result in corrugated potentials which have been observed to cause fragmentation of atomic clouds [7, 32, 33]. Technical noise within the applied currents leads to heating via modulation of the potential and can induce spin-flip losses [34, 35]. The electrical conductance of wires also results in Johnson noise that can lead to significant losses which may jeopardise the efficacy of traps [36].

Another disadvantage of using current-carrying wires is that there is an inherent limit to the feature size due to considerations of the microfabrication procedures and the fact that one must be able to dissipate the power produced by the wires in an effective manner. Both of these factors make producing high field gradients with current-carrying wires challenging.

Until the advent of microfabrication techniques, current-carrying wires generally afforded the user a greater freedom of design due to their inherent flexibility. However, with the correct tools, the use of permanent magnetic material began to garner favour. Tailoring of magnetic fields by the microscopic design of the bulk magnetisation, $\vec{M}$, became possible. The resulting fields are provided by [37]

$$\vec{B}(\vec{r}) = \frac{\mu_0 \vec{\nabla}_r}{4\pi} \int \frac{\vec{\nabla}_{r'}.\vec{M}(\vec{r}\,')}{|\vec{r} - \vec{r}\,'|} \mathrm{d}^3\vec{r}\,'. \tag{1.3}$$

The first demonstrations of patterned magnetic material controlling atomic motion were realised in magnetic mirrors [38, 39]. Since then permanent magnetic material has been used to create a variety of atom traps.

When using permanent magnetic material there are a number of benefits, directly related to the points made above. Because there is no current flowing there are no issues with power dissipation when using permanent magnetic material. Together with the inherently small characteristic length-scales afforded by microfabrication techniques this allows for the creation of very large magnetic field gradients, potentially up to the order of around 10^6 T/m [40]. In addition, the fact that no electrical connections are required provides greater flexibility of design and practicability; some topologies are in fact only possible when using permanent magnetic material [41]. Another advantage of not using electric currents is that a number of the sources of noise previously discussed are simply not present. The use of material which has minimal electrical conductance can in fact extend the lifetimes of atomic traps from the order of seconds to being vacuum limited [42]. One caveat to this is that one must still take care to avoid inhomogeneities within the material which, in a manner similar to current-carrying wires, can induce fragmentation of an atomic cloud [43].

There is one significant disadvantage associated with the use of permanent magnetic material in atom chip experiments, which is that the fields created are not dynamic: they can not be tuned or switched. Whilst there have been some realisations of dynamic atom traps using permanent magnetic material [44], these rely on the application of additional external magnetic fields and the induced motion of the trapping minima is always significantly constrained using such techniques [45]. The characteristically small feature size and freedom of design afforded by microfabrication techniques is not reflected in the motion that is possible. There is, however, a fluorishing technology that utilises lithographically deposited permanent magnetic material which does have inherent mobility, and it is this which we discuss in the following section.

1.2 Nanowires and spintronics

Whilst lithographic techniques have fuelled the developing trend of atom chip experiments, the same technology has long been the mainstay of many other burgeoning areas of research. Perhaps one of the most exciting and broad of these is the field of spintronics. Whilst ultracold physics exploits and investigates the atom, the particle of interest for spintronics is the electron. It is the electron that is responsible for the physics of both solid-state magnetism and electric current. Spintronics combines these phenomena in a technology exhibiting properties associated with both. This typically manifests itself as spin waves, i.e. the propagation of spin, exhibited as a magnetic moment, and is normally characterised in the form of a magnetic domain.

Magnetic domains are macroscopic regions where the magnetisation direction of a material is uniform, and they are present in many different magnetic materials. Perhaps the most popular material for studying magnetic domains is permalloy, as it has a number of physical characteristics which lend itself to the creation, positioning and control of domain walls.

Permalloy is a ferromagnetic material with the chemical formula $Ni_{80}Fe_{20}$. One of the most important physical characteristics of permalloy is that it is a highly magnetic material, having a saturation magnetisation of around 8.6×10^5 A/m, comparable to iron [46]. This makes it an ideal material for studying spintronic behaviour and phenomena associated with magnetisation in general. It also means that divergences in the magnetisation will result in large magnetic fields.

Permalloy is also an extremely soft magnetic material, having a magnetic permeability of the order of 10^2–10^3 μ_0 [47, 48] (for iron this is around 200

[49]), and a coercivity of the order of 1 Oe[1] [50]. This means that reconfiguration of the magnetisation structure of permalloy requires relatively low applied fields. This property also lends itself to the study of spintronics as it facilitates the creation and manipulation of magnetic domains.

Domains of different orientations are separated by domain walls. The orientation of domains is governed by anisotropies in the magnetic material, either in the crystal structure, or the macroscopic shape. For the case of permalloy, there is a negligible magnetocrystalline anisotropy, meaning there is no preferred axis for the magnetisation according to the microscopic structure. This is characterised by the energy density associated with magnetisation aligned along a particular crystal axis and is quantified by the parameter K_1. The closer this is to zero, the more isotropic the material. Permalloy has a vanishingly small (in some cases < 10 J/m^3) value of K_1 [51, 52]. By comparison, iron has a value of K_1 of around 5×10^4 J/m^3 [53]. Thus the magnetic structure of permalloy is governed almost entirely by macroscopic anisotropies. When working with nanowires, objects with obvious inherent shape anisotropy, the domains which they host naturally align with the long axis of the wire; this is the energetically favoured magnetisation configuration. There is of course a degeneracy as there are two possible directions for domains within such nanowires. Thus, the domain walls that form are always between domains of opposite orientation. We label these domain walls as being either 'head-to-head', where the surrounding magnetisation points towards the domain wall, or 'tail-to-tail', where the surrounding magnetisation points away from the wall.

The reversal of the magnetisation that occurs at the domain wall is a quasi-discontinuous one that occurs over a lengthscale of the order of the nanowire width (the thickness of the wire is considered to be less than the wire's width). Over this lengthscale there is a rotation of the magnetisation direction. The structure of this rotation is generally complex in nature. An example of the resulting magnetisation structure is illustrated in Figure 1.1, as calculated using micromagnetic techniques (Schrefl et al.). These

---

[1] We note here that there is a disparity between the units conventions for the use of units between the magnetics community and the atomic physics community. The former tends to use gauss and oersted to signify the magnetic flux density ($\vec{B}$) and the magnetic field ($\vec{H}$) respectively. In vacuum we have that 1 G = 1 Oe = 0.1 mT.

techniques, and the resulting magnetisation structure are discussed in more detail in Chapter 2.

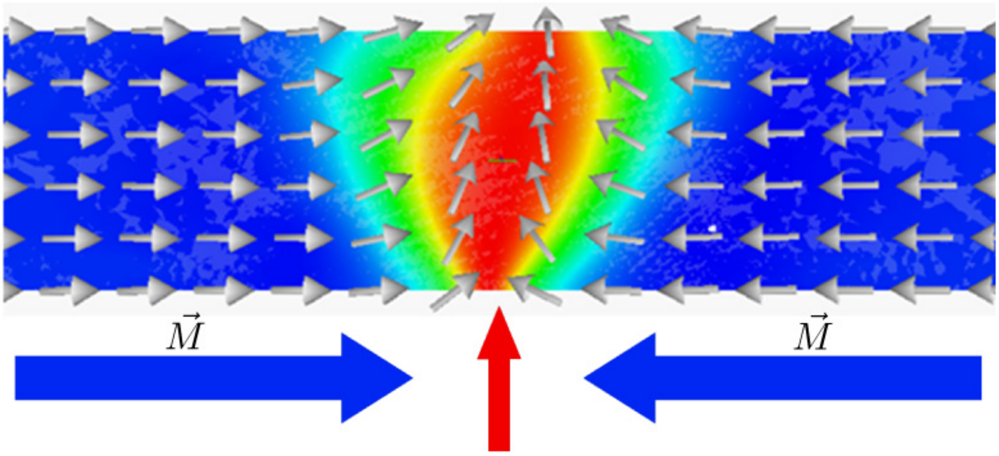

Figure 1.1: The magnetisation structure of a head-to-head domain wall, as calculated via micromagnetic simulations (Schrefl et al.) in a planar permalloy nanowire of cross section 200 nm × 5 nm. Shading represents the component of the magnetisation transverse to the wire axis. Arrows represent the magnetisation direction in the plane of the wire. The magnetic structure can be approximated by two head-to-head magnetic dipoles, separated by a transversely orientated dipole.

Domain walls are inherently dynamic objects and it is the motion and interaction of domain walls that forms the basis of spintronic technology. Once populated, domain-wall motion can be induced by a number of methods, all of which directly modify the magnetisation structure of the material. Consider the picture shown in Figure 1.1. Applying an external magnetic field, orientated along the nanowire length, pointing to the right, will cause domain wall motion. The left hand domain, which is aligned parallel with the applied field will grow in size, as this is energetically favourable. Correspondingly, the right hand domain, aligned anti-parallel to the applied field, will reduce in size. As a consequence, the region between these domains, the domain wall, will be shifted to the right accordingly.

A similar process occurs when one applies a current through the wire. Injected current causes the transport of electrons through the domain wall. Upon transmission through the wall the electron experiences a spin flip, i.e.

a reversal of angular momentum. Due to conversation of angular momentum there is a corresponding shift in the position of the domain wall. Thus, a current of given magnitude (and polarisation) will then cause the domain wall to propagate at a speed which is well defined in the steady state regime.

Alternative methods of inducing domain wall motion are also possible, such as by the application of stress to the magnetic material. Through the energy changes due to magnetostriction the position of the domain wall is changed [54].

The motion of domain walls has been quantitatively studied in great detail [55, 56, 57, 58, 59, 60] and has given rise to a number of exciting technological applications, such as alternative forms of memory storage and data transfer [61, 62], logic gates [63], and magnetic sensors [64].

One characteristic of domain walls that we have yet to consider is the presence of fringing fields. As previously stated, the divergence of magnetisation within permalloy can lead to significant magnetic fields, and this occurs at the locations of domain walls. Fringing fields are in fact a vital component of the realisation of magnetic memory (MRAM) technology. In a manner entirely analogous to conventional hard disk drives, a read/write head converts the magnetic fringing fields present at heights of around 10 nm above domain walls into an electrical signal [65]. In the following section we will consider the use of these fields as a tool with which to interact domain walls and quantum particles, thus combining the fields of atom optics and spintronics.

1.3 Nanowires and atoms

In this work we present an amalgamation of two disparate yet flourishing areas of research. The fringing fields which provide the ability to remotely sense the magnetisation structure of spintronics-based memory devices may also be harnessed within atomic physics applications. The two technologies are naturally complimentary: spintronic devices provide the deterministic production of large, dynamic magnetic fields on submicron lengthscales, whilst chip-based atom optics devices demand precisely this kind of precision and flexibility on a commensurate lengthscale in order to realise new and exciting applications.

By exploiting spintronic technology to produce a new type of atom chip architecture a number of advantages over conventional devices can be realised by combining the benefits of both current-carrying wires and permanent magnetic material. As spintronic devices utilise permanent ferromagnetic material which can be manipulated by external magnetic fields, technical noise due to electrical currents can be completely eliminated. Similarly, Johnson noise can be removed through the use of ferrite materials which have very low conductivity.

Whilst potential inhomogeneities are present in atom chips based on permanent magnetic material, this is not necessarily the case for spintronics-based devices. The fringing field source can be precisely confined to a region of around 100 nm in size, at the location of a domain wall. Thus, at sufficient distance, the field source becomes point-like in nature and any magnetisation inhomogeneity present within the domain wall is not reproduced in the resulting magnetic field. Spintronic devices also benefit from not requiring careful consideration of power dissipation within the device, or the need for electrical connections to be made (although the use of such connections would enhance dynamic control by allowing addressing of individual nanowires).

Whilst many of the problems inherent in current-based devices are avoided, some of the associated benefits are kept. Current-carrying wires afford tunability of the resulting potentials, which in turn leads to the production of dynamic behaviour. This will also be possible with potentials based on domain walls. We anticipate that a trapping potential created using domain wall fringing fields will be inherently mobile due to the ability to reliably move domain walls [66]. The result is an architecture analogous to ion-trap chips which have demonstrated the shuttling and interaction of individual ions within circuits of very tight trapping potentials. The realisation of an equivalent device for atoms will yield the same benefits whilst providing an alternative route to achieving high-fidelity interactions.

The marriage of spintronics and atom optics into a hybrid device heralds exciting possibilities for producing controlled quantum interactions. However, significant work must be done to overcome the technical and fundamental challenges faced in such novel experiments. This is the subject of much of the work presented in this thesis. In the same way that atomic mirrors based on patterned magnetic media represented a precursor to more elaborate atom chips, we present a proof-of-principle experiment that demonstrates the feasibility of realising an interface between spintronics and ultracold atoms. We observe a reliable and tunable interaction is realised which promises much for the new hybrid quantum device that we promote and lays the foundations for future work.

1.4 Thesis layout

This thesis presents the first work which combines spintronic technology with ultracold atoms. The foregoing discussion has motivated the development of tight, mobile atom traps based on nanomagnetic domain walls, and it is this goal towards which we work.

In Chapter 2 we consider the calculation of fringing fields from nanomagnetic domain walls. An analytic model is derived in a phenomenological manner and is compared to standard numerical techniques. We show that the model we developed provides a quick, easy and intuitive method of accurately calculating the fringing fields.

In Chapter 3 we move on to describe an experiment that demonstrates the interaction between domain walls and ultracold atoms via the realisation of a magnetic atom mirror. The design of the mirror is discussed, with comparison to the ideal magnetic mirror, followed by a description of the manufacture and characterisation of the nanowire device. The experimental setup and procedure are then described.

In Chapter 4 we present the results of the mirror experiment, showing the reflection of ultracold atoms from the nanowire array, as well as the use of the atom cloud as a probe of the associated micromagnetic reconfiguration.

In Chapter 5 we describe the theory and methods used to simulate the atom mirror experiment. The interactions between the atomic cloud and the optical and magnetic fields are considered in detail.

In Chapter 6 we describe the implementation of a moving molasses scheme to launch atoms closer to the surface of the nanowire array. Initial data obtained using this scheme are presented and compared to theoretical predictions. In particular we look at the feasibility of using this technique to carry out studies of the van der Waals surface interaction.

In Chapter 7 we describe the technique of magnetic trapping and present the scheme that we hope to implement, which is based on the fringing field produced by a single domain wall. We then discuss one of the major obstacles to realising a magnetic trap based on a domain wall, which is the presence of Majorana spin-flip losses. We also describe how the conventional methods used to circumvent this problem are not appropriate in the regime of exceptionally tight traps.

In Chapter 8 we present a solution to the problem of spin-flips in very tight traps, which is a time-averaged potential based on the mechanical oscillation of a field source via piezoelectric devices. We describe how this method is inherently better suited to producing a deep, adiabatic and harmonic trap for atoms than conventional time-averaging techniques, both in a fundamental and a practical sense. We also discuss the possibility of using the same technique to produce more elaborate trapping geometries, such as a ring trap.

In Chapter 9 we summarise the conclusions drawn from this work.

1.5 Publications arising from this work

Design and characterization of a field-switchable nanomagnetic atom mirror
T. J. Hayward, A. D. West, K. J. Weatherill, P. J. Curran, P. W. Fry, P. M. Fundi, M. R. J. Gibbs, T. Schrefl, C. S. Adams, I. G. Hughes, S. J. Bending and D. A. Allwood
J. Appl. Phys. **108**, 043906 (2010)

Nanomagnetic engineering of the properties of domain wall atom traps
T. J. Hayward, A. D. West, K. J. Weatherill, T. Schrefl, I. G. Hughes and D. A. Allwood
J. Appl. Phys. **110** 123918 (2011)

A simple model for calculating magnetic nanowire domain wall fringing fields
A. D. West, T. J. Hayward, K. J. Weatherill, T. Schrefl, D. A. Allwood and I. G. Hughes
J. Phys. D **45** 095002 (2012)

Realization of the manipulation of ultracold atoms with a reconfigurable nanomagnetic system of domain walls
A. D. West, T. J. Hayward, K. J. Weatherill, P. W. Fry, T. Schrefl, M. R. J. Gibbs, C. S. Adams, D. A. Allwood and I. G. Hughes
arXiv:1112.0485

Piezoelectrically-actuated time-averaged potentials
A. D. West, C. G. Wade, K. J. Weatherill and I. G. Hughes
In preparation

Many of the ideas discussed in this thesis are also closely related to the following paper:

Mobile atom traps using magnetic nanowires
D. A. Allwood, T. Schrefl, G. Hrkac, I. G. Hughes and C. S. Adams
Appl. Phys. Lett. **89**, 014102 (2006)

Chapter 2

Domain Wall Fields

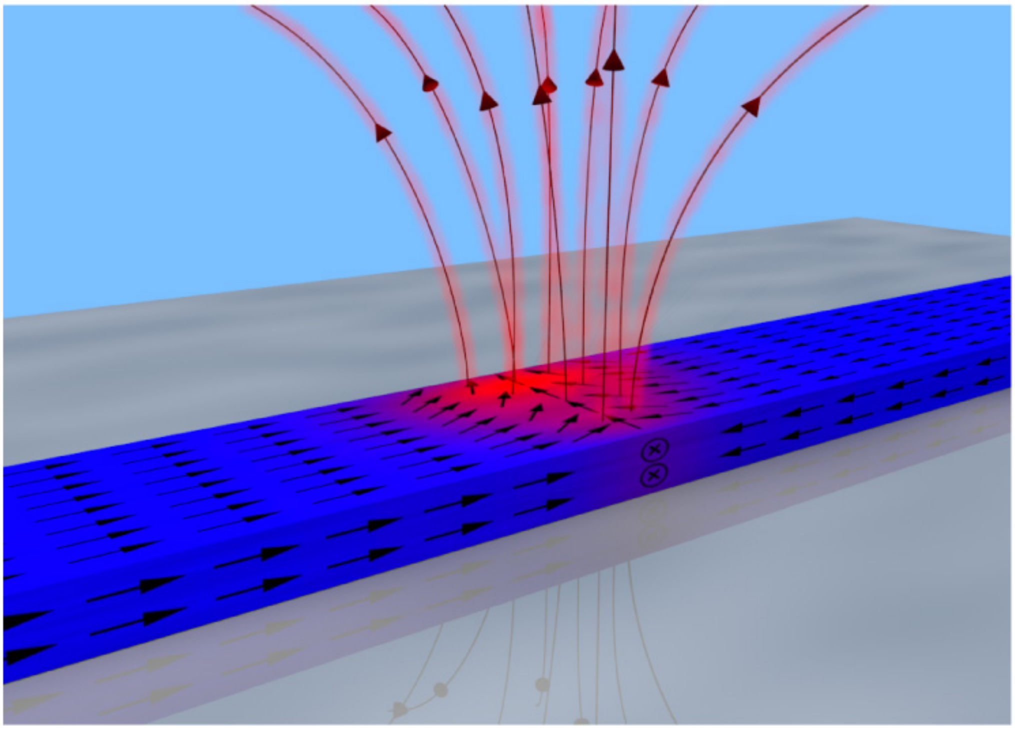

Schematic of a transverse domain wall within a planar magnetic nanowire. A quasi-discontinuous reversal of the magnetisation results in a complex magnetic structure which gives rise to fringing fields out of the plane of the wire.

The work in this section forms the basis of the following paper:

A simple model for calculating magnetic nanowire domain wall fringing fields
A. D. West, T. J. Hayward, K. J. Weatherill, T. Schrefl, D. A. Allwood and I. G. Hughes
J. Phys. D **45** 095002 (2012)

2.1 Introduction

The fringing fields produced by nanomagnetic domain walls have been harnessed within the field of spintronics. We plan to utilise the same fields to interact atoms with nanomagnetic domain walls. The character of this interaction is determined by the precise nature of the magnetic fringing fields. In order to design, realise and analyse an experiment which produces the aforementioned interaction it is important to be able to quickly and accurately calculate the fringing fields created by domain walls for a range of experimental parameters. In this section we will discuss a theoretical model which allows us to do precisely that. We will derive the model from a phenomenological consideration of the structure of domain walls and then analyse the fidelity of the model through a comparison with established numerical techniques.

The calculation of nanomagnetic fringing fields from domain walls is in general a difficult task. Micromagnetic techniques represent the most accurate method of calculation [67, 68]. Throughout this work, references to calculations carried out according to micromagnetic techniques correspond to work carried out by colleagues at The University of Sheffield (Schrefl, Hayward et al.). Whilst described in detail elsewhere [69] we will give just a brief overview of the method here. The Landau-Lifshitz-Gilbert equation is solved within a finite element framework [68] whilst accounting for energy contributions due to magnetostatics, magnetocrystalline anisotropy, Zeeman interactions and exchange interactions. A bi-domain structure is introduced into the simulated wires which are allowed to relax to equilibrium. The resulting magnetisation structure is then used as the basis of a calculation of the associated magnetic fields according to the quasi-static Maxwell equations using finite element/boundary element methods [65]. The fringing fields created at the discontinuities of the wire ends are subtracted.

In this work we consider domain walls within planar nanowires which form between oppositely orientated domains. Examples of the resulting magnetisation structure are shown in Figure 2.1(a). Sufficiently far from the domain wall the magnetisation is uniformly aligned along the wire length. Between the two domains the quasi-discontinuous reversal of the magnetisation over the width of the domain wall produces a much more complicated magnetisation structure. This non-trivial direction change produces a region of magnetisation divergence, pictured in Figure 2.1(b), which results in fringing fields out of the plane of the wire. Away from the domain wall there are no such out-of-plane fields. The same features have also been observed via experimental methods [71]. The domain walls form in two characteristic shapes, transverse or vortex, with the latter being found in wires of larger cross section.

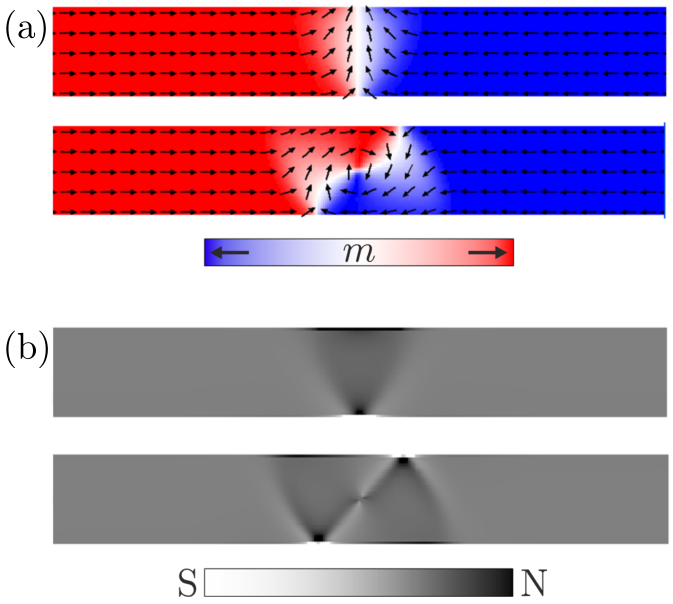

Figure 2.1: Magnetisation structures as calculated via micromagnetic methods (Schrefl et al.) [70]. In both parts the upper wire contains a transverse-type domain wall (200 nm × 5 nm cross section) and the lower a vortex-type wall (200 nm × 15 nm cross section). (a) shows the direction of the magnetisation, shading represents the longitudinal magnetisation component. (b) shows the divergence of the magnetisation. Dark (light) areas represent positive (negative) $\vec{\nabla}.\vec{M}$, or effective 'north' ('south') poles.

Whilst the use of micromagnetic techniques is the most rigorous and accurate method of calculating fringing fields, it is also time consuming and requires specialist knowledge and software to perform. A quicker and more accessible method is desirable, particularly during the planning of experimental applications, as excellent precision is not vital at all times.

The divergence of the magnetisation can also be thought of as a concentration of magnetic poles, from which magnetic field emanates. In this way an analogy is drawn between electrostatics, and we can associate a magnetic charge density with the domain wall region. This picture is the basis of the analytic models for calculating the fringing fields.

2.2 Derivation of models

2.2.1 Monopole model

The simplest analytic model assumes that a domain wall is a point object — an assumption which is increasingly valid as one considers going further from the wall. The result is that the domain wall is represented by a magnetic monopole. Whilst this is explicitly forbidden by Maxwell's equations, magnetic monopoles have been posited and observed as quasiparticles [72, 73, 74]. We will use the monopole as a theoretical construct to which we prescribe an effective magnetic charge. This representation is one followed elsewhere, e.g. [72, 75, 76]. We now derive the associated charge, following the treatment in [77].

Consider a planar nanowire of width w and thickness t as illustrated in Figure 2.2. The domain wall is contained within a width s. In the presence of a magnetic medium we have from Maxwell's equations

$$\mu_0 \vec{\nabla}.\left(\vec{H}+\vec{M}\right)=0, \tag{2.1}$$

where μ_0 is the permeability of free space, $\vec{H}$ is the magnetic field and $\vec{M}$ is the bulk magnetisation. The volumetric charge density of the domain wall is given by ρ_{m}. Thus, in analogy to Gauss' law for electrostatics, we have

$$\vec{\nabla}.\vec{H}=\rho_{\mathrm{m}}/\mu_0. \tag{2.2}$$

The charge within the domain wall is due to both the volume charge associated with divergence of $\vec{M}$ within the bulk, and by edge charge regions which

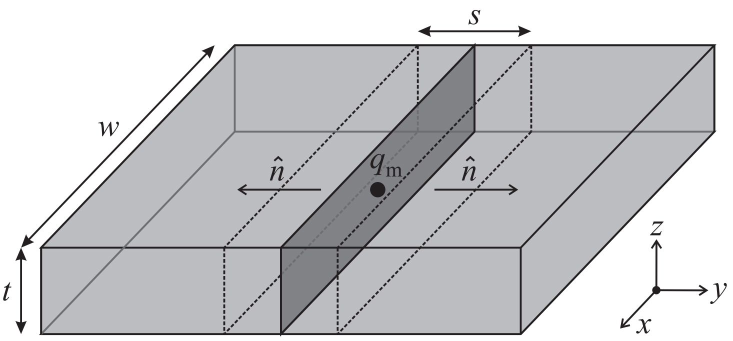

Figure 2.2: Schematic of a planar nanowire of cross section wt containing a domain wall within a region of width s. As $s \to 0$ the wall becomes a discontinuous reversal. The wall is approximated by a charge q_{m}.

occur at the discontinuities of the nanowire edges. We assume for the remainder of this treatment that the former of these is the dominant contributor to the magnetic charge. This is supported by experiment, micromagnetic simulations [71], and the resulting accuracy of our analytic models.

If, as we have assumed, the magnetic charge is confined to a point, its value is then given by the integral of ρ_{m} over the domain wall volume:

$$q_{\mathrm{m}} = \int \rho_{\mathrm{m}} \; \mathrm{d}V = -\mu_0 \int \vec{\nabla}.\vec{M} \; \mathrm{d}V. \tag{2.3}$$

This can be recast, by using the divergence theorem, in terms of the magnetisation through an enclosing surface. If we take the limit of the domain wall being a discontinuous reversal of magnetisation, i.e. $s \to 0$ in Figure 2.2, then this yields a simple expression for q_{m}:

$$q_{\mathrm{m}} = -\mu_0 \int \vec{M}.\hat{n} \; \mathrm{d}S = 2\mu_0 M_{\mathrm{s}} wt. \tag{2.4}$$

Here $\hat{n}$ is the unit normal of the surface element $\mathrm{d}S$, with S enclosing V. From hereon we use M_{s}, the saturation magnetisation of the nanowires ($M_{\mathrm{s}} = 8.6 \times 10^5$ for permalloy [46]). We have assumed that the domain wall is of a 'head-to-head' type; a 'tail-to-tail' domain wall has an associated charge of $-q_{\mathrm{m}}$. Note that Equation 2.4 also provides an expression for the surface magnetic charge density, $\sigma_{\mathrm{m}} = -\mu_0 \vec{M}.\hat{n}$. The expression on the right hand side of Equation 2.4 is very similar to that prescribed in other systems, cf. e.g. [75]. The magnetic flux density, $\vec{B}$, ('magnetic field' from hereon), at a position $\vec{r}$ is then given, in direct analogy to Coulomb's law, by

$$\vec{B}\left(\vec{r}\right) = \frac{q_{\mathrm{m}}}{4\pi|\vec{r}|^2}\hat{r}. \tag{2.5}$$

Note that $\vec{B}$ and $\vec{H}$ only differ by a factor of μ_0.

This is the simplest analytic model, and is accurate at large distances from a domain wall, where the approximation of the wall being a point object becomes valid. We will now extend this model to more accurately represent a domain wall as an object of finite size. As already stated, we assume that volume charge is the dominant contribution to the magnetic charge. Thus each refinement of the model produces a more faithful representation of the characteristic shape of the magnetic pole distribution, illustrated in Figure 2.1(b).

2.2.2 1D model

The first extension we present is to model the domain wall as a 1D line of charge, across the width of a nanowire. This situation is illustrated in Figure 2.3. The infinitesimal element of magnetic field, dB, produced by the element of magnetic charge within a length dx_{N} is shown. We use the subscript 'N' to signify coordinates within the nanowire.

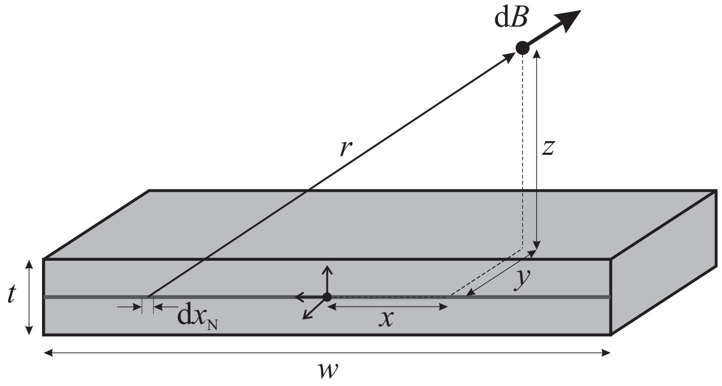

Figure 2.3: Schematic of a domain wall represented by a line of charge across a nanowire width. The wire axis is into the page (along y). The magnetic field, dB, from an element of this line of charge is shown.

The magnetic field from such a line of charge is found by integrating the contributions from infinitesimal elements of charge, $\mathrm{d}q_{\mathrm{m}} = 2\mu_0 M_{\mathrm{s}} t\ \mathrm{d}x_{\mathrm{N}}$, across the width of the wire. We define a position $\vec{r} = (r_x, r_y, r_z) = (x - x_{\mathrm{N}}, y - y_{\mathrm{N}}, z - z_{\mathrm{N}})$ as the vector from an infinitesimal element of charge, located at $(x_{\mathrm{N}}, y_{\mathrm{N}}, z_{\mathrm{N}})$ to the point under consideration. Note in this case that $y_\mathrm{N} = z_\mathrm{N} = 0$. The components of magnetic field are thus

$$B_i = \frac{\mu_0 M_\mathrm{s} t}{2\pi} \int_{-w/2}^{w/2} \frac{r_i}{|\vec{r}|^3}\ \mathrm{d}x_\mathrm{N}. \tag{2.6}$$

Evaluation of these integrals yields:[1]

$$B_x = \tfrac{\mu_0 M_\mathrm{s} t}{2\pi}\left[\tfrac{2}{\sqrt{(w-2x)^2+4(y^2+z^2)}} - \tfrac{2}{\sqrt{(w+2x)^2+4(y^2+z^2)}}\right], \tag{2.7}$$

$$B_y = \tfrac{\mu_0 M_\mathrm{s} t y}{\pi(y^2+z^2)}\left[\tfrac{w-2x}{2\sqrt{(w-2x)^2+4(y^2+z^2)}} + \tfrac{w+2x}{2\sqrt{(w+2x)^2+4(y^2+z^2)}}\right], \tag{2.8}$$

$$B_z = \tfrac{\mu_0 M_\mathrm{s} t z}{\pi(y^2+z^2)}\left[\tfrac{w-2x}{2\sqrt{(w-2x)^2+4(y^2+z^2)}} + \tfrac{w+2x}{2\sqrt{(w+2x)^2+4(y^2+z^2)}}\right]. \tag{2.9}$$

These expressions will be seen to confer significant advantage over the simple point charge model when the distance from the domain wall is reduced.

2.2.3 2D model

The models presented up until now have considered the domain wall to have no extent along the length of the wire, or through its thickness. We now consider both of these situations.

Let us consider first the case of a domain wall having some finite size, s, along the wire length, y. This situation is illustrated in Figure 2.4. The domain wall now resembles a rectangular sheet of magnetic charge of width s. We choose to fix the value of s to be w. This is a rule of thumb which provides the user good accuracy without having to find the optimal value of s. Using $s = w$ is representative of the magnetisation structures calculated via micromagnetic methods [78], and the observed structures of real domain walls. As will be discussed later, there is only a very small loss of accuracy in using this rule of thumb. The corresponding expression for an infinitesimal element of this charge, contained within an element $\mathrm{d}A = \mathrm{d}x_\mathrm{N}\mathrm{d}y_\mathrm{N}$, is $\mathrm{d}q_\mathrm{m} = 2\mu_0 M_\mathrm{s} t/w\ \mathrm{d}x_\mathrm{N}\mathrm{d}y_\mathrm{N}$. In analogy to Equation 2.6 we now have

$$B_i = \int_{-w/2}^{w/2}\int_{-w/2}^{w/2} \frac{\mu_0 M_\mathrm{s} t r_i}{2\pi w\,|\vec{r}|^3}\ \mathrm{d}x_\mathrm{N}\mathrm{d}y_\mathrm{N}. \tag{2.10}$$

---

[1] An alternative route to deriving these expressions is to use the magnetic scalar potential, Φ, and integrating in an entirely analogous manner. The magnetic field is then given by $-\vec{\nabla}\Phi$. Whilst entirely equivalent, we will integrate expressions for the magnetic field directly throughout for the sake of clarity.

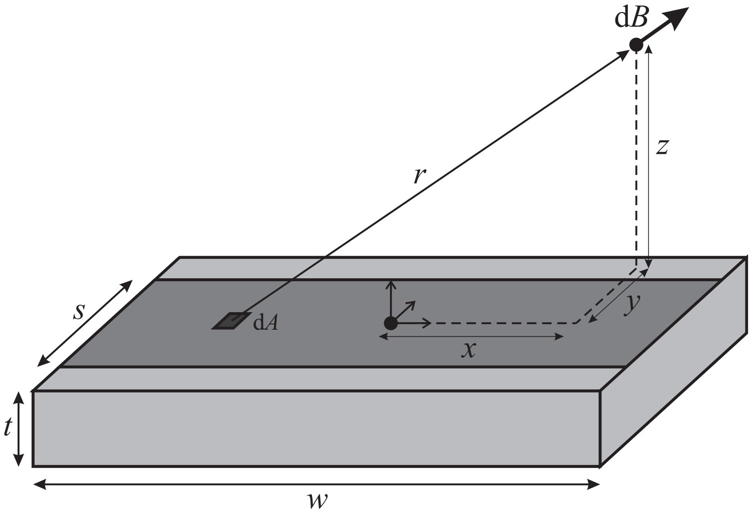

Figure 2.4: Schematic of a domain wall represented by a 2D sheet of charge extending along the wire length. The wire axis is into the page (along y). The magnetic field, dB, from an element of this sheet of charge is shown.

These integrals were performed symbolically [79], see also e.g. [80], yielding:

$$B_x = \tfrac{\mu_0 M_\mathrm{s} t}{2\pi s} \log\left[\frac{(s-2y)+\sqrt{(2x-w)^2+(2y-s)^2+4z^2}}{(s-2y)+\sqrt{(2x+w)^2+(2y-s)^2+4z^2}} . \frac{(-s-2y)+\sqrt{(2x+w)^2+(2y+s)^2+4z^2}}{(-s-2y)+\sqrt{(2x-w)^2+(2y+s)^2+4z^2}}\right], \tag{2.11}$$

$$B_y = \tfrac{\mu_0 M_\mathrm{s} t}{2\pi s} \log\left[\frac{(w-2x)+\sqrt{(2x-w)^2+(2y-s)^2+4z^2}}{(w-2x)+\sqrt{(2x-w)^2+(2y+s)^2+4z^2}} . \frac{(-w-2x)+\sqrt{(2x+w)^2+(2y+s)^2+4z^2}}{(-w-2x)+\sqrt{(2x+w)^2+(2y-s)^2+4z^2}}\right], \tag{2.12}$$

$$\begin{aligned} B_z = \tfrac{\mu_0 M_\mathrm{s} t}{2\pi s} \Bigg\{ & \tan^{-1}\left[\frac{2(w/2-x)(s/2-y)}{z\sqrt{(2x-w)^2+(2y-s)^2+4z^2}}\right] + \tan^{-1}\left[\frac{2(w/2-x)(s/2+y)}{z\sqrt{(2x-w)^2+(2y+s)^2+4z^2}}\right] \\ & + \tan^{-1}\left[\frac{2(w/2+x)(s/2-y)}{z\sqrt{(2x+w)^2+(2y-s)^2+4z^2}}\right] + \tan^{-1}\left[\frac{2(w/2+x)(s/2+y)}{z\sqrt{(2x+w)^2+(2y+s)^2+4z^2}}\right]\Bigg\}. \end{aligned} \tag{2.13}$$

Equivalent expressions were also found for the case of a sheet of magnetic charge in the $x - z$ plane by evaluating the following integrals,

$$B_i = \int_{-w/2}^{w/2} \int_{-t/2}^{t/2} \frac{\mu_0 M_\mathrm{s} r_i}{2\pi \left|\vec{r}\right|^3} \, \mathrm{d}z_\mathrm{N} \mathrm{d}y_\mathrm{N}, \tag{2.14}$$

however this type of 2D model was not seen to confer greater accuracy than the 1D model so shall not be discussed further. This can be understood intuitively by the fact that the wire thickness is in general small compared to the distance from the wire.

2.2.4 Triangular model

The final extension to the model is to incorporate the characteristic triangular shape that is observed in both real domain walls and micromagnetic simulations (cf. Figure 2.1). This shape is particular to transverse-type domain walls; for the case of a vortex wall the region of high $\left|\vec{\nabla}.\vec{M}\right|$, and hence volume charge, is approximately rectangular, so the 2D model of the previous section is more appropriate. We now consider a triangular region of magnetic charge that emulates this characteristic shape. The geometry of this triangular model is illustrated in Figure 2.5. As with the 2D model of the previous section there is a free parameter, s, which is the size of the base of the triangle. Again we implement the rule of thumb $s = w$ which is representative of real domain walls [78] and provides a good accuracy.

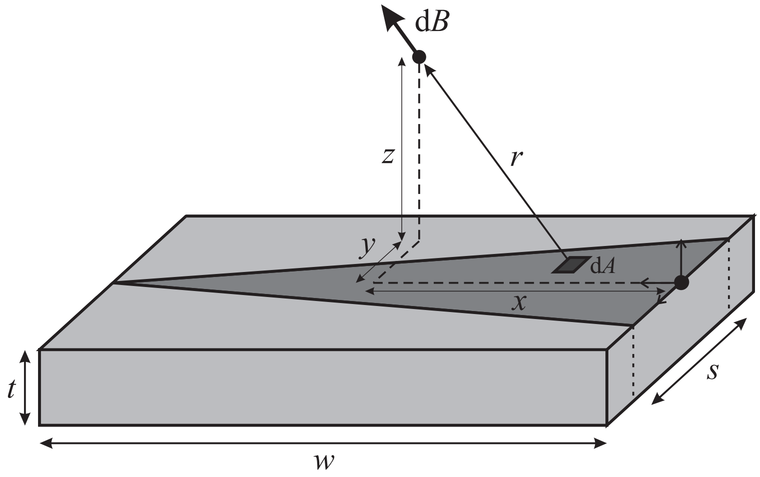

Figure 2.5: Schematic of a transverse domain wall represented by a triangular sheet of charge. The wire axis is into the page (along y). The magnetic field, dB, from an element of this sheet of charge is shown.

It is easy to modify the equations of previous sections in accordance with the new geometry. The same amount of charge is now contained in half the area so we have $\mathrm{d}q_{\mathrm{m}} = 4\mu_0 M_{\mathrm{s}} t/w \;\; \mathrm{d}x_{\mathrm{N}}\mathrm{d}y_{\mathrm{N}}$. Equation 2.10 is modified so that the bounds of integration now describe a triangle:

$$B_i = \int_0^w \int_{-x_{\mathrm{N}}}^{x_{\mathrm{N}}} \frac{\mu_0 M_{\mathrm{s}} t r_i}{\pi s r^3} \, \mathrm{d}y_{\mathrm{N}} \mathrm{d}x_{\mathrm{N}}. \tag{2.15}$$

Note again that we have made the assumption $s = w$. Unfortunately it was not possible to find a closed expression for all 3 components of the magnetic fields (or equivalently, 2 components and $|\vec{B}|$). Thus it was necessary to perform the integration numerically. Performing this integration is quicker and easier than performing micromagnetic simulations for comparable resolution, but it is significantly slower than the analytic expressions which we have used up until now. It is possible, however, to speed up the integration significantly by using the result for a 2D (rectangular) domain wall.

We consider dividing a triangular domain wall into a series of infinitesimally wide rectangular elements, as shown in Figure 2.6. The form of the field from each of the rectangles is known analytically. It is then a simple matter to perform a coordinate transformation between each rectangle (whilst modifying the length of the rectangle appropriately) and sum the field contributions. This provides a much quicker method of calculating the field from a triangular domain wall. For example it takes around 2 seconds to calculate the field from each rectangle on a desktop PC. It is possible to use as few as 40 rectangles with negligible loss of accuracy.

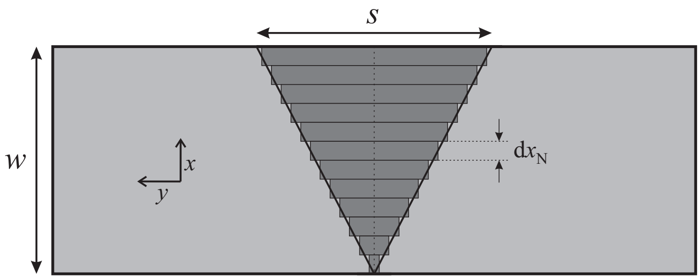

Figure 2.6: Schematic of a triangular domain wall divided into a set of thin rectangular sheets of magnetic charge. The wire axis is along y. Typically around 40 rectangles are used.

2.3 Analysis of models

As has already been stated, calculations based on micromagnetic simulations are the most accurate possible. To assess the accuracy of the models we present we shall compare their results with those from micromagnetics. The fields produced by the latter are considerably more complex than those produced by the analytic models, indicating the complicated magnetisation structure. This detailed structure becomes increasingly apparent nearer the domain wall – moving further away the approximation of the wall as a point object becomes increasingly valid. This behaviour is illustrated in Figure 2.7. From here on we will label these two regimes as the 'near-field' and 'far-field' regions. We will now discuss the quantitative analyses of the accuracy of the calculated fringing fields.

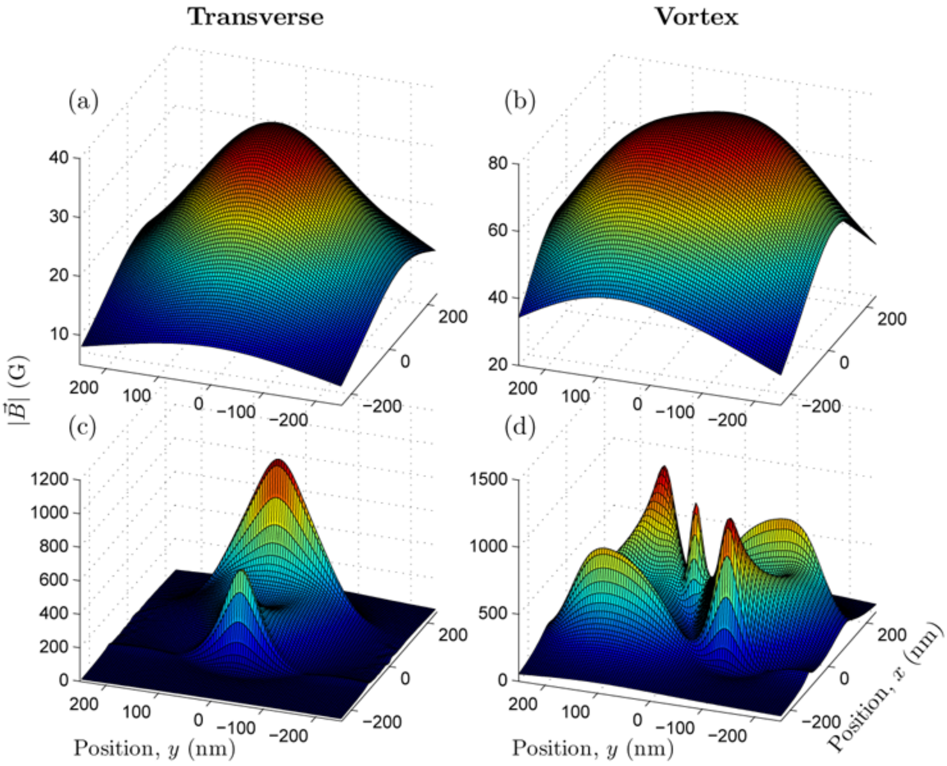

Figure 2.7: Plots of the magnetic fringing field magnitude calculated via micromagnetic simulations (Hayward et al.) [70]. (a) and (c) correspond to a transverse-type domain wall (cross section = 200 nm × 5 nm), whilst (b) and (d) correspond to a vortex-type domain wall (cross section = 200 nm × 15 nm). (a) and (b) show the field magnitude at a height of 200 nm whilst (c) and (d) show the field at 12.5 nm. Note the complex field structure at short distances, indicative of the domain wall's complicated magnetisation.

The magnetic fringing fields from six different nanowires were calculated. The geometries of these wires are summarised in Table 2.1. For the sake of brevity we will present analysis for just one wire geometry, wire B, but data

Table 2.1: The six geometries of wire examined in comparisons with fields from micromagnetic methods.

Label	**Width (nm)**	**Thickness (nm)**	**Wall type**
A	100	5	Transverse
B	200	5	Transverse
C	400	5	Transverse
D	100	15	Vortex
E	200	15	Vortex
F	400	15	Vortex

for all six wires considered is provided in Appendix A. We consider a region of size 1 µm × 1 µm × 1 µm, evenly divided into a mesh of 10^6 points. The base of this cube is centred on the middle of the domain wall. This region is representative of the typical regime that atomic physics applications aim to work within. The size of the field outside this region is typically less than 1 G.

In the following analysis we will make comparisons of the magnitude of the magnetic field, for clarity. Comparison of the field direction is also provided later in the section.

2.3.1 Maximum field error

The first figure of merit to be considered is the maximum field at a given height. This provides a good indicator of the models' accuracy and is also an important quantity in relation to magnetic trapping applications as it can define the position of the trap minimum. Figure 2.8 shows the maximum field at a given height according to the models presented and as calculated via micromagnetic simulations. One can immediately see that there is very good agreement with micromagnetic simulations at heights above around 100 nm. Below this height the analytic models begin to show significant inaccuracy, with the largest error being apparent in the 'monopole' model. At smaller heights the approximation of the wall as a point object becomes increasingly inaccurate and in general the micromagnetic structure becomes much more important. As will be seen this is an unavoidable problem with

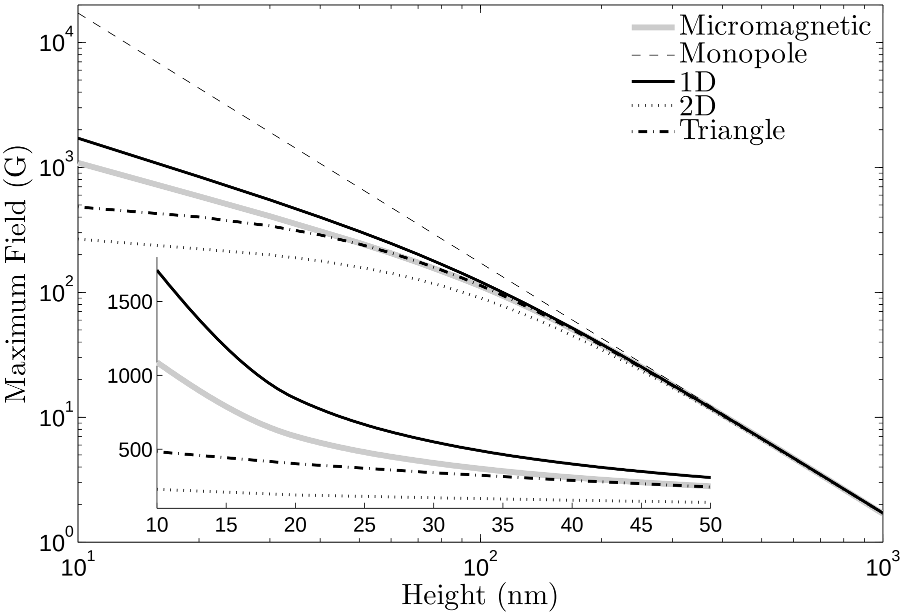

Figure 2.8: The maximum fringing field magnitude at a given height above a transverse domain wall (cross section = 200 nm × 5 nm) as calculated by the various analytic models and via micromagnetic simulations. Note the log scale on the main figure.

the analytic models — in the near-field region none of the models accounts for the complex structure of real fringing fields.

The observant reader will note that within this near-field region there are points where the 1D model provides better accuracy than the 2D model. The accuracy of the 2D model can be improved significantly by tuning the parameter s, however this is contrary to the aim of the analytic models as this would require optimisation against micromagnetics for each wire geometry. We also note that whilst this may improve the accuracy of the maximum field value, it also decreases the overall accuracy of the fields, which is a figure of merit we will now consider.

2.3.2 RMS field error

A more thorough analysis of the fidelity of the models is provided by examining the accuracy of the fringing fields over the entire 1 μm^3 region. We now calculate the root mean square (RMS) error, E_{RMS}, over all points at a given height, expressed as a percentage. For an analytic field, $|\vec{B}|$, and the field calculated via micromagnetics, $|\vec{B}_{\mathrm{M}}|$, given over a set of N points $\{\vec{r}_i\}$ we have

$$E_{\mathrm{RMS}} = \sqrt{\frac{100^2}{N}\sum_{i}^{N}\frac{(|\vec{B}(\vec{r}_i)| - |\vec{B}_{\mathrm{M}}(\vec{r}_i)|)^2}{|\vec{B}_{\mathrm{M}}\,(\vec{r}_i)\,|^2}}. \tag{2.16}$$

Figure 2.9 shows E_{RMS} over the 1 μm range of heights for all the analytic models presented.

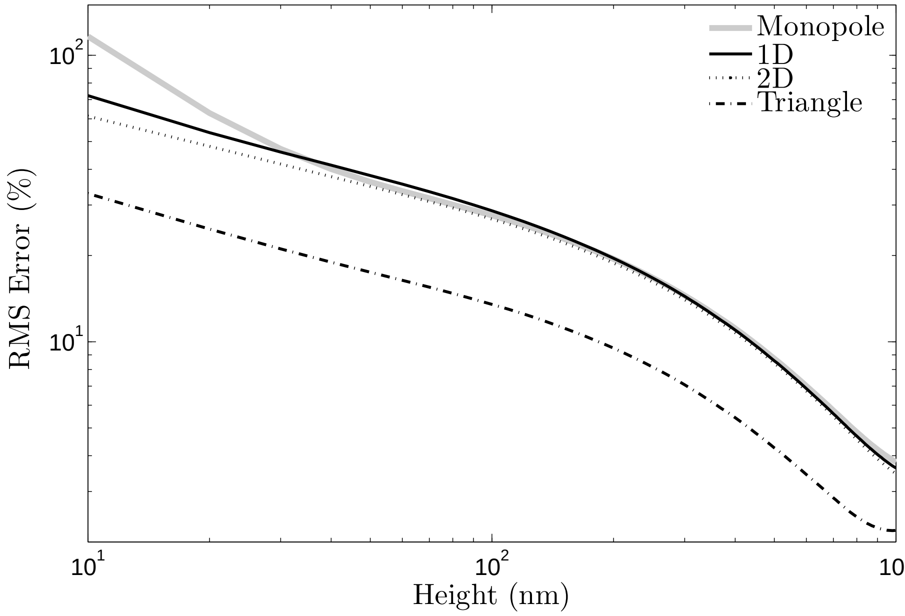

Figure 2.9: The RMS percentage error in the fringing field magnitude at a given height above a 200 nm × 5 nm domain wall according to the analytic models presented. Note the log scale.

As with the analysis of the maximum field magnitude in Figure 2.8 there is an obvious trend — the error significantly increases as one enters the near-field region. There are also some clear distinctions between the models. There is little difference between the accuracies of the monopole, 1D and 2D models until small heights, where increasing the dimensionality of the model of the domain wall gives an improved accuracy, in particular moving from the monopole model to a 1D line of charge gives great improvement. This is an intuitive result as nearer the domain wall the approximation of it being a point object becomes less appropriate. A smaller improvement is seen by giving the domain wall finite extent along the wire.

There is a stark improvement gained by incorporating a triangular shape.

This change provides a much more accurate representation of the magnetic field shape. Examination of Figure 2.7(a) shows that the field is in fact skewed across the width of the wire, with larger fields observed closer to the triangle's base. This observation supports our choice of representing the domain wall by a region of volume charge; the magnetic pole distribution is an important determining factor when considering the resultant fringing fields.

We note that for heights of 100 nm or greater we achieve accuracies of 15% or less. Whilst the accuracy breaks down lower than this it is unlikely that magnetic trapping schemes will aim to work within this region as such traps may suffer from anharmonicities due to the complex field shape and from noise due to thermal fluctuations [31]. Some spintronics applications require knowledge of fields at distances of the order of 10s of nm, e.g. read/write heads for 'racetrack memory' [61] can be located at heights of around 10 nm [65]. For these kinds of applications one must use calculations based on micromagnetics.

The RMS error over the entire 1 $\mu\mathrm{m}^3$ region for all wires and models is quoted in Appendix A. We also provide the mean percentage error,

$$E_{\mathrm{M}} = \frac{100}{N} \sum_{i}^{N} \frac{\left| (|\vec{B}(\vec{r}_i)| - |\vec{B}_{\mathrm{M}}(\vec{r}_i)|) \right|}{|\vec{B}_{\mathrm{M}}(\vec{r}_i)|}. \tag{2.17}$$

2.3.3 Domain wall width

In the derivations of the 2D and triangular models the free parameter s was introduced. This describes the physical extent of the charge region used to describe the domain wall. To establish the rule of thumb, $s = w$, the RMS, mean and maximum (E_{max}) percentage errors were analysed as s was varied. By doing so it was possible to find the optimal values of s for each wire geometry and for both the 2D and triangular models. For example, Figure 2.10 shows the variation of these errors with s for the case of a 200 nm × 5 nm domain wall modelled according to the triangular model. In this instance s represents the length of the base of the triangular sheet of charge. As can be seen there are clear minima in the errors. Through an examination of this dependence on s the rule of thumb of $s = w$ was chosen. As can be seen in Figure 2.10 this value is close to the minima of all the measures of the error

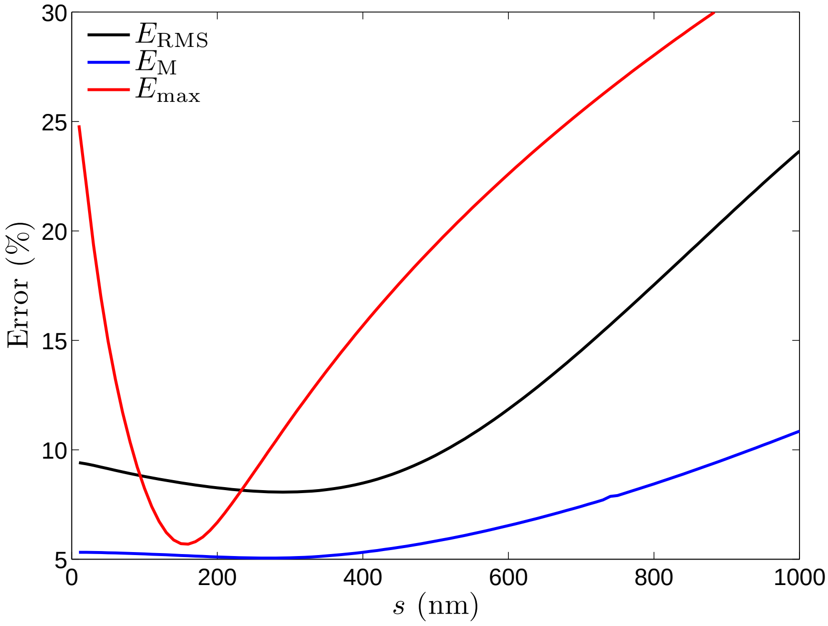

Figure 2.10: The RMS, mean and maximum percentage errors in the field above a 200 nm × 5 nm domain wall, calculated over a 1 μm^3 region according to the triangular model, as the parameter s is varied.

(recall $w = 200$ nm in this case).

To assess the loss of accuracy associated with by employing this rule of thumb, the RMS error using an optimised value of s was also calculated. This is given by E'_{RMS} and values are provided where appropriate in Appendix A. It is clear that the loss of accuracy is very small.

The relative insensitivity to the parameter s is perhaps counterintuitive but unsurprising when one notes that the distribution of charge across the wire width is independent of s for both the rectangular and triangular models. Whilst the former of these is obvious, the inifinitesimal element of charge located at a position x_{N} within a triangle of base s is given by

$$\mathrm{d}q_{\mathrm{m}}(x_{\mathrm{N}}) = 4M_{\mathrm{s}}\mu_0 t/s \;\, \mathrm{d}A = 4M_{\mathrm{s}}\mu_0 t x_{\mathrm{N}}/w \;\, \mathrm{d}x_{\mathrm{N}}, \tag{2.18}$$

which is clearly independent of s. This result is related to the geometric fact that all triangles have centres of mass at barycentric coordinates (1/3,1/3,1/3). This is reflected in the fields calculated according to the triangular model. When sufficiently far from the wire the maximum field at a given height is located at $(x, y) = (w/3, 0)$. Recall, as per Figure 2.5, the coordinate origin is defined to be at the centre of the triangle's base. Note that integrating Equation 2.18 with respect to x_{N} yields Equation 2.4.

2.3.4 Distribution of error

The figures of merit analysed so far indicate that it is possible to achieve a good accuracy using a simple analytic model, in particular the triangle model reproduces the shape of real fringing fields well. However, the best indicator of the accuracy of a model is found by examining the distribution of error. It is possible that measures such as E_{RMS} or E_{M} hide the fact that there are regions of very high error. In order to check this the distribution of the percentage error over all points was analysed. An example of this is given in Figure 2.11 for the case of the 200 nm × 5 nm wire, using the triangular model. The distribution of error shows that the figures of merit used thus far are suitable indicators of the accuracy of the calculated fields; there are no regions with unexpectedly high error. The large majority of points have an error of 20% or less at all heights. It is reasonable to expect that the points with the largest error at a given height are those closest to the domain wall barycentre, i.e. those near to $x = w/3, y = 0$. The field further from the domain wall varies much more smoothly and is more easily replicated. To an extent this is true – points far from the wall generally have a lower associated error. However the white line in Figure 2.11 represents the points above the barycentre and it can be seen that there are a number of points with both larger and smaller error. Although the error generally increases as one goes closer to the wall centre there is not a simple reason for the observed deviations from this trend, particularly at small heights.

2.3.5 Field isosurfaces

As should be apparent from the previous discussion, the error that one associates with the calculated fields can depend on the region over which the fields are examined. The overall error can be minimised by comparing the field over a larger region as this includes more points with very small field which are more easily accurately reproduced by our models. However, a small absolute (percentage) error in calculating a small (large) field produces

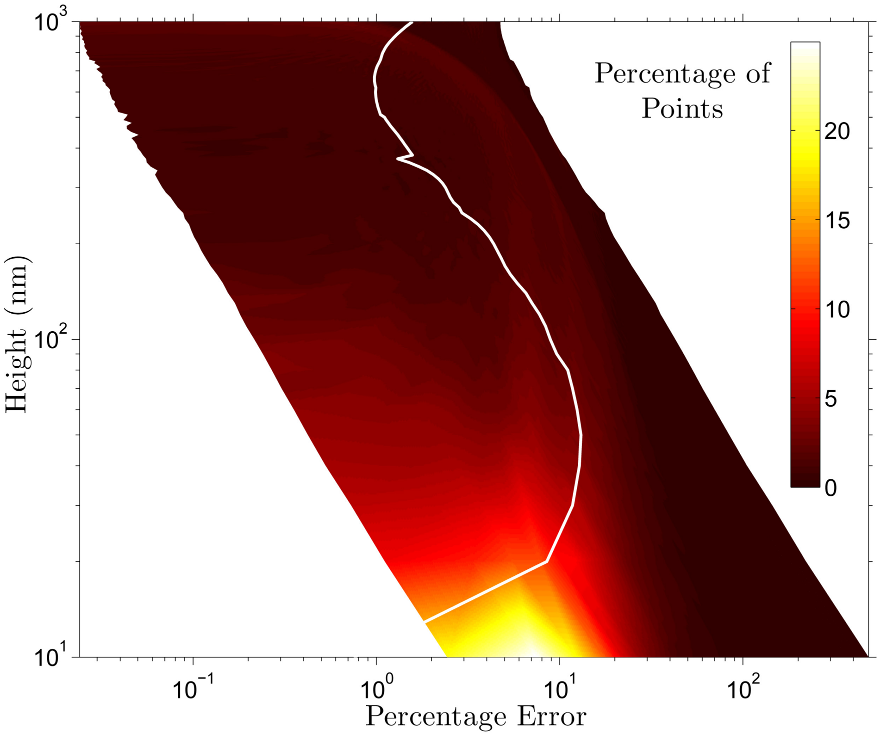

Figure 2.11: The distribution of the percentage error in the fringing field magnitude above a 200 nm × 5 nm domain wall, calculated according to the triangular model. At each height the data are divided into 100 evenly distributed bins (note the bin centres vary dramatically across the range of heights). The white line represents the error in the maximum field at each height.

a deceptively large percentage (absolute) error.

Whilst it will be clear that the desired application will define the region of space to consider, and that few applications are likely to utilise the fields very far from nanomagnetic domains, for the purpose of this analysis a scale-invariant figure of merit is desired. This is provided by examining the models' accuracies over regions of specific field strength, rather than regions of space.

Figure 2.12 shows the RMS percentage error associated with a set of points located around an isosurface of $\vec{B}_{\mathrm{M}}$. For a given B_0 the RMS error is calculated over all points that satisfy $0.9B_0 \leq \left|\vec{B}_{\mathrm{M}}\right| \leq 1.1B_0$. Thus the error is analysed over different magnetic field strengths, removing biases associated with the size of the region examined, or the size of the nanowire, whilst still permitting a meaningful analysis of the fidelity of the models to the shape of the magnetic fields. This can be a particularly useful measure as in many applications it is the field, rather than the physical location, that defines the working regime.

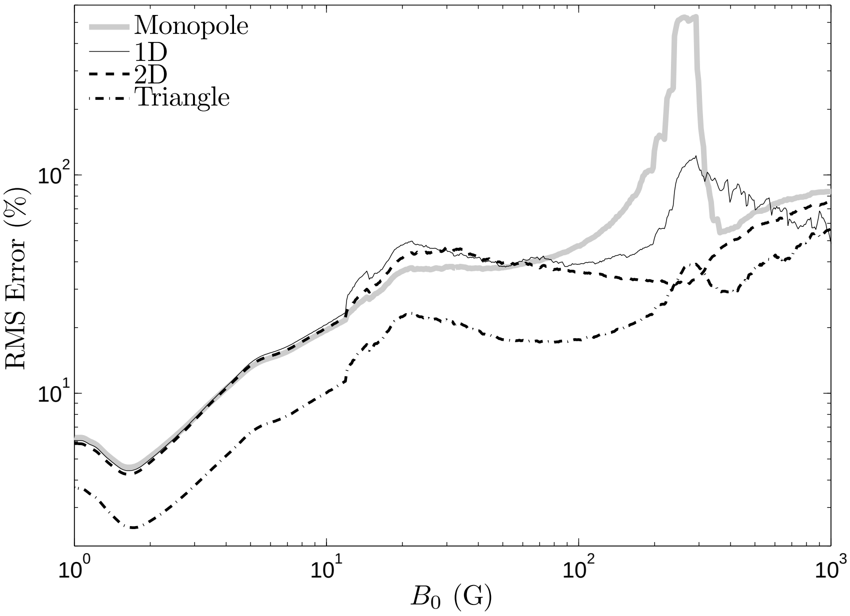

Figure 2.12: The RMS percentage error of fringing fields associated with regions surrounding isosurfaces of field strength. Calculations are performed for a 200 nm × 5 nm domain wall, according to the triangular model. For a given B_0 the error is calculated over all points for which $|\vec{B}_\mathrm{M}|$ is within 10% of B_0.

Examining Figure 2.12, familiar trends are observed. There is an increase in the error of the model as the magnetic field increases — this corresponds to points which are generally closer to the wire. There is also a clear improvement by incorporating a triangular shape to the model. For small fields (large distances) the monopole, 1D and 2D models converge as the approximation of the domain wall as a point object becomes more appropriate. For very large fields the distinction between the different models becomes less clear. This is indicative of the fact that none of the models accurately reproduces the complex field shape seen in regions of high field (cf. Figure 2.7), and that there are fewer points with very high field over which a comparison can be made. The regime where there is the clearest difference between the accuracy of the models is around 10–100 G — the triangular model shows a three- or four-fold improvement over other models. It is within this regime that the asymmetry of the transverse wall becomes apparent in the fringing fields, without displaying the complex structure seen at very short distances.

2.3.6 Field direction

Discussion up to this point has deliberately focussed on the magnitude of the magnetic field. We now examine the direction of the field. Comparing the magnetic field components, B_i, has the inherent problem that B_x and B_y have zero points for all z. Instead we compute the relative angle between the magnetic field vectors $\vec{B}_\mathrm{M}$ and $\vec{B}$. The error observed shows a very similar trend to the errors in the magnetic field magnitude. As expected, none of the models reproduces the field direction well at very short distances, but the error above around 100 nm is small. For example, Figure 2.13 shows the RMS error in the direction of the field from a 200 nm × 5 nm domain wall, modelled by a triangular sheet of charge.

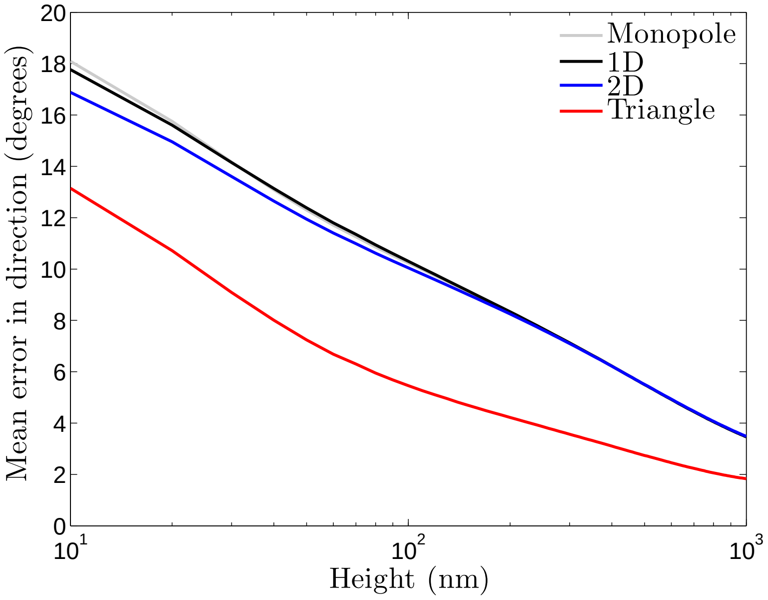

Figure 2.13: The RMS error in the fringing field direction at a given height for a 200 nm × 5 nm domain wall, calculated using each of the analytic models.

Through an examination of the various models it is clear that there is very little difference in the accuracy of the field direction calculated using the monopole, 1D and 2D models. This is intuitively expected as the shapes of the fields are very similar, especially in the far-field region, for example moving from 1D to 2D can simply be thought of as a small 'spreading out' of the magnetic field source, which from sufficiently far away has very little effect on the field direction (although, as has been seen, it can have a significant effect on its magnitude). In contrast, the triangular model confers a significantly more accurate field shape at all heights. This reflects the fact that the triangular model reproduces the skewed shape apparent in transverse domain wall fringing fields (cf. Figure 2.7(a)) at all heights.

The computed RMS error values suggest a high level of accuracy — when using the triangular model there is an error of less than 10° (5°) at heights above 25 nm (125 nm). The corresponding errors when using the 2D model are 14° and 9°. However there are regions within the near-field where there are large discrepancies. This is due to the fact that the magnetisation structure of real domain walls gives rise to areas of negative magnetic charge. This is indicated in Figure 2.1(b) by the small region of edge charge at the apex of the triangle — the sign of the divergence is opposite to that of the volume charge within the triangle itself. Thus the direction of the magnetic field near this point is primarily into the nanowire, rather than out of it. As would be expected, this feature is not well reproduced by any of the models we have developed, but its influence is limited to very close to the apex of the domain wall, and has significantly less influence on the field magnitude.

The analysis presented here has considered one nanowire geometry in particular. Analysis was carried out for all six of the geometries given in Table 2.1. For each of the wires the trends are very similar to those already presented. Between the wires there was also a noticeable trend – the error is generally larger for wires of larger cross section. This is an intuitive result as the near-field region of larger wires occupies a greater proportion of the 1 μm^3 region examined, and it is this region which produces the largest errors.

2.3.7 Case study — a time-averaged-potential

As a demonstration of the utility of the models that we have presented we consider one particular application — that of a time-averaged potential (TAP) based on domain wall fringing fields. The details of TAPs will be discussed further in Section 7.3.2. For now we will simply compare the calculated values of the trap frequency associated with these magnetic traps, ω_{Trap}. We consider in particular traps formed at a height of 1 µm, as per the simple scheme illustrated in Figure 7.1, and TAP fields in the range 2–10 G. We also consider four different domain wall geometries. The trap frequency is then calculated by fitting the resulting potentials with a quadratic function over a distance of ±100 nm from the trap minimum. The resulting values are given in Table 2.2.

Table 2.2: Errors associated with our analytic (2D) model when calculating the trap frequency of a time-averaged potential (see Section 7.3.2 or [69] for details), as compared with results based on micromagnetically simulated structures. We consider a trap height of 1 µm and TOP fields in the range 2–10 G.

Wire Cross Section (nm)	**Mean/Max Error in ω (%)**
200 × 40	3.4/3.8
400 × 20	12.6/13.5
800 × 10 (vortex)	40.5/41.6
800 × 10 (transverse)	5.0/5.4

The accuracy of the calculated trap frequencies is generally good, particularly for wires of smaller widths and wires hosting transverse-type domain walls. For larger wires the near-field region becomes larger. We also obtain larger errors for vortex-type domain walls, which have a more complex near-field structure (cf. Figure 2.7(d)). We conclude that our model shows great utility when modelling trapping potentials above domain walls, particularly for smaller wires.

2.4 Alternative models

Micromagnetic simulations show that the magnetic fringing fields are complex in nature, as illustrated in Figure 2.7; there are features which the simple analytic models presented here do not account for. One obvious failing of the models presented is that real domain walls show regions of both positive and negative charge, which are primarily associated with edge charges. For example a transverse-type domain wall has a concentration of charge of opposite parity at the apex of the triangle. Efforts were made to emulate this structure by incorporating a spatially dependent charge density and parity, which we now briefly detail.

The magnetic charge density of a triangle of height w and base s is given by $\rho_{\mathrm{m}} = 4\mu_0 M_{\mathrm{s}} t/s$. We now consider ρ_{m} to be spatially varying. This variation could in principle take any form but to keep the model simple we assume a linear variation with $\rho_{\mathrm{m}} = 0$ at $x_{\mathrm{N}} = 0$ (the wire centre). This yields a modified charge density

$$\tilde{\rho}_{\mathrm{m}}(x) = \rho_{\mathrm{m}} \times (w/2 - x)\,, \tag{2.19}$$

It is also necessary to renormalise this expression by a constant, C, so that the total charge is not altered. For this, we require that

$$\begin{aligned} q_{\mathrm{m}} &= 4CM_{\mathrm{s}}\mu_0 t/s \int_0^w (w/2 - x)\ \ \mathrm{d}A \qquad &(2.20)\\ &= 4CM_{\mathrm{s}}\mu_0 t/s \int_0^w (w/2 - x)\,(s - xs/w)\ \ \mathrm{d}x = 2M_{\mathrm{s}}\mu_0 wt. \qquad &(2.21)\end{aligned}$$

Evaluating this integral yields $C = 6/w$ and hence

$$\tilde{\rho}_{\mathrm{m}}(x) = \frac{24M_{\mathrm{s}}\mu_0 t}{sw}\,(w/2 - x)\,. \tag{2.22}$$

This process can also be carried out in an entirely analogous manner for a domain wall with a trapezoidal shape. For both shapes we observe that the accuracy of the model is significantly less than that of the models already presented.

The models presented thus far have been based on the volume charge contributions within the domain wall, as these are dominant, however an alternative representation can be formulated based on sheets of charge around the domain wall region, as illustrated in Figure 2.14. Previous models have represented the volume charge by 2D sheets of charge because the thickness of the nanowire, t, is negligible. As such, the fields according to the representation shown in Figure 2.14 can be easily calculated from previous results. Again, a trapezoidal shape was also investigated in an analogous manner. We note again that the calculated fields are less accurate than those according to the models presented in detail.

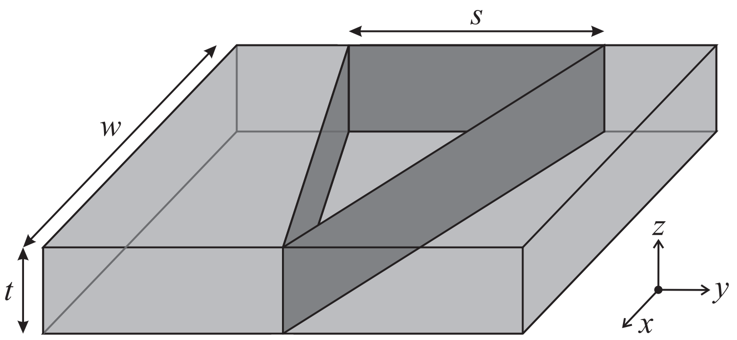

Figure 2.14: A schematic of a transverse domain wall represented by sheets of magnetic charge around the wall.

2.5 Conclusions

In this chapter we have developed an analytic model which allows for the rapid and accurate calculation of the fringing fields produced by domain walls within planar magnetic nanowires. The model prescribes an effective charge to the domain wall, with a value defined by the geometry of the nanowire. The shape of the charge is made to replicate the characteristic shape of the domain wall — for the case of a transverse (vortex) type domain wall this is triangular (rectangular). This methodology assumes that the volume charge within the domain wall is the dominant contributor, rather than surface charges.

Through a comparison of the calculated fringing fields with those generated via micromagnetic simulations we found that the model provides a good accuracy, particular in the 'far-field' regime (heights $\gtrsim$100 nm). Nearer the wire our model breaks down as the complex magnetisation structure becomes more important. We also note that models which more accurately represent the shape of the magnetisation divergence produce more accurate fringing fields. We have shown that it is possible to use a rule of thumb to define the shape of the corresponding charge distributions so that the models can be used without any *a priori* information, allowing for fast and accurate computation of the fringing fields.

We note that the model performs well for fields of $\sim$1–10 G, which is the regime in which we expect atomic physics applications to be based. This analytic model is an important tool when considering atom-nanowire interactions and is used extensively in the work presented here. In the following chapter we describe our first realisation of an interaction between atoms and domain wall fringing fields.

Chapter 3

Mirror Experiment

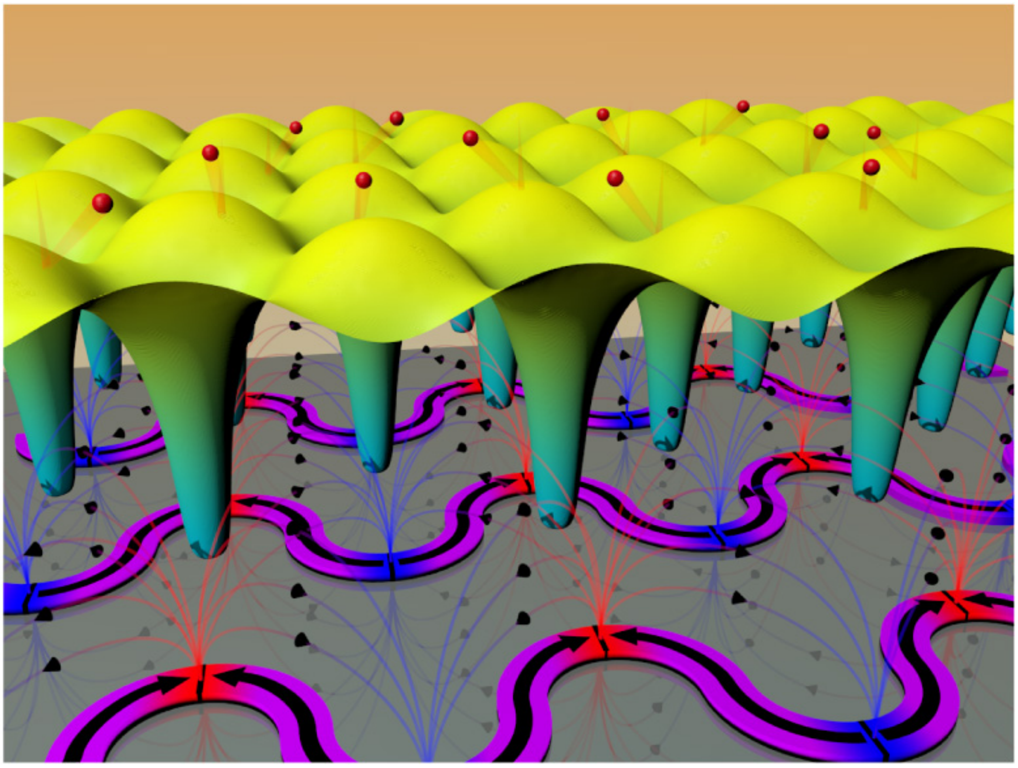

Schematic image of our atom mirror. Pictured are the undulating nanowires with domain walls of alternating parity, giving rise to fringing fields. Above this is an effective isosurface from which the atoms can be considered to reflect.

Some of the work in this chapter forms the basis of the following paper:

Design and characterization of a field-switchable nanomagnetic atom mirror
T. J. Hayward, A. D. West, K. J. Weatherill, P. J. Curran, P. W. Fry, P. M. Fundi, M. R. J. Gibbs, T. Schrefl, C. S. Adams, I. G. Hughes, S. J. Bending and D. A. Allwood
J. Appl. Phys. **108**, 043906 (2010)

3.1 Introduction

In Chapter 1 the use of spintronic technology to create a magnetic atom trap was briefly discussed. Whilst such an application of planar nanowires would offer a number of benefits over conventional atom chip architectures, this is offset by the difficulties associated with realising such a trap, which will be discussed in detail in Chapter 7. Even after overcoming some of the fundamental obstacles to creating such a trap, there are many technical challenges which still remain. The difficulties faced are largely due to the regime we aim to work in, i.e. using a single domain wall to trap a very small number of atoms in an exceptionally tightly confining potential.

Instead we desire an experiment that demonstrates the possibility of exploiting the magnetic interaction between atoms and domain walls on a larger scale. This is achieved by turning our objects of interest from single domain walls and atoms to collections of both which we can much more easily manipulate and observe. This regime shift is provided through the creation of an atom mirror. Atom optics elements based on patterned magnetic material were first realised through atom mirrors, which provided a stepping-stone to more complex systems. We hope that the spintronics-based atom mirror we present will fulfill the same role.

3.2 Atom mirrors

3.2.1 Introduction

A classical mirror is most familiar as an object which reflects light. Whilst this mirror may vary in shape, efficiency or spectral response, the characteristic feature is a momentum reversal through a transient interaction. For the case of light, this interaction is an electromagnetic one. However, we wish to reflect matter, not radiation. This is easy to achieve with macroscopic objects as their internal structure can facilitate an elastic interaction. Moving to the microscopic realm of individual atoms makes the realisation of such an elastic interaction difficult. An atom incident on a hard surface is typically either scattered in a stochastic manner or adsorbed. This behaviour is again governed by electromagnetic interactions, but they are not tractable or predictable ones. To produce an atom mirror which is analogous to a classical mirror we must employ a more controllable and deterministic interaction.

Realisations of mirrors that reflect microscopic particles can be roughly divided according to the type of field employed. In this work we shall not consider the realm of quantum reflection (i.e. the reflection of particles by a nominally attractive potential) as the mirror that we use always operates classically in this sense. The choice of field is governed mainly by the interaction created. Electric fields have been used extensively to reflect molecules [81, 82, 83], and more recently, Rydberg atoms [84], both of these types of particles experience large Stark shifts due to their large polarizabilities. This in turn has lead to the development of Stark decelerators which controllably modify this electric interaction to produce a cooled beam of molecules [85, 86].

Optical fields have been used in an analogous manner to slow or reflect molecules [87, 88] and to reflect atoms [89, 90], as the electric component of an optical field also produces a Stark shift. This interaction has also been used to confine atoms [91], molecules [92, 93] or even macroscopic objects [94, 95], in the form of the dipole trap.

Whilst molecules in an electric field can exhibit a large electric dipole moment, atoms in their ground states typically have comparitively small polarizabilities, but can have large associated permanent magnetic dipole moments (although the direction of such a dipole is poorly defined in the absence of a magnetic field to define the quantisation axis). A permanent magnetic dipole in an applied field will experience a Zeeman interaction. For a particle with magnetic dipole moment $\vec{\mu}$ in a magnetic field $\vec{B}$ this is given by

$$E_{\mathrm{Z}} = -\vec{\mu}.\vec{B}. \tag{3.1}$$

For the case of an atom the magnetic dipole moment is given, in a sufficiently weak magnetic field, by

$$\mu = -m_F g_F \mu_{\mathrm{B}}, \tag{3.2}$$

where m_F is the magnetic quantum number, g_F is the Landé g-factor and μ_{B} is the Bohr magneton. Note that this quantisation of the magnetic moment relies on the presence of a magnetic field to define a quantisation axis. The interaction energy can thus be expressed as

$$E_{\mathrm{Z}} = m_F g_F \mu_{\mathrm{B}} |\vec{B}|. \tag{3.3}$$

A spatially varying magnetic field will produce an associated Stern-Gerlach force,

$$F_{\mathrm{SG}} = -\vec{\nabla} E_{\mathrm{Z}} = -m_F g_F \mu_{\mathrm{B}} \vec{\nabla} |\vec{B}|. \tag{3.4}$$

Atoms which are in a state that fulfils $m_F g_F > 0$ are said to be in a 'weak-field-seeking' state and are attracted to minima of magnetic field. Atoms in a 'high-field-seeking' have $m_F g_F < 0$ and are attracted to field maxima. For the specific case of $m_F g_F = 0$ the atoms experience no magnetic interaction in weak fields.

Due to the comparitively strong interaction, magnetic fields are often the preferred tool for realising atom mirrors. In this work we interface atoms with sources of magnetic field, so we restrict the following discussion to magnetic mirrors.

3.2.2 Ideal magnetic mirror

To reflect atoms we use the Stern-Gerlach force, as defined in Equation 3.4, to oppose motion towards a surface. Hence we require a magnetic field which decays away from the surface. An ideal mirror will have such a decay perpendicular to the mirror's surface with no field variation in transverse directions. Such an ideal magnetic atom mirror can be realised through the use of an infinite sheet of magnetic material, which we define to be in the x-y plane, with a sinusoidally varying in-plane magnetisation pattern given by [22]

$$\vec{M}(x) = M_0 \cos(kx)\hat{x}, \tag{3.5}$$

where $k = 2\pi/\lambda$, with λ being the wavelength of the magnetisation pattern. The shape of the resulting magnetic fields is illustrated in Figure 3.1. This configuration gives rise to a magnetic field magnitude of the form

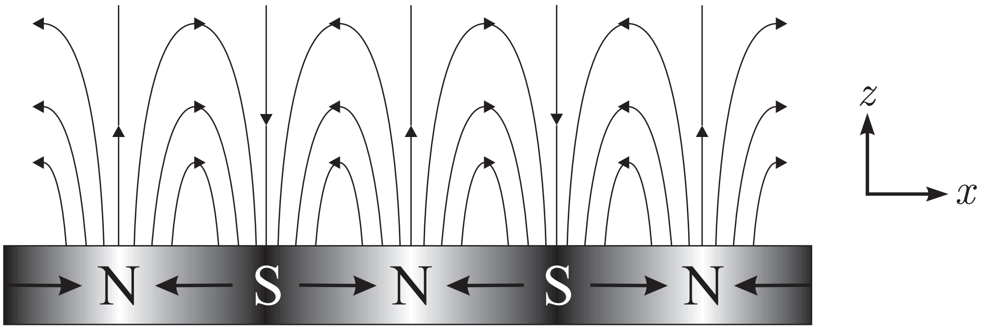

Figure 3.1: Magnetic field shape arising from an ideal magnetic mirror. The magnetisation is directed within the plane of the material and varies sinusoidally.

$$|\vec{B}| = \frac{\mu_0}{2} M_0 (1 - e^{-kt}) e^{-kz} = B_0 e^{-kz}, \tag{3.6}$$

where t is the thickness of the magnetic material. We recall that the magnetic potential is given by $E_\mathrm{Z} = m_F g_F \mu_\mathrm{B} |\vec{B}|$. As can be seen, the magnetic field magnitude does not vary with either x or y, so the mirror is in this sense a 'flat' one. Given such a configuration the trajectory of an atom entering this field can be derived analytically and results in a reflection which (on a scale larger than the length over which the reflection takes place) is completely specular. A similar field shape is obtained by considering a sinusoidally varying out-of-plane magnetisation [22]. We note that the characteristic decay length of the magnetic field is prescribed by the wavelength of the magnetisation variation — a smaller characteristic size gives rise to higher gradients, and thus a larger force on an atom entering the field.

If the pattern of the magnetisation deviates from a purely sinusoidal form this introduces a degree of corrugation to the shape of the magnetic field magnitude [96]. This in turn changes the nature of the reflection of atoms from specular to diffuse. In the following section we will describe how we used the domain walls present in planar magnetic nanowires to replicate an analogue of an ideal magnetic mirror.

3.3 Nanowire atom mirror

3.3.1 Mirror design

In Section 1.2 the current applications and technologies associated with magnetic nanowires were briefly described. We now consider in particular the planar magnetic nanowires which we used to create an analogue of the conventional atom mirror. The most important feature of such nanowires, in both the work presented here and other spintronic applications, is the fact that they host highly controllable magnetic domains. We will show that the ability to populate, position and control such domains is vital to the realisation of an atom mirror based on domain walls.

The atom mirror which we have created relies on exactly the same physics as a conventional magnetic mirror. The difference lies in the sources of magnetic field used, and subsequently, the behaviour of these sources. In Section 2 the nature of the fields emanating from nanomagnetic domain walls was studied in detail. The task at hand is now to use these fields to create a flat, decaying magnetic field. The way in which this is achieved is to create a checkerboard of domain walls, as illustrated in Figure 3.2.

The picture we have is one of a 2D array of alternating dipoles. In Section 2 the domain wall was described as a point source of fringing fields akin to a monopole. If one restricts consideration to one side of the nanowire array, i.e. either above or below the wires, then this situation is entirely analogous to an array of magnetic dipoles of alternating orientation.

The magnetic field line pattern that is yielded from the 2D array is qualitatively very similar to that of an ideal mirror (cf. Figure 3.1), and is shown in Figure 3.3. However there is an important difference: the magnetisation produced by the domain wall array is significantly more discretised than the ideal case due to the point-like nature of the domain walls. This results in a significant deviation of the field magnitude shape from the flat one achieved in the ideal case. This is indeed observed in the field magnitude plotted in Figure 3.3. The result is an atomic potential which displays a great deal more roughness than an ideal mirror. This is clearly detrimental — we desire as flat a mirror as possible. To minimise this effect, the domain walls were chosen to be as close together as permitted by the lithographic processes used.

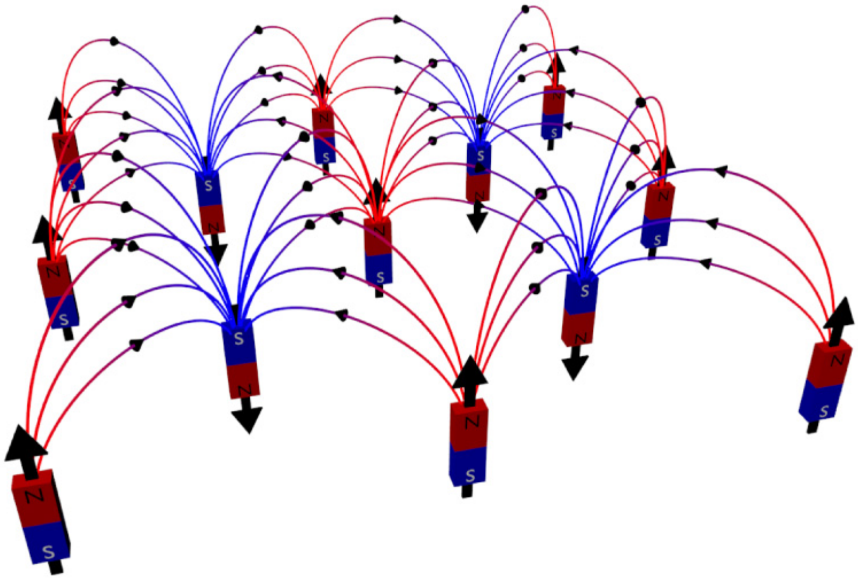

Figure 3.2: A schematic of the configuration of nanomagnetic domain walls which we use to create an analogue of the ideal magnetic mirror. The walls are arranged in a square checkerboard pattern with alternating parity. The resulting magnetic field lines are illustrated.

This effect will be analysed quantitatively in Section 5.2.3 when we examine the nature of the atom-nanowire interaction. With the basic principle of the domain wall mirror established we now consider the manner in which such a 2D lattice of domain walls can be achieved.

The crucial feature of the nanowires when considering the production of our magnetic mirror is the freedom afforded by the use of lithographic fabrication techniques. This allows for the creation of patterned magnetic material of almost any shape and on macroscopic scales. In order to realise the domain wall lattice we need to be able to populate reliably domain walls at precise positions. The primary technique for governing domain wall position within nanowires is simply the choice of wire shape. Domain walls will tend to form and reside at positions which minimise the associated magnetic energy. Bearing this in mind, the shape that we choose for our nanowire array is an undulating one.

By using an undulating pattern of magnetic material we create a macroscopically anisotropic shape which can be populated with (and removed of) numerous domain walls. This is facilitated by the application of external

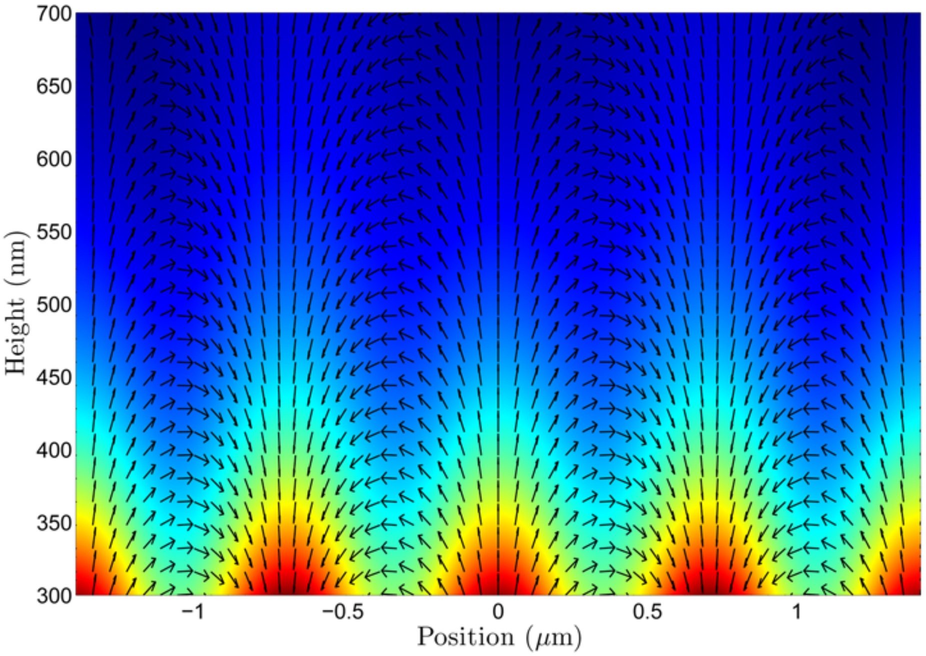

Figure 3.3: The magnetic field from an array of domain walls, as calculated analytically (cf. Chapter 2) as the sum of the field from many individual domains. A wire period of 1 μm, a wire width of 125 nm and a wire thickness of 30 nm are assumed. The data shown are a diagonal slice through domain walls of alternating parity, i.e. at an angle of 45° to the wire length. Shading represents the magnitude of the magnetic field, arrows represent the magnetic field direction within the extracted plane.

magnetic fields which switch the wires between two different magnetisation configurations, illustrated in Figure 3.4. The upper figure shows the ground state configuration of the nanowire, where there is one single continuous magnetic domain orientated along the length of the wire, which defines the easy axis. There are thus no domain walls present, and no fringing fields. The lower figure shows the higher energy metastable state which is populated with domain walls at each apex of the undulating shape. The nanowires can be forced into this configuration via the application of an external magnetic field pulse orientated transverse to the wire length (labelled in Figure 3.4(b)). The applied field saturates the magnetisation in this direction which aligns to local wire edges after the application of the pulse. The result is the formation of two magnetic domains per period of the wire structure, with domain

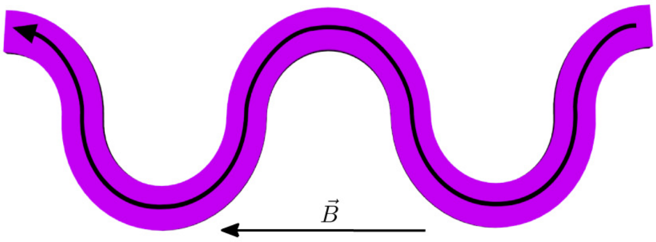

(a) ‘Off’ configuration

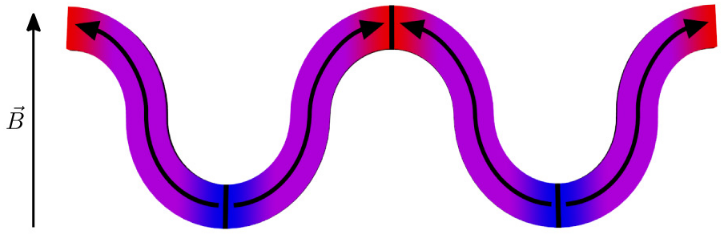

(b) ‘On’ configuration

Figure 3.4: The two magnetisation configurations of our undulating nanowires. The ground state is shown in (a), where there are no domain walls present. A higher energy metastable is shown in (b) which has domain walls present at each apex. The required external field to switch into each state is also shown.

walls dividing them at each apex. With multiple nanowires arranged next to each other, separated by a distance equal to the wire period, this results in a square 2D array of domain walls. The ground state of the wires can be recovered by applying a magnetic field pulse orientated along the wire length (labelled in Figure 3.4(a)) which causes the pairwise annihilation of domain walls within the wire. These processes occur on extremely short timescales (∼10 ns), typical of micromagnetic reconfiguration [97], and thus the length of the magnetic pulse used to switch the nanowire state can be very short indeed.

Whilst the shape of the nanowires dictates the micromagnetic structure, the characteristic sizes of the pattern govern the precise nature of the interaction between atoms and the domain wall, and is discussed in detail in Section 5.3. Alternative geometries that produce the same distribution of domain walls are also possible. For example a triangular shape could be used to produce apexes for domain wall sites. However the stronger pinning of the domain walls that this would produce would lead to much larger fields being required in order to annihilate the domain walls and switch into the 'off' configuration. The nanowire shape used provides both a well defined and stable array of domain walls whilst maintaining the reconfigurability inherent to domains within permalloy nanowires.

3.3.2 Mirror fabrication and characterisation

The manufacture and subsequent analysis of the nanowires which we use in our experiment were performed by colleagues at the University of Sheffield, also in collaboration with the University of Bath. In this section we will briefly outline the methods used. The interested reader can refer to [77] and other sources referenced herein for further information.

The lithographic process used to produce the nanowire array was electron-beam lithography via lift-off processing. This procedure is outlined in Appendix B.

The shape of the resulting nanowire pattern was inspected using a scanning electron microscope (SEM). An example image obtained is shown in Figure 3.5. Inspection of the nanowire structure via SEM imaging reveals that there is excellent accuracy of the written nanowire shape. While there is some inherent roughness to the wire edges it is likely that this enhances the stability of the metastable 'on' state as it helps to provide localised pinning of the domain walls [98].

Analysis of the magnetic behaviour of the fabricated nanowire was performed via a number of techniques. The collective magnetisation reconfiguration was analysed using hysteresis measurements via magneto-optical Kerr effect (MOKE) microscopy. The first description of the phenomenon of MOKE and the associated microscopy techniques are outlined in detail in [99] and [100]. The behaviour of the fabricated nanowire array was analysed during a uniaxial switching field pulse sequence, i.e. the fields to switch into the 'on' and 'off' states were both orientated along the wire length. The resulting data indicated the presence of two distinct states. The 'on' state corresponds to all domain wall sites being populated. The application of a moderate oppositely-orientated field produces the 'quasi-off' state; domain

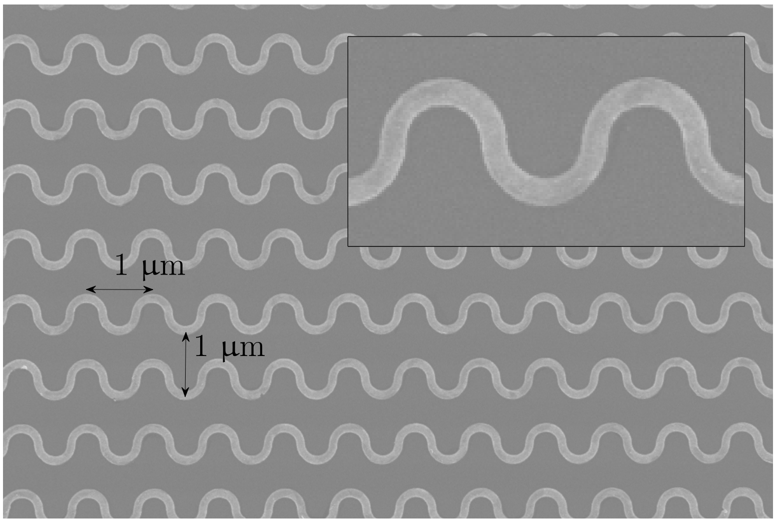

Figure 3.5: A scanning electron micrograph of a section of the nanowire array. The periodicity of the serpentine pattern is 1 μm and each wire is displaced by a distance of 1 μm.

walls are both annihilated and populated by this pulse, meaning the domain wall sites are partially populated.

Additional analysis of the dynamic micromagnetic behaviour was provided through the use of scanning Hall probe microscopy (SHPM), a tool which provides much greater resolution compared to MOKE microscopy [101, 102, 103], permitting a direct observation of the alternating field pattern. The annihilation and population of domain walls is observed for both a uniaxial and biaxial switching scheme. It was found, as expected, that the biaxial scheme produced a more extensive annihilation of the domain walls. Together with the MOKE microscopy we observe that 100% of the domain wall sites become populated, and 98% of these remain populated at remanence. Population of the domain walls is achieved by a field of 120 mT transverse to the wire length. Complete removal of the domain walls is achieved by a longitudinal field of around 22 mT.

3.4 Experimental setup

In this section we will discuss the details of the experimental apparatus used to carry out the nanowire atom mirror experiment. The emphasis is placed on elements of the setup which are novel or in some way particular to the experiment. For more details on the general apparatus referred to within this section the reader is advised to consult other sources which will be referenced where appropriate.

3.4.1 Vacuum chamber

The basis of most studies of ultracold atoms is a vacuum chamber in which the experiment takes place, and it is the details of the experiment which govern the requirements placed upon such a chamber. The vacuum system used in our experiment is shown schematically in Figure 3.6. Perhaps the most

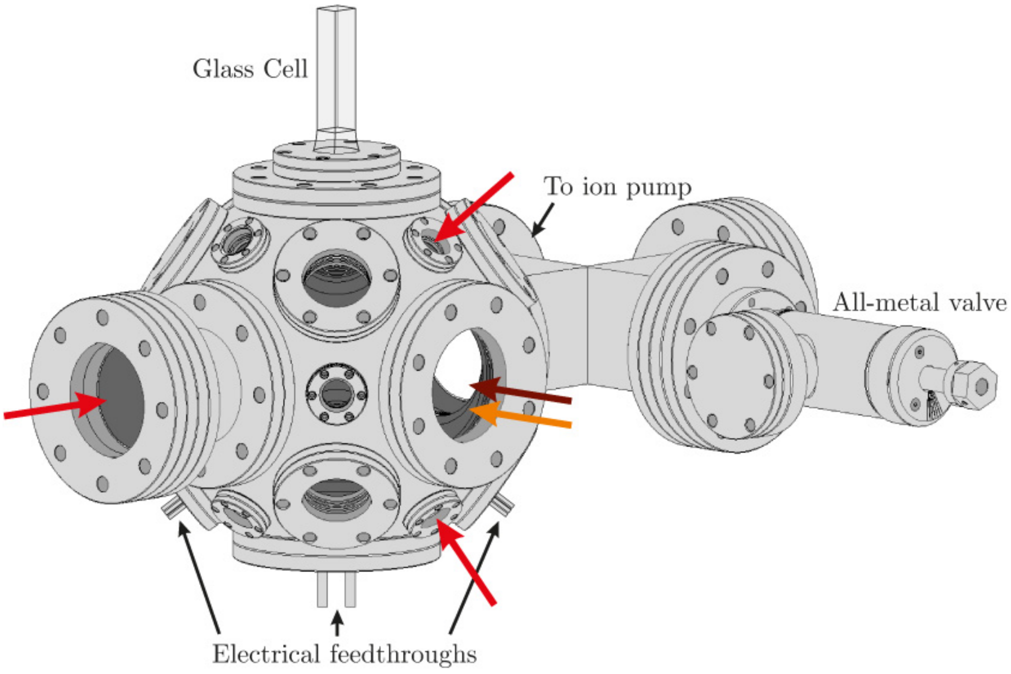

Figure 3.6: Schematic illustration of the vacuum system used in the experiment. The flange sizes are as per the expanded spherical cube referred to in the text. A nipple and 4-way cross are connected to either side of the chamber. The latter is then connected to an ion pump (not pictured) and an all-metal valve, which is open during baking out. A glass cell is shown connected on top of the chamber. The axes used for the cooling beams are shown in red. The axes for the optical pumping beam and light sheet are shown in maroon and orange respectively (cf. Figure 3.8). The supports for the chamber are not shown.

important feature to consider when designing the vacuum system was flexibility and freedom, and this was afforded by the use of a chamber with a large amount of optical access. The chamber used is the Kimball 4.5” expanded spherical cube (MCF450-SphCube-E6C8A12) [104]. The large number of ports allows for very good optical access. This was particularly advantageous given that the experiment was the first to incorporate a nanowire based chip in vacuum; with the large amount of access available this allowed for some degree of contingency. The vacuum in the chamber was achieved using a combination of a backing pump, turbo pump and ion pump combined with a bakimg out procedure at 200°C. The ion pump with which the vacuum was maintained is a Varian VacIon Plus 55 StarCell [105]. The final pressure inside the vacuum system according to the ion gauge used during baking out was observed to be around 1×10^{-9} mbar. The load measured on the ion pump controller after baking out was around 32 μA which corresponds to around 6×10^{-9} mbar according to the calibration of the controller. An estimate of the vacuum pressure was also achieved by performing lifetime measurements of an ultracold atom cloud in a magnetic quadrupole trap. A lifetime of 43 ± 2 s was measured from which we can use a rule of thumb to estimate the background pressure to be around 3×10^{-10} mbar [106].

In comparison to some other ultracold atom experiments, the vacuum system is a relatively simple one. Three electrical feedthroughs were incorporated to provide connections to the coils which reconfigure the state of the nanowire array, which are described in Section 3.4.3, and also to connect the dispensers (SAES Getters [107]) which act as the source of rubidium. An all metal valve (Caburn-MDC MAV-150-V [108]) was used in order to make the connection to the vacuum chamber during the bake-out procedure. The final part which was attached to the chamber was a cuboidal glass cell. The purpose of this cell is to allow for imaging of atoms launched upwards in a manner akin to an atomic fountain [109], allowing analysis and optimisation of the moving molasses procedure, which is described in detail in Section 6.2.

3.4.2 Lasers

Overview

As well as the vacuum chamber, the other ingredient essential to any ultracold atom experiment is the laser system. This is the tool which we require in order to cool, and often to manipulate, the atoms being studied. Efficient laser cooling of alkali atoms requires at least two different laser frequencies. For the case of ^{87}Rb, the species which we use, we need two. This requirement is set by the energy level structure of the D2 transition, which is illustrated in Figure 3.7. The two transitions required to cool ^{87}Rb are labelled by red (pump transition, $F = 2 \rightarrow F' = 3$) and blue (repump transition, $F = 1 \rightarrow F' = 2$) arrows. As required by the technique of laser doppler cooling [106], the pump laser is red-detuned from resonance by a frequency Δ, whose value

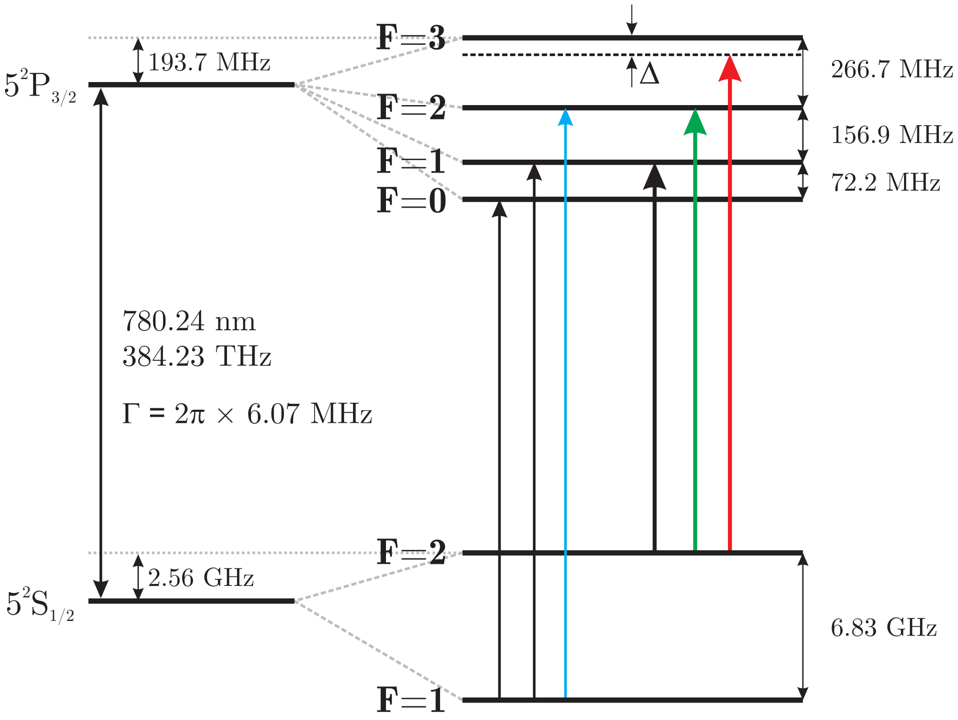

Figure 3.7: Energy level structure of the D2 transition in ^{87}Rb. The possible transitions between states of different F are labelled. The red arrow represents the cooling or pump transition, which has a detuning from resonance of Δ. The blue arrow represents the repump transition. Also labelled in green is the transition associated with optical pumping. Diagram is not to scale. Values are taken from [110].

is typically around 2Γ, where Γ is the natural linewidth of the transition.

An overview of the laser system that was built for this experiment is shown schematically in Figure 3.8. A number of acousto-optic modulators (AOMs) are shown in green that are used to shift the frequency of the light. The AOMs used for the optical pumping and repump beams (AA Opto-electronic MT80-A1-IR [111]) have a central operating frequency of 80 MHz. The remainder (AA Opto-electronic MT200-A0.5-800) all have a central operating frequency of 200 MHz. The signal for all these AOMs is produced by voltage-controlled oscillators (VCOs) which were built in-house (with the in-

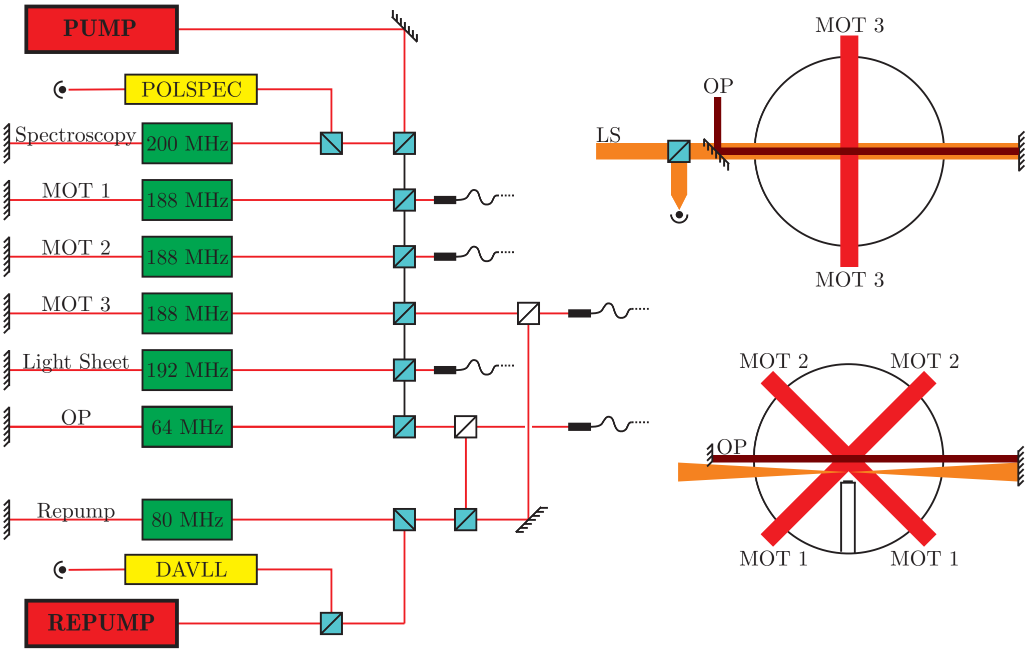

Figure 3.8: An overview of the optical setup of the experiment. Green boxes represent AOMs with typical operating frequencies labelled. For the case of the AOMs for the magneto-optial trap (MOT) beams the frequencies labelled correspond to the end of the molasses ramp. Blue cubes are polarising beam splitters, white cubes are 50:50 beam splitters. After passing through the AOMs the light is coupled into fibers and passed to the chamber. The chamber setup is shown on the right. The top drawing of the chamber is a view from above, the bottom drawing is a view from the side — the mount holding the nanowire chip is shown beneath the intersection of the MOT beams. The drawing is not to scale and many optical elements have been omitted for clarity.

corporation of moving molasses, described in Section 6.2, arbitrary function generators are also used). The signal from these then passes to amplifiers (AA Opto-electronics AMPA-B-34) before being used to drive the corresponding AOM. For all of these AOMs the light is double passed, which helps minimise any steering of the beam as the frequency of operation of the AOMs is altered. In each case the +1 order of the diffracted light is selected, corresponding to an increase in the frequency of the light. The uses of each of these AOMs will be described in the following sections.

Laser cooling

The pump light required to cool the atoms is provided by a Toptica DL100 diode laser, which outputs a maximum power of around 150 mW [112]. This laser is frequency stabilised using a polarisation spectroscopy (‘polspec’) reference [113, 114]. This choice of locking technique was made as it provides a fairly narrow locking signal (width typically around 20 MHz [115]) within a setup which is easy to build. The actual locking procedure is performed by a Toptica PID controller module. We note that the light for the polspec setup is taken after a double pass through an AOM, thus the pump laser is not in fact locked on resonance, but at a frequency approximately 200 MHz lower. Subsequent AOMs then shift the frequency by an amount slightly less than 200 MHz, thus allowing for a realisation of the small detunings required for the experimental procedure.

The pumping light for the MOT has three associated AOMs. The reason for this, as discussed in Section 6.2, is that the moving-molasses technique requires three different frequencies of light. When not performing moving molasses all three of these AOMs operate at the same frequency. The frequency labelled for these AOMs in Figure 3.8 is the frequency at the end of the molasses ramp.

The repump light is provided by an external cavity diode laser which was built in-house. This laser outputs a maximum power of around 30 mW and is frequency stabilised using a dichroic atomic vapour laser lock (DAVLL) setup [116]. This method was chosen for the repump laser because it is easy to set up and provides a very stable lock: the effective ‘capture range’ of the lock is large compared to other locking methods. This does, however, mean that the width of the locking feature can be of the order of 1 GHz [117]. Whilst this may lead to a relatively imprecise laser lock this is not a problem for the repump transition, given the relatively low scattering rate required to ensure that the atomic population in the lower hyperfine ground state is effectively transferred back into the cooling transition. There is also an offset associated with the zero point of the DAVLL lock signal. Because the spectroscopy does not resolve sub-Doppler features, i.e. we can't resolve the individual upper hyperfine energy levels, the associated absorption is due to the contributions of all the upper states. The locking signal is thus centred at a frequency associated with the transition from the $F = 1$ ground state to the unsplit $5^2\mathrm{P}_{3/2}$ excited state manifold. Because of the broad nature of the locking signal, the aforementioned offset, and the fact that the position of the locking point is easily tuned through a variation of the optical or electronic setup, it is only necessary to use one AOM for the repump light. It is a simple matter to lock at a frequency which is offset away from resonance by an amount which is then accounted for by the AOM frequency shift.

The other necessary component of producing a MOT is the magnetic field, which takes a quadrupole form. This is produced by coils which are placed in vacuum, which shall be described in Section 3.4.3.

Following the loading of the MOT the atoms are cooled further by the use of the optical molasses technique [118]. During this process the magnetic field is removed and the size of the detuning of the lasers is increased (a reduction in frequency). In its simplest form, the frequency is simply stepped as the magnetic field is removed, however we find that a lower temperature is achieved by ramping the frequency in a continuous manner. Either of these two schemes is easily implemented through the use of VCO control. The optimisation of this cooling procedure will be briefly discussed in Section 3.4.4.

Optical pumping

After the atoms are cooled they undergo an optical pumping procedure. The purpose of this part of the experimental sequence is to prepare the sample in the correct m_F state. We desire the atoms to be in the $F = 2, m_F = 2$ ground state as this is the weak-field-seeking state which experiences the largest Zeeman shift. In order to do this we must stimulate atomic transitions which transfer the population from lower m_F values into this state. This is achieved through the use of σ^+ transitions, i.e. transitions from the state m_F to $m_{F'} = m_F + 1$, which are driven by circularly polarised light. In order to be able to define meaningfully the necessary polarisation of light to induce this transition we must define a quantisation axis to which the magnetic dipoles align. This is achieved via the application of a weak magnetic field, which is described in Section 3.4.3, in the direction of propagation of the optical pumping beam.

For the case of ^{87}Rb atoms there are in fact two main options for pumping the population into the $F = 2, m_F = 2$ state. The first is to use a single laser frequency which addresses the transitions between $F = 2$ and $F' = 3$. Due to quantum mechanical selection rules, the atoms cannot decay into the $F = 1$ ground state unless, as in the case of laser cooling, they are off-resonantly excited into the $F' = 2$ state. Given the short duration of the optical pumping sequence ($\sim$1 ms) and the relatively low intensity of the beams we can neglect this effect. Thus there is no need for a repump beam when we pump on this transition. The disadvantage to this scheme is that once the atoms reach the $F = 2, m_F = 2$ state it is not dark, i.e. the atoms continue to scatter photons. Whilst this does not significantly perturb the polarisation of the atomic sample it does lead to heating of the atoms.

To avoid this heating effect we use an alternative scheme. We now consider driving the transition between $F = 2$ and $F' = 2$. Unlike the previously mentioned scheme this allows for decay back to the $F = 1$ ground state, at which point the atoms no longer scatter light from the optical pumping beam. Thus a repump beam is required. This beam addresses the same transition as the repump beam used in laser cooling, i.e. the $F = 1$ to $F' = 2$ transition. The complete optical pumping scheme is shown in Figure 3.9. Whilst it is less convenient to use two light frequencies to perform optical pumping, there is a significant benefit in that the atoms are pumped into a dark state. When they reach the $F = 2, m_F = 2$ ground state they no longer scatter any photons. This has the benefit of dramatically reducing the heating of the atoms. Simulations which are described in Chapter 5 show that the scheme we adopt results in each atom scattering on average around 3.7 photons, whilst the single frequency scheme results in the scattering of around 160

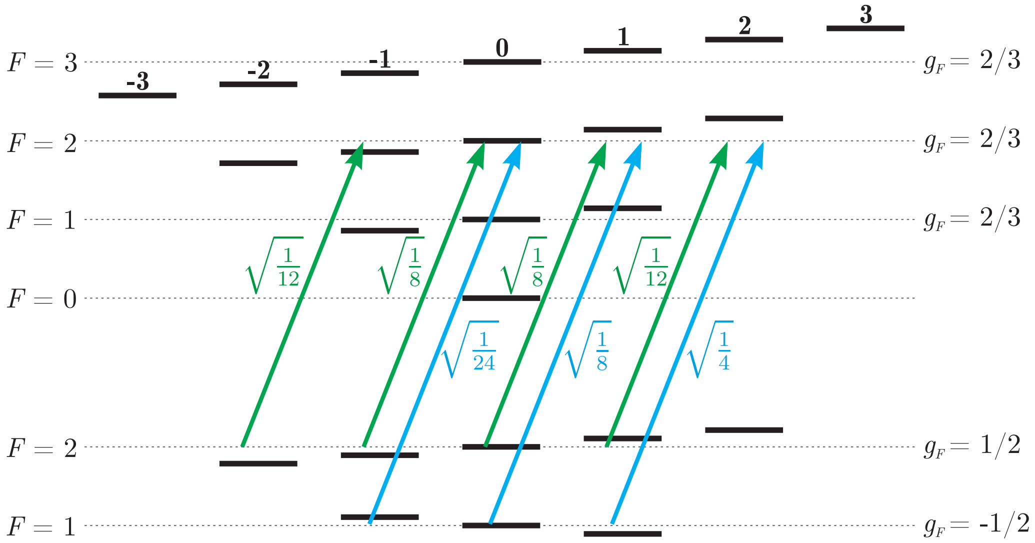

Figure 3.9: Energy levels of ^{87}Rb with the transitions addressed by the optical pumping beams labelled. Green arrows represent the pumping transitions, blue arrows represent the repumping transitions (cf. Figure 3.7). The numbers labelling the arrows are the corresponding dipole matrix elements, indicating the relative strength of the transitions. Note that the magnetic sub levels are drawn shifted by a magnetic field. The atoms are pumped into the $|F = 2, m_F = 2\rangle$ ground state, which is dark. The separations of the energy levels are not to scale.

photons (cf. Section 5.2.2). The resulting momentum kick is in fact reduced further due to the retroreflection of the beam.

To realise this scheme we use an 80 MHz AOM to shift the pumping light to the correct frequency (note in Figure 3.7 that the frequency difference between $F' = 3$ and $F' = 2$ is 267 MHz $\approx (200 - 80) \times 2$). The repumping light is the same as that used for laser cooling, so this light is split by a polarising beam splitter and sent to two different fibers (cf. Figure 3.8). The $1/e^2$ radius of the optical pumping beam is around 1.4 mm and 0.6 μW (40 μW) of pumping (repumping) light is typically used.

One difficulty encountered when implementing the optical pumping was due to the need for it to share an axis with the light sheet. This required careful alignment to ensure correct positioning of the beam. Using a crescent mirror allows for the optical pumping beam to be directed onto a path just above the light sheet, and also ensures that no optical pumping light is detected by the photodiode associated with the light sheet.

Imaging

Once the atomic sample has been prepared, we desire to track the motion of the atoms. The most direct way of doing this is to take an image of them. This is achieved by illuminating them with resonant light which is then scattered and observed on a detector. This light is derived from the same AOM that we use to produce the pump light for laser cooling, but using a different AOM frequency, which shifts it onto resonance. The required frequency was determined by maximising the observed scattered light, and was in general different to the frequency used for the light sent to the polarisation spectroscopy setup (as can also be seen for the AOM associated with the light sheet in Figure 3.8). The reason for this is likely due to some small offset on the locking signal used, and/or the presence of a magnetic field which Zeeman shifts the energy levels of the atomic sample.

The imaging light is switched on in synchronisation with the triggering of a Pixelfly VGA camera [119]. An image of the scattered light is then taken from a distance of around 30 cm using a pair of lenses such that a magnification of around 1.7 is achieved. The direction from which the cloud is imaged is shown in Figure 3.8. The camera is connected to a computer via an ethernet cable and the image is read in via the associated Labview drivers.

Additional imaging is also provided using another camera (Computar FC-65 II [120]) which is run continuously, providing real time observation of the atom cloud which aided in optimisation of various aspects of the experiment.

Light sheet

Whilst the imaging techniques described in the previous section are undoubtedly very useful, a more sensitive and precise measure of the atom dynamics is provided through the use of a light sheet. This is realised via the focussing of a laser beam in one dimension. This beam then passes between the initial position of the atom cloud, and the nanowire array, as pictured in Figure 3.10. The height of the light sheet is 4 mm above the nanowire array, which was chosen in accordance with the theoretical predictions presented in Section 5.3. In the context of our atom mirror, atoms which fall onto

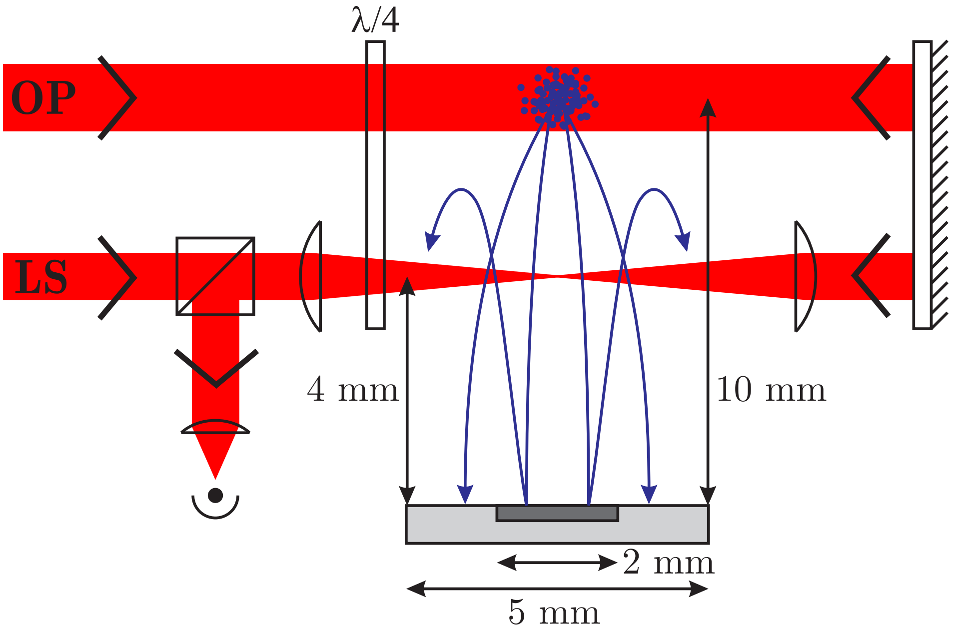

Figure 3.10: Schematic of the experimental setup showing the position of the light sheet between the atomic cloud and the nanowire array. Diagram is not to scale.

the nanowire array pass through the light sheet, scattering light. Some of the atoms are then reflected and subsequently pass through the light sheet a second time, again scattering light. A photodetector recording the transmitted power of the beam will then observe a reduction in the light level as the atoms pass through.

In our setup the beam is linearly polarised such that it is transmitted by a polarising beam splitter before being focussed by a telescope of cylindrical lenses (Thorlabs LJ1212L1 [121]) with a focal length of 30 mm. This results in a beam profile with semi-major axes which have $1/e^2$ widths of 7.8 mm and 0.18 mm. Because the light sheet shares the same axis as the optical pumping beam we choose to circularly polarise the light sheet in the same sense such that the polarisation of the atomic sample is perturbed as little as possible as the atoms pass through the light sheet. Thus the optical pumping beam and light sheet pass through the same quarter-wave plate before entering the vacuum chamber. After passing through the vacuum chamber (and the telescope of cylindrical lenses) the light sheet is then retroreflected. As will be shown in Section 5.3 this is very important in order to minimise the perturbation of the atomic cloud. The light sheet then passes back through the chamber and the quarter-wave plate such that when it reaches the polarising beam splitter again it has undergone a $\pi/2$ rotation of polarisation and is reflected out of the opposite port. It is then focussed onto a photodetector (Hamamatsu C5460 APD), which has a 10 MHz bandwidth and a photosensitivity of 1.5×10^6 V/W. Care was taken to place the photodector sufficiently far from the optical pumping coils to avoid ringing in the photodiode signal caused by the switching of these coils. The setup we have described is illustrated in Figure 3.11. The signal from the photodetector is then amplified a further 10 times by a TTi WA301 waveform amplifier.

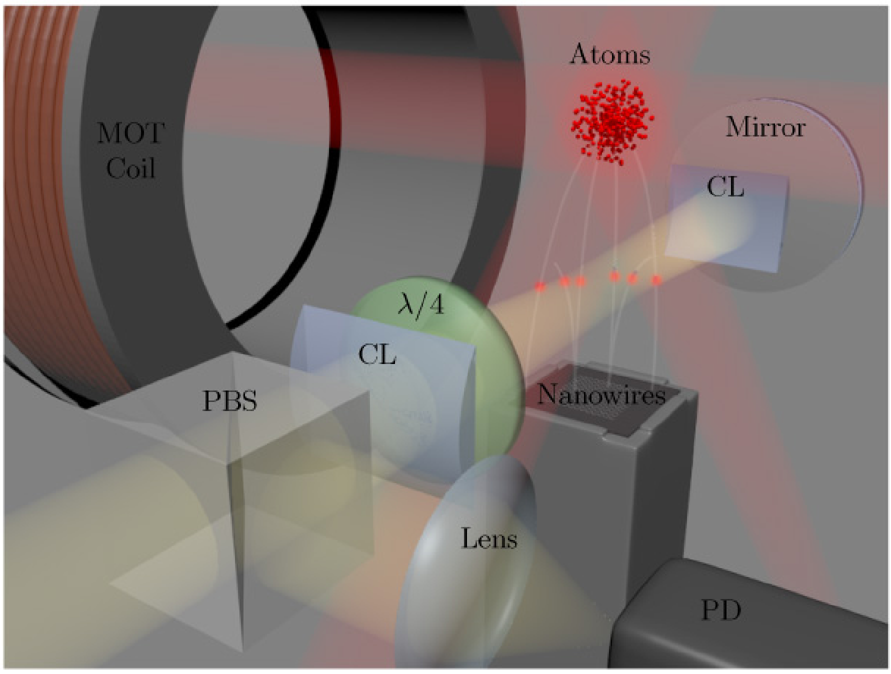

Figure 3.11: Illustration of the setup used to create and detect the light sheet used in the experiment. PBS is a polarising beam splitter, CL is a cylindrical lens $\lambda/4$ is a quarter-wave plate, and PD is a photodiode. Diagram is not to scale.

In order to minimise the aforementioned perturbation to the atoms as they pass through the light sheet we must ensure that the power used is very small (around 50 nW). At the same time it is important that the relative stability of this power is very precise, as we predict that reflected atoms will scatter only around 1% of the light. Because of factors inherent to the laser setup, such as pointing of the beam, polarisation drift and deviations about the locking point, there are significant fluctuations in the power within the light sheet that vary on timescales comparable to the duration of the signals we wish to extract. To eliminate this we utilise a locking technique which servos the power within the light sheet to a set level. This is achieved by picking off a small amount of the laser light and monitoring it on another fast photodiode (Hamamatsu C5460 APD). The position of the servoing photodiode was chosen to be as close to the light sheet as possible so that fluctuations in the beam caused after the point of servoing (e.g. due to passing through an optical fiber) are eliminated. The signal obtained is servoed against a stable DC voltage, which can be manually tuned. The electronic circuit used to achieve this servoing is shown in Appendix C.2. An estimate of the sensitivity of the light sheet can be inferred by considering the noise on the signal. If we assume that atoms falling through the light sheet spend a time δt in the beam we can then calculate the standard error on the signal over this time period. Using the scattering rate of an atom in the $F = 2, m_F = 2$ state allows us to convert this into an estimated sensitivity of around 10^3 atoms. Increasing the power in the light sheet would allow increased sensitivity but, as will be shown in Section 5.3, would cause a detrimental perturbation of the atomic cloud.

3.4.3 Magnetic fields

Switching coils mount

Within the vacuum chamber described in Section 3.4.1 there is a mount which holds the nanowire chip as well as the coils used to both form the MOT and to switch the magnetic configuration of the nanowires. This mount is shown in Figure 3.12.

A number of factors were borne in mind when designing this mount. Firstly, the optical access afforded by the choice of vacuum chamber should be jeopardised as little as possible by the inclusion of the mount. This imposes some constraints on the size and shape of the mount — the minimum requirement is the need for access through which to pass MOT beams. Extra

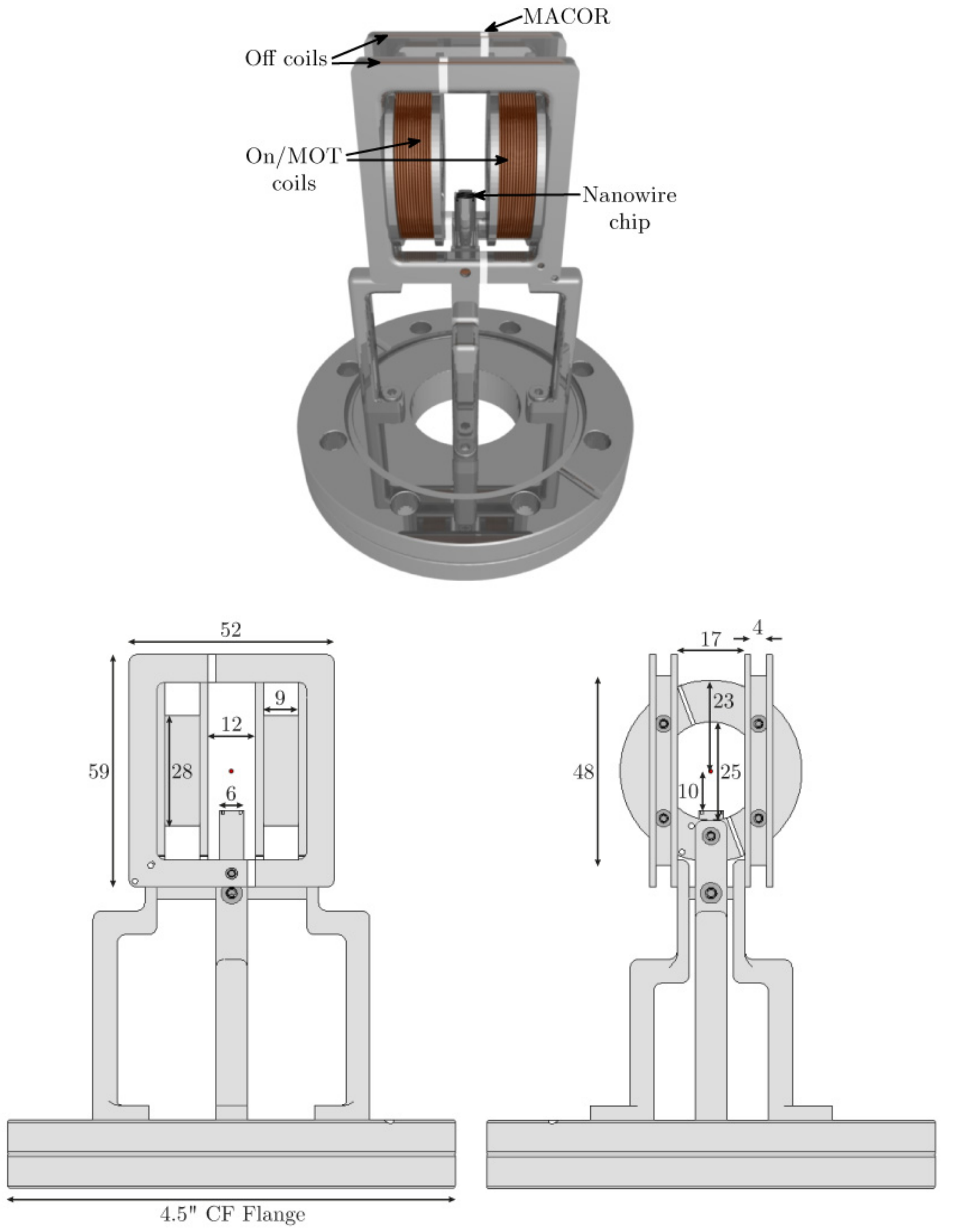

Figure 3.12: The mount used to hold the nanowire chip and associated coils. The lower images are drawn to scale and dimensions are labelled in millimetres. The entire structure is screwed into a 4.5 inch Conflat flange.

access is also desired through which to perform imaging and optical pumping. Efforts were made to minimise the amount which the mount and associated electrical feedthroughs blocked the axes of the spherical cube.

Another important point to consider is that the mount should be as non-magnetic as possible, as the mount will be subjected to large magnetic fields, given that it holds the coils used to switch the nanowire array. This requirement is effected by using grade 316 stainless steel for the construction of the mount, which has a relative magnetic permeability very close to 1 [122] and is thus non-magnetic. Eddy currents are also minimised by avoiding conducting loops in the structure. This is achieved by utilising MACOR ceramic spacers within the loops that the wire of the coils is wound onto (cf. 3.12). MACOR is an excellent insulator, so effectively prevents the creation of eddy currents. It also has a number of characteristics that make it favourable for use in experiment — it has very little thermal expansion, high compressive strength, is easily machinable and is UHV compatible with negligible outgassing.

Other factors that were accounted for when designing and building the mount include such things as the ease with which electrical connections could be made to the coils; ensuring sufficient turns in the coils which are wound onto the mount in order to achieve the desired field; and using methods of construction compatible with working under a UHV environment, e.g. the use of vented screws to prevent virtual leaks.

A consideration of all these factors culminated in the design illustrated in Figure 3.12. The mount is screwed in place on a CF flange adapter. The other side of this adapter has an electrical feedthrough attached which provides the connections to the coils which switch the nanowire array into the 'on' configuration and provide the magnetic field for the MOT. A second electrical feedthrough is used on an adjacent port of the expanded spherical cube to provide a connection for the coils which switch the array into the 'off' configuration. The chip upon which the nanowires are written is held within a mount such that the array is located equidistant between the on coils, equidistant between the off coils, and 1 cm below the axes of the coil pairs.

Switching/MOT field characterisation

To study the micromagnetic behaviour of the nanowires we shall be changing the magnetisation configuration through the use of coils in vacuum. As such we need to know the field which these coils apply to the chip. This was done both theoretically and empirically. The axial field produced by both sets of coils was measured using a Hall probe. For the square 'off' coils this was performed with the current flowing in Helmholtz configuration and a maximum field of 7.60±0.06 G/A was measured, located at the centre of the coil pair. For the circular 'on' coils, which also produce the quadrupole field required for our MOT, the field was measured in both Helmholtz and anti-Helmholtz configuration. In Helmholtz configuration the field at the centre of the coil pair was found to be 12.7±0.1 G/A. The maximum field on axis was found to be located away around 10 mm either side of the centre of the coil pair, with a value of 13.6±0.1 G/A. In anti-Helmholtz configuration a field gradient of 10.0±0.5 G/A/cm was measured at the centre of the coil pair.

The data taken were compared with a simple theoretical treatment according to the Biot-Savart law, which states that the on-axis field at a distance z from the centre of a current loop of radius R, carrying a current I, is given by [37]

$$\vec{B}(z) = \frac{\mu_0 I}{2} \frac{R^2}{\left(R^2 + z^2\right)^{3/2}} \hat{z}. \tag{3.7}$$

Whilst there is reasonable agreement between the measured fields and theoretical calculations, the discrepancies between the two are significant. This is expected as the theoretical model is an approximation which doesn't take into account factors such as the finite width of the wire, or technical imperfections such as inaccuracies in the winding of the coils. Thus the measured values are chosen as the basis for calibrating the fields that we apply to the chip.

The data presented give a good estimate of the field experienced by the nanowires but we would like to assess the shape of the magnetic field on the scale of the chip. This kind of sub-millimetre resolution is not possible through a direct measurement, and the simple theoretical treatment presented above is not appropriate as the coils are not centred on the nanowires themselves, but on the MOT position, 1 cm above. Thus the analytic form is rather more complicated than the 'on axis' case, but the form of the fields can be derived from the Biot-Savart law. The radial and axial components of field, $\vec{B}_r$ and $\vec{B}_z$, are then given by [123]

$$\vec{B}_r(r,z) = \frac{\mu_0 I}{2\pi} \frac{z}{r\sqrt{(R+r)^2+z^2}} \left[\frac{R^2+r^2+z^2}{(R-r)^2+z^2} E(k^2) - K(k^2) \right] \hat{r}, \tag{3.8}$$

$$\vec{B}_z(r,z) = \frac{\mu_0 I}{2\pi} \frac{1}{\sqrt{(R+r)^2+z^2}} \left[\frac{R^2-r^2-z^2}{(R-r)^2+z^2} E(k^2) + K(k^2) \right] \hat{z}, \tag{3.9}$$

where we define $k^2 = 4Rr/\left[(R+r)^2+z^2\right]$, and K and E are the complete elliptic integrals of the first and second kind respectively. Using these expressions it is then possible to calculate the field present across the nanowire chip for either Helmholtz or anti-Helmholtz configuration coils. The results are shown in Figure 3.13. In both cases we assume a current of 1 A is applied. For the Helmholtz case the fields are quoted relative to the field at the centre of the chip.

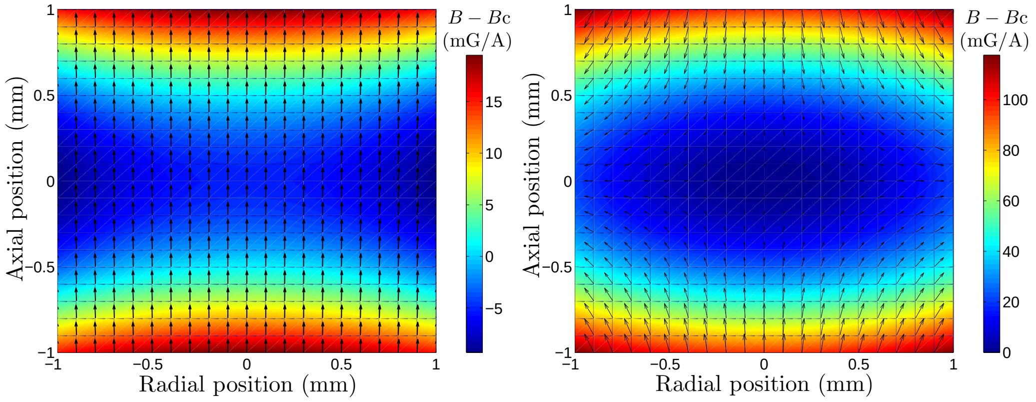

(a) Helmholtz

(b) Anti-Helmholtz

Figure 3.13: The magnetic field present across the nanowire chip due to the MOT coils. The field is shown for both a Helmholtz and anti-Helmholtz configuration, with 1 A of current in both cases. Shading represents the magnetic field magnitude. Arrows represent the direction of the field in the plane of the chip.

When we consider coils in Helmholtz configuration we note that there is almost no variation of the field over the chip; the maximum deviation of the field from that in the centre is around 48 mG/A and the maximum deviation in direction from a purely axial field is an angle of around 0.8°. This is intuitively expected as the chip is significantly smaller than the coils and their separation. This uniformity is desired as the field used to switch between magnetisation states should be orientated axially with respect to the coils. It is likely that the accuracy with which the chip is physically orientated in the mount is less than the fidelity of the field to an axial one. When the coils are in anti-Helmholtz configuration there is of course much greater variation in both the field direction and size.

The MOT coils have a further use, which is as a purely magnetic trap for the atoms. This is achieved by running them in an anti-Helmholtz configuration, but with a larger current. The magnetic field gradient required to levitate atoms against gravity is given by $m_F g_F \mu_{\mathrm{B}} \vec{\nabla}|\vec{B}| = mg$, where m is the mass of the atom and g is gravitational acceleration. This corresponds to a value of $\vec{\nabla}|\vec{B}|$ of 15.4 G/cm for a ^{87}Rb atom in the $F = 2, m_F = 2$ ground state. Using the measurements of the field from the coils this then corresponds to a current of around 1.5 A. However, using this value would provide a trap of zero depth, so the atoms would be almost immediately lost. Instead a current of around 6 A is used when trapping atoms in the quadrupole trap. Because the current passing through these coils must be changed on a short timescale, the voltage supplied to them is controlled using a couple of field-effect transistors (FETs) which combine two separate power supplies in parallel. Analysing the switching behaviour of these coils using a Honeywell current sensor (CSNF661 [124]) we observe a rise (fall) time of around 0.5 ms (0.2 ms).

Electronic control

In order to drive the MOT coils a circuit was developed to switch between operation in Helmholtz and anti-Helmholtz configuration and to control the application of the switching field. When in Helmholtz configuration a current pulse is created which is drawn from a bank of three car batteries (Bosch S5 [125], 12 V, 520 A). A rheostat was used to tune the magnitude of this current pulse. The circuit used to provide the pulse is detailed in Appendix C.1. Since the characteristic timescale of micromagnetic reconfiguration is of the order of tens of ns [97] we aim to apply as short a pulse as possible in order to limit any heating which occurs. The speed of this pulse is limited by the inductance of the coils and a minimum duration of around 500 μs was observed (as discussed in Appendix C.1 the edges of the pulse are slowed to ensure proper operation of the FET used to gate the high current pulse, thus at the minimum pulse duration the pulse shape is approximately triangular). Testing of the circuit out of vacuum showed that constant operation with a pulse generated at a rate of 1 Hz did not produce any observable heating, which was deemed satisfactory given that in practice the duty cycle of operation is orders of magnitude less.

Bias fields

There are two more uses of magnetic fields within the experimental procedure which are yet to be described. These are the weak bias fields used to cancel residual background magnetic fields and to define a quantisation axis for optical pumping. The bias (quantisation axis) coils are produced using square loops of current carrying wire of 23 (26) turns, 58 × 51 cm and 58 × 58 cm (58 × 51 cm) in size, which are mounted on a construction rail frame around the vacuum chamber. The field produced at the centre of these coil pairs is calculated to be approximately 0.36 G/A and 0.43 G/A (0.40 G/A) when operated in Helmholtz configuration. The coils which are used to define the quantisation axis for optical pumping are operated dynamically and are thus controlled by a FET. For these coils we observe a rise time of around 0.5 ms. Ringing in the coils is minimised by ensuring that an overvoltage does not occur. For the other two axes the current passing through the wires does not vary so the coils are connected directly to power supplies.

3.4.4 Experimental procedures

Atom reflection

In this section we shall describe the experimental routines employed to carry out the experiment and optimisation procedures. The timing for the routines was achieved via Labview computer control, using one digital (PCI-6713) and one analogue (PCI-DIO-32HS) PCI card [126] to process the required outputs and triggers.

The first routine that we shall consider is that associated with the experiment proper, i.e. the realisation of the magnetic atom mirror. A schematic of the timing sequence is shown in Figure 3.14. The procedure is as follows: the

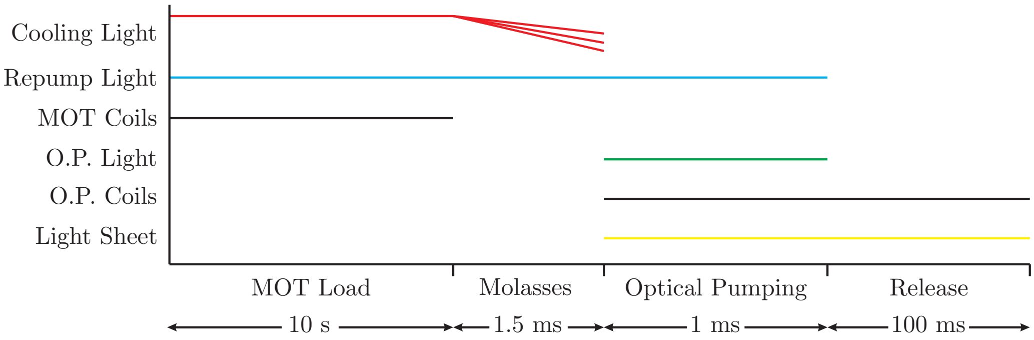

Figure 3.14: Experimental sequence performed when observing the reflection of atoms from the nanowire array. The individual lines represent whether the individual elements are on or off. For the cooling light the line height represents qualitatively the frequency of the light. During moving molasses three distinct frequencies are used, for normal molasses the central frequency is used for all beams. Typical durations of the individual steps are labelled. Diagram is not to scale.

MOT is loaded for a duration of around 10 s, producing a cloud of around 2×10^7 atoms at a temperature of around 100 μK. During this MOT phase the detuning of the beams is $-2\pi \times 12$ MHz and the current passing through the MOT coils is around 2 A, corresponding to a magnetic field gradient of approximately 20 G/cm.

After loading the MOT a molasses phase is carried out for a duration of around 1.5 ms whereby the quadrupole magnetic field is turned off and the detuning of the pumping light is ramped down linearly to a value of around $-2\pi \times 62$ MHz. This ramp is controlled via an analogue signal supplied to the VCOs which control the pumping light. With the implementation of moving molasses a slight modification is made to the experimental procedure. Three separate AOMs, controlled by arbitrary function generators (Tektronix AFG3252), are used to produce three different frequencies of light (cf. Section 6.2). Thus in Figure 3.14 we see that the frequency of light is split into three during molasses. With the implementation of moving molasses the function generators were also used when performing conventional molasses.

The atoms are then optically pumped for a duration of around 2 ms with the beams described in Section 3.4.2. During the optical pumping procedure a bias field is applied along the direction of the beam to define a quantisation axis. This field is provided by one pair of the coils that act to cancel residual background fields. In practice we found that this coil pair could be switched off when a quantisation axis was not needed, with no detriment to the temperature of the atomic cloud. A current of around 10 A is applied to the coil pair, resulting in a magnetic field of around 4 G.

At the end of the optical pumping sequence the atoms are then released and allowed to fall under gravity. During this time the only light field present is the light sheet. The magnetic field defining the quantisation axis for optical pumping is kept on in order to maintain the polarisation of the atoms; the magnetic dipoles of the atoms remain aligned with this applied field as they fall, and this helps to ensure an adiabatic passage into the large fringing fields from the nanowire array.

MOT load optimisation

One of the most basic parameters in any ultracold atom experiment is the number of atoms that are cooled. To measure this we make use of the light scattered from the MOT. A large lens is used to focus this light onto a photodiode. Due to practical considerations the best signal was obtained by using a lens with a diameter of 2" with only a fraction of the area of the lens collecting the MOT fluorescence. To measure this fraction quantitatively a photograph of the lens was taken in situ. The number of pixels within the area of the lens exposed to the fluoresced light was then counted, as well as the number of pixels within the lens as a whole. Because a large amount of scattered light not associated with the MOT was detected at the photodiode it was necessary to measure the signal with reference to a background level. This was simply achieved by automating a repeated loading and emptying of the MOT. It is then possible to make an estimate of the atom number, N_{MOT}, according to the following formula which describes the photodiode voltage produced, V_{MOT}:

$$V_{\mathrm{MOT}} = R E_{\mathrm{p}} N_{\mathrm{MOT}} f \eta Z, \tag{3.10}$$

where R is the corresponding scattering rate of the cycling transition, assuming a two-level atom (cf. Equation 5.7), E_{p} is the energy per photon, f is the fractional solid angle over which light is collected, η is the responsivity of the photodiode (in A/W) and Z is the impedance of the photodiode circuit. Note that care must be taken to use the correct value of light intensity — for a six-beam MOT this is the total intensity from all six beams.

Whilst the above formula provides a reasonable estimate of the atom number, it is not particularly accurate as a large number of the quantities used have significant errors in their measurement. A better estimate of the atom number is possible by using the light sheet. By fitting the acquired light-sheet signal, either to Monte Carlo simulations, or analytic expressions [127], allows for a much more accurate measure.

Time-of-flight measurements

To optimise the temperature of the atomic cloud fluorescence images were used to make time-of-flight measurements [118]. A cloud of atoms in thermal equilibrium under freefall will evolve according to Newtonian mechanics with a Maxwell-Boltzmann distribution of velocities. We assume that the initial atom positions are described by a Gaussian with standard deviations $\sigma_i(0)$ for each of the cartesian directions. The standard deviation in a particular direction evolves according to

$$\sigma_i(t) = \sqrt{\sigma_i(0)^2 + \frac{k_\mathrm{B} T_i t^2}{m}}, \tag{3.11}$$

where T_i is the temperature in the corresponding direction, k_B is Boltzmann's constant and m is the mass of the atom. To infer the temperature we simply have to measure the width of the cloud as a function of time. Whilst such a measure of the temperature could be achieved using the light sheet [127] it was found to be less precise than using fluorescence images. The experimental sequence employed is shown in Figure 3.15 and is described as follows. The atomic cloud is loaded and cooled via optical molasses. Because the optical pumping procedure can cause a small amount of heating it is also included in the routine. After optical pumping the cloud is released and allowed to fall under gravity. Some time later, the MOT beams are flashed on again briefly, now at a resonant frequency, and an image is taken of the scattered light. In order to remove any scattered light not produced by the atoms, dark-frame subtraction is used. A second image is taken under the same conditions at

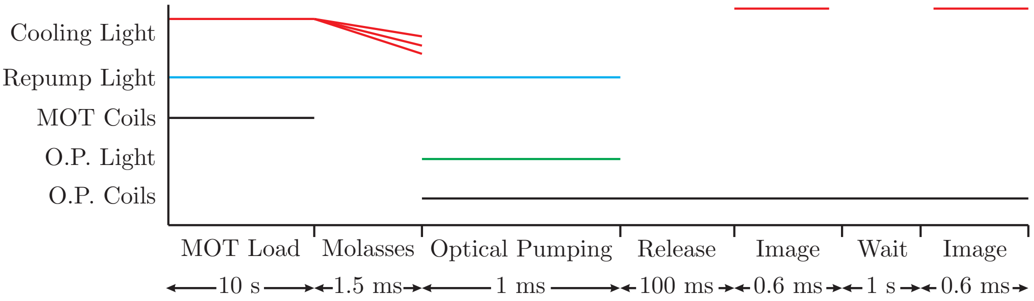

Figure 3.15: Experimental sequence performed when carrying out time-of-flight measurements of the atomic cloud temperature. The diagram is laid out as per Figure 3.14.

a later time, when the atoms have moved out of the imaged region. After background subtraction the image is smoothed and the profile of the scattered light is fitted to a Gaussian form in both the x and y dimensions. This process is repeated for a range of different times of flight and the resulting evolution is fitted according to Equation 3.11.

Through the use of this time-of-flight procedure it is possible to optimise a number of aspects of the experimental procedure such as the molasses duration, molasses detuning, shim fields etc. to produce as low a temperature as possible. Through this optimisation we estimate we can cool the atomic cloud to temperatures of around 10-15 μK with atom numbers of around 10^7 (temperatures as low as around 5 μK were possible at the expense of atom number).

Optical pumping optimisation

There is one other important quality to optimise for the experiments that were carried out, and that is the polarisation of the atomic cloud. This was achieved by loading the atoms into a magnetic quadrupole trap. The experimental sequence is illustrated in Figure 3.16 and is as follows: the atomic cloud is loaded and cooled using optical molasses, and then optically pumped. Immediately after optical pumping the magnetic quadrupole trap is turned on, and maintained for a short duration whilst any untrapped atoms move away from the imaged region. The coils are then turned off at the same time as a fluorescence image is taken. A dark frame is also acquired a short time later when the imaged region is empty of atoms. As a reference, a

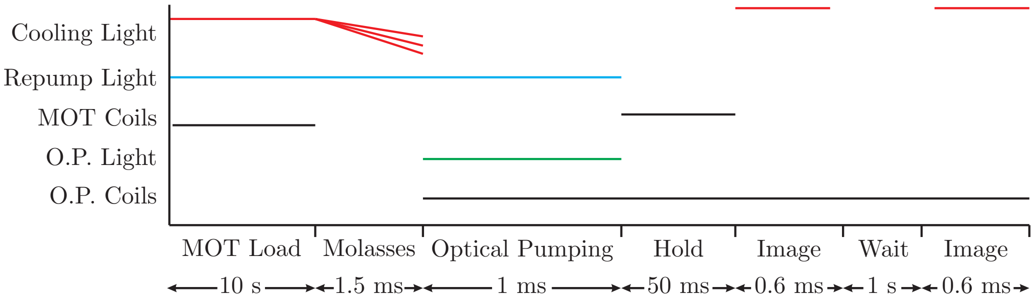

Figure 3.16: Experimental sequence performed when loading the quadrupole trap. The diagram is laid out as per Figures 3.14 and 3.15. Note that the variation in current through the MOT coils is represented qualitatively by the height of the corresponding line.

fluorescence image is taken without the quadrupole trap hold, i.e. so that all of the cooled atoms are imaged. The fraction of atoms that are magnetically trapped is then found by summing the total counts for both images, and finding the ratio.

Ideally we wish to analyse the number of atoms that are pumped into the $F = 2, m_F = +2$ state. In order to do this we must choose the magnetic field gradient of the quadrupole trap appropriately. As per Section 3.4.3, a field gradient of around 15.4 G/cm is required to levitate $m_F = +2$ atoms against gravity, however we require a trap which is deep enough to trap these atoms, yet not deep enough to hold $m_F = +1$ atoms. Whilst calculations can provide an estimate of the field required to do this, the best method is to use the signal from the quadrupole trap. By varying the current passed through the coils one can observe an increase in the signal as atoms in the $m_F = +2$, and subsequently $m_F = +1$, state become trapped. The signal change is not a stark one however, as there is a continuous increase in the number of atoms trapped as the potential depth is increased. To help assess the points where magnetic sublevels begin to be trapped it is also possible to observe motion of the atoms in a weakly confining potential by varying the hold time within the quadrupole trap. Using these methods a current of around 6 A was chosen to create the quadrupole trap.

This method of loading a quadrupole trap was used to optimise the optical pumping procedure by analysing the variation in signal as parameters such as the beam power and polarisation were varied. Through this optimisation we estimate we are able to pump around 90–95% of the atomic cloud into the $m_F = +2$ state, which we consider to be an excellent efficiency, comparable to some of the best reported polarisations [128].

3.5 Conclusion

In the foregoing discussion we have outlined the experimental equipment and techniques that were used to realise an atom mirror based on nanomagnetic domain walls. Whilst many of the features described are common to other cold atom or atom mirror experiments, we have described in detail the features characteristic of our setup. In particular, the method for sensitively detecting the atoms via an intensity-stabilised light sheet and the manner in which the micromagnetic reconfiguration of the nanowire array is realised have both been discussed. In the following chapter the experimental results achieved using this setup are presented.

Chapter 4

Mirror Results

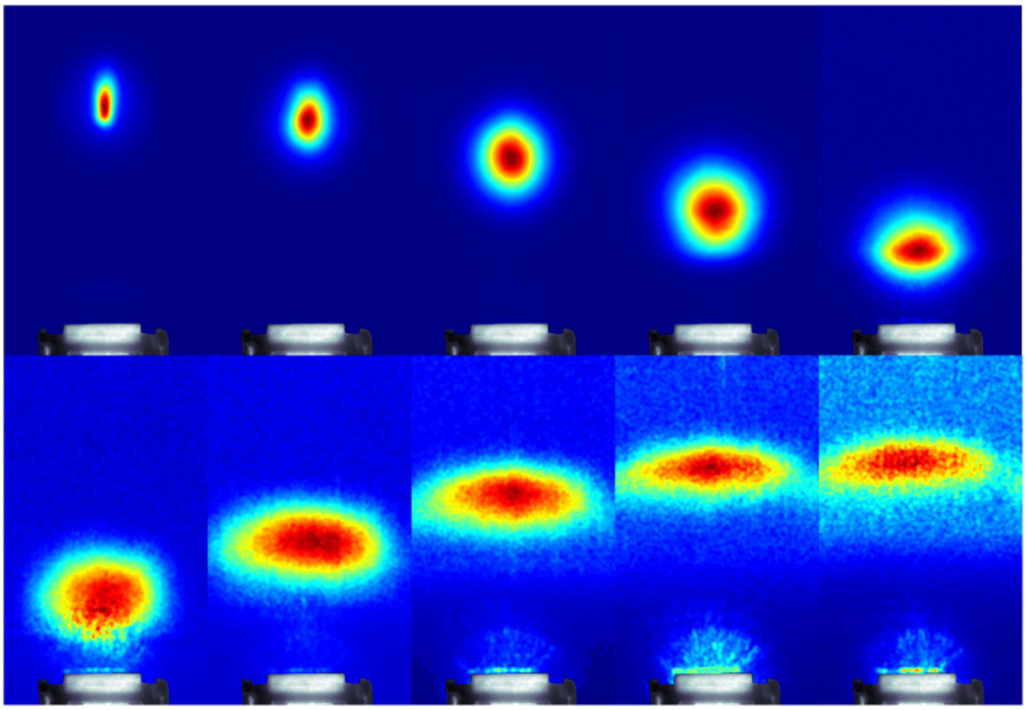

Fluorescence images of a cloud of ultracold ^{87}*Rb atoms reflecting from the fringing fields produced by a 2D array of nanomagnetic domain walls.*

The work in this chapter forms the basis of the following paper:

Realization of the manipulation of ultracold atoms with a reconfigurable nanomagnetic system of domain walls
A. D. West, T. J. Hayward, K. J. Weatherill, P. W. Fry, T. Schrefl, M. R. J. Gibbs, C. S. Adams, D. A. Allwood and I. G. Hughes
arXiv:1112.0485

4.1 Introduction

In this chapter we present the results from the atom-mirror experiment. We have observed the first interaction between ultracold atoms and nanomagnetic domain walls. We shall discuss the nature of this interaction, and what we can deduce, both about the dynamics of the atoms and about the nature of the micromagnetic reconfiguration of the nanowires.

We shall see that the atom-nanowire interaction is manifested as the diffuse reflection of the atoms from the fringing-field region above the nanowire array, in a manner consistent with theoretical predictions and approximations. Some discrepancy is observed when analysing the dynamics in detail. Reasons for this discrepancy are suggested.

The use of the atoms as a probe of the micromagnetic behaviour of the nanowire array is also examined by exploiting the switchability of our device. We demonstrate that this switching process can be employed in a highly deterministic and reliable manner. However, examination of the nature of this reconfiguration procedure reveals that it displays elements of stochasticity. We will see that this switchability permits an accurate and repeatable tuning of the interaction between the atomic cloud and the nanowire array.

4.2 Atom dynamics

4.2.1 Overview

The primary result of the experiment described in the previous chapter is the controllable interfacing of atoms with domain walls. This is realised via the transient interaction of atoms with our nanowire array, acting as a magnetic atom mirror. This reflection process is pictured on the previous page, and is shown annotated in Figure 4.1. The images are taken at the labelled times

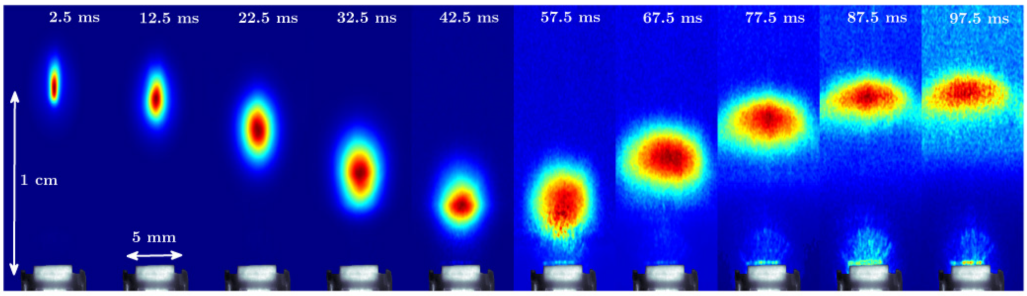

Figure 4.1: A sequence of fluorescence images showing the reflection of a cloud of ultracold ^{87}Rb atoms from the nanowire array. Superimposed on the fluorescence images is an image of the chip and surrounding mount. The colour map is not to scale between frames.

after the optical molasses and optical pumping sequences. Each frame is an average of multiple fluorescence images. The number of repetitions increases as the time increases, because the signal to noise decreases. The maximum number of images averaged over is 20. Each frame has an image of the chip and mount superimposed. There is a significant amount of scattered light from the mount which makes it difficult to resolve the cloud when it is close to the nanowires. Because of this some background subtraction was carried out by hand for these frames, which manually supresses the scattered light[1].

4.2.2 Light-sheet signal

Whilst the images shown in Figure 4.1 provide a good overview of the experimental realisation of an atom mirror, we demand a more quantitative handle on the atom dynamics, and this is provided by the light-sheet signal (cf. Section 3.4.2). An example of the resulting signal is shown schematically in Figure 4.2 as a reference for the following discussion. There are two clear features to the light-sheet signal. The first peak corresponds to atoms which are falling under gravity through the light sheet. The second

---

[1] The cloud size is determined from the side furthest from the chip. The signal is then suppressed in a gradated manner below an equivalent distance on the other side of the cloud.

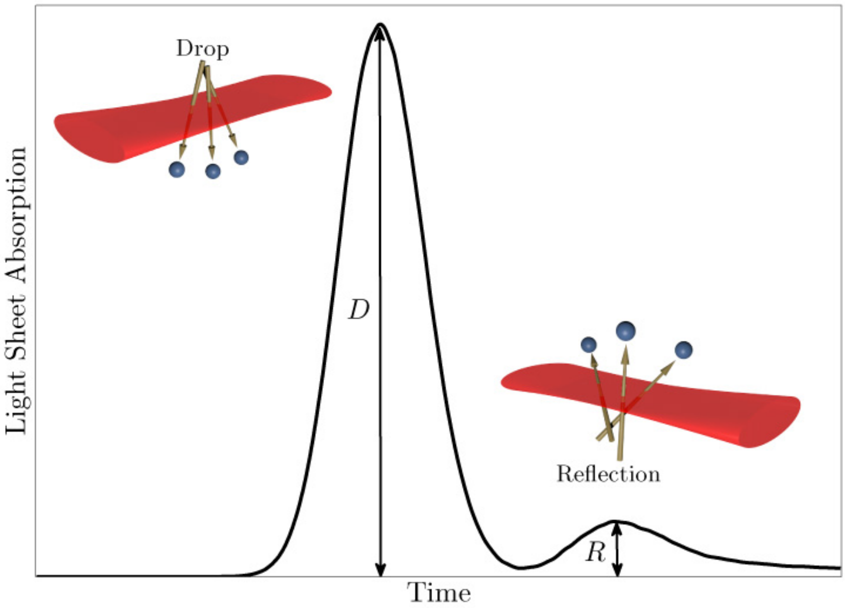

Figure 4.2: An example of the signal obtained via the light sheet. The features corresponding to falling and reflected atoms are labelled. We define the 'reflection signal' as the height of the reflection feature divided by the height of the drop feature, i.e. R/D.

peak corresponds to atoms which have been reflected and are travelling back up through the light sheet (for sufficiently high atom temperatures the two features become less well resolved and the assignment of falling or reflected atoms becomes less appropriate). Unless otherwise stated, from hereon the 'reflection signal' is defined as the ratio between the heights of these two features (R/D in Figure 4.2). Whilst the number of atoms is strictly proportional to the integrated signal, this definition of the signal suffices provided the initial temperature of the atomic cloud is kept constant.

Figure 4.3 shows the light-sheet signal obtained for a range of initial cloud temperatures. Also displayed are the predicted lineshapes according to Monte Carlo simulations, which are discussed in Chapter 5. The temperatures labelled are those according to independent time-of-flight measurements.

The shape of the features we observe has a strong dependence on temperature which can be intuitively explained. For higher cloud temperatures the atoms are on average moving more quickly. Thus the cloud will spread out

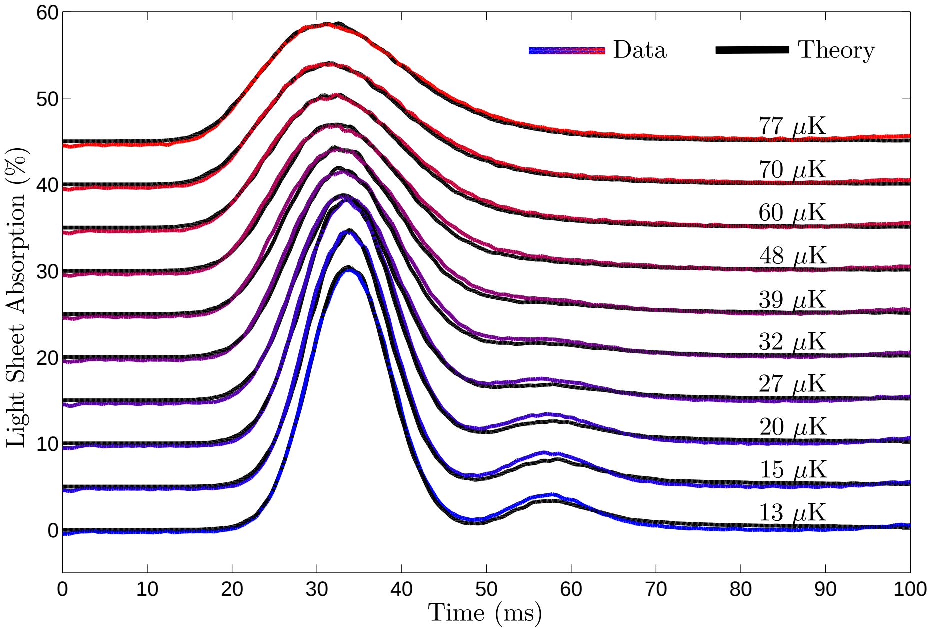

Figure 4.3: Observed light-sheet signal during the reflection of atoms from the nanowire array for a range of initial cloud temperatures. Coloured lines represent experimental data, black lines represent predictions according to Monte Carlo simulations. Data sets at different temperatures are vertically offset by increments of 5% for clarity.

more. This has a number of consequences. Firstly the cloud is more diffuse when it passes through the light sheet which means that the resulting signal is broader and has a smaller height. We note that the integrated area of the drop feature is approximately constant as very few atoms miss the light sheet for the temperatures considered, since the light sheet is large compared to the size of the atomic cloud at the height of the light sheet.

Perhaps the most striking feature of the light-sheet signals obtained is the smallness of the reflection signal. This is simply because the atom cloud is significantly larger than the nanowire array when it reaches the chip. Thus a large proportion of the atoms miss the region where the fringing fields are located and are not reflected. An estimate of the fraction of atoms that will hit the chip can be calculated analytically by considering the dynamics of a Gaussian cloud of atoms in thermal equilibrium.

We consider a cloud of atoms falling onto a chip in the x-y plane at height $z = 0$, with size $d \times d$. An atomic cloud in thermal equilibrium has a spatial distribution described by a Gaussian in each dimension. This is a good approximation of the cloud shape following an optical molasses sequence, as evidenced by fluorescence images. We label the standard deviations of the distribution σ_i. As the cloud falls under gravity these standard deviations evolve according to Equation 3.11:

$$\sigma_i(t) = \sqrt{\sigma_i(0)^2 + \frac{k_\mathrm{B} T_i t^2}{m}}. \tag{4.1}$$

$\sigma_i(0)$ is the standard deviation of the initial spatial distribution and T_i is the temperature in the corresponding direction. Note that as t increases the approximation of a Gaussian cloud becomes more accurate. The time taken to reach the nanowire array is given by $t_\mathrm{fall} = \sqrt{2h/g}$. Thus one can calculate the sizes of the cloud in the x and y directions at the height of the chip, $\tilde{\sigma}_{x,y} = \sigma_{x,y}(t_\mathrm{fall})$. Given a square chip we have $\tilde{\sigma}_x = \tilde{\sigma}_y$. The fraction of atoms that have an x coordinate within the bounds of the chip, χ_x, is then given by an integral of the spatial distribution, i.e.

$$\chi_x = \int_{-d/2}^{d/2} \frac{1}{\sqrt{2\pi}\tilde{\sigma}_x} \exp\left(-\frac{x^2}{2\tilde{\sigma}_x^2}\right) = \mathrm{erf}\left(\frac{d}{2\sqrt{2}\tilde{\sigma}_x}\right), \tag{4.2}$$

where erf is the error function, given by $\mathrm{erf}(x) = 2/\sqrt{\pi}\int_0^x e^{-t^2}\mathrm{d}t$ [129]. If we make the assumption that the cloud is initially isotropic in size and temperature the total fraction that hit the chip is then provided by χ_x^2. Evaluating this expression using the width of our nanowire array $d = 2.0$ mm, and values of $T = 13$ μK and $\sigma_x(0) = \sigma_y(0) = 0.74$ mm from time-of-flight measurements (cf. Section 3.4.2) yields the result that only around 19% of the atomic cloud will actually hit the chip.

Examining Figure 4.3 we can compare this prediction with experimental observations. By evaluating the integrated signal associated with both the falling and bouncing atoms we can calculate an associated fraction (we assume that all falling atoms pass through the light sheet). Doing this yields a fraction of around 14%. The fact that this is lower than the fraction hitting the chip indicates that a number of atoms are being lost for another reason. This reason, which has been discussed before, is that the effective isosurface that the atoms reflect from is corrugated and is not continuous. As such, some atoms will be incident on the area of the chip but are not reflected, or are reflected at such angles that they do not reach the light sheet again.

The most noticeable discrepancy between simulation and experimental data is observed in the reflection feature — this is somewhat expected as the nature of the reflection is the least well understood aspect of the experiment. We note that theory predicts a smaller reflection signal than observed in experiment. One possible explanation for this discrepancy is an inaccuracy in the shape of the isosurface. The isosurface was calculated via an approximate analytic model of the fringing fields, rather than by more accurate micromagnetic methods. If the degree of corrugation of the calculated surface is greater than that of a real domain wall then one would expect a larger proportion of the atoms to be reflected. Unfortunately it is very difficult and time consuming to perform a full micromagnetic calculation of the fringing fields — doing so for the case of a large array of domain walls is computationally unfeasible.

Another possible explanation for the discrepancy is an inaccuracy within the simulation of the atom-field interaction. In Section 5.2.3 we will discuss how the atom-nanowire interaction is approximated as a point one. Whilst this is demonstrated to be an accurate approximation, the possibility of multiple interactions with the fringing fields is not considered which may occur for atoms which are reflected at large angles relative to normal.

4.2.3 Time-of-flight image analysis

Whilst the light-sheet signal provides a more quantitative and precise measure of the atom dynamics, the data are somewhat limited as we observe an integrated signal at one particular height and the spatial distribution of the atoms is only examined in the vertical direction. Fluorescence imaging, however, provides more data on the shape of the atom cloud, and we can use these data to infer the nature of the effective isosurface from which the atoms are reflected.

In Section 5.2.2 we describe the manner in which the time-of-flight imaging procedure is simulated. Using the data obtained from fluorescence images and the predictions from simulation, efforts were made to measure the effective roughness of the mirror, i.e. the mean angle of the effective isosurface, through a comparison between experiment and theory. The resulting data are shown in Figure 4.4. The initial cloud width and temperature for the

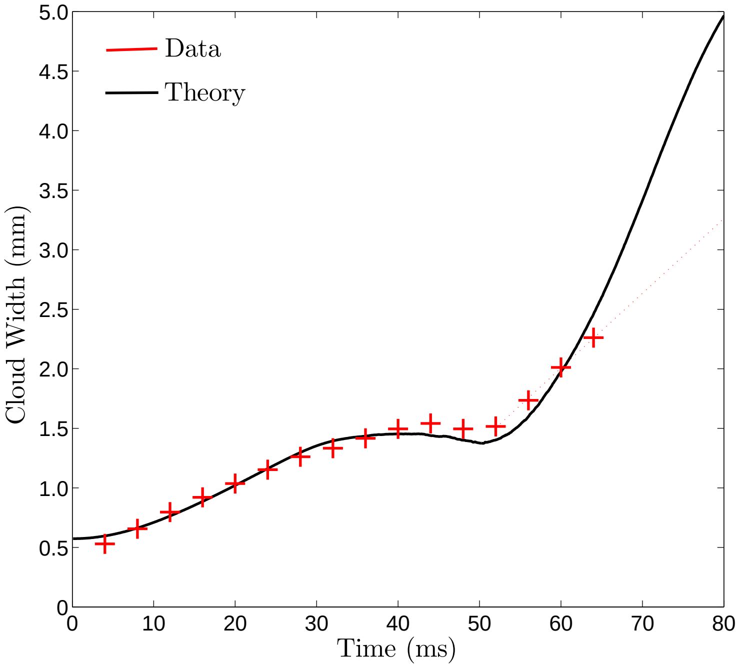

Figure 4.4: Comparison of the experimentally observed and theoretically predicted evolution of the atomic cloud width. The theory curves are calculated via Monte Carlo simulations. Error bars are smaller than the data points. The range of data is limited by poor signal to noise preventing an accurate fit of fluorescence images.

theoretical simulations are set by independent time of flight measurements.

The most important observation to make from this comparison of data and theory is that the data are poorly fit by the theory curve which uses the calculated isosurface. We note that the expansion of the cloud is observed to be slower than expected. This suggests that the effective isosurface from which the atoms are reflected is less corrugated than we calculate. The possibility of this inaccuracy was also posited as possible explanation of the discrepancy between observed and expected light-sheet signals shown in Figure 4.3.

A number of approaches were adopted to try and fit the data. A rescaling of the calculated isosurface from which the atoms are reflected was attempted, as was the use of a manually defined isosurface, either with a fixed angle, or a distribution of angles with a fixed mean. These approaches are described in more detail in Section 5.2.3. Unfortunately none of the theoretical traces achieved a good agreement with the experimental data. This is expected near the time when the atoms are reflected (around 50 ms) as the cloud width is poorly defined here and the atoms have moved out of the imaging beams by this point. After the reflection one might anticipate a better fit but this is not found. The reflection of the atoms maps the initial atom trajectories (well fitted by theory) onto new trajectories, and a possible explanation for the inaccuracy is that this map is inaccurate. Because the nature of the reflection is defined not only by the mean angle of the surface but by its overall shape it is difficult to produce a good fit.

We also note that the cause of the discrepancy may be an experimental one — as will be shown explicitly in the following section, the signal obtained via fluorescence imaging of the atomic cloud is small when observing the reflected atoms. Because of this the range of data obtained is limited. It may also be the case that there are some effects that are unaccounted for and contribute to modifying the cloud shape, for example the presence of stray fields from the experimental apparatus. Future work could modify the experimental setup to aid in providing a more accurate measure of the atom cloud evolution. For example, the use of an imaging beam separate from the MOT beams would permit the moving of this beam so that it followed the atomic cloud and would hence provide a much larger signal. However, the diffuse nature of the reflection is the price knowingly paid for using a spintronic device as the basis for our mirror. The reward, and the feature we shall now focus on, is the dynamic nature of the magnetic sources.

4.3 Micromagnetic reconfiguration

The data presented thus far have primarily examined the behaviour of the atoms and the nature of the interaction with the fringing fields produced by our chip. As demonstrated by the good agreement exhibited in Figure 4.3, this behaviour is well understood. Given this, we now consider the use of the atoms as a probe of the behaviour of the nanowires.

4.3.1 Switching of the array

It is possible to use the reflection signal as a measure of the micromagnetic reconfiguration. An initial examination of the behaviour of the nanowire array is obtained by switching the chip between the 'on' and 'off' states described in Section 3.3.1. Previous magnetometry has provided values of the fields for which the array is considered to be switched fully, i.e. where the domain wall sites are either all vacant or all populated [77]. As described in Section 3.4.3, the field that we produce is well in excess of the required switching fields in both magnitude and duration. Thus we expect to be able to switch fully the chip state and completely remove or maximise any interaction, and thus reflection. The behaviour of the chip was examined by observing the light-sheet signal between switching events. The resulting data are shown in Figure 4.5. The chip was switched with a single magnetic field pulse of maximum possible strength.

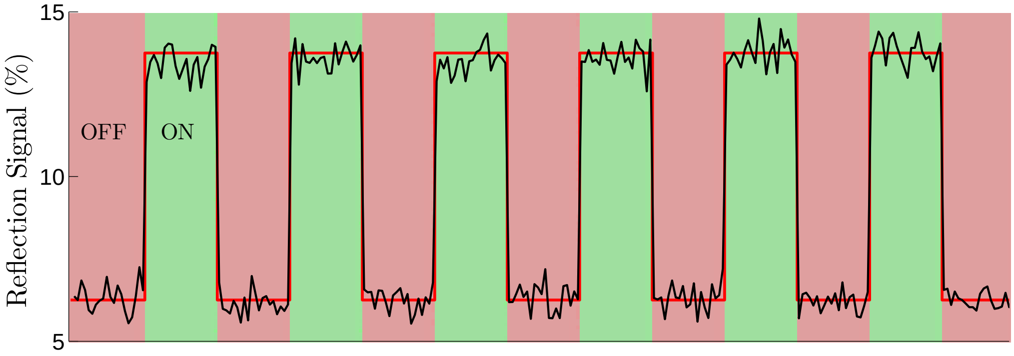

Figure 4.5: The reflection signal observed as the nanowire array state is toggled. The black line represents data. Each data point is extracted from a single shot (one reflection). Each rising/falling edge is due to a switching of the array caused by a single magnetic field pulse. The red line and shading represent the desired mirror state.

When switching the array we observe that there is a very high level of repeatability; every magnetic field pulse produces a stark change in the observed reflection signal. Thus we can toggle the interaction between the atoms and chip with 100% reliability. However, there is an unexpected feature of the signal that we observe. When the array is switched into the 'off' state there is still a non-negligible reflection signal. This shows that a fraction of the atomic cloud is still being reflected, despite the expectation that all the domain walls have been removed from the array. Upon switching into the 'off' state there is a reduction in the reflection signal by a factor of almost 2.5. This is also representative of the corresponding reduction in atom number, which is found by integrating the reflection signal. We estimate that around 6% of detected falling atoms are subsequently detected again after reflection. This compares to a fraction of around 14% when the chip is in the 'on' state.

Given the unexpected light-sheet signal observed, further investigation was carried out using fluorescence imaging. The resulting images are shown in Figure 4.6. As expected, we observe a cloud of atoms reflected from the surface of the chip when the latter is in the nominally 'off' configuration. The colour map used in Figure 4.6 is such that it is approximately to scale compared with Figure 4.1. Significant effort was required to get adequate signal to noise as the scattered light from the chamber masks the atom fluorescence. To demonstrate this we provide an example of the data obtained from fluorescence imaging. Figure 4.7(a) shows the data obtained using dark frame subtraction, and (b) shows the data after additional processing, both for a time of flight of 87.5 ms. The removal of the remaining background light is relatively easy when the atomic cloud is spatially distinct from the atom chip mount (the primary source of scattered light), near the point of reflection noise subtraction becomes increasingly difficult. This effect is exacerbated by the fact that as the atoms approach the chip they move out of the imaging beams so the fluorescence is significantly reduced.

The technique of release-recapture was also investigated as an alternative measure of the reflected atom number. The method is outlined as follows: the MOT is loaded and the fluorescence produced during the load is measured by a photodiode. The fluorescence at the start of the loading sequence is noted. The atom cloud is then dropped and reflected from the nanowire array. The MOT is then turned back on again, at the point in time when the reflected atoms are returning to the original position. The fluorescence at the start of the new MOT load is recorded and compared to that for a normal MOT load (i.e. without the presence of reflected atoms). Unfortunately, the

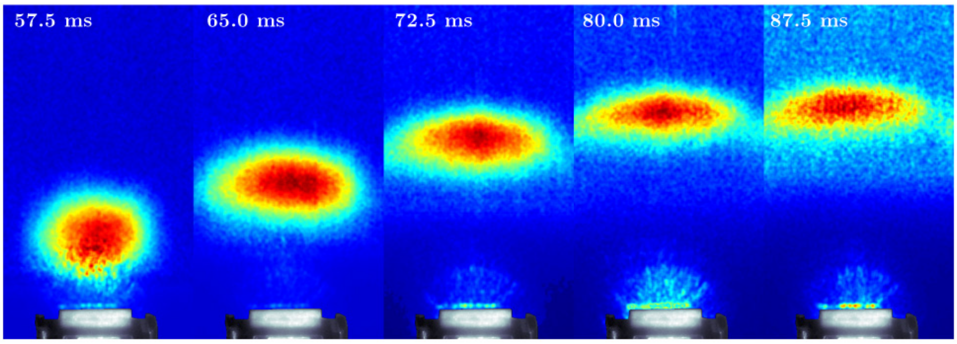

(a) Chip on

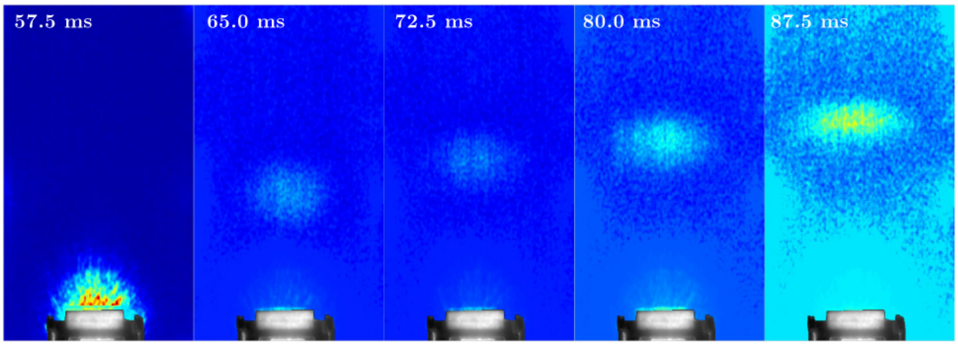

(b) Chip off

Figure 4.6: A series of time-of-flight fluorescence images taken when the chip has been switched off, shown in (b), is compared to the equivalent images with the chip on, shown in (a). A small fraction of the atomic cloud can be seen to reflect when the chip is off. The colourmap is not to scale between frames, but is approximately to scale between the on and off sequences.

number of reflected atoms and their corresponding contribution to the MOT fluorescence is too small to make a noticeable difference. This is supported by simulation as we predict that the maximum fraction of atoms that will return to the MOT region at any time is only around 1%[2]. Thus we conclude that the methods of fluorescence imaging or light-sheet absorption are much better measures of the atom number reflected.

The images shown in Figure 4.6 show a rather suprising result. There are two explanations as to why we observe atom reflection when the nanowire

---

[2] This fraction is defined by the number of atoms that are observed to be within the $1/e^2$ radius of at least one of the MOT beams — the atom velocity is significantly lower than the MOT capture velocity so we assume that all atoms entering the beams are recaptured.

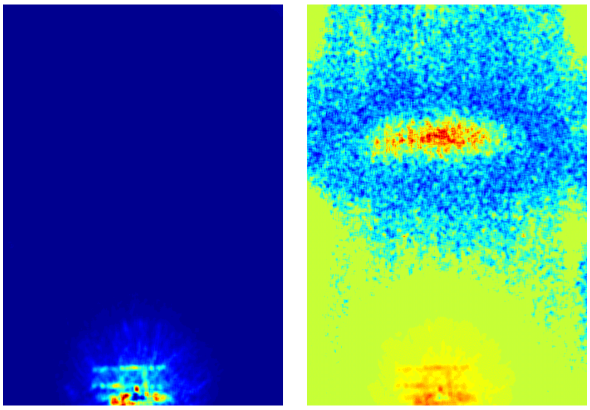
(a) Raw data (b) Processed data

Figure 4.7: Example data from fluorescence imaging. The left hand figure shows data obtained from an average of multiple images, using dark frame subtraction, note that there is still a significant amount of background light. The right hand image shows the result once the remaining noise from scattered light has been manually suppressed. The image shown is for the case of the nanowire array in the off configuration.

array is turned ‘off’. Firstly, our assumption that the chip is indeed ‘off’ may be untrue — there may be fringing fields that remain despite the application of the switching off pulse. Many alternative magnetometry techniques exist, but could not be carried out with the nanowire array in situ. Efforts were made to carry out magneto-optical Kerr effect (MOKE) microscopy (cf. Section 3.3.2) but this was not possible. In MOKE microscopy the magnetisation reconfiguration is obtained by analysing the polarisation rotation of a laser beam reflected from the magnetic material. This rotation is then observed as a small intensity change of the output of a polarising beam splitter, during the reconfiguration process. Unfortunately, the application of the magnetic pulse to switch the array caused a small amount of motion of the chip which also caused intensity changes of the beam, thus masking the desired signal.

The alternative explanation of this unexpected behaviour is that the reflection observed when the chip is in the off state is not caused by magnetic fields. To test this possibility a simple null experiment was performed. Rather than pumping the atoms into a weak-field-seeking magnetic sublevel, which will be repelled from the fringing fields, we pump the atoms into a strong-field-seeking state, which should never be reflected, regardless of the state of the nanowire array. Experimentally this is an easy adjustment to make and we do not observe any atoms reflected from the nanowire array, according to both the light-sheet signal and fluorescence images. Given the sensitivity of the light sheet (cf. Section 3.4.2) this corresponds to less than around 0.01% of the atomic cloud being reflected. Examples of the light-sheet signal obtained are shown in Figure 4.8.

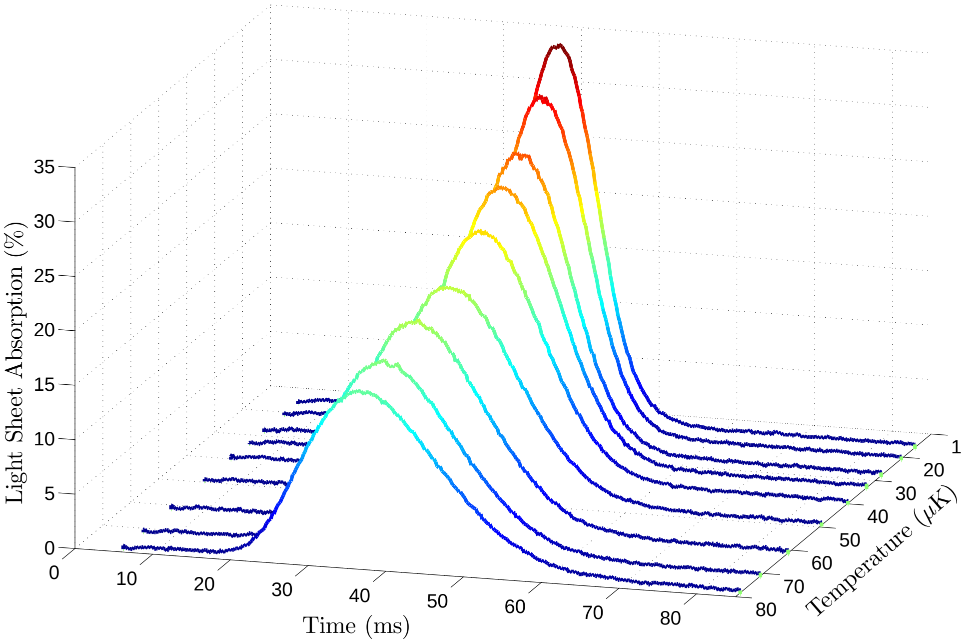

Figure 4.8: Light-sheet signals for a cloud of atoms pumped into the $F = 2, m_F = -2$ state. These atoms are strong-field-seeking so there is no reflection signal at any temperature.

There is a clear result: no reflection of the atoms is observed at any temperature. This is also the case when examining fluorescence images of the cloud. This clearly demonstrates that any reflection of atoms is caused by a magnetic interaction, as expected, and suggests that the unexpected reflection of atoms when the mirror is supposedly in a non-interacting state is due to the presence of remaining magnetic fields. Unfortunately, further investigation of the source of these magnetic fields is not possible whilst the chip is incorporated in the current setup, but analysis in the future would be of great interest.

4.3.2 Tuning the atom-nanowire interaction

Whilst Figure 4.5 demonstrates the tunability of the atom-nanowire interaction, this modification is a purely digital one. We now consider tuning the interaction in a continuous manner. This is achieved by varying the field used to switch the array configuration. The chip was prepared in either the 'on' or 'off' state through a repeated application of a maximal field pulse in the appropriate direction. The array is then switched into the opposite state through the application of a single orthogonal magnetic pulse. The magnitude of this pulse is varied. The reflection signal is examined after application of the single switching pulse. The resulting data are shown in Figure 4.9.

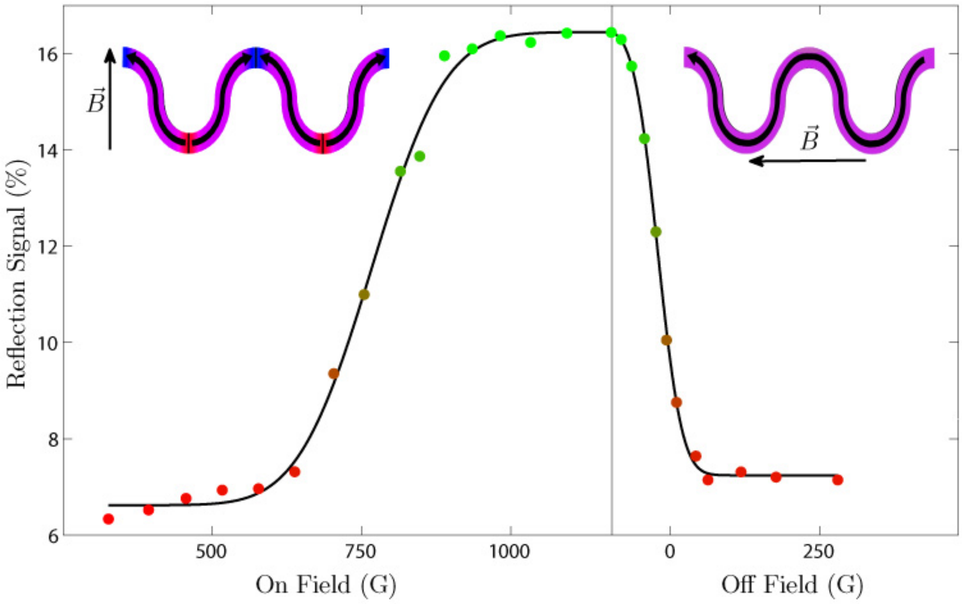

Figure 4.9: Dependence of the observed reflection signal on the field used to switch the chip. The left half of the figure shows the nanowires being switched on, populating domain walls. The right hand half shows the nanowires being switched off, annihilating domain walls. The resulting domain wall configuration and corresponding switching field directions are illustrated in the corresponding insets. The error bars are smaller than the data points and represent the standard error on the mean. The black lines are fits of the form of error functions.

By varying the magnetic field pulse size we observe a continuous variation in the size of the reflection signal. This can be intuitively understood by considering a gradual population or annihilation of the domain walls. As the switching on (off) field is increased, more domain walls are populated (annihilated) and more (less) of the array has associated fringing fields, meaning a larger (smaller) fraction of the atoms impinging on the array are reflected. Once the field pulse is sufficiently large there is no further variation in the reflection signal as the array is considered to be fully switched.

The data in Figure 4.9 are fit by functions of the form

$$c_1 + c_2 \ \mathrm{erf}\left(\frac{B-\bar{B}}{\sqrt{2\sigma^2}}\right), \tag{4.3}$$

where c_1 and c_2 are fitting constants, B is the applied field and erf is the previously defined error function [129]. As will be elaborated upon, $\bar{B}$ and σ are the associated mean and standard deviation of the field distribution. The data are fit well by a function of this form, with reduced χ^2 values of 5.3 and 1.0 for the on and off fields respectively. This agreement with the form of an error function suggests that the required switching field for individual sites follows a normal distribution. This suggests that the variation in the required field is goverened by random fluctuations in the lithographic pattern across the chip. Small changes in the width, thickness, roughness or shape of the wire can lead to slightly different magnetic behaviour [98, 130]. From the fits we can extract parameters characterising the shape of the corresponding normal distribution. The standard deviation of the 'on' ('off') field distribution is 103 ± 10 G (32 ± 3 G). The mean 'on' ('off') field is 771 ± 8 G (78 ± 2 G). These values are observed to agree well with values obtained using alternative magnetometry techniques [77]. In particular we note that the values that fully switch the array are in agreement with those measured following the fabrication of the chip.

4.3.3 Stochastic behaviour

It is well known that the micromagnetic reconfiguration processes which occur in superparamagnetic objects exhibit a degree of stochasticity [97, 131, 132], i.e. when subjected to a magnetic field pulse there is some probability that the magnetisation structure will macroscopically reconfigure. We used the reflection signal to search for evidence of the presence of this stochastic behaviour in our system. To do this we apply a particular switching field multiple times. If there is some stochastic character to the switching process, one would expect that not all of the domain walls that could switch with the provided field, would do. Subsequent applications of the same switching pulse would then lead to additional switching of the chip. In an effort to maximise the apparentness of this effect a field which, according to Figure 4.9, switches approximately half of the domain wall sites, was used. This would imply that a significant number of domain wall sites would be initially switched, producing a noticeable signal change, but there would be a significant number of unswitched sites which could then switch upon a repeated application of the switching field. Example data achieved through this process are shown in Figure 4.10 for the case of switching the chip off.

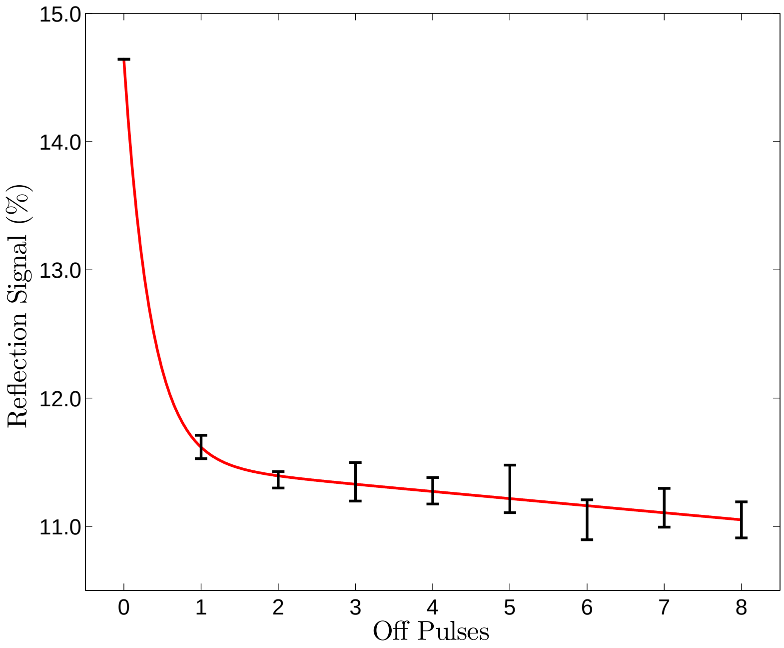

Figure 4.10: Evolution of the reflection signal during multiple single applications of a switching off field of roughly 90 G. Error bars indicate the standard error on the mean. The data are normalised relative to the reflection signal before switching off. The red line is a fit to guide the eye.

The data clearly suggest a stochastic element to the behaviour of the chip. The first application of the switching off field produces a big change in the reflection signal as a large number of domain wall sites are switched. However, subsequent applications of the same field produce a discernible change in the reflection signal as well. These subsequent field pulses switch additional domain wall sites and hence reduce the fraction of the chip from which fringing fields are produced.

This observation of stochastic behaviour highlights the sensitivity of the reflection signal to the magnetic configuration of our chip; we use a macroscopic atomic cloud to analyse the collective state of an array of nanoscale objects with good precision in a quick and repeatable manner. This represents a robust interface between a quantum ensemble and a condensed matter ensemble, both of which contain $\sim 10^7$ particles.

It is difficult to make quantitative deductions from the data presented for a couple of reasons. Firstly, this method of analysis is significantly less precise than other magnetometry techniques, and secondly the formulation of the stochastic behaviour is complex, and may be of limited applicability for the processes we are considering. This is especially true since the typical characteristic timescale of stochastic superparamagnetic reconfiguration is of the order of tens of ns [97], which is much smaller than the length of magnetic pulses we employ, which are typically 0.5 ms or greater.

4.4 Conclusions

The application of nanowires as a magnetic mirror was designed to facilitate a collective interaction, between a large number of domain walls and a macroscopic ensemble of atoms. This has clearly been achieved, and is well understood. The data presented are shown to agree well with theoretical predictions. We observe a diffuse reflection which produces a dispersion of the atomic cloud. The behaviour of the atomic cloud shows good agreement when we consider the signal obtained from the light sheet — this is the most accurate measure of the atom dynamics. Greater discrepancy is observed when we analyse the evolution of the atomic cloud via direct imaging methods. Reasons for this discrepancy have been suggested, but improved agreement would require significant effort to investigate a feature which we know to be a drawback when one considers our device simply as an atom mirror.

Instead we consider this experiment as a successful demonstration of a new type of interaction and an exposition of the benefits of spintronic technology which paves the way to more elaborate atom-nanowire interfaces. Whilst we have observed that the domain wall array acts as an imperfect mirror, the data also show it provides extremely reliable switching and tuning of the magnetic interaction; we are able to use the interaction as a probe of the device's behaviour. We see that the dynamic nature of domain-based material provides a new kind of functionality to permanent magnetic field sources which we hope will confer great utility to atom-trapping applications of domain walls.

In Chapters 7 and 8 we will discuss how the small characteristic size of our device provides massive field gradients which act as a double edged sword, both presenting challenges and conferring benefit. In the context of the mirror experiment they allow the close approach of the atoms and the use of the point interaction approximation which provides us with our effective isosurface. In Chapter 6 we will consider extending study beyond the region of this isosurface, and utilising the close approach of the atoms to examine new physics. In the following chapter we will discuss the simulations which provided the theoretical predictions with which the experimental data were compared.

Chapter 5

Mirror Simulation

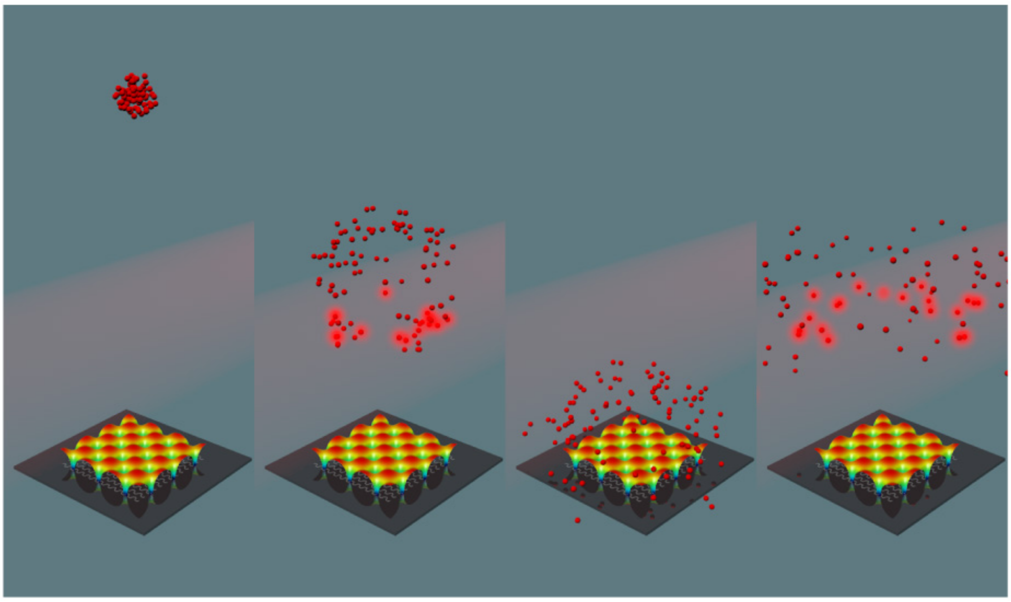

Schematic of the simulation of atoms falling onto and being reflected from the effective isosurface associated with a nanowire array populatead with domain walls. Atoms passing through the light sheet are highlighted.

5.1 Introduction

This section will detail the simulation, via Monte Carlo methods, of the mirror experiment. The corresponding Matlab code is provided in Appendix D, and will be referred to by line number in the following discussion. We will consider the theoretical description of the experiment in a chronological progression through the experimental routine as this is perhaps the most intuitive. Some results used to guide the experimental design are then presented.

5.2 Theory

Monte Carlo simulations are based on a fundamental feature: randomness. The goal of any Monte Carlo simulation is to reproduce the behaviour of a distribution by observing a representative and randomly sampled subset of that distribution. In the case of the work at hand, i.e. the magnetic atom mirror, we wish to know the behaviour of a distribution of atoms as they interact with our nanowire array, and also with the light fields that they experience.

5.2.1 Initial conditions

Our starting point is a cloud of ultracold atoms. The experimental procedures for producing such a cloud were outlined in Chapter 3. In order to characterise the atomic cloud we need just a couple of parameters: the temperature and the size of the cloud. We make the assumption that the cloud has Gaussian distributions of position and velocity components — an assumption supported by observations made via fluorescence imaging. The position coordinates $\{r_i\} = \{x, y, z\}$ are thus described by a probability distribution

$$f_r(r_i) = \frac{1}{\sqrt{2\pi\sigma_i^2}} \exp\left(-\frac{r_i^2}{2\sigma_i^2}\right), \tag{5.1}$$

where σ is the standard deviation of the distribution, which we derive from time of flight measurements (cf. Section 3.4.4). Note that the mean of the distribution is zero — we define the origin to be at the cloud's centre. We can define a similar distribution for the components of the atoms' velocities. In this case we know that a Maxwell-Boltzmann distribution of velocities comprises Gaussian distributions of velocity components with standard deviations equal to $\sqrt{\frac{k_\mathrm{B}T_i}{m}}$, where k_B is the Boltzmann constant, T_i are the temperatures in each of the cartesian coordinates and m is the atomic mass. Thus the distribution of speeds is given by

$$f_v(v_i) = \sqrt{\frac{m}{2\pi k_\mathrm{B}T_i}} \exp\left(-\frac{mv_i^2}{2k_\mathrm{B}T_i}\right) . \tag{5.2}$$

We make the assumption that the cloud of atoms is isotropic, such that all σ_i and all T_i are equal.

These distributions are macroscopic descriptions of the atomic ensemble. We now change regime and consider what happens to a particular atom within this distribution. This is an easy task which we can repeat many times by taking multiple samples from the distribution. By propagating the behaviour of many microscopic particles we will then recoup the macroscopic properties of the system.

The remaining question is then how to appropriately sample the distribution in a random manner. This is the basis of the Monte Carlo method, which we will now describe briefly. For a more rigorous discussion see e.g. [133, 134]. There are two main methods for achieving this, the first, which will be described here, relies on the existence of an inverse cumulative distribution, the second is the ‘accept-reject’ method, which, whilst computationally less efficient, is more versatile.

The cumulative of a distribution describes the probability of occurence of a variable less than or equal to some value. This then maps onto the interval $[0, 1]$. Thus if we make a uniform random sampling on this interval we can use the inverse cumulative distribution to map the values appropriately onto the associated probability distribution. This can be understood intuitively by considering that regions of low probability density will occupy small regions of the interval $[0, 1]$ when the cumulative is taken.

For a normal distribution $f_\mathrm{N}(x)$ of standard deviation σ and mean μ, defined as

$$f_\mathrm{N}(x) = \frac{1}{\sqrt{2\pi\sigma^2}} \exp\left[-\frac{(x-\mu)^2}{2\sigma^2}\right] , \tag{5.3}$$

the inverse cumulative distribution is well defined, given by

$$\Phi(p) = \mu + \sigma\sqrt{2}\ \mathrm{erf}^{-1}(2p-1) , \quad p \in (0, 1) , \tag{5.4}$$

where erf is the so-called error function [129]. Note that $\Phi(p)$ is poorly defined for $p = 0$ or $p = 1$. Using this inverse cumulative it is a simple matter to select a number randomly and derive the corresponding velocity and position. This is carried out on lines 219–230 of Appendix D.

5.2.2 Atom-light interactions

During their journey to the nanowire array and back, the atoms are interrogated by light fields. These are, to some degree, perturbative to the atoms' motion, so cannot be neglected.

Optical pumping

Once laser cooling has occured the external degrees of freedom of the atoms are defined. We must also define the internal states. This is achieved via optical pumping, as described in Section 3.4.2, and the efficiency of this process is measured. Hence we know the fraction of atoms in the $m_F = +2$ state, and assume that the small number that remain are not in a weak-field-seeking state. This is an assumption that represents a worst-case scenario given the information we have, but also simplifies the calculation by not considering atoms in an $m_F = +1$ state. We can justify this choice by considering that atoms in the $m_F = +1$ state will experience a potential which is significantly more corrugated than for the $m_F = +2$ atoms so are unlikely to be detected as being reflected. The nature of this potential is discussed in more detail in Section 5.2.3.

The optical pumping process involves the scattering of photons through absorption and subsequent spontaneous or stimulated emission. As such there is momentum imparted onto the atoms by the light. Recall in Section 3.4.2 we discussed two different optical pumping schemes. We have chosen to address the $F = 1 \rightarrow F' = 2$ and $F = 2 \rightarrow F' = 2$ transitions as this pumps the atoms into a dark state, thus minimising the number of photons scattered during the optical pumping sequence. To calculate how many photons are scattered on average, we use a Monte Carlo simulation.

We consider the atoms to be initially evenly distributed amongst the five magnetic sublevels in the $F = 2$ ground state and then propagate their internal dynamics when they are subject to two laser beams. Choosing an atom at random it has a limited number of transitions possible due to quantum mechanical selection rules. We define the 'strength' of a particular transition as

$$S_i = c_i R_i, \qquad \text{excitation/stimulated decay} \tag{5.5}$$

$$S_i = \Gamma, \qquad \text{spontaneous decay} \tag{5.6}$$

where Γ is the atomic linewidth, c_i are the relative strengths of the squared dipole matrix elements (see e.g. [106]) and R_i are the scattering rates, given by [135]

$$R = \frac{\Gamma}{2} \frac{I/I_{\text{sat}}}{1 + I/I_{\text{sat}} + 4\left(\Delta^2 \pm k^2 v^2\right)/\Gamma^2}, \tag{5.7}$$

where I is the intensity of the incident light I_{sat} is the saturation intensity of the transition, Δ is the detuning from resonance, k is the magnitude of the wavevector of the light and v is the speed of the atom resolved along $\vec{k}$. In using this formula we assume that the approximation of a two-level atom is appropriate. We also assume for the case in hand that $v = 0$ as the atoms are approximately at rest when they are optically pumped. The probability of a particular transition occuring is then simply $S_i / \sum_i c_i R_i$, where the sum is over all possible transitions. A simple accept/reject method is then used to randomly determine which transition occurs. A random number, p, on the interval $[0, 1]$ is chosen and transition n occurs, with n being the smallest integer satisfying

$$p < \sum_i^n S_i. \tag{5.8}$$

This process is repeated until the atom reaches the dark state.

Note that during the optical pumping process a quantisation axis is defined by the application of an external magnetic field. This has the effect of Zeeman splitting the magnetic sublevels, introducing an extra detuning of the energy levels given by

$$\Delta_Z = \pm m_F g_F \mu_{\text{B}} B/\hbar, \tag{5.9}$$

with a positive sign corresponding to the ground states and the negative sign to the excited states. A positive detuning corresponds to the applied laser field being of greater frequency than the transition frequency.

To deduce the net momentum kick due to the optical pumping procedure one simply counts the photons absorbed and emitted. Each excitation of the atom is accompanied by the absorption of a photon which we define as providing a quantum of positive momentum. A stimulated emission of a photon thus corresponds to a quantum of negative momentum. Spontaneous emission has no preferred direction of emission, but the random nature of the process leads to heating. Thus, spontaneous emission breaks the symmetry, and the number of photons that are scattered defines the net momentum kick in $\hbar k$. Carrying out this procedure yields Figure 5.1 which shows the distribution of the net momentum imparted on a collection of atoms.

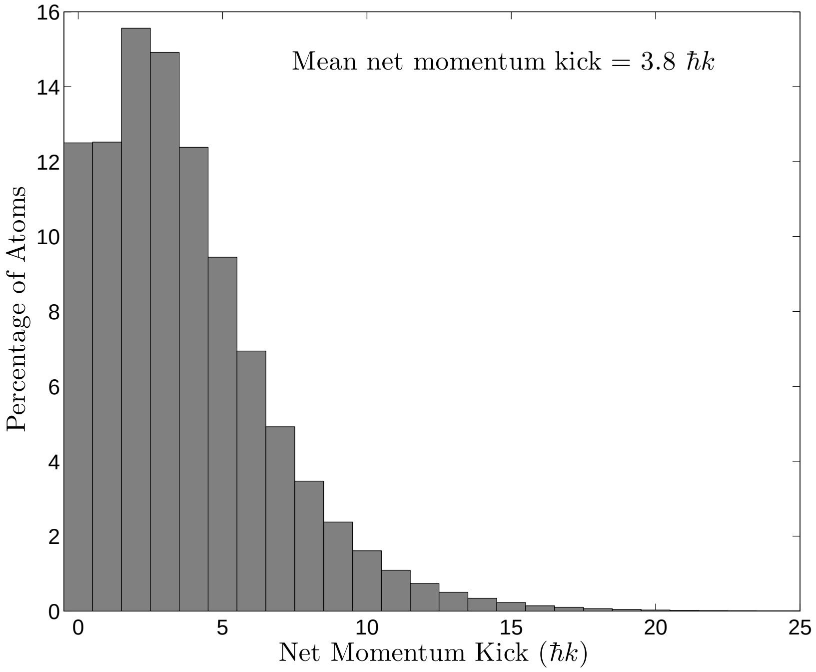

Figure 5.1: The distribution of the net momentum imparted on a collection of ^{87}Rb atoms being optically pumped as per the scheme illustrated in Figure 3.9. The intensities of the two beams are as per experimental values; the pump beam has $I/I_{\text{sat}} = 5.6 \times 10^{-3}$ and the repump has $I/I_{\text{sat}} = 0.37$. A magnetic field of 4 G to define the quantisation axis is assumed.

The result is a favourable one; only a very small net momentum kick is imparted during the optical pumping procedure, with a mean kick of 3.8 $\hbar k$. Less than 10% of the atoms receive a net momentum kick of greater than 7 $\hbar k$. We note that this result is extremely insensitive to the intensities of the beams (and indeed to the magnetic field applied). However both of these factors strongly affect the rate at which the optical pumping procedure occurs. There are some assumptions inherent to this model which may not be exactly true, for example the polarisation of the beams may not be perfectly circular, and the initial distribution of the m_F states of the atoms is not known. Again, the result we obtain is largely independent of such factors.

The result is that the optical pumping scheme we choose imparts only a very small momentum kick on the atoms. In practice we also retroreflect the optical pumping beam to reduce the effect even further; the mean net momentum kick is thus reduced (assuming perfect alignment and no loss of beam power on reflection) to around $\sqrt{3.8}\ \hbar k$. The effect of this momentum kick is applied to the atom trajectories manually based on the average value (lines 505–510 of Appendix D).

With the optical pumping procedure complete the atoms then simply fall under gravity, according to classical mechanics, i.e. $\vec{r}(t) = r_0 + v_0 t - 1/2gt^2$ (lines 369–372 of Appendix D).

Light sheet

In our experiment there is another optical field which perturbs the atoms during their journey — the light sheet. Similar considerations to those described for the optical pumping beams are applicable. However there is an important difference in that we are addressing a closed transition. Thus there is no dark state and the rate at which photons are scattered is now important in determining the perturbation to the atoms. For the case of optical pumping the momentum kick from the laser had no associated timescale — a fact illustrated by its independence of beam intensity and hence scattering rate. This is no longer the case.

The transition that the light sheet resonantly addresses is $F = 2, m_F = 2$ to $F' = 3, m_{F'} = 3$. The scattering rate is again given by Equation 5.7 (we assume $\Delta = v = 0$). The rate of spontaneous emission is simply given by Γ and the rates of absorption and stimulated emission can also be found via a solution of the optical Bloch equations [136]. It is immediately clear that for small I/I_{sat} it is a good approximation that all of the atoms decay by spontaneous emission, rather than stimulated emission, since $R \ll \Gamma$. For the intensities used in our experiment this approximation is appropriate. The force imparted by the light sheet on the atoms is given by

$$F_{\mathrm{LS}} = \hbar k R = \frac{\hbar k \Gamma}{2} \frac{I/I_{\mathrm{sat}}}{1 + I/I_{\mathrm{sat}}} \approx \frac{\hbar k \Gamma I}{2 I_{\mathrm{sat}}}, \tag{5.10}$$

i.e. it is proportional to intensity. For a power of 1 μW the probability of decaying by stimulated emission is around 2.5%. We typically use powers of around 50 nW, and the probability scales linearly with intensity. Thus we can use Equation 5.10 to accurately calculate the force imparted by the light sheet.

We now include a feature ignored in the treatment of the optical pumping beams — the intensity profile of the laser beam. The light sheet is focussed in one direction, so it has an asymmetric intensity profile, given by

$$I(x, z) = I_0 \exp(-4x^2/w_x^2) \exp(-4z^2/w_z^2) \tag{5.11}$$

where I_0 is the maximum beam intensity, and w_x and w_z are the $1/e^2$ widths along the semi-major axes of the profile. Note that $I_0 = 8P/\pi w_x w_z$ where P is the power of the beam.

To compute numerically the appropriate modification of the trajectories of the atoms the following process is applied. For each timestep all atoms that are within two $1/e^2$ widths of the light sheet are found. The intensity at each of these positions is then computed according to Equation 5.11. The force on the atom is then found using Equation 5.10. For a time step $\mathrm{d}t$ this then modifies the velocity according to $v'_y = v_y + F_{\mathrm{LS}}/m\ \mathrm{d}t$. Note that only one component of the velocity is affected – that along the direction of the light sheet.

In order to represent accurately the random nature of the scattering of photons from the light sheet we also incorporate Poissonian fluctuations of photon number. To achieve this we again utilise an inverse cumulative distribution. However, the corresponding distribution does not have a closed form. Instead we use the normal distribution as an approximation in the limit of large numbers of events. The Poisson distribution describes the probability of scattering $N = R\ \mathrm{d}t$ photons, given some mean $\bar{N} = \bar{R}\ \mathrm{d}t$, as

$$P\left(N, \bar{N}\right) = \frac{\bar{N}^N e^{-N}}{N!}. \tag{5.12}$$

For the case of large N this can be very well approximated by a normal distribution of mean $\bar{N}$ and standard deviation $\sqrt{\bar{N}}$. Thus for each atom we incorporate fluctuations around the expected scattering rate by randomly sampling a normal distribution.

As with the optical pumping beam the light sheet was retroreflected in order to minimise the effect on the atoms. In doing so, a significant push on the atoms is reduced to a 1D heating effect. The net momentum kick on an atom is on average reduced from $N\hbar k$ to $\sqrt{N}\hbar k$. The retroreflection is incorporated by computing the scattering rate for the incoming and retroreflected beams independently and then calculating the net momentum imparted. This calculation is performed on lines 470–502 of Appendix D.

Upon simulating the reflection of the atoms the importance of using a low power and retroreflecting the beam is observed. Using the experimentally adopted power of 50 nW we observe that without retroreflecting the beam most of the atoms will be pushed such that they completely miss the nanowire array. If the beam is retroreflected we note that for powers of greater than 1 μW there is a significant reduction in the number of atoms that are reflected. It is also a simple matter to simulate the beam imbalance resulting from absorption of the light sheet at the retroreflecting mirror. This simulation of the atom-light interaction was an important tool in configuring the experimental setup and is described further in Section 5.3.

Whilst the discussion of the light sheet thus far has focussed on the perturbation of the atoms' trajectories, its purpose is of course to detect the passage of the atoms. This is performed by observing the corresponding dip in intensity as the atoms pass through. Computation of this is simple given the preceding discussion. Each atom scatters a known number of photons, which yields an associated light power scattered, calculated by multiplying by the photon energy, $E_\mathrm{p} = hc/\lambda$. This then yields the percentage absorption of the light sheet for the number of atoms simulated. The actual signal is then the same shape as that calculated, but for the correct number of atoms, i.e. multiplied by some prefactor. This prefactor is treated as a fitting parameter; as previously mentioned the light sheet is in fact a very good way of determining the atom number [127].

The light sheet in our experiment is circularly polarised in the same sense as the optical pumping beam in order to maintain the polarisation of the atoms. It is possible to solve the rate equations from an assumed initial distribution of m_F states, as in Section 3.4.2. However doing so we observe that given an initial population of the $m_F = 2$ state of around 90–95%, and the fact that we are driving a closed transition, the effect on the population distribution is negligible.

Imaging

The final light field which we consider is that of the imaging beams. These are identical to the MOT beams, except with a different frequency of light. They are used to carry out time-of-flight fluorescence imaging. The observed signal is predicted in a similar manner to that already described for the light sheet and optical pumping beams. The intensity of the light from each of the imaging beams at a given position is calculated according to measured values of the beam width and power. Together with the atom velocity along the direction of the beam this allows for a calculation of the scattering rate for each atom. The photons scattered are then binned spatially and time-of-flight fitting is performed in an identical manner to the experimental procedure (cf. Section 3.4.4). Thus we extract a predicted cloud width as a function of time which we can compare with the experimentally observed behaviour. The simulated time-of-flight fitting procedure is carried out on lines 239–313 of Appendix D.

5.2.3 Atom-nanowire interaction

The simulation details presented thus far have considered aspects of this work which are common to other atom mirror experiments. It is the interaction between the atoms and the nanowire array which is the novel aspect of the work and thus perhaps the most important/interesting aspect to consider.

Atom-magnetic field interaction

The magnetic fields emanating from the domain walls hosted by the nanowires were examined extensively in Chapter 2. We now consider the nature of the interaction of ultracold atoms with these fields.

In Section 3.2 we considered the linear Zeeman shift associated with placing an atom in a magnetic field. This picture of the interaction energy is in fact an approximation valid for low fields. For a trapping application atoms will be localised near a field minimum so will never experience very high fields. A more rigorous treatment of the energy shift is obtained through a solution of the complete Hamiltonian. In general this must be done numerically, however it is possible for the case of $J = 1/2$ to derive an analytic expression known as the Breit-Rabi formula[1] [110, 137, 138]:

$$E_{\mathrm{BR}} = -\frac{\Delta E_{\mathrm{hfs}}}{2(2I+1)} + g_I \mu_{\mathrm{B}} m_F |\vec{B}| \pm \frac{\Delta E_{\mathrm{hfs}}}{2}\sqrt{1 + \frac{4 m_F x}{2I+1} + x^2}. \tag{5.13}$$

Here ΔE_{hfs} is the hyperfine splitting and I is the nuclear spin (3/2 for ^{87}Rb). x is equal to $(g_J - g_I)\,\mu_{\mathrm{B}}|\vec{B}|/\Delta E_{\mathrm{hfs}}$, with g_J and g_I being the Landé g factors associated with the quantum numbers J and I.

Applying this formula to the $F = 2$ ground state manifold of ^{87}Rb yields Figure 5.2. We see that the energy shift is approximately linear for fields of up to around 0.1 T at which point the prescription of m_F as a quantum number is no longer appropriate. In this regime, expressing the magnetic potential in the form given by Equation 3.3 is not accurate. In general if we expect the atoms to experience magnetic fields of this magnitude we should adopt this more rigorous treatment when considering the resulting potentials. The exceptions to this are for the stretched states where $m_F = \pm 2$, for which the interaction energy is linear at all fields.

To translate the Breit-Rabi diagram into something a little more useful for our particular application we now map the field strength onto the distance from the wall, i.e. we can compute $V(z)$, the potential curve associated with an atom approaching a domain wall. However there is additional complexity due to the variation of the field in x and y. For the sake of this analysis we will choose x and y such that we consider a line of z above the point of

---

[1] Note that care must be taken to choose the appropriate sign in Equation 5.13. As described in the derivation provided in [137], the labelling applied is such that we use ± when $F = I \pm 1/2$ as defined in zero magnetic field. Defining $f(x) = 1 + 4m_F x/(2I+1) + x^2$ the change in sign occurs where $f' = 0$, i.e. where $\mu_{\mathrm{B}}|\vec{B}| = -\Delta E m_F / 2(g_J - g_I)$. For the case at hand this is approximately where the linear Zeeman shift is equal to $-\Delta E_{\mathrm{hfs}}/2$. As it is the stretched state that experiences this sign change it is easier in practice to simplify Equation 5.13 analytically.

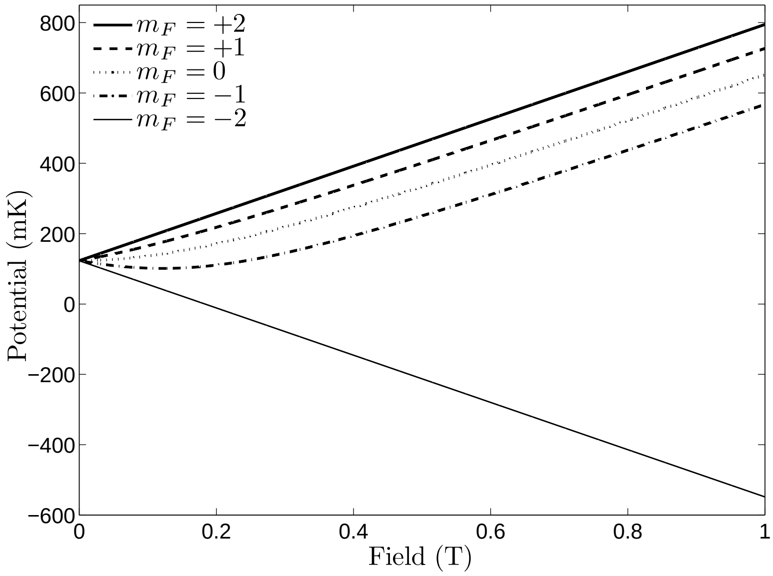

Figure 5.2: The Breit-Rabi diagram for the $F = 2$ ground state manifold of ^{87}Rb. The states are labelled by m_F values for convenience.

maximum field at the nanowire's surface. Using fringing fields calculated via micromagnetic techniques (Hayward et al.) for a nanowire of cross section 125 nm × 30 nm yields the potential curve shown in Figure 5.3.

The overall shape of the potential curves is for the most part as one would intuitively expect considering the nature of the Zeeman interaction, and the approximate form of the magnetic fields, i.e. there is an increase (decrease) in the potential for positive (negative) m_F states. Deviations from the potential assuming that m_F is an appropriate quantum number become more noticeable at heights of less than 100 nm, which corresponds to fields above around 500 G (this is the region in Figure 5.2 where the dependence on field begins to deviate from a linear one). This can easily be seen by comparing the curves using the Breit-Rabi formula (black) and those for a simple linear Zeeman interaction (grey). For the stretched states ($m_F = \pm 2$) the potential is of course just that due to a linear Zeeman shift, as prescribed by the Breit-Rabi formula (Equation 5.13). Provided we work in the weak-field-seeking stretched state we need not worry about deviations from a linear Zeeman shift. We anticipate being able to polarise the atomic sample with around 90–95% of the population in the $m_F = +2$ state and the remaining atoms will either experience a significantly more corrugated potential or will

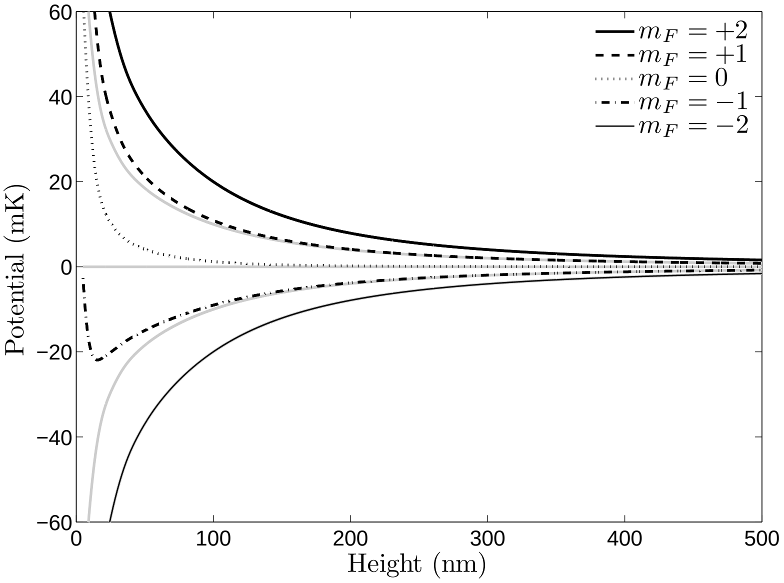

Figure 5.3: Potential curves associated with a ^{87}Rb atom in the $F = 2$ ground state manifold approaching the nanowire array. This is simply a rescaling of the Breit-Rabi diagram shown in Figure 5.2 according to the height dependence of the magnitude of the magnetic field. Note also that the offset of the potential present in Figure 5.2 due to the hyperfine splitting has been removed. Also included are the potentials solely due to a linear Zeeman interaction, indicated by light grey lines.

not be repelled from the fringing fields. Hence we can approximate the atomic potential as being solely due to a linear Zeeman interaction with the magnetic field.

Point interaction approximation

Perhaps the most remarkable feature of the calculated potential curves is the size of the gradients. Because of this feature we use an approximation which allows for great simplification of the atom-nanowire interaction. We assume that the interaction is point-like in nature, i.e. it is analogous to elastic reflection from a hard surface. The corresponding equivalent surface is then defined by a level set of the atomic potential. This set is at a value equal to the atom's initial gravitational potential energy. We will now demonstrate that detailed analysis of the precise nature of the interaction supports approximating it as a point one, which will facilitate rapid computation of the interaction for large numbers of atoms.

We numerically simulate a ^{87}Rb atom in the $F = 2, m_F = 2$ state falling from a height of 1 cm directly onto a domain wall and being reflected by the associated fringing fields, which are calculated according to the 1D model provided in Section 2.2.2. The resulting dynamics are illustrated in Figure 5.4. The most important feature of the data shown is the range over which a significant interaction takes place, which is around 1 µm or 0.1 µs. Also plotted are the dynamics associated with reflection from an ideal magnetic mirror of equal periodicity. The corresponding analytic expressions for

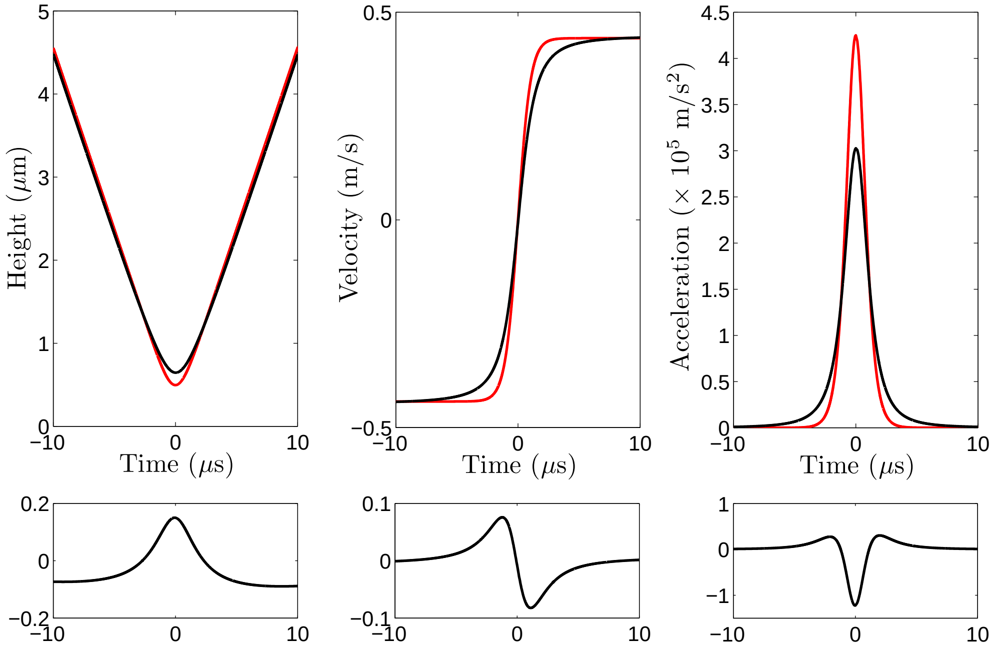

Figure 5.4: Trajectory of an atom falling onto a nanomagnetic domain wall. The black line shows the numerically calculated trajectory using the 1D analytic model for the magnetic fringing fields. The red line shows the analytic result for an ideal mangetic mirror of the same characteristic feature size, i.e. with an exponentially decaying magnetic field. The lower plots show residuals using the same scale.

the atom trajectory are [96]:

$$z(t) = v_0\tau \log\left[\cosh\left(t/\tau\right)\right], \tag{5.14}$$

$$\dot{z}(t) = v_0 \tanh\left(t/\tau\right), \tag{5.15}$$

$$\ddot{z}(t) = (v_0/\tau)\,\mathrm{sech}^2\left(t/\tau\right), \tag{5.16}$$

where v_0 is the initial velocity upon entering the magnetic field region. Given the small size of the region of interaction, v_0 is simply given by $\sqrt{2gh}$ for some drop height h. $\tau = \lambda/\pi v_0$ is a timescale which characterises the interaction, with λ being the period of the magnetisation pattern.

Because the interaction with the magnetic field occurs over such a small region/time it can be well approximated by a point interaction, i.e. an instantaneous change in velocity. Under this assumption the atom-field interaction can be pictured as the atoms being reflected from a hard surface, located at the turning point of the atoms' trajectories, i.e. an isosurface of magnetic field strength.

The resulting computation required to simulate the reflection from a hard surface is significantly less intensive than a consideration of the incremental interaction with the magnetic field. In order to demonstrate the validity of the approximation of a point interaction, we take the case of non-normal incidence with a magnetic field. To simplify the picture further we actually consider an atom dropped into an angled magnetic field. In our experiment the angle of incidence of the atoms will be approximately normal, but the magnetic field magnitude is by no means flat. We calculate the trajectory of such an atom for the case of a point interaction and for a continuous one. Examples of the results of this are shown in Figure 5.5 for a range of angles of magnetic field.

The discrepancy between the trajectories for the different models is negligible outside the region of interaction. This result can be predicted intuitively by considering the analytic expressions of Equations 5.14 to 5.16. Far away from the ideal mirror the trajectories predicted by the aforementioned expressions, and those for a point interaction, converge. It is perhaps unsurprising then that this is also the case for a magnetic field that decays according to our fringing field models, rather than those of an ideal mirror. Because the region over which there is significant interaction is small, the discrepancy in

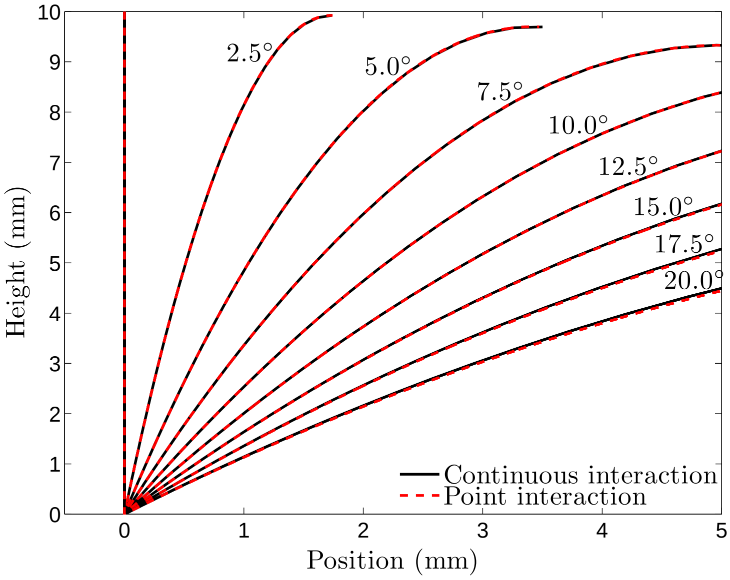

Figure 5.5: Trajectories of atoms interacting with a decaying magnetic field. Black traces represent those using a continuous interaction with a fringing field from a domain wall (modelled as per Section 2.2.2). Dashed red traces represent those using a point interaction with a hard surface.

the calculated trajectories in the near-field does not yield an observable discrepancy in the trajectories in the far-field. We consider the simple analysis presented here sufficient to support our use of the point interaction as the model of the reflection of the atoms from the nanowire array. The calculation of the isosurface is carried out on lines 122–146 of Appendix D.

Mirror roughness

With the validity of the point interaction approximation established we now consider the nature of the atomic reflection through the use of an effective isosurface. To compute this isosurface one must find all the points where the magnetic interaction energy is equal to the initial gravitational potential energy, i.e.

$$|\vec{B}| = \frac{mgh}{m_F g_F \mu_B}, \tag{5.17}$$

where m is the mass of the atom, g is the acceleration due to gravity and h is the drop height. For a ^{87}Rb atom in the $F = 2, m_F = 2$ state dropped from a height of 1 cm this is equal to 15.4 G. The magnetic field is calculated analytically for each of N_{DW} domain walls in a 2D array of alternating parity (cf. Figure 3.2). The contributions from these are then summed, i.e. the total field is given by

$$\vec{B}_{\mathrm{tot}}(\vec{r}) = \sum_{i}^{N_{\mathrm{DW}}} P_i \vec{B}_i(\vec{r}), \tag{5.18}$$

where P_i is the parity of the ith domain wall. A unit cell of the corresponding isosurface is pictured in Figure 5.6. The most striking feature of the field isosurface is its roughness. For an ideal mirror the magnetic field magnitude is flat in the x-y plane. The fact that the calculated surface has a strong degree of corrugation reflects the fact that our mirror is non-ideal. Because the sources of magnetic field are highly discretised, being localised at the domain

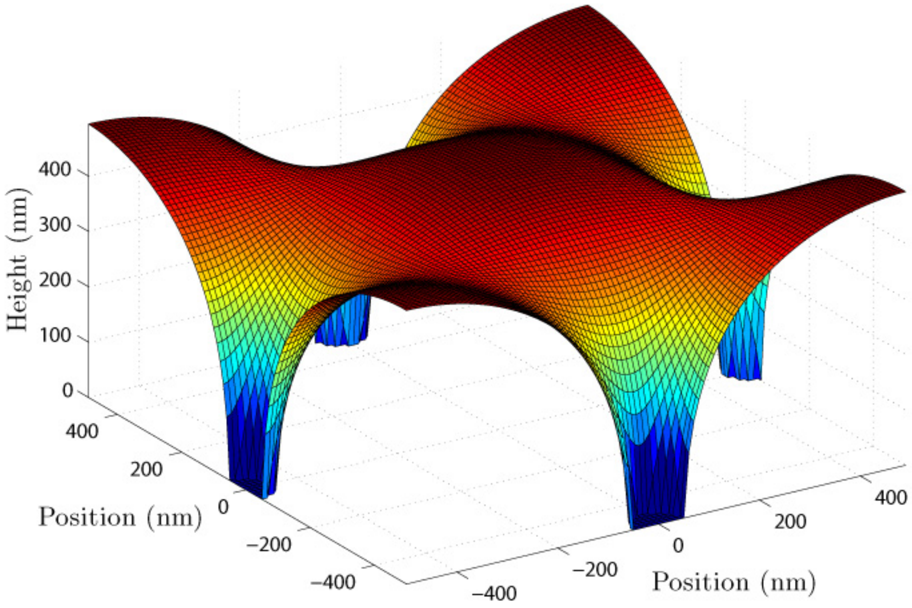

Figure 5.6: An effective isosurface from which we approximate atoms to reflect from the nanowire array through a point interaction. The surface is a level set of the magnetic fringing field magnitude at a value of 15.4 G — the field at which the Zeeman energy is equal to the initial gravitational potential energy. Note that there are regions where there is insufficient field to reflect the atoms. Nanowire dimensions are as per experiment, i.e. width = 125 nm, thickness = 30 nm and the period of the undulation is 1 µm.

wall positions, the equivalent magnetisation pattern is poorly described as a purely sinusoidal variation.

We also note that there are regions where there is insufficient magnetic field to reflect the atoms. This occurs midway between the nanowire apexes, i.e. furthest from the domain walls. Atoms which are incident at or near to these regions are likely to be either adsorbed onto the substrate of our chip, or scattered stochastically from the surface.

To characterise the roughness of the isosurface we analyse the angle it makes relative to flat. This is achieved by numerically differentiating the isosurface in both the x and y directions. The corresponding angles of inclination are then given by $\theta_x = \tan^{-1} x'$ and $\theta_y = \tan^{-1} y'$. However the flatness of the isosurface is defined by the combination of these two angles. The corresponding angle, ϕ, is given by the following formula:

$$\theta = \cos^{-1}\left\{\left[\frac{1}{\sqrt{\tan^2\theta_x + \tan^2\theta_y + 1}}\begin{pmatrix}1\\0\\\tan\theta_x\end{pmatrix}\times\begin{pmatrix}0\\1\\\tan\theta_y\end{pmatrix}\right].\hat{z}\right\}. \tag{5.19}$$

That is we take the normalised cross product of two vectors tangential to the plane at the point under consideration, to give a unit normal vector, then take the dot product with $\hat{z}$ to give the appropriate angle. Performing this analysis over the entire isosurface is carried out on lines 164–208 of Appendix D and yields Figure 5.7.

The resulting mean angle is 27.8° relative to flat, which is rather high[2]. Clearly there will be a significant change in direction of the atoms when reflecting from this surface compared to a flat surface. The result is that the specular reflection of the individual atoms will manifest itself as an overall diffuse reflection of the atom cloud. One point to bear in mind, however, is that it is the atoms that impinge on the flatter areas of the isosurface that are more likely to enter the light sheet; the mean isosurface angle associated with these atoms will be significantly lower.

---

[2] We note that a consideration of the full trajectory of the atoms as they approach the nanowire array (beyond the point interaction approximation) suggests that the actual degree of corrugation experienced by the atoms is likely to be slightly less. As the atoms enter the magnetic fringing fields they will experience a smoother magnetic field than at the turning point of their trajectory. The transverse momentum imparted is an integral over the fringing field region.

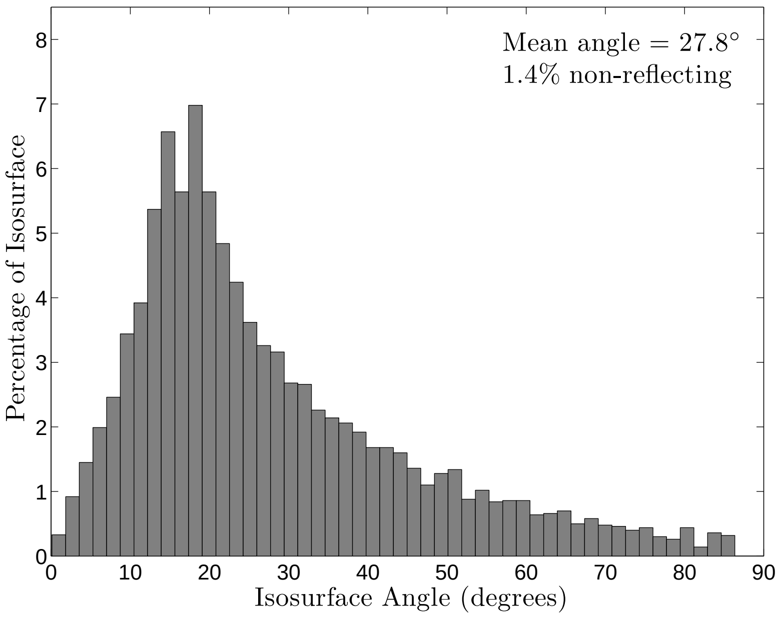

Figure 5.7: The distribution of the relative flatness of the isosurface from which the atoms are considered to reflect specularly. The angle of the surface is defined at the angle relative to flat. Regions of the isosurface where there is insufficient field to reflect the atoms are binned separately and do not contribute to the mean.

Given that it is unfeasible and unnecessary to compute the field using the entire domain wall array we choose N_{DW} to be a small number. How small this can be whilst providing an accurate result was investigated. This was simply achieved by observing convergence of the calculated result. This is illustrated in Figure 5.8. It is clear from an examination of the isosurface shape there is a stark difference between the field due to an array of 5 domain walls and that from 9 domain walls, i.e. with the next nearest neighbours included. However we note that the isosurface shape displays negligible difference when comparing an array of 9 domain walls with an array of 61. Thus we use an array of 9 domain walls when calculating the isosurfaces associated with our chip.

Within the simulation we also incorporate the ability to simulate the dynamics of the atoms with an effective isosurface other than that provided by a particular nanowire geometry. This was performed in a number of different ways. The simplest manner in which this is achieved is by specifying

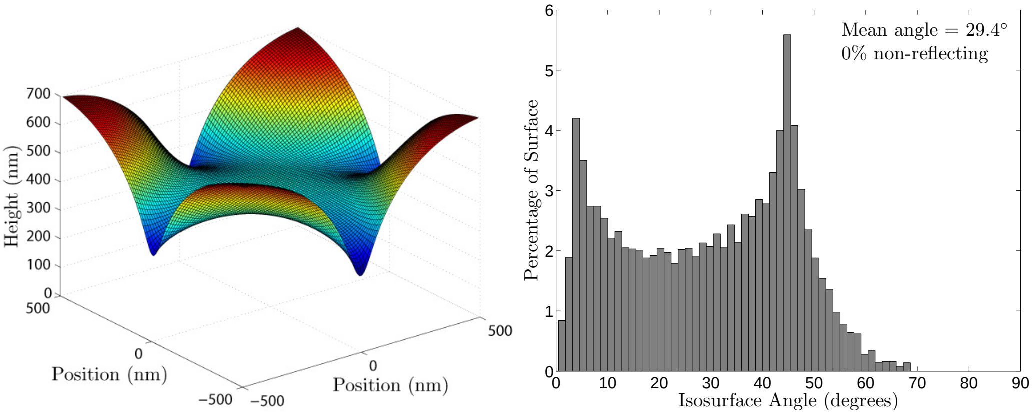

(a) 5 domain walls

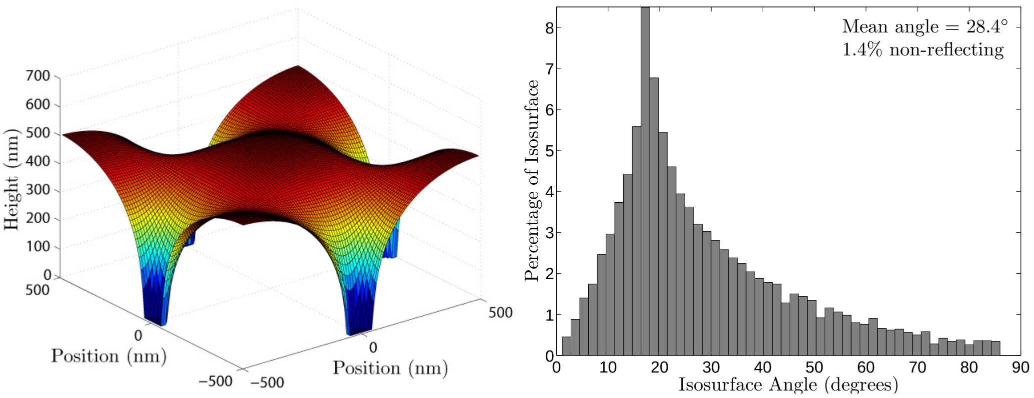

(b) 9 domain walls

Figure 5.8: Effective isosurfaces and associated distributions of the associated angle relative to flat for different numbers of domain walls. The field is calculated analytically by summing the individual contributions from multiple domain walls. (a) shows the result using 5 domain walls, (b) shows the result using 9 domain walls.

a single angle, θ, for the isosurface. This angle characterises the inclination relative to flat of the surface. The orientation of this inclination is then defined by a second angle, ϕ, which is chosen at random for each reflection event. This situation is illustrated in Figure 5.9.

This treatment is clearly inaccurate however, as the reflection from a surface of constant angle θ is not the same as that from a surface of mean angle θ. The latter will have regions or greater angle which will lead to a reduction in signal. To simulate better an arbitrary isosurface we try and replicate the angle distribution of an actual isosurface, as shown in Figure 5.7.

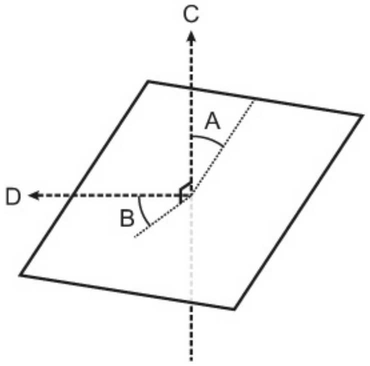

Figure 5.9: Schematic of an isosurface of fixed angle θ. The azimuthal angle ϕ is picked at random.

This was achieved firstly by a simple scaling of the calculated isosurface — the desired mean angle was set by an empirically deduced scaling factor. An alternative approach was also used whereby the distribution of the calculated isosurface was reproduced with a modified mean angle. This was achieved by fitting the shape of this distribution with a function of the form

$$c_1 + c_2 \exp(c_3 x - c_4), \quad x < c_5 \tag{5.20}$$

$$c_6 + c_7 \exp(c_8 x - c_9), \quad x > c_5. \tag{5.21}$$

Because this requires the optimisation of all nine c_i this process was carried out separate to the simulation for a given mean isosurface angle. This produces an appropriate distribution of θ which is used with an accept-reject method to randomly assign the angle of inclination of the surface from which individual atoms are reflected. Again ϕ is chosen at random. Analysis shows that this more elaborate simulation of an isosurface of prescribed average inclination angle produces a noticeable difference in the obtained light-sheet signals when compared to a model with fixed angle. The calculations using these manually defined isosurfaces are carried out on lines 395–438 of Appendix D. In Section 4.2 we comment on how the calculated trajectories of the atoms are modified by these approaches.

Reflected trajectory computation

Under the approximation of a point interaction it is an easy matter to compute the reflection of the atoms. The first step is to compute the angle of the surface. This is achieved by numerically differentiating the magnetic isosurface. Once an atom reaches the surface (defined as when its movement in the subsequent $\mathrm{d}t$ will give $z < 0$) we randomly pick a point on the isosurface, and its corresponding angles relative to flat, θ_x and θ_y. The normal vector of the surface at this point, $\hat{n}$, is then given by

$$\begin{aligned}\hat{n} &= \frac{1}{\sqrt{\tan^2\theta_x + \tan^2\theta_y + 1}} \begin{pmatrix} 1 \\ 0 \\ \tan\theta_x \end{pmatrix} \times \begin{pmatrix} 0 \\ 1 \\ \tan\theta_y \end{pmatrix} \\ &= \frac{1}{\sqrt{\tan^2\theta_x + \tan^2\theta_y + 1}} \begin{pmatrix} \tan\theta_x \\ \tan\theta_y \\ 1 \end{pmatrix}.\end{aligned} \tag{5.22}$$

The atom will have some incident direction, $\vec{v}_i$, and the reflected direction, $\vec{v}_r$, is given by

$$\vec{v}_r = \vec{v}_i - 2(\vec{v}_i.\hat{n})\hat{n}. \tag{5.23}$$

If a position on the isosurface corresponding to a region of insufficient magnetic field is chosen the atom is considered to be lost from the system, and is removed. Atoms which are outside the area of the nanowire array as z becomes negative are also removed. This reflection process is carried out by lines 379–393 and 451–457 of Appendix D.

Following reflection the atoms continue to propagate classically, passing through the light sheet again. In this manner the signal which we extract from our experiment is simulated. Averaging this process produces a signal which can be easily compared with experimental data, as shown in Chapter 4.

5.3 Simulation results

5.3.1 Light sheet

A number of features of the experimental realisation of our magnetic atom mirror were guided by the results of the Monte Carlo simulation. One aspect in particular which benefitted from such simulations was the setup of the light sheet used to detect the atoms.

Light sheet height

One of the first things to be considered was the position and size of the light sheet. The size of the light sheet is determined by experimental constraints, described in Section 3.4. A certain degree of freedom is possible in the choice of the position of the light sheet. The ultracold atomic sample is initially formed at a height of 1 cm above the nanowire array. This choice was based on a reasonable distance within which to accommodate the necessary beams and associated optics to perform the experiment. The exact position of the light sheet can thus vary by several millimetres, and is predicted to have a noticeable effect on the signal observed. The dependence of the signal on the height of the light sheet was analysed through simulation and the results are shown in Figure 5.10. Note that here the absolute size of the reflection signal is used since varying the light sheet height also affects the size of the drop feature.

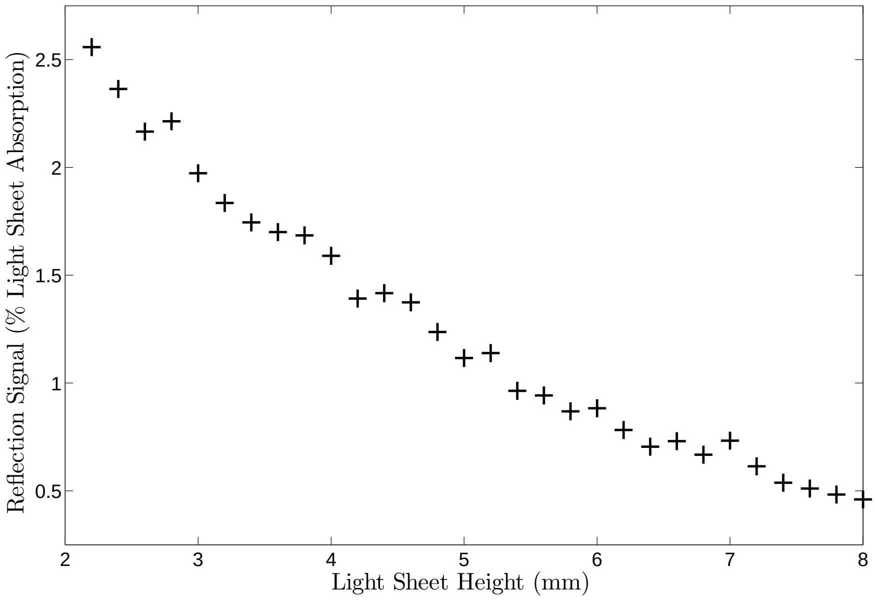

Figure 5.10: The reflection signal obtained from the light sheet as the height of the sheet is varied as calculated via Monte Carlo simulation. Note that the reflection signal is given as the absolute percentage absorption of the light sheet (R in Figure 4.2), as the size of the drop feature (D in Figure 4.2) also varies with light sheet position. We observe that the larger signal obtained for lower heights is compromised by poorer resolution, as shown in Figure 5.11.

When the light sheet is located close to the substrate the drop and reflection signals become temporally overlapped, making it difficult to resolve the two peaks. However, the size of the reflection signal is larger as there is less chance of atoms reflected at large angles missing the light sheet. As the light sheet is moved further from the substrate the reflection signal becomes smaller, but better resolved. This behaviour is illustrated in Figure 5.11

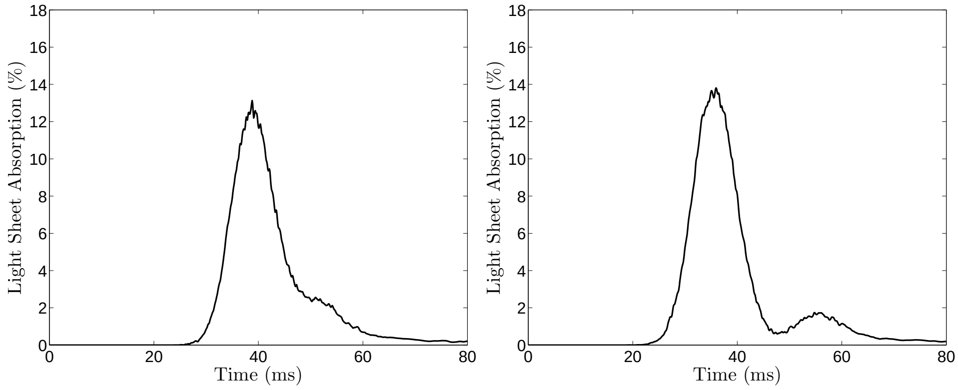

(a) 2.2 mm (b) 3.4 mm

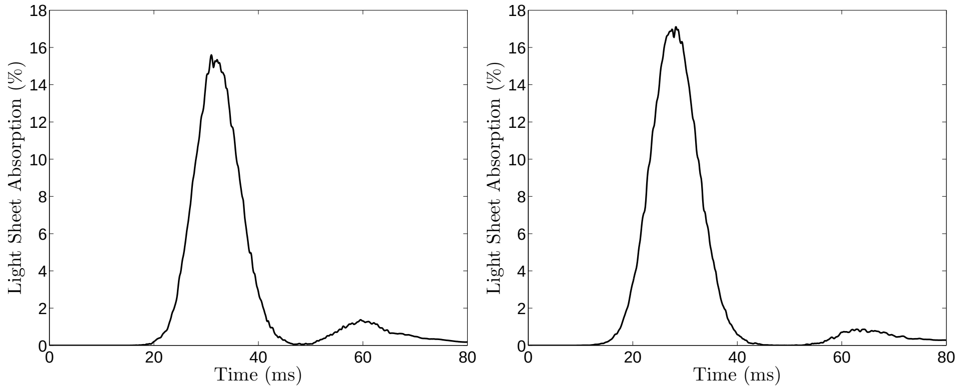

(c) 4.6 mm (d) 5.8 mm

Figure 5.11: Sequence of simulated light-sheet signals with varying light sheet height above the nanowire array. The atoms are dropped from a height of 1.0 cm. The initial temperature of the cloud is 13 μK.

As a result of this analysis a height of 4 mm was chosen as this was the minimum height at which the drop and reflection features were predicted to be completely separate for our expected cloud temperature, i.e. the light-sheet signal drops to zero between the two peaks.

Light sheet intensity

In Section 5.2.2 the heating effect of the light sheet was discussed. It is clear that one must take care to ensure that there isn't too much power in the light sheet as this can impart significant momentum onto the falling atoms. Figure 5.12 shows the dependence of the reflection signal on the intensity of the light sheet for both the retroreflected and non-retroreflected case, as calculated via Monte Carlo simulations. When the beam is retroreflected we see that for intensities of above around 3 × 10^{-3} I_{sat} the perturbation to the atoms is sufficient such that there is a detrimental effect on the light-sheet signal. For our experimental setup this corresponds to a power of around 50 nW. The use of higher intensities in the light sheet will provide a larger absolute signal, but we note that the signal to noise obtained with intensities of light lower than 3 × 10^{-3} I_{sat} is more than adequate. Thus a power of 50 nW was chosen such that the highest signal to noise was obtained whilst ensuring no significant perturbation of the atoms' motion.

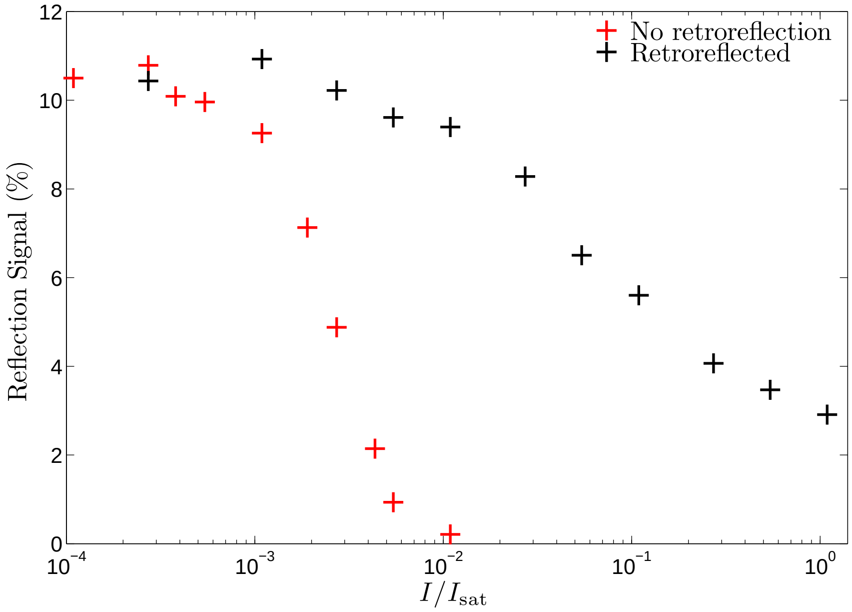

Figure 5.12: Dependence of the reflection signal on the intensity of the light sheet. Note the log scale for the abscissa. Black data points are generated with a retroreflected light sheet, red data points are generated without retroreflection.

The case of a non-retroreflected beam shows similar behaviour, but on a completely different scale. Analytic expressions for the effect of the atom cloud are given in Appendix E but we consider here just the results from numerical simulations. We find that the light sheet power is required to be around 5 nW or less in order to circumvent jeopardising the reflection signal. This is infeasible as this would give an inadequate signal to noise. We also note that there is a much more rapid reduction in the bounce signal with an increase in power. Without retroreflection the bounce signal is reduced to less than 1% for powers above around 100 nW. By comparison a retroreflected beam with two orders of magnitude more power produces a signal of around 4%. The reason for this disparity is the very different manifestations of the imparted photon momentum. A retroreflected beam produces heating in one dimension with a distribution of imparted momentum centred around zero. Without retroreflection the momentum kick is always in one direction, and is centred around a finite mean that increases with the power; the atoms are simply pushed away as the power is increased. From this analysis it is clear that it is greatly advantageous to retroreflect the light sheet.

The preceding discussion describes how simulation motivated the choice of setup for the light sheet. In reality it was a combination of both experimental observation and theoretical prediction that was used to interpret and optimise the interaction of the atoms with the light sheet.

Nanowire array dimensions

Perhaps the most striking feature of the light-sheet signal that we obtain is the size of the reflection feature — only a small fraction of the initial atomic cloud is in fact detected as being reflected, as shown in e.g. Figure 4.3. As previously stated, the primary reason for this is that the size of the atomic cloud once it has reached the height of the chip is large compared to the size of the nanowire array.

Equation 4.2 suggests that a significant increase in the reflection signal can be obtained through the use of a bigger nanowire array. Whilst the size of 2 mm × 2 mm was chosen as the largest possible given the technical limitations of the lithographic techniques used, it is of interest to investigate the benefit that working to increase the size would provide. The most accurate way to analyse this is through the use of the Monte Carlo simulation described in Section 5. We employ this technique to look at the dependence of the signal on the size of the array from which the atoms are reflected. Performing this analysis yields Figure 5.13. We observe that there is an approximately linear increase of the reflection signal with the characteristic length of the chip, d. Thus increasing the chip size would be an effective method of achieving a larger reflection signal.

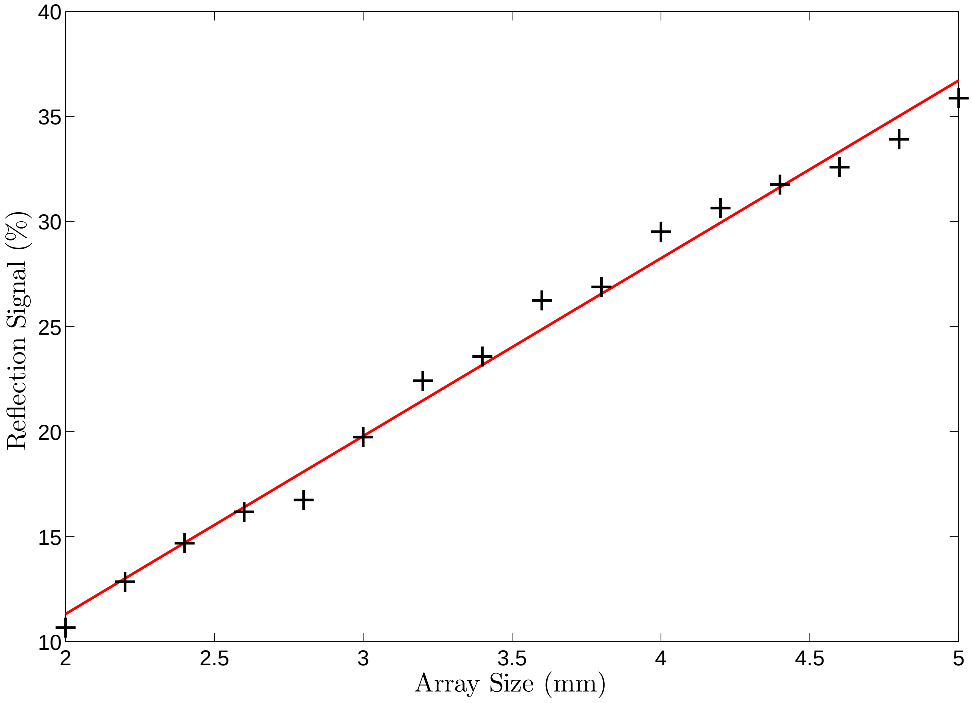

Figure 5.13: Reflection signal predicted by Monte Carlo simulation with a varying nanowire array size. The size specified is the length of a square array. The red line is a straight line fit. The atomic cloud is dropped from a height of 1.0 cm with a measured initial temperature, $T = 13$ μK and width $\sigma(0) = 0.74$ mm.

During the design of the chip, the geometry of the wires was a key point of consideration in order to maximise the efficacy of our device. We now consider the effects of varying nanowire geometry in a quantitative manner. The first aspect we consider is the period of the nanowire pattern. Calculation was carried out in the manner already described with a varying characteristic length of the undulating pattern, d. The results are shown in Figure 5.14. The general trend observed is that the roughness of the effective isosurface

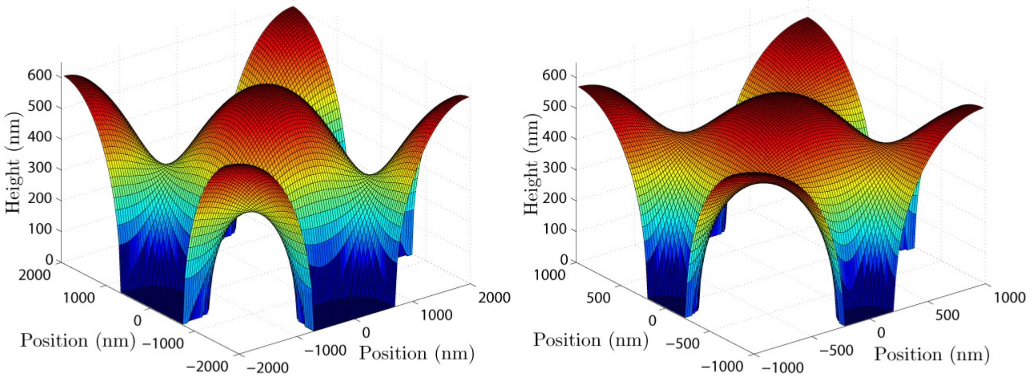

(a) $d = 2.0$ µm (b) $d = 1.5$ µm

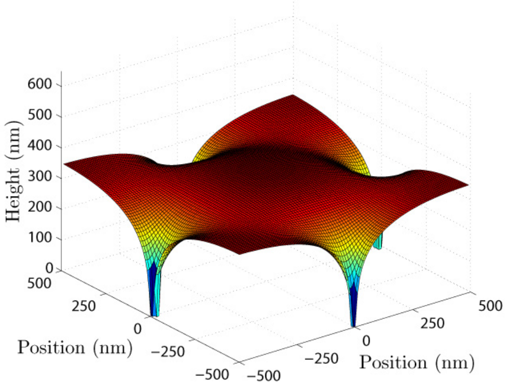

(c) $d = 0.5$ µm

Figure 5.14: Effective isosurfaces calculated for a range of nanowire undulation wavelengths. A decrease in corrugation is observed for smaller periods. Also cf. Figure 5.6.

decreases with the period of the nanowire pattern. This is intuitively expected as by decreasing the distance between neighbouring domain walls the magnetisation pattern becomes more similar to that of an ideal magnetic mirror, i.e. a continuous variation of magnetisation. In order to achieve as specular a reflection of atoms as possible we use as small a value of d as possible — as described in Section 3.3.1 this is 1 µm.

The next aspect of the nanowire geometry which we consider is the cross section. As per Section 2, a larger cross section results in a larger effective magnetic charge prescribed to the domain walls, and hence a larger field is produced. A result similar to the preceding analysis is found. As the width of the nanowire is increased the limit of a continuous magnetisation variation is approached and the resulting isosurface becomes flatter in a manner very similar to that shown in Figure 5.14. The choice was made to use as large a nanowire cross section as possible whilst maintaining an appropriate and stable domain structure. The corresponding wire width and thickness are 125 nm and 30 nm.

The quantitative analysis presented here confirms the discussion of Section 3.3.1. The smoothest isosurface is achieved by using the smallest d and largest w and t, within the restrictions of practicability.

5.4 Conclusions

In this chapter we have presented the numerical methods employed to simulate the reflection of an atom cloud from a nanowire array, as realised in experiment. The interactions of the atoms with the addressing light fields and, in particular, the interaction with the magnetic fringing fields, are examined in detail. We use a point interaction approximation to significantly simplify the simulation of the magnetic interaction, and we show that this approximation is a very good one.

We have also described how the results of the simulation were used in conjunction with empirical observations to optimise the experimental setup, both in terms of the design of the nanowire array and the configuration of the laser system and experimental procedure.

The true test of the simulations is of course the fidelity with which it reproduces experimental data. In Chapter 4 we have provided examples that show the accuracy with which we can replicate the light-sheet signal obtained. In the following chapter we will discuss the extension of the atom mirror experiment to incorporate the launching of atoms towards the nanowire array.

Chapter 6

Launched atom interactions

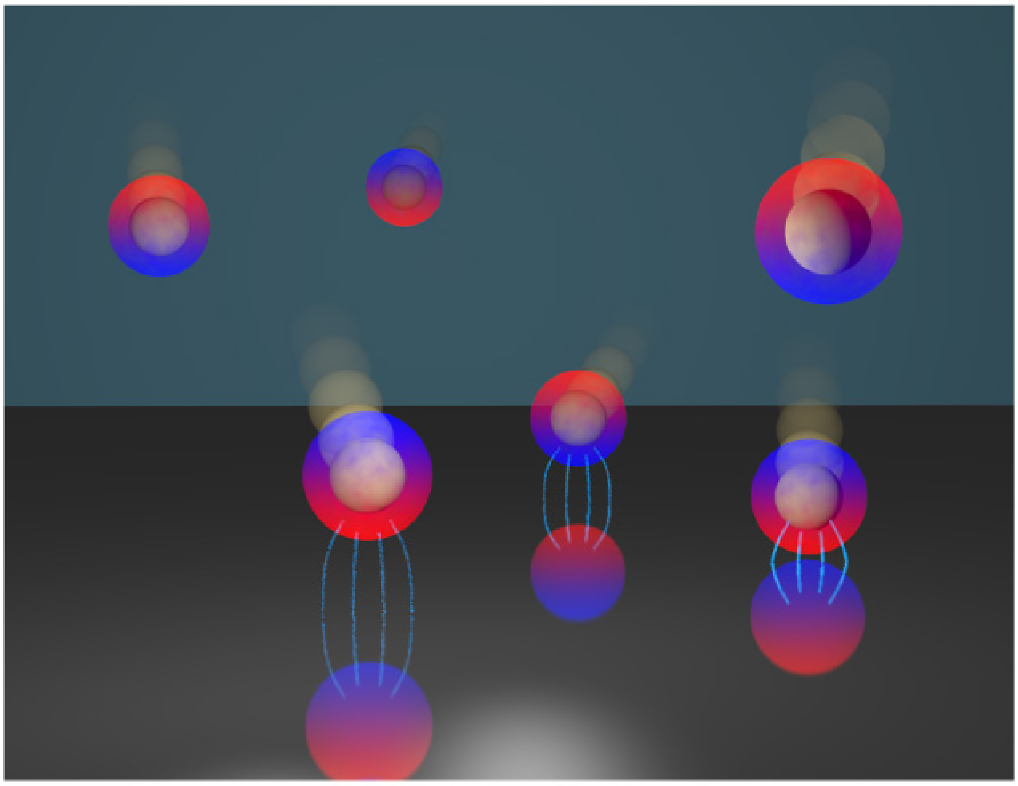

Atoms launched via moving molasses can enter the van der Waals regime. Their fluctuating dipoles interact with an induced image dipole.

6.1 Introduction

In Chapters 3 and 4 we discussed in detail the nature of the atom-mirror interaction and what we can deduce from an examination of the atom dynamics. However there is an inherent limitation to our study. Because the atoms are dropped from a fixed height above the nanowire array, and the approximation of a point interaction is a good one, the atoms can be considered to only reflect from one particular isosurface. The result is that we are only examining a small part of the region where the atoms interact with the chip. We would like to extend our investigation to explore the nature of the atomic interaction with the nanowire array over a large range of distances.

We shall consider two aspects to the extension of the work described up to this point. The simpler of these is further investigation of the magnetic interaction the atoms experience with the domain wall fringing fields; by reflecting atoms at different heights we may further test our understanding of the interaction and the nature of the fringing fields. Such a study is inherently particular to our system, but the results may be extended to nanomagnetic domain walls in general: by extending the region over which we consider the atom cloud to reflect we are able to directly probe nanomagnetic fields at a range of heights, including the near-field where we know that they adopt a complex shape [70].

The second way in which we may extend our study is to consider a new contribution to the interaction between the atoms and the nanowire array, i.e. the attractive surface interaction. This avenue of research allows us to probe a brand new aspect of the physics of our system, and has the ultimate goal of providing a more fundamental test of physical models. Experimental studies of surface interactions have been attempted for over half a century, and remain challenging to this day. A number of different approaches have been adopted, such as examining the deflection of atomic or molecular beams [139, 140, 141], interferometric methods [142, 143], spectroscopy of atoms [144, 145] or interactions with cavities [146]. However perhaps the most direct method of examining surface interactions is via an observation of their mechanical effects on normally incident atoms, which has also facilitated the observation of quantum reflection, e.g. [147, 148]. This methodology has been aided by the advent of laser cooling, yet experiments of this ilk have been relatively rare [149, 150]. However, the work presented here is an example of an alternative method for performing such a study.

We will consider the way in which we can extend our study, and also discuss the difficulties associated with doing so. In particular, it will be seen that the complex nature of both the magnetic interaction and the surface interaction makes a separation of these two contributions extremely challenging.

6.2 Moving molasses

6.2.1 Theory

In order to extend the region which we probe we must alter the effective isosurface from which the atom cloud is considered to reflect. This can be done in a number of ways, such as using a different quantum mechanical state, or by changing the height from which we drop the atoms. However these have the disadvantages of only providing a small range of different isosurfaces, or being logistically difficult. Indeed we anticipate that to approach the array at a height where surface interactions become important would require a drop height of the order of 0.1–1 m. The method which we use instead is that of moving molasses.

This technique harnesses the scattering force that is employed when performing laser cooling in order to launch atoms in a controlled manner [151, 152] and has been used extensively in atomic fountains [109, 153, 154, 155]. During conventional optical molasses the scattering force experienced by a two-level atom is given by [135]

$$\vec{F} = \hbar\vec{k}\frac{\Gamma}{2}\frac{I/I_{\mathrm{sat}}}{1+I/I_{\mathrm{sat}}+4\left(\Delta^2+k^2v^2\right)/\Gamma^2}, \tag{6.1}$$

where k is the wavevector of the light, Γ is the atomic linewidth, I is the light intensity, I_{sat} is the saturation intensity of the cycling transition we cool on, Δ is the detuning of the laser from resonance and v is the velocity of the atom.

The key to the cooling effect of optical molasses is the balance between Δ and v. Atomic motion produces a Doppler shift which modifies the frequency of a laser beam in the atom frame. This principle is used to laser cool atoms through the use of red-detuned laser beams. An atom moving between counter-propagating beams experiences a force imbalance such that the net scattering force opposes the atomic motion. The result is a strong confinement in velocity-space. In contrast to the conditions of a magneto-optical trap (MOT), there is no magnetic field present during optical molasses, and thus no spatial confinement. During optical molasses we also typically choose a larger value of detuning than in a MOT in order to produce a more efficient cooling. Using optical molasses we find that we can achieve temperatures as low as around 5 μK. As described in Section 3.4.2, optimum cooling is achieved by ramping the detuning of the lasers through the molasses phase.

The moving-molasses technique modifies conventional optical molasses such that the cooling mechanism occurs in a moving frame. This is achieved by introducing a frequency difference between beams. Depending on the particular geometry of the setup this may be between single beams, pairs, or sets of three, corresponding to 1D, 2D and 3D moving molasses respectively. The geometry of our setup, and the one considered in the following discussion, is 2D, as illustrated in Figure 6.1.

Because of the frequency difference between the beams a force imbalance is produced. The resulting velocity of the atoms can then be deduced by considering this force imbalance and the moving frame in which all beams appear to be the same frequency.

We consider the resonant frequency of the cycling transition to be f_0. We shall now express the detuning applied for conventional molasses as a linear frequency, Δ_{L}. We define $\tilde{f}_0 = f_0 - \Delta_{\mathrm{L}}$. We now consider an atom which is moving with a velocity v in the negative z direction, bisecting two pairs of beams, with each beam at an angle of ϕ to the z axis, as shown in Figure 6.2. f_1 and f_2 are then the frequencies of the pairs of laser beams observed by the moving atom, i.e. with the Doppler shift incorporated. These (linear) frequencies are given by

$$f_1 = \tilde{f}_0 \left(1 - \frac{v}{c}\cos\phi\right), \tag{6.2}$$

$$f_2 = \tilde{f}_0 \left(1 + \frac{v}{c}\cos\phi\right). \tag{6.3}$$

The effective frequency difference between these two pairs of beams is then

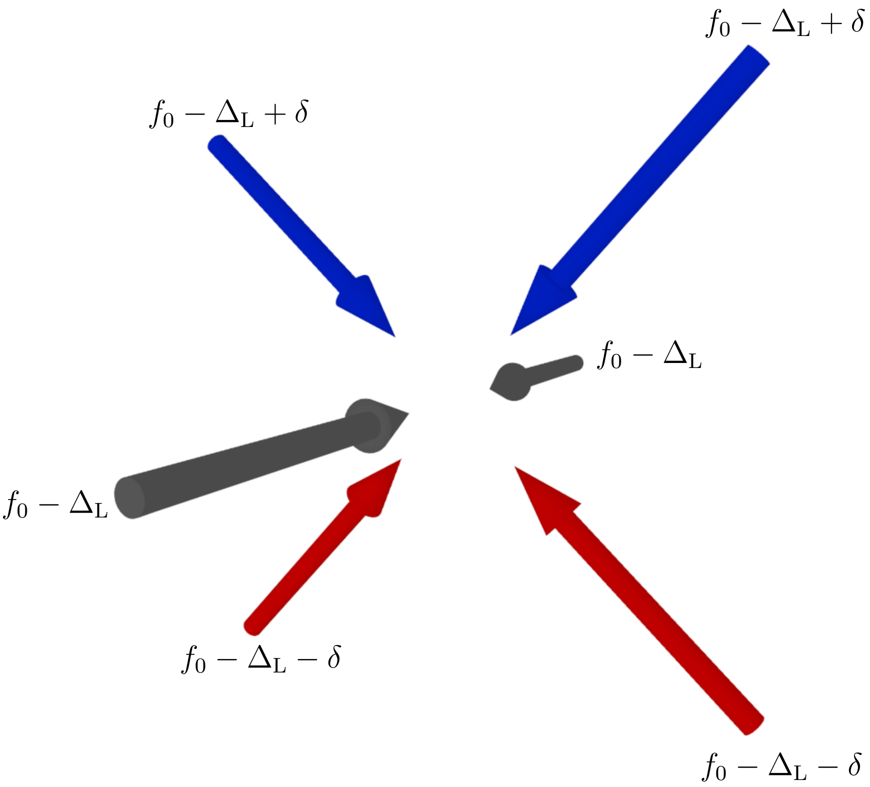

Figure 6.1: Schematic of moving molasses for the case of a frequency difference introduced between two pairs of beams. The upper pair of beams receives an additional blue (positive) detuning of δ and the lower pair receives an additional red (negative) detuning of δ.

simply equal to

$$\Delta f = f_2 - f_1 = \frac{2v\tilde{f}_0}{c}\cos\phi = \frac{2v}{\lambda}\cos\phi. \tag{6.4}$$

Thus an atom in motion produces an effective frequency difference, Δf, which is equivalent to 2δ as per Figure 6.1. The converse is of course also true; a frequency imbalance will cause atoms to move at a speed which is given, according to Equation 6.4, by

$$v = \frac{\lambda\Delta f}{2\cos\phi} = \frac{\lambda\Delta\omega}{4\pi\cos\phi}, \tag{6.5}$$

where we now express the frequency difference more conventionally in terms of an angular frequency difference, $\Delta\omega$.

We note the somewhat counterintuitive result that the larger the angle ϕ, the larger the velocity achieved. This can be understood by considering that

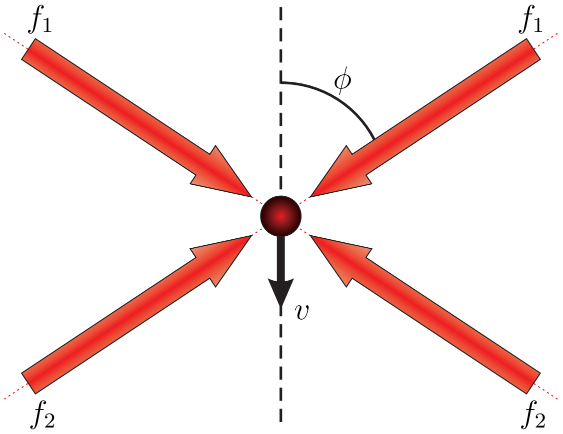

Figure 6.2: Diagram showing the geometry of 2D moving molasses for some arbitrary beam angle, ϕ. f_1 and f_2 are the frequencies of the beams as observed by an atom which moves with a speed v in a direction bisecting the beams within both pairs.

for large angles only a small component of the atom's velocity is resolved along the direction of the laser beam, and thus the atom must move very quickly in order to create the Doppler shift necessary to equilibriate the forces. However one must bear in mind that using large values of ϕ may jeopardise the efficiency of the moving molasses procedure as it will take a relatively long time to reach equilibrium as the scattering forces in the direction of motion are comparitively small. Our value of ϕ is set by the experimental setup to be 45°. Evaluating Equation 6.5 with λ=780 nm and $\phi = 45°$ we find that the launch velocity is given by

$$v = \sqrt{2}\lambda\delta = 0.55 \text{ ms}^{-1}\text{MHz}^{-1}. \tag{6.6}$$

It is thus a simple matter to 'dial up' the desired velocity by setting δ appropriately. We shall now consider how this is achieved in practice.

6.2.2 Experimental setup

In order to achieve efficient moving molasses we require a well defined and stable frequency difference between the beams. It is also advantageous, as with the application of conventional molasses, to ramp the frequencies to the required values, as stepping them can result in the atoms not responding quickly enough and being 'left behind'. To achieve such a stable ramp we make use of arbitrary function generators (Tektronix AFG3252 [156]).

As described in Section 3.4.2 optimal cooling is achieved by ramping the laser detuning, and this methodology is maintained for moving molasses. Thus the central frequency, f_0, is ramped down by Δ_{L} whilst a frequency difference between the beams of 2δ, is ramped up, over a molasses duration of t_{mol}. That is the frequency of the upper, middle and lower beams are described respectively by

$$f_u(t) = f_0 - (\Delta - \delta)\, t/t_{\mathrm{mol}}, \tag{6.7}$$

$$f_m(t) = f_0, \tag{6.8}$$

$$f_l(t) = f_0 - (\Delta + \delta)\, t/t_{\mathrm{mol}}. \tag{6.9}$$

Recall that our realisation of conventional molasses uses voltage controlled oscillators (VCOs) to supply the appropriate signal to acousto-optic modulators (AOMs) via which we control the laser beam frequency for both the MOT and molasses phases. It is unfavourable in terms of practicality to use arbitrary function generators to supply the necessary signals throughout an entire experimental routine, due to the length of the MOT load, so we make use of RF switches in order to change between the two signal sources (VCOs and function generators). The function generators are synchronised and calibrated with respect to each other to ensure an accurate and timely application of the frequency ramp. A schematic of the apparatus used to achieve this is shown in Figure 6.3.

During the MOT load a VCO creates the waveform required which is amplified before passing to a three-way power splitter (Minicircuits ZFSC-3-1-S+ [157]). Each of the outputs is then passed to one input of an RF switch (Minicircuits ZX80-DR230-S+ [157]). During the moving molasses sequence three separate waveforms are produced from two arbitrary function generators. The three outputs are then passed to the other inputs of the three RF switches. When the change from the MOT load to moving molasses occurs the arbitrary function generators are triggered and the RF switches are switched. Once this setup was developed it was also used for conventional molasses for experimental consistency.

For the efficient realisation of moving molasses it is important to ensure that the beams have sufficient power in order to quickly accelerate the atoms

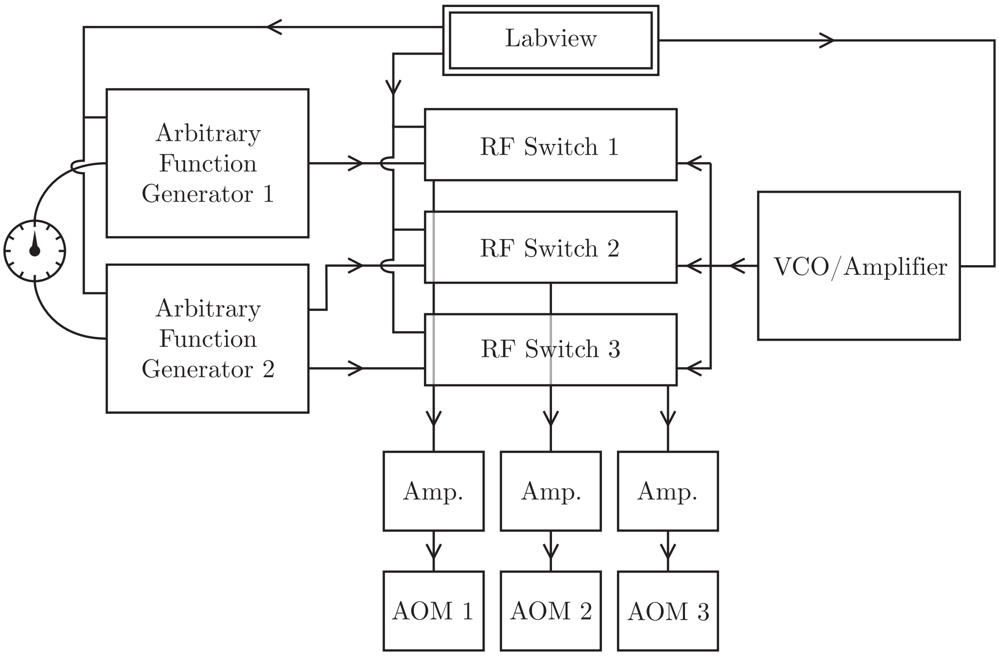

Figure 6.3: Schematic of the setup used to incorporate the moving molasses technique. The three pairs of MOT beams are driven by individual AOMs. The RF source passed to these AOMs is either produced by arbitrary function generators (for the moving molasses frequency ramp) or by a VCO (for the MOT load). Both of these are controlled/triggered by Labview. The source is selected using RF switches which are controlled by TTL signals generated by Labview.

into the moving frame, and also that beams of the same frequency are well balanced so that there is no net lateral force, i.e. the atoms are accelerated straight down. Experimental observations indicated that this was indeed the case for a large range of launch velocities as very few atoms were ‘left behind’ after the moving molasses sequence.

The experimental sequence for launching atoms towards the nanowire array was carried out in a manner entirely analogous to that for dropping atoms (cf. Section 3.4.4). After application of the molasses beams an optical pumping sequence was used, yet we anticipate that significant evaluation and optimisation of the efficiency of this procedure for a launched cloud is required.

6.2.3 Launching simulations

We now consider the effect that launching the atoms has on the reflection signal. There are two important effects which one must account for. The first is the behaviour within the light sheet. If the cloud of atoms moves more quickly it will obviously reach the light sheet sooner and will have spread out less due to thermal motion in this time. The increased speed of the atoms in the light sheet means that the associated signal is significantly narrower. The fact that the cloud has spread out much less means that fewer atoms miss the light sheet and there are more atoms in the sheet at a given time, meaning more photons are scattered and the size of the signal increases. This reasoning is also true of the reflection signal — the atoms will move upwards more quickly and will have spread out less due to thermal motion. However, there will still be a significant spreading of the cloud due to the diffuse nature of the reflection from the corrugated isosurface, and this is the second effect to consider.

Atoms which are launched more quickly have more kinetic energy as they enter the magnetic fringing fields and thus the Zeeman energy, and hence magnetic field magnitude, required to reflect them is greater. Because of this the isosurface which is pictured in Figure 5.6 is no longer appropriate. To observe how the isosurface from which the atoms reflect changes, and how we expect this to alter the observed light-sheet signal, we make use of the Monte Carlo simulations detailed in Chapter 5, which are easily modified to incorporate an initial launch speed. The results are shown in Figure 6.4.

As the launch speed of the atoms is increased the level set which defines the effective isosurface is associated with a larger field magnitude and is thus located closer to the domain walls. In the limit of a large field the isosurfaces are to a very good approximation described by ellipsoids [77]. Reflecting this fact, the ‘holes’ in the isosurface where there is insufficient field that are found between domain walls become larger for larger field. Thus there is an overall increase in the corrugation of the surface and a reduction in the mean height above the nanowires at which the atoms are reflected. The result is that for larger speeds a larger proportion of the atomic cloud will impinge on the nanowire array but a smaller proportion of these will be reflected.

The effect on the feature of the light-sheet signal associated with the

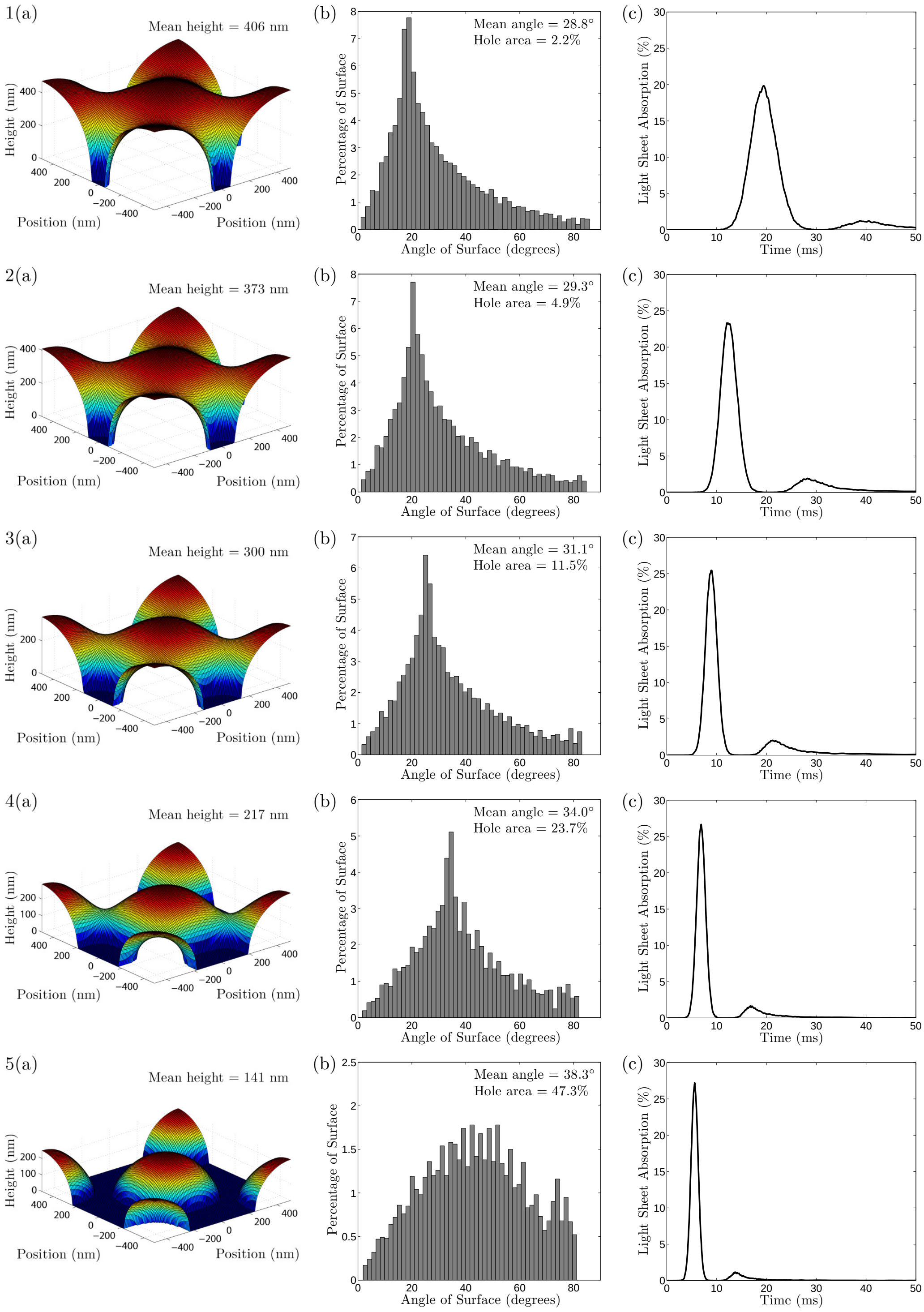

Figure 6.4: The effects of moving molasses. 1-5 correspond to launch speeds of 0.2, 0.4, 0.6, 0.8 and 1.0 m/s. (a) shows the corresponding isosurface, (b) shows the distribution of the isosurface angle relative to flat and (c) shows the corresponding simulated light-sheet signal.

falling atoms is as intuitively expected — it becomes higher and narrower for higher launch speeds. The variation in the reflection signal is as per the two effects described above. The reflection signal initially becomes higher and narrower in a similar manner to the feature associated with the falling atoms. In this regime the reduction of the spread of the cloud and increased speed through the light sheet are the dominant effects. As the launch speed continues to increase we see a reduction in the size of the reflection signal. This indicates that for higher launch speeds the shape of the isosurface becomes the dominant effect. The increased corrugation of the isosurface due to a higher atom energy causes a change in the shape of the reflection signal. We find that the largest reflection signal is predicted for a launch speed of around 0.6 m/s.

6.2.4 Experimental data

The theoretical treatment we have described makes some approximations that are not valid in experiment. We assume that the atoms are instantaneously accelerated to the appropriate launch speed without any displacement from their initial position. In practice the atoms are accelerated over the duration of the frequency ramp and during this time there is a displacement of the atom cloud in the direction of the launch. This displacement is observed to be larger for larger launch speeds and indicates the fact that the position of the atom cloud depends on the frequency imbalance in the beams. As previously mentioned, we also observe that not all of the atoms are successfully launched — there is a small fraction which remain in the MOT region.

Initial experimental data using the moving-molasses technique have been acquired, and show behaviour which qualitatively reflects the expected behaviour shown in Figure 6.4. Examples of such data are shown in Figure 6.5.

As the launch speed is increased we note that the feature associated with the falling atoms becomes narrower in a manner similar to theory. A small discrepancy is observed for larger launch speeds. This is likely to be due to the fact that the position of the cloud is offset during the moving molasses ramp. We observe an initial increase in the height of the drop feature, however this

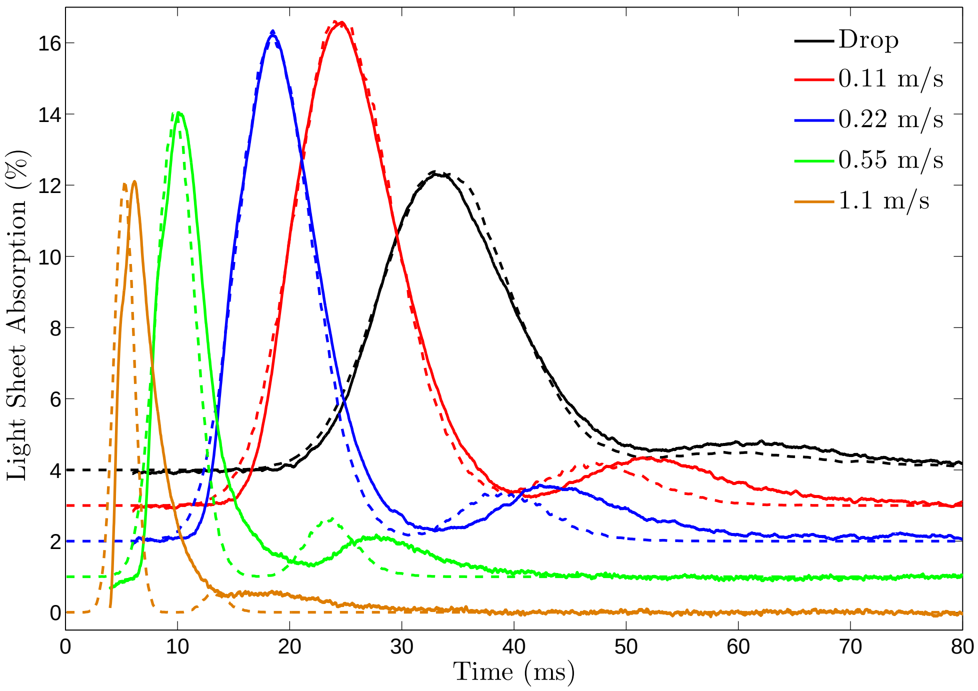

Figure 6.5: Example light-sheet signals obtained using moving molasses to vary the speed at which the atom cloud approaches the nanowire array. The speeds labelled are those according to the applied frequency difference between the beams. The theoretical curves from Figure 6.4 are also shown as dashed lines. Successive curves are offset vertically by 1% for clarity.

is then followed by a subsequent decrease, which is not predicted by theory. This could be due to inefficiency of the moving molasses procedure for larger speeds resulting in some atoms not being launched.

Examining the feature of the light-sheet signal associated with reflected atoms also shows qualitative agreement with simulation. There is an initial increase in the bounce signal, directly due to the increased speed with which the cloud moves. This is then followed by a reduction in the signal as the associated effective isosurface becomes more corrugated and the proportion of the chip providing sufficient fringing fields decreases. This decrease in the bounce signal is mitigated, however, by the fact that there is a remnant bounce signal observed when the nanowire array is in the nominally non-interacting configuration (cf. e.g. Figure 4.6).

There are a couple of notable differences between data and theory. Firstly the timings of the drop and reflection features are not as expected for higher launch speeds. This is likely due to the displacement of the atomic cloud during the moving molasses sequence (possibly together with some inaccuracy in the height of the light sheet). We also note that the reflection signal decreases sooner than predicted by theory. The reason for this is unclear, although one possibility is that this is due to the effect of surface interactions.

In order to better compare the data with theory there are a number of possible approaches. Further analysis, possibly out of vacuum, to ascertain the nature of the reflection when the chip is in the nominally non-interacting state may allow us to prevent such reflection. Alternatively the bounce signal could be measured relative to this null value. It would also be advantageous to combine fluorescence imaging with light sheet measurements to observe the behaviour of the cloud both during and after the moving molasses sequence. However, further unexpected behaviour was observed when optimisation (aligning/balancing of beams, timing of experimental routine, increased beam power) of the moving molasses procedure was carried out, and this is shown in Figure 6.6.

We see that as the launch speed associated with the moving molasses procedure is increased there is a stark change in the shape of the light-sheet signal, in particular in the feature associated with the falling atoms. At speeds of around 0.15 m/s and above the peak associated with the falling atoms becomes split into two. As the speed continues to increase this splitting becomes more pronounced. It is in fact possible to observe a light-sheet signal with such a dip corresponding to zero absorption.

This behaviour is entirely unexpected as there is no obvious mechanism that should produce this structure. The force produced by the moving molasses procedure should be an isotropic one, and the atoms are almost all pumped into the same quantum mechanical state. It seems we are faced with two options: either there is a real density variation imparted on the atomic cloud, or there is a modulation of the internal state of the atoms. The more likely of these two options seems to be the former. The moving molasses procedure clearly modifies the spatial distribution of the atoms as it cools and launches the cloud, and whilst there is no clear reason why this process should produce such a stark change in shape, it seems more feasible than the alternative. The latter option would require a mechanism which

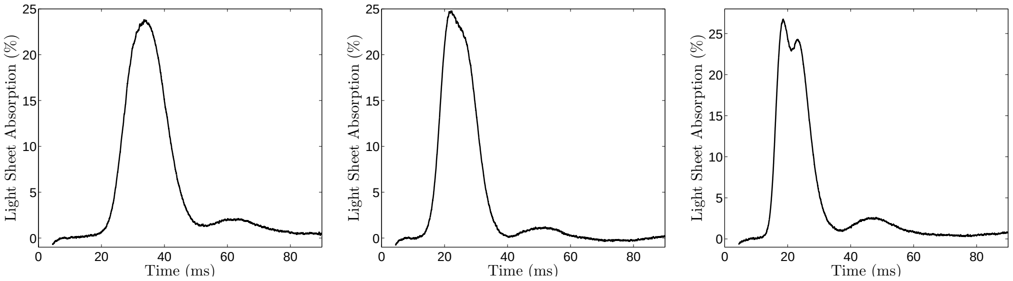

(a) Drop (b) 0.11 m/s (c) 0.17 m/s

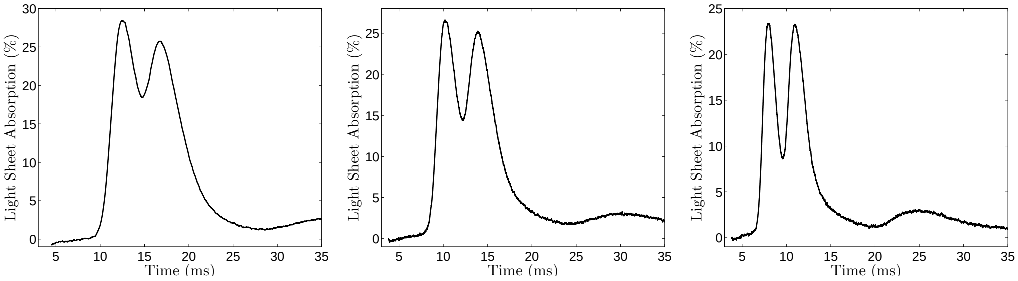

(d) 0.33 m/s (e) 0.44 m/s (f) 0.55 m/s

Figure 6.6: Example light-sheet signals for a range of moving molasses launch speeds. We note the appearance of a new feature, not present in Figure 6.5. After optimisation (described in main text) of the moving molasses procedure we observe that the peak associated with the falling atoms is split into two as the launch speed is increased.

redistributes atoms into an energy level which has a much lower (indeed zero in places) scattering rate. Given that the size of the beams used to address the atoms are always larger than the cloud itself, and that they are known to be addressing specific transitions, it seems unlikely that a central portion of the cloud should be transferred to a different state. In order to add evidence to this idea a number of simple tests were carried out. Repump light was used to image the atoms, in case some had been transferred to the lower hyperfine ground state, and the laser frequency and magnetic fields applied during the optical pumping and molasses phases were altered to examine the possibility of a redistribution amongst the m_F states. No evidence was obtained to suggest that any such redistribution was occurring.

Fluorescence images of the cloud also showed evidence of the presence of the bimodal structure within the atomic cloud, although the structure was not as well resolved using this method. An example fluorescence image is shown in Figure 6.7.

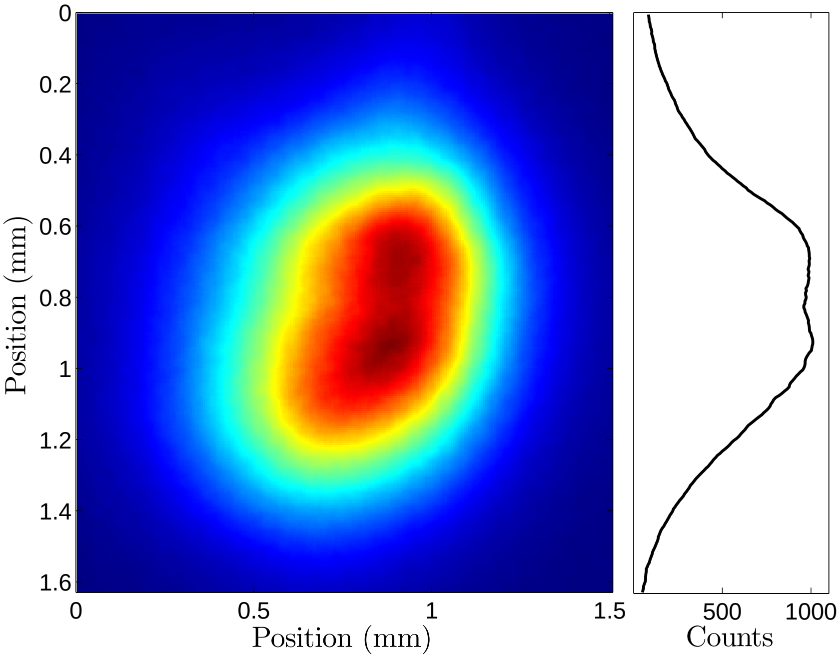

Figure 6.7: Fluorescence image of the atom cloud showing the bimodal structure. Also shown is a slice through the maximum of the image. Gravity acts down the page.

Further investigation of the nature of this new feature was carried out as follows: the distance from the initial cloud to the light sheet was determined by simply dropping the atoms and observing the time taken to reach the light sheet, using its associated signal. Next, the moving-molasses procedure was carried out. Fluorescence images were taken during the moving molasses ramp to determine how much the atomic cloud was shifted during the ramp. This was then deducted from the previous distance to determine how far the cloud had to fall to reach the light sheet when moving molasses was used. The speed at which the atoms were moving was then deduced from the drop feature of the light-sheet signal, for both of the peaks. These speeds were then compared to the speed expected according to the frequency difference between the beams, and to the speed measured according to time-of-flight images (the bimodal structure of the cloud was in general not evident in fluorescence images, so the time-of-flight technique could still be meaningfully applied).

The result was that for almost all the data taken the speed expected according to the beam frequencies and the speed measured according to time-of-flight images both agreed significantly better with the first of the two peaks in this new bimodal feature, i.e. the faster of the two speeds. This suggests that a fraction of the atoms are launched at a significantly slower speed than expected. We also note that for larger expected speeds the observed speed, by all measures, becomes less than that expected. This analysis is summarised in Figure 6.8.

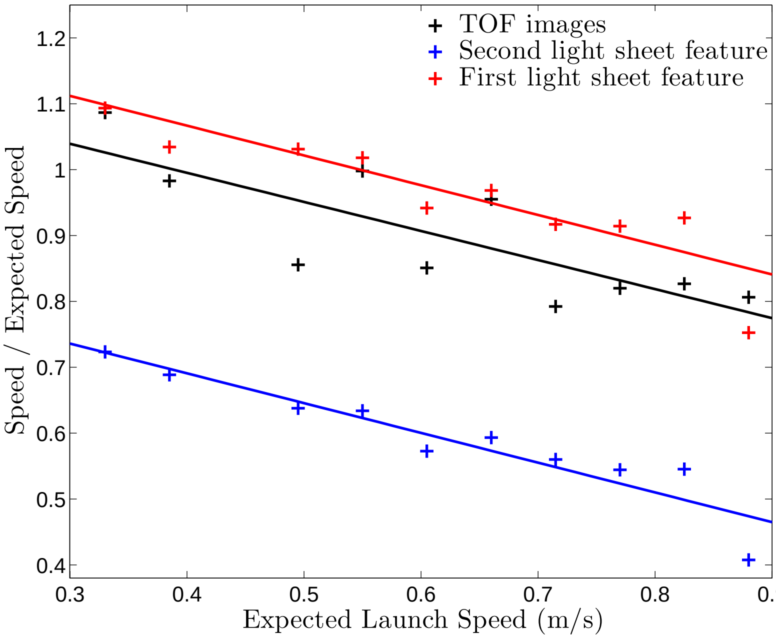

Figure 6.8: Variation in atom cloud speed with frequency difference during the moving-molasses procedure. One measure of the speed is provided by time-of-flight images. Another measure is provided by using the light-sheet signal to infer the speed from the time at which either of the drop features occurs. The lines are straight-line fits to guide the eye.

It is clear that there is a mechanism at work which is poorly understood and is dramatically modifying the structure of the cloud, either directly or in terms of the internal states of the atoms. Whilst the former seems a more likely explanation, there is no clear evidence to show the manner in which this modification occurs. Further work to investigate the nature of this mechanism together with a theoretical treatment of the moving molasses process are likely to be of significant interest, since, as far as we are aware, no evidence of this kind of behaviour has been previously reported.

6.3 Surface interaction

6.3.1 Introduction

Through the realisation of a magnetic atom mirror we have used ultracold atoms as a tool with which to probe a nanowire array. By controllably and transiently interacting the atoms with the magnetic fringing fields we can obtain information about the interaction. As discussed in the previous section the technique of moving molasses extends the region from which we can extract information; we are no longer limited to a single isosurface. It can also facilitate a more fundamental extension to the physics we can probe.

6.3.2 Theory

In the examination of the atomic potential so far we have considered two types of interaction: the gravitational acceleration of the atoms and the magnetic interaction of the atoms with the fringing fields associated with the domain walls. We have deliberately ignored another form of interaction, which is the electrostatic interaction with the chip. The reason we have ignored this interaction up until now is that it is very short range, meaning that the energy associated with surface interactions is negligible at the heights from which the atoms are reflected.

However, as shown in Figure 6.4, the distance at which reflection occurs can be dramatically reduced through the use of moving molasses. At these smaller distances we expect surface interactions to become important [150]. In general these interactions take a number of forms but are all derived due to electrostatic fluctuations within the interacting objects that have an associated energy. At very short distances the London-type interactions are dominant [158] (short range is typically defined as being less than the wavelength of the associated electromagnetic fluctuations). At larger distances the finite speed of light becomes an important consideration — this extension to the model was provided by Casimir and Polder [159]. Recent experiments have also observed surface interactions due to thermal, rather than quantum-mechanical fluctutations at larger distances [160].

To retain an accurate description of the potential that the atoms experience we must now incorporate the surface interaction. However, this is extremely difficult to do for our system; analytic expressions for the van der Waals interaction only exist for the very simplest of systems, such as two atoms or an atom and an infinite conducting sheet [161, 162]. Our system is a highly complicated one due to the presence of two different materials (silicon and permalloy) in a structure which is not flat — the nanowires extend a distance of 30 nm from the surface of the substrate. An accurate calculation of the surface potential will require detailed numerical methods.

To continue the discussion of the effect of the surface interaction we will use an approximate form of the interaction. We will assume that the atoms are interacting with an infinite plane of flat silicon at short range, for which the energy of interaction, E_{vdW}, at some distance z, is given by [149]

$$E_{\mathrm{vdW}} = -\frac{\epsilon_{\mathrm{r}} - 1}{\epsilon_{\mathrm{r}} + 1} \frac{1}{48\pi\epsilon_0} \frac{D^2}{z^2}, \tag{6.10}$$

where ϵ_{r} is the relative permittivity of the surface (for the case of silicon this is 11.7 [122]), ϵ_0 is the permittivity of free space and D is a factor determined by the particular atomic transition under consideration, analogous to the atom's electric dipole moment. Details of the derivation and calculation of this expression are provided in [163]. Following this treatment we can express the van der Waals potential in its simplest form as

$$E_{\mathrm{vdW}} = -C_3/z^3, \tag{6.11}$$

where C_3 characterises the strength of interaction. Values of C_3 for the particular case of rubidium interacting with a perfectly conducting surface have been calculated [164, 165], with some work looking more generally at the modification imparted by incorporating dielectric quality [166, 167]. There have also been a number of experimental techniques developed to measure the value directly, e.g. [140, 149, 150]. Following [163] we find a value of C_3 of 8.3×10^{-49} J/m^3 = 5.1 meV/nm^3 = 1.3 a.u. As per [149] the potential can be re-expressed as

$$E_{\mathrm{vdW}} = -A\hbar\Gamma\lambda^3/z^3, \tag{6.12}$$

where we have used the approximation that the atom-field interaction is provided by the strongest dipole transition, and Γ is the atomic linewidth of this transition, which has a corresponding wavelength of λ. A is a numerical factor which for our case is 0.11.

Using this model we now consider modifying the energy level diagram provided in Figure 5.3. The total potential directly above the centre of a domain wall (where the magnetic fringing field is largest) is now given by the combination of the magnetic interaction and the van der Waals interaction, and is shown in Figure 6.9.

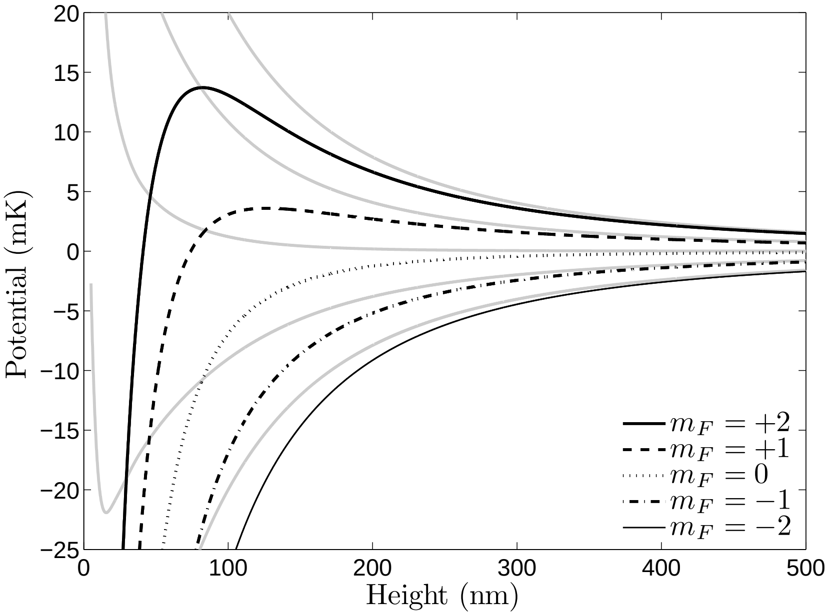

Figure 6.9: Total atomic potential associated with our magnetic mirror when a van der Waals interaction is included. The magnetic potential is calculated via micromagnetic simulations as per Figure 5.3 and is shown in grey. The van der Waals interation is approximated as being due to an infinite sheet of silicon. The height is defined relative to the surface of the nanowires and we consider points that are located directly above the centre of a domain wall. The magnetic states are labelled by m_F values for convenience.

The first point to note is that we observe that the van der Waals interaction only becomes important at short range. This is intuitively expected since the surface interaction potential has a $1/z^3$ dependence, and the magnetic interaction a roughly $1/z^2$ dependence. Down to a height of around

100 nm the van der Waals interaction has a very small effect, after which it quickly begins to dominate and the total potential ‘turns over’ and becomes attractive. By a height of around 40 nm the potential is negative for all magnetic sublevels. One must bear in mind however that this treatment is for the case of a position directly above a domain wall, i.e. where the magnetic fringing fields are strongest. Away from the domain wall centre both the magnetic field and the surface potential will reduce in size. This change will also be nontrivial due to the structure of the nanowire array – the 30 nm difference in height between the substrate and the top of the nanowires is significant.

Given the data in Figure 6.9 it is then an easy matter to calculate the energy required to enter the region where the potential becomes attractive. For the case of atoms in the $m_F = 2$ state we require a launch speed of around 1.6 m/s, which is easy to realise within our setup.

Considering the calculations presented here, and those of the previous section, we can make a qualitative description of how the dependence of the light-sheet signal on the moving molasses launch speed may be modified by the incorporation of the effect of surface interactions. We expect that the bounce signal would decrease in size more rapidly, as the effect of the attractive interaction to prevent reflection of atoms would add to the effect of an increasingly corrugated effective isosurface.

6.3.3 Outlook

It is likely that a quantitative analysis of the nature of the surface interaction experienced by the atoms will be very difficult to obtain. There are two main reasons for this. In order to make deductions about the character of the van der Waals potential we require a theoretical model with which to compare the experimental data. For the geometry of our system this is hard to calculate. However the problem does not seem entirely intractable as a significant amount of work has been carried out calculating surface potentials for regular arrays of material or even objects of arbitrary shape [168, 169, 170, 171, 172].

The second hurdle to overcome is then the challenge of separating the effect of the magnetic interaction on the atom dynamics and the effect of the surface potential. As previously mentioned, a closer approach of the surface yields a more corrugated effective isosurface and also results in the surface interaction becoming more important. Both of these factors will result in a reduction in the bounce signal. Ensuring a correct interpretation of the results would be very challenging.

In addition to this, as described in Section 4.3, we observe a bounce signal in what we expect to be a configuration with no domain walls present. This adds an extra complication to any analysis of the evolution of the signal we obtain. As shown in Section 6.2, we have already achieved launch speeds which we predict will take atoms into the region where the atomic potential becomes attractive, yet a bounce signal is still observed. Whether this is due to the same unexpected reflection of the atoms, or due to an inaccuracy in our understanding of the nature of the potential, is unclear.

In order to use a nanowire array as a method of studying surface forces we may require modification of our setup. A smoothing of the magnetic potential would help separate the effects of the two types of potential; working with a flat mirror would mean any reduction in the number of atoms that are observed to reflect from the surface would be solely due to the attractive surface interaction. A flatter magnetic potential could be achieved with a shorter wavelength of the serpentine pattern, as described in Section 5.2.3.

Working with atoms in a different magnetic sublevel (e.g. $F = 2, m_F = +1$) may seem like a partial remedy to the complexity of the problem, as according to Figure 6.9 the launch speed required to reach the point where the potential turns over is only around 0.8 m/s. However, the potential is halved with the change in m_F and hence the corrugation of the effective isosurface is exacerbated.

In summary, it is probable that quantitative analysis of the surface forces arising from our device will be beyond the reach of the current experimental setup. Such a study would likely require a second generation of nanowire chip which provides a significantly flatter effective isosurface, and/or detailed theoretical analysis of the nature of the van der Waals potential due to the nanowire array, as well as further study into the nature of the magnetic potential as one probes distances closer to the array.

6.4 Conclusions

In this chapter we have presented work which builds upon the atom mirror experiment. The moving molasses technique is seen to be an effective tool to tune the initial energy of the atomic cloud, thus extending the region over which we can probe and interact with the fringing fields. However, whilst the data we obtained qualitatively demonstrate expected behaviour, there are unexpected features which would benefit from further investigation.

A consideration of a simple van der Waals potential shows that we should expect a modification to the reflection dynamics beyond that due to the magnetic interaction. However, accurately discerning such a contribution is likely to be very difficult, especially on a quantitative level. This is due to a number of associated challenges: firstly the unexpected features observed during moving molasses need to be explained; accurate calculation of the surface interaction due to the nanowire array is very demanding due to the complex structure; and a detailed quantitative understanding of the magnetic potential is needed in order to isolate the effect of surface interactions, due to the corrugated nature of the magnetic potential.

Whilst the technique of moving molasses is a useful tool for extending the region over which we probe the atom-field interaction, the system we have is a complex one, which may make the study of surface interactions impractical without a redesign of the nanowire array. A more productive avenue for further study, now that we have demonstrated the interaction of atoms and domain walls, is the realisation of a trapping potential, which we will consider in detail in the following chapters.

Chapter 7

Magnetic Trapping

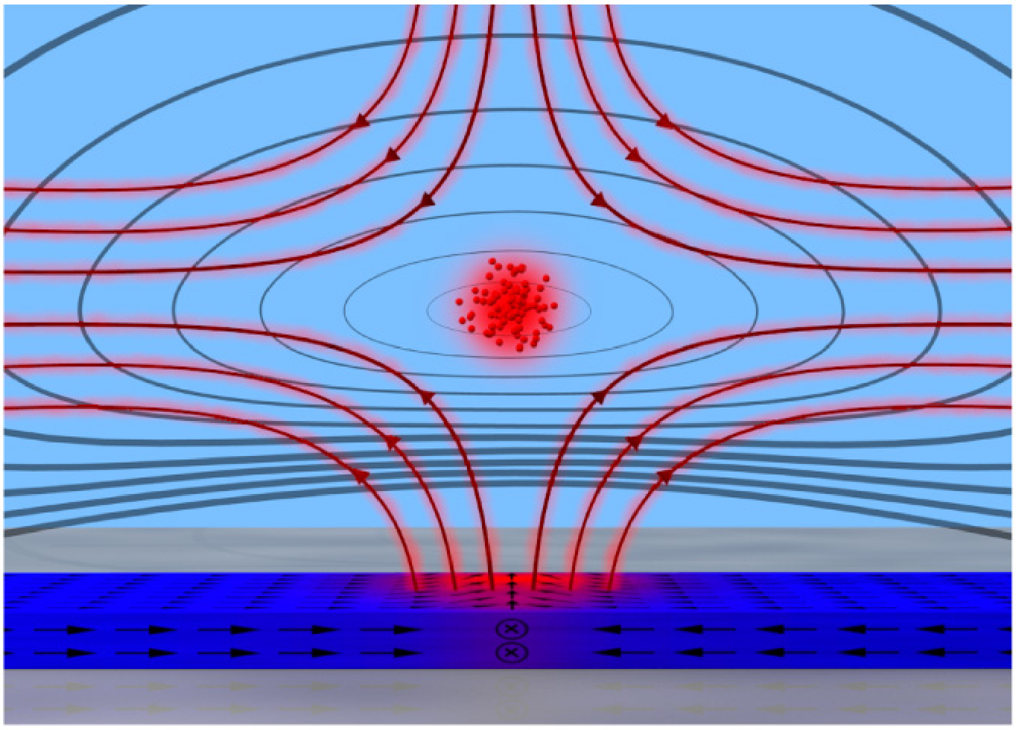

Schematic of a magnetic trap based on a biased domain wall. Magnetic field lines are shown in red and contours of constant magnetic field magnitude are shown in black.

7.1 Introduction

Up until this point, the work that we have presented has been focussed on the realisation of an atom mirror. However, we anticipate that this proof-of-principle experiment should be a precursor to more elaborate realisations of an interaction between atoms and domain walls. In particular, we envisage that individual domain walls can be used as the basis of exceptionally tight and mobile atom traps [66]. In this chapter we will illustrate how this can be achieved and discuss the obstacles and possible limitations to the scheme we propose.

7.2 Theory

Techniques for magnetic confinement of quantum particles were first explored using cold neutrons [173], but it was immediately apparent that the same principles could be used to confine atoms [174, 175]. However, it was over 20 years until this was experimentally realised [21, 176, 177], following the advent of laser-cooling techniques.

Neutrons and atoms have an important common feature — a permanent magnetic dipole moment. It is because of this that both of these particles can be confined via an interaction with a magnetic field. We recall that atoms that are exposed to a magnetic field gradient experience a Stern-Gerlach force given by

$$F_{\mathrm{SG}} = -\vec{\nabla} E_{\mathrm{Z}} = -m_F g_F \mu_{\mathrm{B}} \vec{\nabla} |\vec{B}|, \tag{7.1}$$

where m_F is the magnetic quantum number, g_F is the Landé g-factor and μ_{B} is the Bohr magneton. Atoms with $m_F g_F > 0$ are in 'weak-field-seeking' states. Such atoms can be confined to minima of magnetic field magnitude.

The first realisation of magnetic trapping of atoms used a magnetic quadrupole as the trapping field [21], a configuration which is now ubiquitous and is described by

$$\vec{B}_{\mathrm{Q}}(\vec{r}) = B' \left(x\hat{x}, y\hat{y}, -2z\hat{z} \right), \tag{7.2}$$

where B' is the characteristic magnetic field gradient. The recurrence of the magnetic quadrupole reflects both its utility and the fact that Maxwell's equations prescribe it as the simplest form of a magnetic field which has a zero point. Since its inception a wide variety of alternative geometries have been developed based on permanent magnetic material and current-carrying wires. Notably a number of schemes have been developed that generate harmonic magnetic potentials, i.e. the magnetic field follows an r^2 dependence, rather than a linear one as in the 3D quadrupole. This results in a potential which is much better suited to atom trapping. An atom in such a potential undergoes simple harmonic oscillation.

The shift towards magnetic trapping on microfabricated devices confers a very important benefit: the parameter B' is dramatically increased as the characteristic lengthscale of the magnetic field source is reduced. The result is that the characteristic trap frequency of a confining potential is significantly increased. If we consider the variation of the magnitude of a static magnetic field in one dimension, given by $|\vec{B}_\mathrm{S}(x)|$, we can perform a Taylor expansion to yield:

$$|\vec{B}_\mathrm{S}(x)| = B_0 + B'x + B''x^2/2 + \dots \quad . \tag{7.3}$$

For a harmonic potential the quadratic term is the highest order term present. The effective spring constant associated with the potential, $k = m_F g_F \mu_\mathrm{B} B''$. The resonant frequency of the trap, ω_Trap is then provided by

$$\omega_\mathrm{Trap} = \sqrt{\frac{m_F g_F \mu_\mathrm{B} B''}{m}}, \tag{7.4}$$

where m is the mass of the atom. This is the parameter that we will use later to characterise the 'tightness' of magnetic traps.

We consider the use of nanomagnetic domain walls as sources of magnetic field. They have exceptionally small characteristic size, ∼100 nm, and very high associated magnetic fields (∼0.1 T) and field gradients (∼10^6 T/m). As was derived in Chapter 2, the fringing fields associated with nanomagnetic domain walls follow, under the simplest approximation, a $1/r^2$ relationship. Adding a bias field in opposition to the fringing fields yields a trapping potential [66], described by B_Trap. This is shown in Figure 7.1 for the case of a bias field in the negative vertical (z) direction producing a trap located 500 nm above a domain wall. Also illustrated is the potential near the zero point, defined as $E_\mathrm{Z}/k_\mathrm{B}$ where k_B is Boltzmann's constant. Note that while it is trivial to include the potential energy due to gravity in this analysis, it is exceptionally weak over the lengthscales we consider when compared to

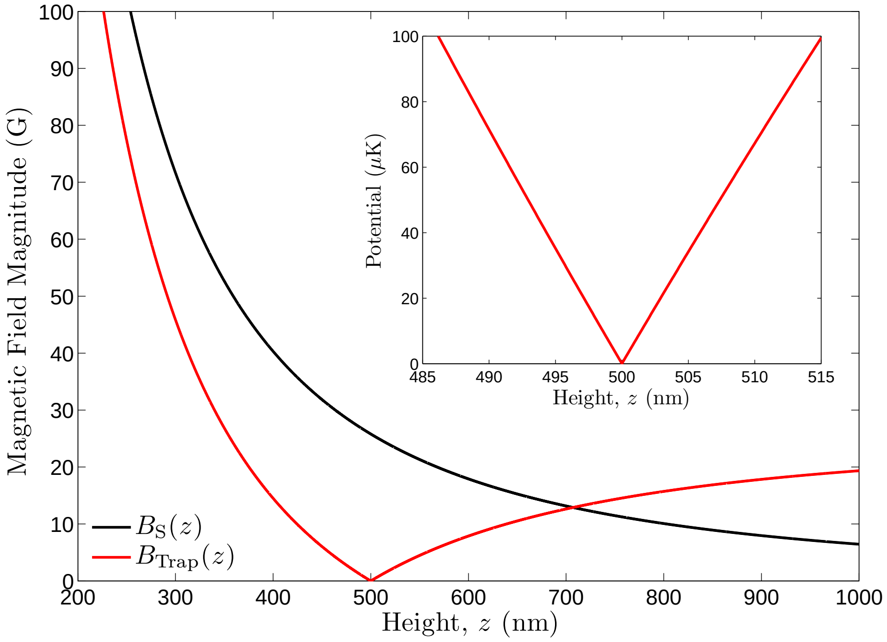

Figure 7.1: The magnetic fringing field directly above a nanomagnetic domain wall (nanowire cross section 125 nm × 30 nm), with and without a bias field, for an atom with $m_F g_F = 1$. With the additional bias field a trapping potential is formed at a height of 500 nm. The inset shows the magnetic potential, $E_{\mathrm{Z}}/k_{\mathrm{B}}$ close to the zero point.

the huge magnetic fields used to create our traps.

Because of the exceptionally high field gradients the trapping potential has a very high associated trap frequency, $\sim 2\pi \times 0.1$–1 MHz. Evaporative cooling will occur quickly [178, 179], until an equilibrium is approached. It is possible to prescribe a rule of thumb which determines an atom temperature from the trap depth [180] and we shall assume that atoms at a temperature T are contained in a potential of depth $10T$. This then defines a region of space to which the atoms are confined, of a diameter of around 50 nm. Within this region the magnetic field is very well approximated as being linear, as seen in the inset of Figure 7.1, i.e. the result is a 3D quadrupole[1].

What we have created is an extremely tight analogue of the very simplest magnetic trap, localised to the position of a domain wall. This affords

---

[1] Note that by the symmetry of the situation the field gradients in the x and y directions are equal. Through an application of Maxwell's equations the field thus has the form $\vec{B}(\vec{r}) = B'\,(x\hat{x} + y\hat{y} - 2z\hat{z})$ close to the zero point.

precise confinement of atoms and the possiblity of investigating new physics associated with traps with dimensions less than an atom's de Broglie wavelength [181]. However, the exceptional tightness produced by nanoscale traps is a double-edged sword as it makes the loading of such traps challenging. There is another fundamental problem associated with the potential we have created, which is common to all magnetic quadrupole potentials and we will discuss this now.

7.3 Majorana losses

The inset to Figure 7.1 shows the potential associated with our nanowire traps. However this is only the case for one particular value of $m_F g_F$ — for most atomic states there will be a manifold of different m_F states. Here we consider the use of ground state ^{87}Rb atoms, i.e. atoms in the $5^2\mathrm{S}_{1/2}$ $F = 2$ state. In a non-zero magnetic field this energy level is Zeeman split into five, corresponding to the five possible values of the magnetic quantum number m_F. As such, there are five different associated potentials, in accordance with Equation 3.3. Without a magetic field, the energy levels are degenerate, and m_F is no longer a good quantum number. Figure 7.1 assumes that $m_F = 2$ ($g_F = 1/2$ for the ground state of ^{87}Rb). A more complete picture is provided by Figure 7.2 which shows all five potentials. Two out of the five m_F states are weak-field-seeking ($m_F = +2$ and $m_F = +1$), corresponding to trapping potentials (black in Figure 7.2). The other three states produce non-trapping potentials (red in Figure 7.2). It is relatively easy to prepare the atomic sample in the correct m_F state through optical pumping (cf. Section 3.4.2). In a sufficiently large magnetic field an atom's magnetic dipole moment will remain aligned (or anti-aligned) with the magnetic field. However, during the atoms' traversal of the trap they will pass through the zero point at the centre. At this point there is a degeneracy, there is no field to define the quantisation of the magnetic dipole moment, and hence no preferred m_F value. Thus an atom that reaches the zero point will be able to change m_F state by undergoing a Majorana spin flip [182, 183].

The adiabatic theorem of quantum mechanics describes in a fundamental manner the way in which the evolution of a quantum mechanical Hamiltonian

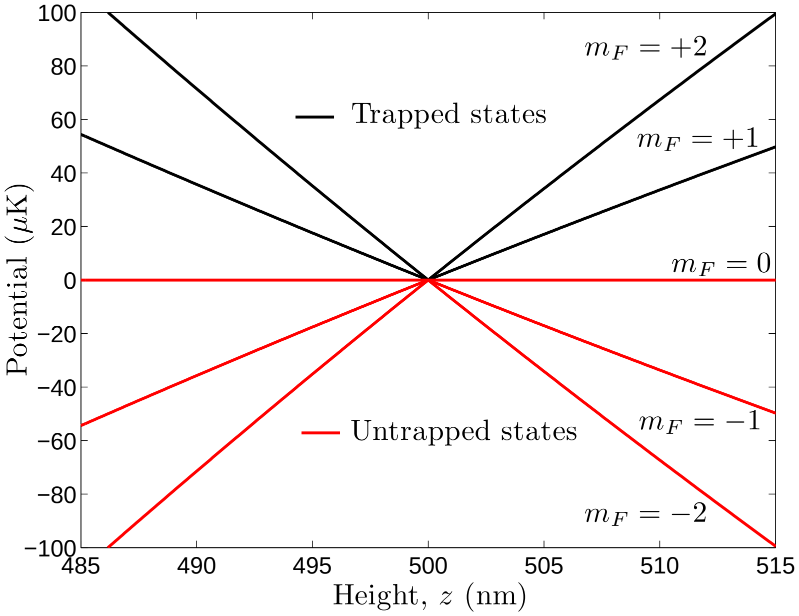

Figure 7.2: A Zeeman split magnetic potential experienced by a ground state ^{87}Rb atom. The potential is formed by adding a bias field of 25.8 G to the fringing fields from a domain wall in a nanowire of cross section 125 nm × 30 nm (fringing fields calculated analytically, cf. Section 2.2.1).

affects the state of the system [184]. Simply put it states that if the Hamiltonian evolves sufficiently slowly the system will remain in its instantaneous eigenstate. Under these conditions we apply the adiabatic approximation (conversely the diabatic or 'sudden' approximation applies). The validity of the adiabatic approximation is an important consideration for magnetic atom trapping. To remain adiabatic an atom must experience a sufficiently slowly-varying trapping potential, such that the atom remains in its prescribed m_F state. If the rate of change is too fast, the sudden approximation is more appropriate, and it becomes more likely that the atom will undergo a Landau-Zener transition, which manifests as a spin-flip. For the case of a magnetic potential the adiabatic criterion can be recast in terms of the Larmor frequency — this is the frequency with which an atom's intrinsic magnetic dipole moment precesses about an applied magnetic field. Provided the magnetic dipole and field remain aligned, the atom will remain in its given m_F state. Thus we can write the adiabatic criterion as [185]

$$\dot{\omega}_{\mathrm{L}} < \omega_{\mathrm{L}}^2, \tag{7.5}$$

where ω_{L} is the angular Larmor frequency of the atom for a change of Δm_F, and is given by $\omega_{\mathrm{L}} = |\Delta m_F|\, g_F \mu_{\mathrm{B}} |\vec{B}|/\hbar$.

The presence of a zero of magnetic field is clearly disastrous — no matter how slowly one moves within the trap, the above inequality will not be satisfied. There is in fact a finite chance of a spin-flip occurring at all points in the potential. In its simplest form the probability of such a transition is described the the Landau-Zener formula. Atoms which enter the vicinity of the zero point are very likely to flip their spin. Magnetic traps with zero points are in fact widely used within atomic physics — their utility often relies on the temperature of the atoms being relatively high, and the trap frequency relatively low, such that the rate of the losses due to spin-flips is low. This would not be the case for nanowire-based magnetic traps. The exceptionally high trap frequency means that any atoms contained in such nanowire traps would traverse the magnetic zero quickly and often — recall we expect trap frequencies of the order of $2\pi \times 0.1$–1 MHz. The result is that any losses due to spin flips would occur extremely quickly, resulting in very short trap lifetimes.

In order to circumvent the problem of spin flip losses it is necessary to remove the zero of the magnetic field to create a non-zero trap minimum in order to satisfy the inequality given in Equation 7.5. Due to the ubiquity of the quadrupole field in magnetic trapping a number of different schemes have been created in order to solve this problem. However, most of them are not compatible with the type of nanoscale traps which we present here.

It is possible to create a static magnetic potential with an approximately harmonic form through the use of a Ioffe-Pritchard type trap [26, 175]. Variations on this type of geometry have given rise to baseball [186] and QUIC (quadrupole and Ioffe configuration) [187] traps which demonstrate slightly different methods of achieving traps of similar magnetic field shape. There is, however, a prohibitive problem associated with using these schemes for nanowire-based traps. To modify a quadrupole potential to a Ioffe type potential one must add magnetic fields which vary on the scale of the quadrupole. Implementing such a scheme for a nanowire trap would require the addition of extra nanoscale magnetic field sources (likely current-carrying wires) at every single trap site, of which there would likely be 10^4–10^5. This would be extremely difficult to implement.

An alternative scheme for overcoming magnetic zeros is the use of a blue detuned laser as a source of a repulsive potential which keeps atoms away from the zero point. Implementation of such a scheme would require the addition of light fields with sizes of the order of 10 nm to every trapping site. This is not feasible due to the diffraction limit.

In order to solve the problem of Majorana spin flips in a manner which does not involve the addition of nanoscale objects to modify the potential a paradigm shift is required. We consider instead the use of time-dependent potentials. The addition of macroscopic time-dependent magnetic fields has been used in many applications to remove zero points. One can divide this methodology into two different regimes, characterised by the frequency of oscillation of the magnetic fields. This provides us with two techniques, whose efficacy and suitability we will now discuss.

7.3.1 RF-dressing

Introduction

The problem of diabatic losses within trapping potentials was well known before the first realisation of cold atom confinement [188]. In comparison, the technique of RF-dressing as a solution to this problem is a relatively new one, with the first application being demonstrated in 2004 [189]. Since its realisation a number of applications have been developed including the production of tight atomic traps on a chip [190] and double well potentials [30]. Many other exciting trap geometries based on the RF-dressing technique have been posited and realised [191, 192, 193]. In this section we will briefly outline the method of using RF frequency magnetic fields to favourably modify an atomic potential. Whilst complicated trap topologies are possible we will restrict our discussion to the simple matter of circumventing trap losses, and unfortunately, to the reasons why this is not possible for our particular application.

The canonical example of the dressed-state picture is a two-level atom in the presence of a light field [136]. If the light field has a frequency close to a transition frequency then the two associated energy levels are resonantly coupled or ‘dressed’ by the applied field. We consider an atom in the basis $|g\rangle$ (ground state), $|e\rangle$ (excited state), and a light field described by a number state $|n\rangle$. Diagonalisation of the joint Hamiltonian incorporates the atom-field interaction and provides the eigenstates of the system. With no interaction and a resonant light field, the states $|g, n\rangle$ and $|e, n-1\rangle$ are degnerate. By permitting a detuning of the light field, δ, these levels are split by $\hbar\delta$. By adding in the interaction term of the Hamiltonian these manifolds then become further split, or ‘dressed’ according to the strength of the interaction, which is characterised by the Rabi frequency, which we define as $\Omega = -\vec{d}.\vec{E}/\hbar$, where $\vec{d}$ is the electric dipole of the atom and $\vec{E}$ is the electric field.

The process described above can be applied in a completely analogous manner to more complicated systems. The most important feature which we are yet to consider is the possibility of spatial dependence. For the case of a confining atomic potential a spatial variation in the atom-light coupling is produced. Through this additional complexity, provided by the vector nature of the interaction, more complicated potentials can be produced.

In this work we will not be considering the use of optical fields, instead our system will be dressed by the addition of an RF magnetic field. However the treatment is identical in nature. One can intuitively prescribe a ‘magnetic photon’ as the particle which dresses the atomic states. Replacing the optical field in our initial example of a simple two-level atom the Rabi frequency can be redefined as $\Omega_B = -\vec{\mu}.\vec{B}/\hbar$. For a spatially dependent Hamiltonian the effective Rabi frequency takes a more complicated form.

The treatment described above can be applied to an atom with a manifold of magnetic sublevels labelled by m_F. The details of the derivation of the resulting potentials can be found in many other works e.g. [191, 192, 194, 195], in particular [196] and following theses provide a rigorous explanation. In this work we will simply quote the result and apply it to our particular traps. The resulting potentials are given by

$$V(\vec{r}) = m_F g_F \mu_{\mathrm{B}} \sqrt{\left(\left|\vec{B}_{\mathrm{S}}(\vec{r})\right| - \frac{\hbar\omega_{\mathrm{RF}}}{|g_F\mu_{\mathrm{B}}|}\right)^2 + \frac{B^2_{\mathrm{RF}_\perp}(\vec{r})}{2}}. \tag{7.6}$$

$\vec{B}_{\mathrm{S}}$ is the static magnetic field (that due to the biased domain wall fringing fields), ω_{RF} is the frequency of the RF field, and $B_{\mathrm{RF}_\perp}$ is the component of the RF field which is perpendicular to the static field at a given point. We are assuming here that the RF field is isotropic, which is a very good approximation given the characteristic size of the static trapping potential. We shall now consider the application of this formula to trapping potentials based on nanomagnetic domain walls.

RF-dressed domain wall traps

We now consider the application of Equation 7.6 to the static potential produced by the biased fringing fields from a nanomagnetic domain wall. Recall that the static field can be very well approximated by a 3D quadrupole (cf. Figure 7.1). As will be shown, there is an intrinsic problem with trying to apply the technique of RF dressing to a field of this form, which is that it is impossible to produce a potential without any zero points. Whilst other realisations of the technique have circumvented this problem by using gravity to ensure that any atoms do not reach the remaining zero points, we will show that this is not a feasible option for the regime in which we work.

The shape of the resulting potentials can be understood intuitively by the schematic shown in Figure 7.3. The static field produces a manifold of potentials, for each of the m_F. These potentials are then coupled by the RF field, manifesting as a shift of the potentials relative to each other, which produces a number of crossings at the corresponding resonant positions. The degeneracies at the avoided crossings are then lifted by the final term in Equation 7.6 which is analogous to the Rabi frequency between adjacent sublevels. This Rabi frequency is dependent on both the direction of the RF field relative to the static field, and the polarisation of the RF field.

It is the calculation of this effective Rabi frequency that is the most challenging part of the calculation, but can be intuitively understood as being a calculation of the component of the RF field which is perpendicular to the static field. For the case of a linearly polarised RF field this is then trivially given by a term proportional to $\hat{e}_{\mathrm{S}} \times \vec{B}_{\mathrm{RF}}$, where $\hat{e}_{\mathrm{S}}$ is the unit vector of the static field direction. For the case of an elliptically polarised RF field the calculation is more challenging, and less intuitive. Following the treatment provided in e.g. [196] we find that the effective Rabi frequency for a circularly

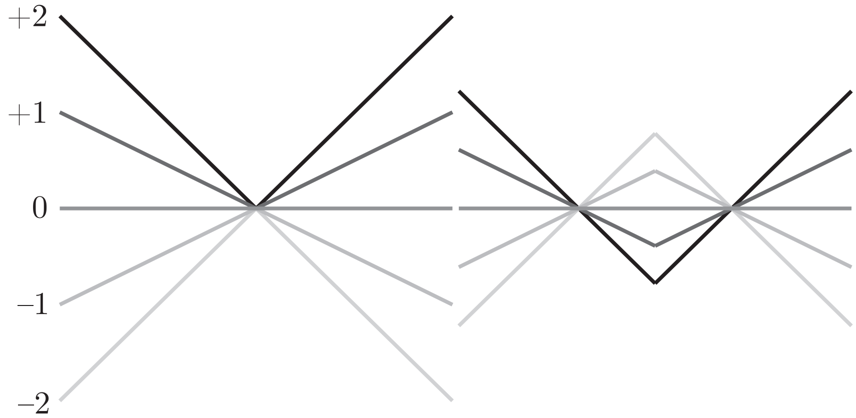

(a) Manifold due to static field (b) Shifted potentials

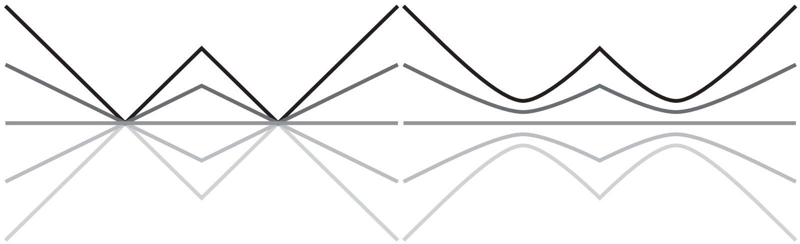

(c) Shifted potentials (relabelled) (d) RF-dressed potential

Figure 7.3: Schematic of the effect of applying an RF frequency dressing field to a manifold of magnetic potentials. The resulting adiabatic potentials can be intuitively understood, with reference to Equation 7.6, as a shifting of the static field potentials followed by a separation of the resulting degeneracies characterised by an effective Rabi frequency. The separate potentials are labelled according to a magnetic quantum number (e.g. m_F).

polarised RF field is described by a term proportional to $1 \pm 2\cos\theta + \cos^2\theta$, where θ is the angle of elevation, relative to the z axis (aligned with gravity), and we have assumed that the RF field is polarised in the x-y plane. From the form of the effective Rabi frequency it is immediately evident that for a static field described by a 3D quadrupole there will always be points where the Rabi frequency has at least one zero point. This is a consequence of the fact that the direction of the static magnetic field takes all possible values. Examples of the resulting potentials are shown in Figure 7.4.

In considering the full 3D potential, a simple form is observed, which can be understood by analogy to Figure 7.3. The static potentials are firstly shifted by the dressing field, producing an ellipsoid of zero points, where

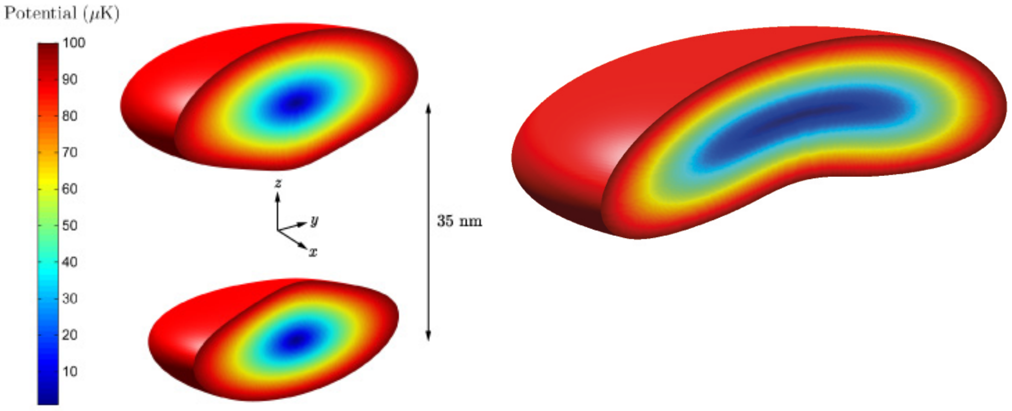

(a) Linearly polarised RF

(b) Circularly polarised RF

Figure 7.4: Example potential isosurfaces created by RF dressing biased domain wall fringing fields. Half of the isosurface is shown, with a slice being shown in the x-z plane, where gravity acts in the z direction (the height above the domain wall). The fringing fields are calculated analytically as per Section 2. The linear RF field is polarised in the z direction, the circular RF field is polarised in the x-y plane. The two figures are drawn to the same scale.

crossings exist. The degeneracies are then lifted by an amount proportional to the effective Rabi frequency. For the case of a linearly polarised RF field this Rabi frequency is zero at two antipodal points. For a circularly polarised RF field there is one zero point.

The best case scenario is then that using a circularly polarised RF field. Given this choice of polarisation the resulting potential can be tuned by varying the amplitude and frequency of the dressing field. The former changes the magnitude of the Rabi frequency, and hence how far the degeneracies are lifted. The latter changes the relative shift of the static potentials, effectively changing the size of the ellipsoid. These variations are illustrated in Figure 7.5.

As mentioned, the problem of a magnetic field zero is still present. However, this has been overcome in other applications of RF dressing by ensuring that this zero point is inaccessible to the trapped atoms [195]. This is achieved through a consideration of the effect of the gravitational potential,

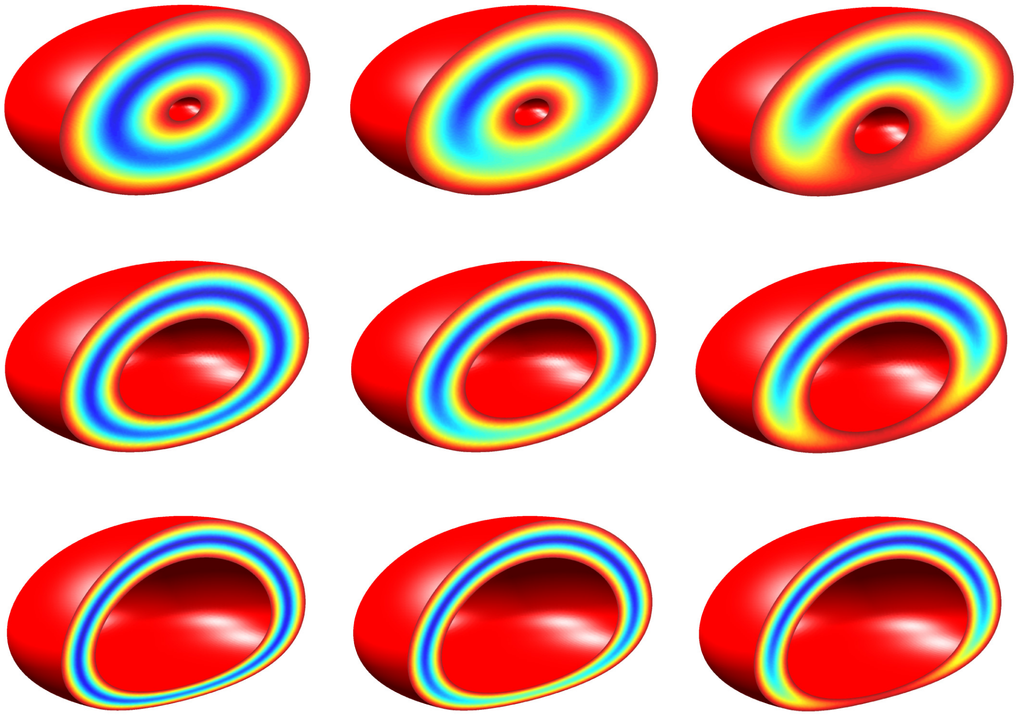

Figure 7.5: RF-dressed potential isosurfaces. The figures are as per Figure 7.4. Isosurfaces extend to 150 μK. Columns left to right represent values of $|\vec{B}_{\mathrm{RF}_0}|$ of 0.5, 1.0 and 2.0 G. Rows from top to bottom represent values of ω_{RF} of $2\pi\,\times$ 2, 5 and 10 MHz. The corresponding diameters of the ellipsoids of minima are 138, 172 and 354 nm in the x and y directions, and 35, 87 and 183 nm in the z direction. The RF field is circularly polarised in the x-y plane.

which, up until now, has been tacitly ignored. By ensuring that the remaining zero point is located at the top of the ellipsoid of minima, as shown in the middle column of Figure 7.5, there is an additional energy cost in moving from the bottom of the ellipsoid to the top, where the zero point is. Because of this additional potential the result is that atoms remain at the bottom of the ellipsoid where there is a finite field minimum.

However, this technique is not applicable in our case. The reason is simple — because the static magnetic field gradients are exceptionally large, the resulting trapping potential is very tight, and hence the ellipsoid of minima that forms is very small (<1 μm). The gravitational potential has a characteristic lengthscale of 9.68 μm/μK for ^{87}Rb atoms. Thus, to create a trap of depth 100 μK we required our ellipsoid to be approximately 1 mm in diameter. This is orders of magnitude greater than what we have. Because we require a finite minimum at the bottom of the ellipsoid, in order to avoid spin-flips, the gravitational potential must also account for this potential difference, further exacerbating the problem.

The result we have found is a simple one — the RF dressing technique is not applicable for the case of a tight 3D quadrupole field, since there will always be at least one zero point in the potential, which we cannot ensure the atoms will keep away from. In the following section we will consider an alternative technique which may present a solution to our spin-flip problem.

7.3.2 Time-averaged potentials

Some of the work in this section forms the basis of the following paper:

Nanomagnetic engineering of the properties of domain wall atom traps
T. J. Hayward, A. D. West, K. J. Weatherill, T. Schrefl, I. G. Hughes and D. A. Allwood
J. Appl. Phys. **110** 123918 (2011)

In the previous section we examined the use of an oscillating magnetic field to modify atomic potentials. In this section, the same tool will be used to look at a different kind of potential. The difference is the characteristic frequency of oscillation. As described in e.g. [197] there are three different regimes. For sufficiently slow frequencies of oscillation the quasi-static regime is appropriate; the potential which atoms experience is simply the instantaneous one and the perturbations of an oscillating field act in an entirely intuitive manner. As previously stated, for high frequencies, close to the Larmor frequency, the dressed-state regime is appropriate and the corresponding eigenstates are those of the joint system, including the atom-field interaction[2]. Between these two regimes lies the realm of time-averaged potentials (TAPs), where the frequency of oscillation is significantly less than the Larmor frequency

---

[2] For this prescription of regimes we also assume that the rotating-wave approximation applies within an RF-dressed system. Beyond this approximation the distinction between regimes is less clear.

between separate energy levels, but is sufficiently large that the atoms do not simply experience a perturbed potential.

The technique of TAPs was first utilised in the context of the Paul ion trap [198] and has since been used to realise a variety of trapping schemes for both atoms and molecules. The development of magnetic TAPs led to the first observation of a Bose-Einstein condensate [199]. As with the RF-dressing technique, a wide variety of TAP geometries have been posited and realised in experiment, such as a double well trap [200, 201]. Through a use of a combination of both time-averaging and RF-dressing techniques it is also possible to create a ring topology [202]. In this section we will simply consider the feasibility of using a conventional TAP scheme to circumvent Majorana losses associated with a zero point in an atomic potential.

The simplest form of magnetic time-averaged potential is also known as the time-orbiting potential (TOP) trap [203]. From hereon we will refer to all potentials reliant on the time-averaging principle as TAPs. The simplest TAP consists of the addition of a circulating magnetic field, $\vec{B}_{\mathrm{TAP}}$ to a static confining magnetic field, $\vec{B}_{\mathrm{S}}(\vec{r})$. These additional fields are given by

$$\vec{B}_{\mathrm{TAP}} = B_0 \left[\cos\left(\omega_{\mathrm{TAP}} t\right)\hat{x} + \sin\left(\omega_{\mathrm{TAP}} t\right)\hat{y}\right], \tag{7.7}$$

i.e. two sinusoidally oscillating fields that are $\pi/2$ out of phase. Adding these fields to a static magnetic field with a zero point has the effect of moving the zero point in a circular trajectory. This is perhaps most simply imagined by considering a static potential of the form of a 3D quadrupole. Adding a bias field of size B_0 to this configuration simply shifts the quadrupole centre by a distance B_0/B'. The direction of this shift then simply rotates in time. The trajectory of the zero point describes a 'circle of death' of radius $r_{\mathrm{D}} = B_0/B'$. It is so called because atoms that approach the circle describing the locus of instantaneous zero points undergo spin-flip losses, as described in Section 7.3. However, if the applied field is rotated quickly enough, atoms with sufficiently low energy do not explore the region near the circle of death. Rather than assuming the atoms experience the instantaneous potential we can consider an effective TAP. The form of this potential is given by

$$U_{\mathrm{TAP}} = m_F g_F \mu_{\mathrm{B}} \frac{\omega_{\mathrm{TAP}}}{2\pi} \int_0^{2\pi/\omega_{\mathrm{TAP}}} \left| \vec{B}_{\mathrm{S}}(\vec{r}) + \vec{B}_{\mathrm{TAP}} \right| \, \mathrm{d}t. \tag{7.8}$$

Assuming the static potential is of the form of a 3D quadrupole this is then given explicitly by

$$U_{\mathrm{TAP}} = m_F g_F \mu_{\mathrm{B}} \frac{\omega_{\mathrm{TAP}}}{2\pi} \int_0^{2\pi/\omega_{\mathrm{TAP}}} \left| \left[B'x + B_0 \cos\left(\omega_{\mathrm{TAP}} t\right)\right] \hat{x} + \right. \\ \left. \left[B'y + B_0 \sin\left(\omega_{\mathrm{TAP}} t\right)\right] \hat{y} - 2B'z\hat{z} \right| \, \mathrm{d}t. \tag{7.9}$$

This expression can be evaluated analytically in terms of a series expansion [204]. The result is that the minimum of the potential is no longer a zero point and the shape of the potential which is yielded is much more harmonic. Thus atoms in the TAP are confined to a region in the middle of the circle of death. This transformation of the potential relies on the time-averaging criterion, which states that the frequency of oscillation must be quicker than the trap frequency, i.e.

$$\omega_{\mathrm{TAP}} > \omega_{\mathrm{Trap}}. \tag{7.10}$$

It is not clear how strict this time-averaging condition is and there has been limited work experimentally testing it [204]. Within this work we shall use the convention that the inequality is strictly greater than, although it should be borne in mind that the better this inequality is satisfied, the more appropriate the use of an effective potential is, and the less likely spin-flips are to occur.

To avoid losses from the trap we must also satisfy the adiabaticity criterion, as described in Section 7.3. As previously stated we require that the magnetic dipole of the atom remains aligned with the applied magnetic field, as this field evolves in time. For the system at hand this can be simply prescribed by requiring that the Larmor frequency is larger than the frequency of oscillation of the magnetic field. Combining this criterion with the time-averaging criterion provided in Equation 7.10 gives

$$\omega_{\mathrm{L}} > \omega_{\mathrm{TAP}} > \omega_{\mathrm{Trap}}. \tag{7.11}$$

As with the time-averaging criterion, this inequality is not absolute; for any given Larmor frequency and TAP frequency there will always be a finite probability of a diabatic transition to a different magnetic sublevel, as prescribed by the Landau-Zener formula. It is obvious that the frequency of oscillation of the TAP fields does not alter the shape of the resulting potential, thus we choose ω_{TAP} such that the above inequalities are satisfied as well as possible. To quantify the stability of the TAP that we create we now define

$\xi = \omega_{\mathrm{L}}/\omega_{\mathrm{Trap}}$ which we shall call the adiabaticity parameter. We can rewrite Equation 7.11 simply as $\xi > 1$. The larger ξ is, the better we consider the trap to be.

There is one more requirement needed in order for the trap we create to be effective: it must be deep enough. Given the rule of thumb that atoms of temperature T can be held in a trap of depth $10T$ we desire a trap depth of around 100 µK or greater. In a conventional magnetic trap the depth is trivially defined — it is the potential energy associated with taking an atom from the minimum of the trap to an untrapped region of space. The picture of an atom spilling over the side of a bowl is intuitive. The definition of depth is complicated for the case of a TAP. The conventional definition of depth still applies, but there is another route out of the trap, through a spin-flip transition. Although the time-averaging procedure has been presented as a way of circumventing the problem of a magnetic field zero, it has not been removed. Thus, any atoms that approach the instantaneous magnetic field zero will still have a very high probability of spin-flipping to an untrapped state. As previously stated, the instantaneous zero travels on the circle of death, and it is this circle which provides a new definition of trap depth — the energy change associated with taking an atom from the trap minimum to a point on the circle of death.

As shown in [69] the trap depth due to the circle of death is in fact independent of all other parameters, including the static magnetic field. This can be understood by considering the size of the TAP at the circle of death. The circle of death is the locus of all points where the net magnetic field is zero in all directions. Because we consider fields oscillating in the xy plane this is always true for the z component of the field. Since all points on the circle of death are equivalent by symmetry let us choose the case where the y component of the static field is zero, i.e. where $y = 0$. This in turn means that the x component of the static field is equal to B_0. Using Equation 7.9 the value of the time-averaged potential at this point is then given by

$$U_{\mathrm{COD}} = m_F g_F \mu_{\mathrm{B}} \frac{1}{T_{\mathrm{TAP}}} \int_0^{T_{\mathrm{TAP}}} \sqrt{\left[B_0 + B_0 \cos\left(\omega_{\mathrm{TAP}} t\right)\right]^2 + \left[B_0 \sin\left(\omega_{\mathrm{TAP}} t\right)\right]^2}\ \mathrm{d}t, \tag{7.12}$$

where $T_{\mathrm{TAP}} = 2\pi/\omega_{\mathrm{TAP}}$ is the period of the oscillating fields. Expanding the terms this then simplifies to

$$\begin{aligned} U_{\mathrm{COD}} &= m_F g_F \mu_{\mathrm{B}} \frac{\sqrt{2}B_0}{T_{\mathrm{TAP}}} \int_0^{T_{\mathrm{TAP}}} \sqrt{1+\cos\left(2\pi t/T_{\mathrm{TAP}}\right)}\ \mathrm{d}t \\ &= m_F g_F \mu_{\mathrm{B}} \frac{2B_0}{T_{\mathrm{TAP}}} \int_0^{T_{\mathrm{TAP}}} \left|\cos\left(\pi t/T_{\mathrm{TAP}}\right)\right|\ \mathrm{d}t. \end{aligned} \tag{7.13}$$

Evaluating this integral yields

$$U_{\mathrm{COD}} = m_F g_F \mu_{\mathrm{B}} \frac{2B_0}{T_{\mathrm{TAP}}} \frac{2T_{\mathrm{TAP}}}{\pi} = m_F g_F \mu_{\mathrm{B}} \frac{4B_0}{\pi}. \tag{7.14}$$

Given that the minimum of the TAP has an associated field magnitude of B_0, we can then write the depth defined by the circle of death, which we express as

$$D = m_F g_F \mu_{\mathrm{B}} \frac{4-\pi}{\pi k_{\mathrm{B}}} B_0. \tag{7.15}$$

The alternative measure of the trap depth, defined by the energy change moving the atom to an untrapped region is labelled $\tilde{D}$. This can be very easily expressed for a domain-wall based trap by considering that far away from the static trapping potential the magnetic field is given by $\sqrt{B_{\mathrm{bias}}^2 + B_0^2}$. Since the field at the time-averaged minimum is simply B_0 the depth is then given by

$$\tilde{D} = \frac{m_F g_F \mu_{\mathrm{B}}}{k_{\mathrm{B}}} \left(\sqrt{B_{\mathrm{bias}}^2 + B_0^2} - B_0\right). \tag{7.16}$$

We now have two definitions of trap depth and it is the lower of the two which is applicable. By equating D and $\tilde{D}$ we can easily determine the regimes under which they apply:

$$\begin{aligned} \frac{m_F g_F \mu_{\mathrm{B}}}{k_{\mathrm{B}}} \left(\sqrt{B_{\mathrm{bias}}^2 + B_0^2} - B_0\right) &= m_F g_F \mu_{\mathrm{B}} \frac{4-\pi}{\pi k_{\mathrm{B}}} B_0 \\ \Rightarrow B_0 &= \frac{\pi}{\sqrt{16-\pi^2}} B_{\mathrm{bias}}. \end{aligned} \tag{7.17}$$

At magnitudes of the oscillating field which are less than this the depth is prescribed by D, and for fields larger than this it is prescribed by $\tilde{D}$. The bias field applied is typically larger than the size of the oscillating fields, so it is generally the trap depth associated with the circle of death that applies.

Through the foregoing discussion we have specified the criteria for a suitable magnetic trap. We will now analyse the suitability of the TAP technique in fulfilling these criteria for the case of a domain-wall based trapping potential.

7.3.3 Nanowire-based TAPs

Example potential

All the potentials we consider in this work were calculated numerically. Whilst the static potential is well approximated by a 3D quadrupole within the trapping volume region, and analytic forms of a TAP exist for such a configuration, we note that the circle of death associated with the TAP can be larger than the region in which this approximation is appropriate. Thus numerical computation of the resulting potential provides a more accurate result and is relatively easy to implement. The static fringing fields are calculated via the analytic model described in Chapter 2 throughout.

An example of the result of the time-averaging procedure is illustrated in Figure 7.6. There is a stark change in the shape of the trapping potential.

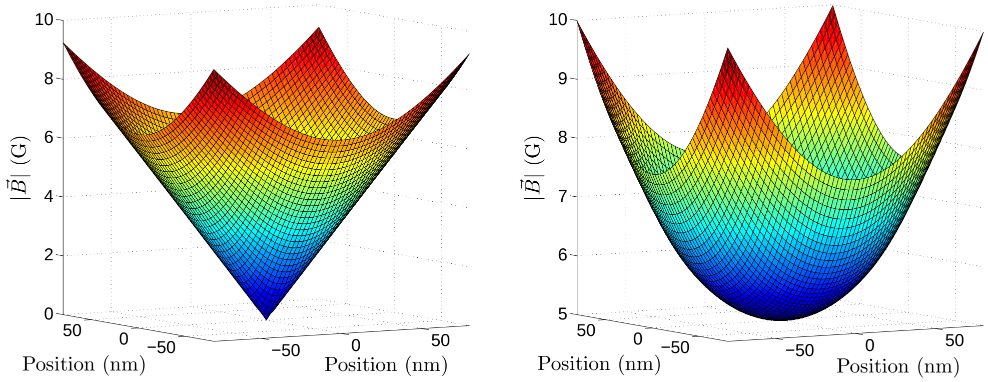

(a) Static potential.

(b) Time-averaged potential.

Figure 7.6: An example of the potential resulting from the time-averaging procedure. Here we consider the fringing fields from a nanowire of cross section 400 nm × 20 nm, biased by a field of magnitude 47.6 G to form a static trapping potential at a height of 500 nm. This is then subject to TAP fields of magnitude 5 G. The resulting TAP has a minimum Larmor frequency of $2\pi \times 7.00$ MHz, a trap frequency of $2\pi \times 326$ kHz and a depth of 93 μK. The adiabaticity parameter, ξ, has a value of around 21.

The desired effect of removing the magnetic zero has been achieved. The mimimum of the potential is now given by $m_F g_F \mu_{\mathrm{B}} B_0/\hbar$. We also note that the shape of the potential is now much more harmonic, rather than linear as for a 3D quadrupole. Both of these things result in a much more appropriate trapping potential – there is much less chance of atoms undergoing spin-flip transitions and being lost. The parameters chosen for Figure 7.6 are those which give a particularly favourable trapping geometry, however we will discuss later the fact that these parameters may present a technically demanding regime to work in.

Tuning the potential

Until now we have mainly discussed the requirements and restrictions associated with the TAP scheme, however there are also a number of variables at our disposal to try and produce a favourable trapping potential. These variables, and their effects on the resulting trapping potential, will now be qualitatively discussed.

As previously stated, the size of the oscillating magnetic field applied has a strong effect on the character of the trap. Increasing the field size produces a proportional increase in the radius of the circle of death (assuming we have a 3D quadrupole static field). The trapping potential becomes 'smeared' by larger fields, resulting in a decrease in the trap frequency. At the same time, the Larmor frequency also increases proportionally. As we will see later, the combination of these two effects leads to an overall increase in the value of ξ. The final effect of increasing the amplitude of the oscillating magnetic field is to increase the trap depth, as per Equations 7.15 and 7.16.

The other methods of tuning the TAP all rely on the modification of the static fields. We already know that for small B_0 such a modification does not have an effect on the trap depth, which depends only on B_0. It also does not change the minimum Larmor frequency, which is also defined by B_0. Thus, modifying the static fields only changes the trap frequency and hence the adiabaticity of the trap, described by ξ.

The height at which the trap is created above a domain wall depends on the size of the bias field in the z direction (recall this is distinct from the oscillating bias fields used to perform the time averaging procedure). A larger bias field produces a smaller trap height, which in turn produces a tighter static trapping potential – the magnetic field gradient, B', becomes larger as one approaches the domain wall. In terms of the TAP, this has the effect of reducing the radius of the circle of death (recall $r_\mathrm{D} = B_0/B'$) which in turn results in a higher trap frequency. One caveat to this is that for sufficiently small TAP fields the region of the trapping potential which is well described as harmonic becomes smaller as the TAP tends to the shape of the original static field.

The trap frequency can also be tuned by changing the properties of the nanowire itself. By increasing the cross section of the nanowire the effective charge which we prescribe to it increases, and hence the size and gradient of the resultant fringing fields increase. A further subtle effect is observed when considering the different types of domain wall. We see that a larger trap frequency is achieved when using a transverse-type domain wall over a vortex-type domain wall, for the same effective magnetic charge [69]. This in turn implies that a more adiabatic trap is formed when using a vortex-type domain wall. This can be understood intuitively by the fact that the magnetisation structure of vortex-type domain walls generally has a larger characteristic size (cf. e.g. Figure 2.1), so the magnetic field source is more extended. This results in smaller magnetic fringing fields and gradients, and hence a smaller trap frequency.

TAP analysis

Given the discussion of the ways in which we can adjust the various parameters of the TAP, we shall now consider quantitative analysis of the traps produced. Whilst we know how best to setup the TAP, specific values of the figures of merit are required to judge what region of parameter space we are happy to work within, and just as importantly, whether this is compatible with a technically feasible setup.

The TAP above a nanowire of cross section 400 nm × 20 nm was calculated using the analytic form of the fringing fields (cf. Section 2) for a range of values of trap height and B_0. Given how well we can approximate the static fields by a 3D quadrupole, the trap height can be expressed equivalently by a static field gradient, which is a more universal measure of the tightness of the static potential. Given the symmetry of the situation, the gradients in the x and y directions are both half that in the z direction, and we choose the former as the measure of the static field gradient, and label it $B_{\mathrm{S}}'^{xy}$. The trap frequency was calculated by fitting the shape of the resulting potential to a purely quadratic function over a region defined by a given potential depth. The Larmor frequency and trap depth are also calculated as previously described, and hence the value of ξ as well. The results are shown in Figure 7.7.

The data shown display all the trends that we have qualitatively discussed. Most importantly we find that we achieve a deep and adiabatic trap for larger TAP fields and for less tight static field gradients. Comparing this with the data shown in Figure 7.7(a) we see that this corresponds to decreasing the resulting trap frequency. That is the time-averaging technique which we hope to apply to nanomagnetic field sources works best when the field gradients are lower. This is an unfortunate result, as the technique is thus poorly suited for working with small scale field sources for which the resulting field gradients are characteristically high. In order to achieve a stable trap we are forced to move further away from the domain wall.

As an example, let us suppose we restrict the trap to having a value of ξ of 100 or greater, giving an order of magnitude between ω_{L} and ω_{TAP}, and between ω_{TAP} and ω_{Trap}. For the range of parameters considered we must then choose a value of B_0 of greater than 2 G, and a static field gradient of less than 15 G/µm, which corresponds to trap heights of around 1 µm or more. Using a value of 2 G for B_0 limits the trap height to being greater than around 1.5 µm and provides a trap depth of around 40 µK. Increasing the size of B_0 to 5 G, while maintaining $\xi = 100$ gives a trap depth of around 100 µK.

The range of parameters which we have chosen to display here represent the kind of regime which we wish to work in, i.e. high adiabaticity, high frequency traps. We find that this regime is reached for larger and more quickly oscillating applied fields. However, technical limitations are likely to make the production of such fields extremely challenging. Creating fields of moderate magnitude at high frequencies is very difficult. Since the inductive reactance of any coils used is given by $X = 2\pi f L$, where f is the frequency of oscillation and L is the inductance, there is a clear trade-off. A larger value of inductance corresponds to a larger field produced, however this increases the reactance and makes it difficult to drive at very high frequencies. Previous realisations of TAPs typically work at oscillation frequencies of up to around

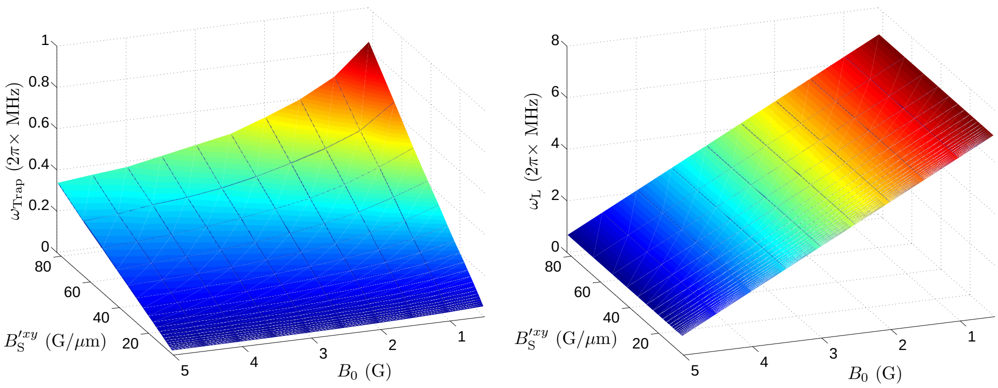

(a) Trap frequency

(b) Larmor frequency

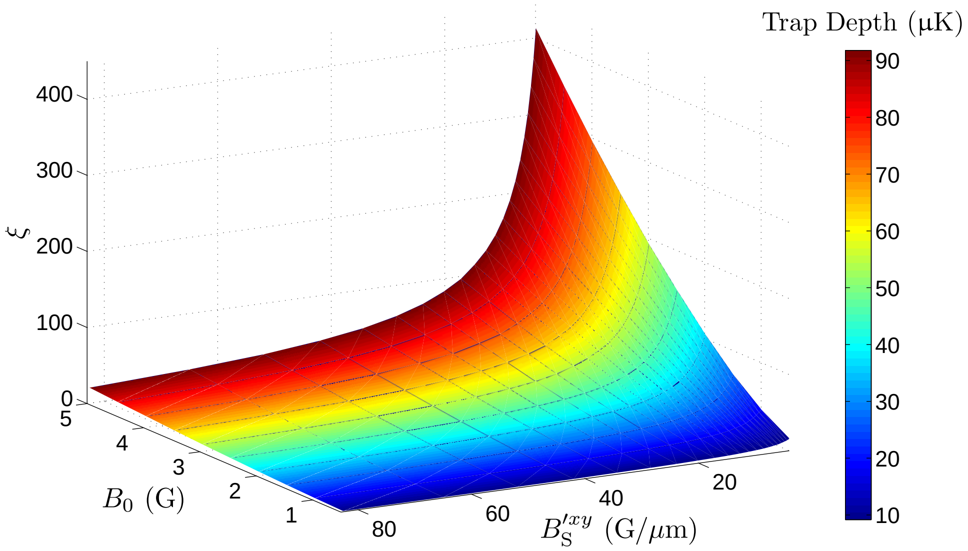

(c) Adiabaticity

Figure 7.7: Trap characteristics of a time-averaged potential formed above a nanomagnetic domain in a wire of cross section 400 nm × 20 nm, for a range of parameters. B_0 is the magnitude of the applied TAP fields. $B_{\mathrm{S}}^{\prime xy}$ is the gradient of the static magnetic field in the x and y directions. The static fields are calculated analytically. Note that in (c) the shading represents the resulting trap depth.

$2\pi \times 10$ kHz, and require the use of custom-built electronic equipment based upon a resonant circuit which sacrifices tunability in order to produce the required fields [205, 206, 207]. Other experiments have used magnetic fields which are slightly faster and significantly larger, for example [208] reports $2\pi \times 40$ kHz fields of around 1 kG. Whilst this is considerably more field than we require, it is also at a significantly lower frequency than desired — these two factors combined suggest that whilst producing the desired high frequency fields is extremely challenging, it at least seems feasible.

7.4 Conclusions

In this chapter we have presented a proposed scheme for realising a tight mobile atom trap based on the fringing fields from a nanomagnetic domain wall. Because of the intrinsically high trap frequency, and the presence of a zero in the magnetic field, spin-flip losses will be very problematic.

A number of schemes to circumvent spin-flip losses are considered, and we find most are unsuitable, for both fundamental and technical reasons. In particular, RF-dressed potentials are shown to be unfeasible on the length-scales characteristic to the traps we propose. In contrast, the TAP scheme presents a theoretically feasible method of circumventing the zero point of a magnetic trap. A judicious choice of parameters must be made in order to ensure that the potential created is both adiabatic and of sufficient depth. The parameters which guarantee this are seen to compromise the trap frequency achieved. We also note that there are significant technical challenges associated with producing the necessary fields, which restricts our choice of parameters further. In conclusion the conventional TAP scheme seems to be extremely difficult to implement for exceptionally tight traps.

Whilst the regime presented by nanomagnetic devices is a fascinating and exciting one due to the enormous field gradients created, it is also difficult to work effectively in this regime using conventional techniques. In the following chapter we will introduce a novel technique for producing stable traps which turns the large field gradients from a burden to an advantage and we hope it will provide a method for producing some of the tightest atom traps in the world.

Chapter 8

Piezoelectrically-Actuated Time-Averaged Potentials

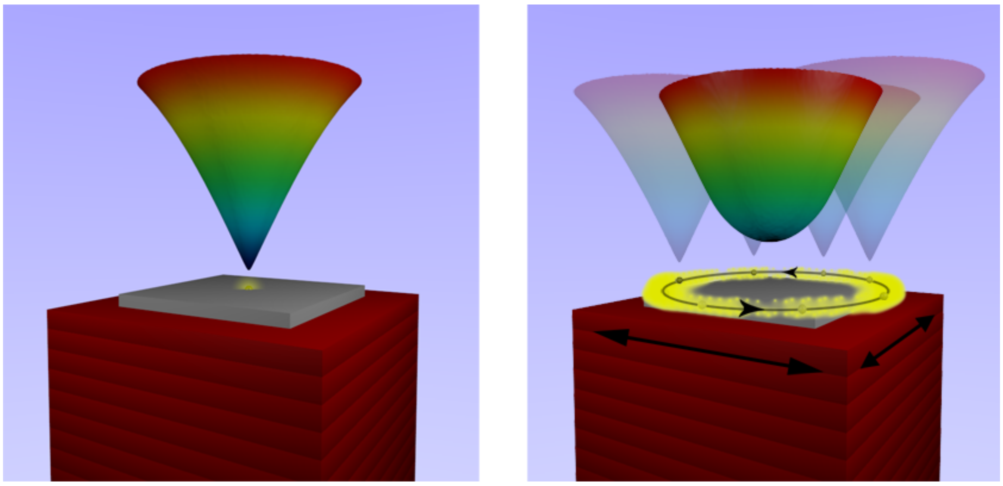

The circular oscillation of an atom chip by a piezoelectric actuator. The zero point of the static potential is removed by the time-averaging process.

8.1 Theory

8.1.1 Conventional schemes

In Chapter 7 a number of different schemes were explored in efforts to try and transform the potential associated with biased domain wall fringing fields into a harmonic and adiabatic trap by removing the magnetic field zero. There were problems with each of the methods considered, all of them deriving from the exceptionally small lengthscales that characterise the trap. The different methods are summarised in Table 8.1:

Table 8.1: A summary of the different schemes aimed at circumventing spin-flips to produce an adiabatic trap.

Scheme	**Example**	**Problem**
Ioffe-type trap	[187]	Requires addition of current carrying devices on the scale of the nanowires, at every trap site — practically infeasible.
Blue-detuned plug	[209]	Requires addition of a laser beam at every site, focussed down to ∼10 nm — not possible due to diffraction limit.
RF-dressing	[210]	RF-dressing a 3D quadrupole leaves at least one zero point. Gravity has a negligible effect on the scale of our trap so will not keep atoms away from the zero.
Time-averaged potential (TAP)	[203]	Best option. Technically challenging to produce fields of several Gauss at very high frequency (∼100 kHz). Adiabatic regime is difficult to achieve.

The best option for removing the zero point of the static potential and producing a stable and harmonic trap is to use time-averaging techniques. However, this is difficult for a number of reasons. It is fundamentally hard to ensure that we are in an adiabatic regime. More specifically it is difficult to ensure that the inequalities in Equation 7.11 are satisfied:

$$\omega_{\mathrm{L}} > \omega_{\mathrm{TAP}} > \omega_{\mathrm{Trap}}. \tag{8.1}$$

As shown in Figure 7.7 the most favourable parameters are provided by working with higher TAP fields and at higher frequencies. This leads to the second problem, which is that it is technically challenging to produce the necessary magnetic fields.

The difficulties associated with applying a TAP scheme for our traps derive from the inherently small scale of the magnetic field sources we use, which produces extremely high field gradients and hence extremely high trap frequencies. As described in Section 7.3.2, applying oscillating fields moves the zero of field around in a 'circle of death'. The larger this circle is, the deeper and more adiabatic the trap becomes. However, a larger circle of death requires larger fields, and the circle becomes smaller as the static field gradients become higher. The result is that we are limited by the inherently tight static potential.

8.1.2 The PATAP scheme

We will now present an alternative scheme that solves the problem of spin-flip losses in our traps and circumvents the difficulties associated with TAPs. This is achieved by transforming the extremely high field gradients from a hindrance to a help.

The scheme is a direct analogue to a TAP such as those given in [69, 203, 211]; we move the magnetic field zero in a 'circle of death', but instead of achieving this via the application of additional magnetic fields, we will consider physically moving the source of the static fields. To produce an analogue of a conventional TAP scheme the position of the static field source, (x, y), must be described by

$$(x(t), y(t)) = x_0 \cos\left(\omega_{\mathrm{TAP}} t\right) \hat{x} + y_0 \sin\left(\omega_{\mathrm{TAP}} t\right) \hat{y}. \tag{8.2}$$

x_0 and y_0 are the amplitudes of motion in the x and y directions respectively, which can in principle be different but from hereon we assume to be the same and equal to r_{D}. The result is almost identical to that of a conventional TAP scheme and the same requirements exist, i.e. we require the trap to be adiabatic and within the time-averaging regime, as per Equation 7.11, and we require the trap to be deep enough to hold ultracold atoms. There is one subtle but significant difference: the movement of the zero point does not require the use of additional fields and hence does not depend on the gradient of the static fields. The result is that this alternative scheme is ideally suited for working with very high field gradients. We will discuss later the practical realisation of this through the use of piezoelectric devices. Hence we shall label this new scheme as a piezoelectrically-actuated TAP (PATAP) from hereon.

8.1.3 Fundamental advantages

The motion of the 'circle of death' is now parametrised by r_{D} — the 'radius of death', this is the analogue to B_0 in a conventional TAP scheme (cf. Equation 7.7). Let us assume that the region of the static fields we consider is purely linear (as seen in Figure 7.1 this is a very good approximation) with gradient $B_{\mathrm{S}}'^{xy}$ in the x and y directions. In a conventional TAP scheme the displacement of the zero point, d, is given by $d = B_0/B_{\mathrm{S}}'^{xy}$. Thus we achieve a larger d for smaller field gradients. Working with smaller gradients leads to less tight traps, but the resulting adiabaticity and trap depth suffer as we move to tighter traps. In contrast, the PATAP scheme has r_{D} independent of the static field. The result is that for a given r_{D} the corresponding change in field is larger for larger field gradients, giving a deeper and more adiabatic trap. This is best illustrated by analysing the dependence of ξ on the relevant trap parameters for a PATAP. Recall we define $\xi = \omega_{\mathrm{L}}/\omega_{\mathrm{Trap}}$ with ω_{L} being the minimum Larmor frequency and ω_{Trap} the trap frequency. We numerically calculate the TAPs in a manner analogous to Section 7.3.2. The result, along with that for the case of a conventional TAP scheme (Figure 7.7), is shown in Figure 8.1. The ranges of B_0 and r_{D} were chosen to roughly represent technically feasible values.

The differences between the two schemes are clearly shown. Firstly, the contrast between the dependences on the gradient of the static field is stark. As discussed above, the conventional TAP scheme produces a more adiabatic trap when the field gradients are low, whereas the opposite is true for the PATAP scheme. Even for fairly low field gradients the value of ξ is significantly greater for the PATAP scheme for almost all r_{D}. A very rapid drop in ξ is observed for the TAP scheme around $B_{\mathrm{S}}'^{xy} = 10$ G/μm where the efficacy of the trap greatly reduces.

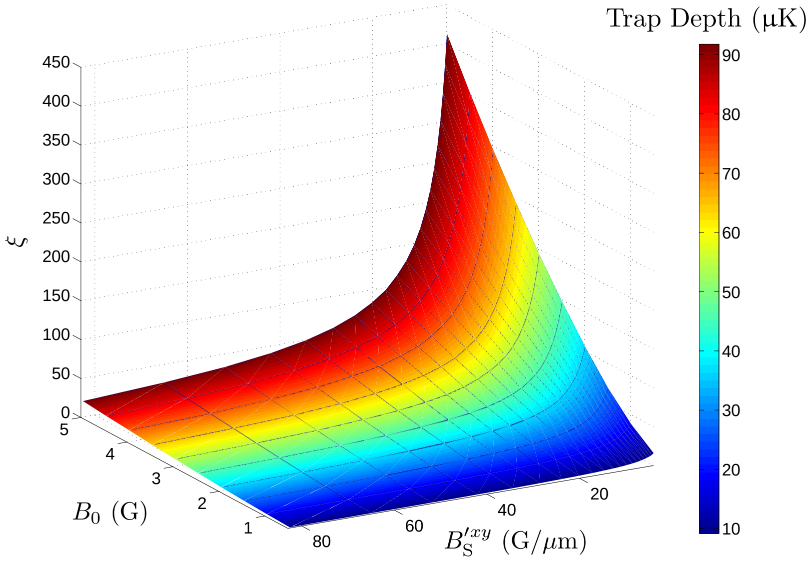

(a) Conventional TAP

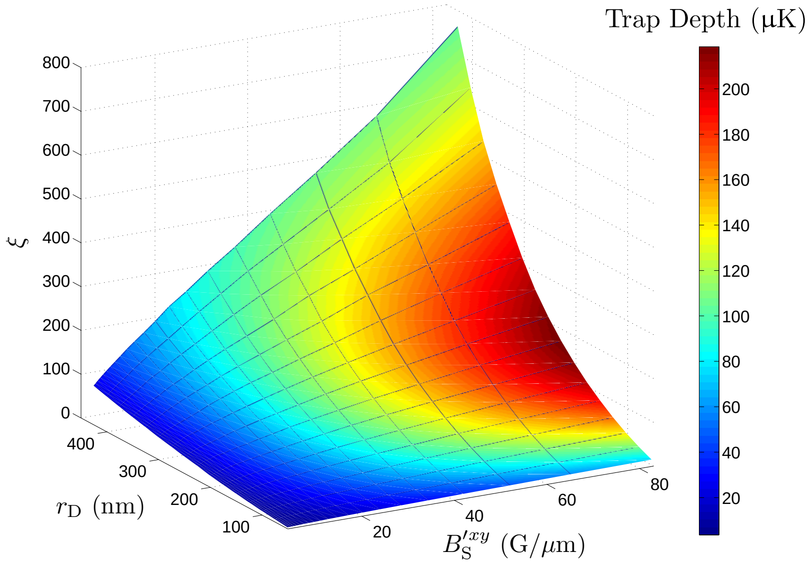

(b) Piezoelectrically-actuated TAP

Figure 8.1: A comparison of the efficacy of the TAP and PATAP schemes. Figure (a) corresponds to a conventional TAP scheme realised through the addition of oscillating fields. B_0 is the magnitude of the applied fields, $B_S'^{xy}$ is the gradient of the static magnetic field in the x and y directions and ξ is the adiabaticity parameter equal to $\omega_L/\omega_{\text{Trap}}$. Figure (b) corresponds to a piezoelectrically-actuated TAP scheme. r_D is the amplitude of movement. N.B. the $B_S'^{xy}$ axis is reversed between (a) and (b).

There is also a very different dependence of the trap depth. We see that the trap depth increases for higher magnetic field gradients. As previously discussed this is because a given physical oscillation corresponds to a larger field change for higher values of $B_{\mathrm{S}}'^{xy}$, thus the field at the 'circle of death' is higher. For the TAP scheme the depth does not depend on the static field gradient, only on the magnitude of the oscillating fields [69] (cf. Section 7.3.2). In contrast there is a more complicated dependence for the PATAP scheme; the trap depth depends on both the amplitude of oscillation and the static field gradient. We also see, however, that the dependence on r_{D} is not monotonic. There is an optimum value of r_{D} above which the trap decreases again[1]. This behaviour is due to the fact that the static field has a finite size over which it forms a trapping potential. As r_{D} becomes comparable to the size of the static potential there is a flattening out of the time-averaged potential which leads to a reduction in depth. This regime will be discussed further in Section 8.3 when we consider more complex trapping geometries. We also note that the trap depth achievable is considerably higher for a given static field gradient. For very tight static potentials a conventional TAP scheme requires rather large additional fields in order to produce a good trap depth, whereas the PATAP scheme needs only very small physical oscillation for the same depth.

In order to achieve an effective PATAP we must ensure that the inequalities of Equation 7.11 are fulfilled. Whilst ξ gives an indicator of how feasible this is, it does not indicate an appropriate oscillation frequency. In order to find this we consider Figure 8.2 which shows both the trap frequency, ω_{Trap} and the Larmor frequency, ω_{L}, as calculated for the parameters given in Figure 8.1(b).

8.1.4 Technical advantages

We have discussed the fundamental benefits of the PATAP scheme over conventional TAPs, but there are further advantages conferred by this change

---

[1] This is in fact also true for the conventional TAP scheme; for very large B_0 the trap depth is no longer determined by atoms reaching the circle of death, but by atoms reaching a non-trapping region, determined by the size of the bias field (cf. Figure 7.1) — see [69] for details.

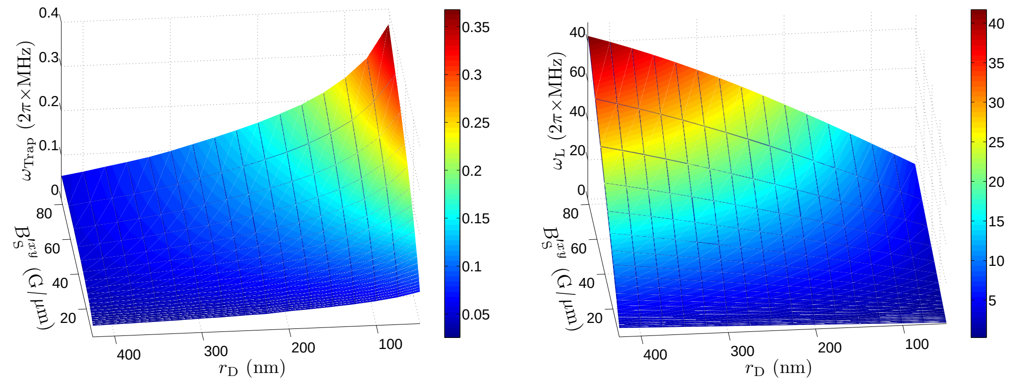

(a) Trap Frequency

(b) Larmor Frequency

Figure 8.2: The trap frequency and minimum Larmor frequency for a trapping potential created via a PATAP scheme. The oscillation frequency of the actuator must be chosen to be between these two frequencies in order to achieve an adiabatic trap.

of methodology. We will now consider the details of how we achieve the required motion, and how this could be a technically easier route to achieving a time-averaged potential.

To produce PATAPs we need to move the source of the static magnetic field in a ‘circle of death’. From Figure 8.1 we note that the amplitude of this movement needs to be around 200–300 nm for the best traps. This motion can be achieved through the use of piezoelectric actuators. A schematic of the setup is shown in Figure 8.3. The schematic shows two separate shear

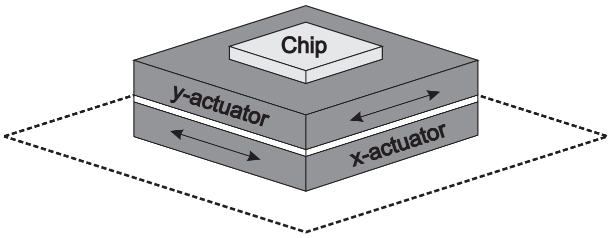

Figure 8.3: A schematic of the setup required to realise a PATAP. A chip which hosts a source of magnetic field is mounted on top of a piezoelectric actuator operating in shear mode. This in turn is mounted on top of another orthogonally orientated shear actuator.

actuators providing independent motion in x and y. The axes are driven by two separate voltages which follow the form

$$V_x(t) = V_0^x \cos\left(\omega_{\mathrm{TAP}} t\right), \tag{8.3}$$

$$V_y(t) = V_0^y \sin\left(\omega_{\mathrm{TAP}} t\right), \tag{8.4}$$

in direct analogy to Equation 7.7. We shall limit our study to the case of $V_0^x = V_0^y = V_0$. This configuration of actuators is commercially available in a single device [212]. Because one actuator is mounted on top of the other there is no strain when one moves in a direction orthogonal to the other. An alternative setup is to use two separate piezo devices to push against a mounted chip. This has the benefit that one can use stack actuators operating in longitudinal (rather than shear) mode which can typically provide higher displacements and frequencies of motion [212]. However in this scheme the motion of the actuators is not independent; the motion of one will introduce shear strains in the other. The configuration illustrated avoids this at the (small) expense of frequency and displacement.

The methodology that we have outlined to achieve the desired movement has a number of advantages compared to a conventional TAP scheme. To achieve a conventional TAP one must produce magnetic fields of several gauss which oscillate at several hundreds of kHz. This is conventionally achieved through the use of coils of current carrying wire. This is a difficult task in itself as the high inductance of such coils means the application of fairly large voltages is required to achieve the desired currents. Amplifiers which can operate under these conditions are either prohibitively expensive, or more often, built specifically for the task.

In contrast, piezoelectric actuators are almost purely capacitive devices that draw very little current. Instead they rely on an applied voltage to move them. Because of their low inductance they can have resonant frequencies of up to around $2\pi \times 300$ kHz. If we consider an actuator with a capacitance of 1 nF (typical for this type of device) which oscillates with an amplitude of 200 nm, the required voltage to move it this distance is 50 V. The corresponding average current drawn by an actuator of capacitance C operating at a frequency f is given by [213]

$$\langle I \rangle = 2fCV_0. \tag{8.5}$$

For the aforementioned values this yields a required current of 30 mA. Providing this combination of voltage and current at the required frequency is a much easier task than the requirements for a conventional TAP scheme as there are many commercially available piezoelectric drivers which are suitable, e.g. [214].

The corresponding power required for such a device is then around 1.5 W. An estimate of the power dissipated into a chip which weighs 0.1 mg suggests that we would expect a corresponding temperature rise of around 5 K/s. Given that both the operation duration and duty cycle of such a device are likely to be small we expect that heating would not be problematic, especially with good heatsinking in place. By contrast, supplying sufficient current to produce the fields necessary for a TAP will most likely use 100s of watts of power which would need careful management in order to avoid problems of overheating.

Other practical benefits of using a PATAP scheme include the fact that the devices are both small and UHV compatible, meaning that they can be easily incorporated into an ultracold atom setup. It is in fact possible to amalgamate two technologies into a single device by using the PZT (lead zirconium titanate) material of a piezoelectric actuator as the substrate for lithographic patterning [215]. This adds the benefit of removing the load associated with an atom chip from the piezoelectric device, which will increase the resonant frequency. It also circumvents the need to fix the magnetic field source onto the actuator. The bond used to achieve this is naturally a weak point with higher compressibility than the PZT crystal itself, leading to a damping of the desired oscillation. No such effect would arise for a lithographically patterned device. Further study may be required before attempting such a hybrid device though as departures from ideal shear motion such as bending of the actuator would necessarily bend the patterned material. One would have to ensure that this did not have a detrimental effect either to the constitution of the lithographically patterned material or to the magnetic fields produced — it has been shown that applying strain to a nanomagnetic domain can have a significant effect on its magnetisation structure [54].

We conclude, therefore, that the presented PATAP scheme provides numerous fundamental and technical advantages over conventional TAPs, particularly in the regime of small-scale traps with high associated frequencies. To demonstrate the feasibility of such a device we must now verify the suitability of the motion of the piezoelectric actuators.

8.2 Investigating actuator motion

We now describe two methods which were used to analyse the motion of a selection of piezoelectric actuators. We shall show that the movement observed suggests that we can actuate an atom chip at suitable frequencies over sufficient distance. However we also find that further work is required to verify the fidelity of circular motion.

8.2.1 Michelson interferometer

Setup

Initial studies of the motion of the actuators used a Michelson interferometer. A schematic of the experimental setup is shown in Figure 8.4. Although

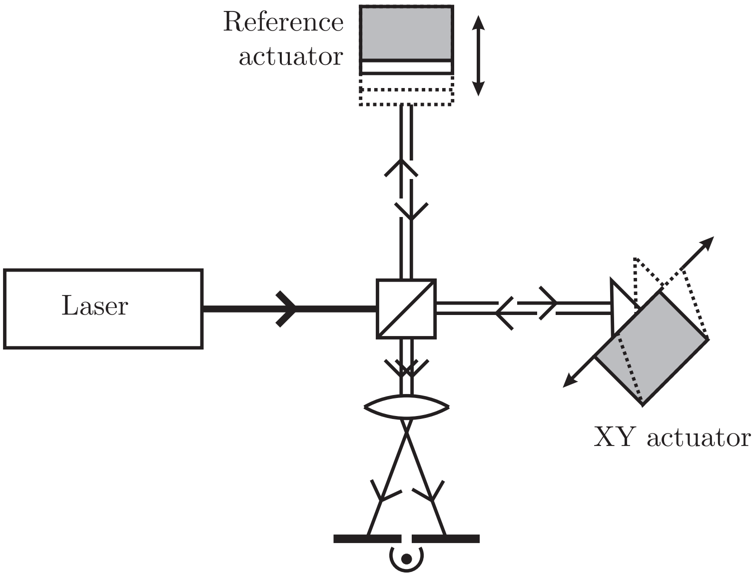

Figure 8.4: Schematic of the interformeter setup used to analyse the motion of the piezoelectric actuators. A laser beam is passed through a 50:50 beam splitter. One arm is then reflected from a silvered prism on a shear actuator. The other is reflected from a mirror on a reference actuator. The beams are then recombined and passed to an AC photodiode.

such optical interferometery is a standard technique there are a couple of subtleties that must be considered. Firstly, the shear motion of the actuator does not induce a path length change in a reflected laser beam. Thus we must translate the shear movement into movement along the beam direction. This is achieved by affixing a prism onto the surface of the actuator (cf. Figure 8.4). The prism is made from a diagonally halved 1 mm × 1 mm × 1 mm cube, with a silvered hypoteneuse (Tower Optical MPCH-1.0 [216]), and is glued using Epotek H77 epoxy, which was chosen for its low compressibility, high thermal conductivity, low electrical conductivity and suitability for use in an ultra-high vacuum [217]. Care was taken to ensure that the axis of the prism's hypoteneuse was parallel to one of the actuator's axes. Misalignment would mean that orthogonal actuation would also produce a small path difference change. The silvered surface of the prism is then orientated such that the laser beam is normally incident. The result is that a shear displacement of d causes a path difference change of $\Delta s = \sqrt{2}d$. In practice, two such prisms are used to allow for analysis of motion along both axes.

It is also important to note that the displacement of the device is typically less than the wavelength of the light we are observing (780 nm). For a path difference change of Δs the corresponding phase difference is $\delta\phi = 2\pi\Delta s/\lambda$. If we consider a laser beam of initial intensity $I \propto E_0^2/2$, with the corresponding electric field given by $E_0 \sin(\omega t + \Phi)$, the field at the photodiode is given by

$$E_{\mathrm{PD}} = E_0/2\left[\sin(\omega t + \Phi + \phi_1) + \sin(\omega t + \Phi + \phi_2)\right], \tag{8.6}$$

where ϕ_1 and ϕ_2 are the phases in the two arms. Defining $\delta\phi = \phi_1 - \phi_2$ and setting $\Phi = 0$ we have an observed intensity of

$$\begin{aligned} I_{\mathrm{PD}}(t) &\propto E_0^2/4\left[\sin(\omega t) + \sin(\omega t + \delta\phi)\right]^2 & (8.7)\\ &= E_0^2 \cos^2(\delta\phi/2)\sin^2(\omega t + \delta\phi/2). & (8.8)\end{aligned}$$

Removing the time dependence by taking the average (ω is much larger than the actuator oscillation frequency) gives

$$I_{\mathrm{PD}} \propto E_0^2/2\cos^2(\delta\phi/2). \tag{8.9}$$

From our definition of $\delta\phi$ this corresponds to a periodicity of λ. Displacements of a few 100s of nanometres thus correspond to a phase difference change of less than 2π. In order to deduce the movement of the actuator we use a reference actuator in the other arm of the interferometer which moves slowly compared to the actuator we are investigating, but also moves significantly further.

Analysis

To describe how the movement of the shear actuator is extracted from the resulting signal we consider the time dependence of the observed intensity. From Equation 8.9 we know that the intensity is of the form $\cos^2(x)$, where x is the position of the mirror. However, x is time dependent. The reference actuator is driven by a triangular waveform and the shear actuator by a sinusoidal waveform. The observed signal is thus of the form

$$I_{\mathrm{PD}}(t) \propto \cos^2\left[t + A\sin(\omega t)\right] = 1/2\cos\left[2t + 2A\sin(\omega t)\right] + 1/2, \tag{8.10}$$

where A is typically less than 1 (the amplitude of movement of the shear actuator is less than that of the reference acutator) and ω is significantly greater than 1 (the movement of the shear actuator is significantly faster). We choose to centre the signal around 0, which yields a signal of the form

$$I_{\mathrm{PD}}(t) \propto \sin\left[t + A\sin(\omega t)\right]. \tag{8.11}$$

Throughout the preceding discussion we have deliberately ignored the precise prefactors that quantitatively describe the shape of the signal. This is because it is an entirely self-referenced process; the total amplitude of the signal relates to a known displacement, against which we then reference the smaller modulation. For the same reason we shall not quantitatively label any of the signals illustrated. We shall now describe how the motion of the shear actuator is inferred from the photodiode signal. The process is illustrated with experimental data in Figure 8.5.

The photodiode signal and the shear actuator drive voltage are shown in (Figure 8.5(a)). The signal is normalised and centred around 0, and the inverse sine is taken (Figure 8.5(b)). This yields a signal of the form $t + A\sin(\omega t)$. The envelope of this signal is then found (Figure 8.5(c)), from which it is possible to fit a straight line. Note that near the extrema of the slow modulation there is some deviation from a purely linear behaviour.

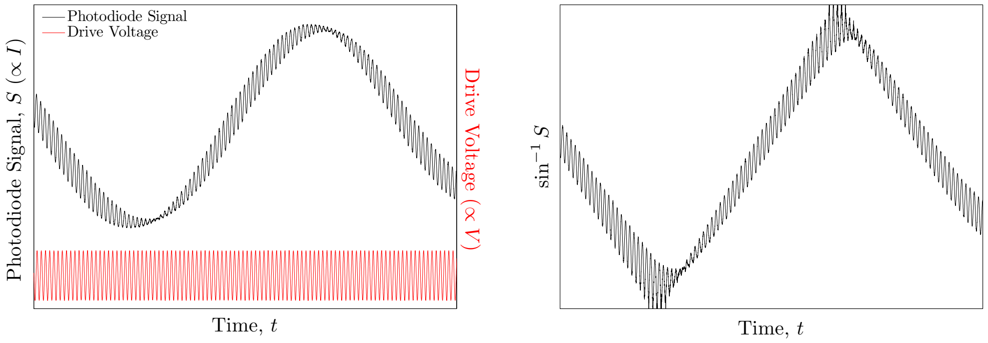

(a) Photodiode signal and the driving voltage for the shear actuator.

(b) Inverse sine of the (normalised) photodiode signal.

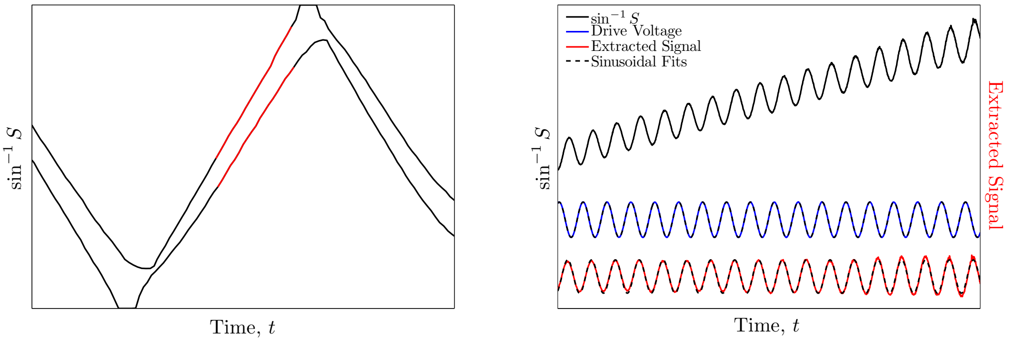

(c) Envelope of the signal in (b). The red lines indicate the region which we extract to fit straight lines.

(d) The signal from (b) in the red region given by (c) and corresponding driving voltage.

Figure 8.5: Illustration of the numerical procedure for determining the motion of the shear actuator. The amplitude of the slow modulation is measured, then this modulation is removed to determine the amplitude of the fast modulation.

To preserve the accuracy of the method, a region where good linearity is observed is extracted (red region). Dividing by the gradient of this line provides a signal of the form $A \sin(\omega t)$. The amplitude of movement of the shear actuator is given by

$$A_{\text{piezo}} = \frac{A\lambda}{2\sqrt{2}}. \tag{8.12}$$

Note that the amplitude of the low frequency signal oscillation corresponds to a path difference change of $\lambda/2$, we must divide by 2 to give the motion of the prism, rather than the path difference change, and we must multiply by $\sqrt{2}$ in order to give the movement of the actuator, rather than the prism.

Although the explanation of this procedure is quite involved, it is a very quick process to automate once the program to analyse the data has been optimised. Care must be taken when continuously taking data to ensure a small duty cycle in order to avoid overheating of the (fast) actuator.

The simultaneous recording of the driving signal permits an independent check of the amplitude and frequency of the driving voltage. It also allows measurement of the phase of the response of the actuator. This is achieved by fitting sine waves to both the driving voltage and photodiode signal. One can assign an absolute phase to both of these fits. Comparing the two gives the relative phase.

Results

Using the process described the frequency response of a shear actuator was obtained and is shown in Figure 8.6. The shear actuator used to acquire the data is the P-112.01 model x-y shear actuator produced by Physik Instrumente [212]. From hereon any quoted frequencies are linear unless otherwise stated.

The frequency dependence observed is a complicated one but there are clearly regions where there is a much larger displacement of the actuator. We note in general that the amplitude of oscillation decreases as the frequency increases. The predicted resonant frequency of the actuator is quoted as 230 kHz, and given the data shown in Figure 8.6 we can deduce that the loading of the actuator by the prisms (objects of comparable weight to an atom chip) does not dramatically reduce the resonant frequency. We also note that the measured amplitude of oscillation is in agreement with that suggested by the quoted voltage response. A displacement of 1 µm is predicted for an applied voltage of 150 V. Thus one would expect for a drive voltage of amplitude 25 V that one would observe oscillations of amplitude around 170 nm. This is indeed what we observe at resonant peaks within Figure 8.6.

Another notable point is that the frequency response is markedly different for the different axes of motion. Because of this it is important to choose a frequency at which both of the axes respond strongly. Applying appropriate drive voltages to the two axes will then allow for circular motion to be

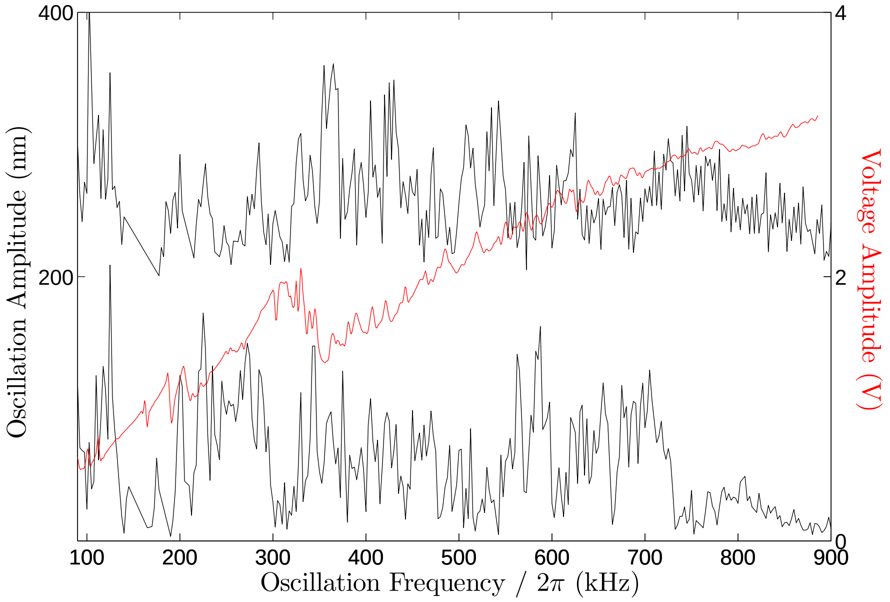

Figure 8.6: Frequency response of the oscillation of a shear actuator (black lines), examined by optical interferometry, for both axes of movement. The different axes are offset by 200 nm for clarity. The amplitude of the voltage applied to the actuator is 25 V. The red line shows the signal obtained via impedance spectroscopy.

achieved. Any asymmetry in the movement of the axes will simply modify the motion of the device from a circle to an oval, and the shape of the resulting potential to being an ellipsoid which is asymmetric in x and y. Note that in such a case the depth of the trap will be determined by the smaller of the two amplitudes of movement.

We also carried out some basic impedance spectroscopy (see e.g. [213, 218, 219, 220]) of the actuator to try and provide an alternative measurement of the frequency response. Performing optical interferometry on the actuator is logistically very difficult within a UHV environment and could jeopardise the utility of the device by requiring the fixing of a prism to the actuator. Impedance spectroscopy is a purely electrical measure of the frequency response of the actuator which does not perturb the device or require any significant additional equipment. The procedure we used was very simple — the voltage drop across a 1 Ω resistor placed in parallel with the actuator is measured, corresponding to the current drawn. Theory predicts that mechanical resonances should correspond to frequencies where the current drawn is lowest [213]. Example data are shown in Figure 8.6. As can be seen, there is not a clear cut correlation between the displacement inferred by the optical interferometry and the impedance spectrum, however there is a large feature in the latter around 350 kHz where we do observe the device to undergo large amplitude oscillations. We anticipate that further development of the impedance spectroscopy technique will provide a more detailed and clear indication of the device's frequency response.

The picture of the frequency response shown in Figure 8.6 shows a very complicated spectrum from which we must choose a frequency to work at. Analysis of a region where we observe large oscillations reveals a greater degree of smoothness — around a frequency of 360 kHz there is a region of almost 20 kHz width within which the amplitude of oscillation is greater than three quarters of the maximum value. The maximum possible movement of the actuator was also examined by applying a driving voltage of amplitude 125 V (the maximum possible with our combination of function generator and amplifier). Whilst quantitative analysis of the displacement is difficult using the method described, we observe peak-to-peak displacements that are significantly larger than $\lambda/2\sqrt{2}$

The dependence of the oscillation amplitude on the amplitude of the drive signal was also analysed. This was done away from a resonance to ensure small displacements so that the analysis method described could still be applied. We observe that the amplitude of movement varies almost linearly with the size of the voltage used to drive the actuator. There is a small negative deviation from linear for large drive voltages. Fitting the data with a quadratic function yields a reduced χ^2 of 1.8.

Another feature of the actuator motion that was examined was the phase relative to the driving voltage. This is important as the realisation of circular motion requires there to be a constant phase of $\pi/2$ between the motion of the individual axes. The phase relative to the driving was measured across a range of frequencies for both axes. From this the relative phase between the two axes was inferred (simultaneous independent driving of the two axes was not possible as this requires a second amplifier). Unfortunately, the data obtained using this method were not useful — no obvious trends within the data could be observed. This was also the case when focussing on a resonant feature of the spectrum. This suggests the presence of an unexpected and fluctuating delay within the experimental procedure. Further investigation could be carried out to determine the cause of this behaviour, but we shall see later that an alternative method provides a better measure of the phase.

In the analysis considered so far we have tacitly assumed a fundamental feature of the motion of the device: applying a voltage to drive motion in the x direction does not produce movement in the y direction, and vice versa. To test whether this was indeed the case we simply examined the movement of the prism orientated orthogonally to the axis being driven. The result was a rather suprising one. We found that there was a significant signal observed on the 'wrong' axis, of comparable magnitude to that observed for the correct axis.

Clearly this behaviour is not expected, however there are a couple of possible reasons as to why a signal would be produced in such a manner. The first of these is simple misalignment — if the reflective surface of the prism is not perfectly orthogonal to the direction of the beam then movement along the 'wrong' direction will also produce a change in the path difference. However, one would expect that even if such misalignment existed the corresponding signal would be small. Thus this is unlikely to account for all of the signal we see.

Another mechanism for producing the unexpected signal we observe could be that the motion of the actuator is in fact not as faithful as we expect. The most obvious mechanism behind this is that shear motion is induced in both axes, however we are assured by the manufacturers that this should not happen. Alternatively, more complex motion could also be present, such as that illustrated in Figure 8.7. The ideal motion that we aim to replicate with

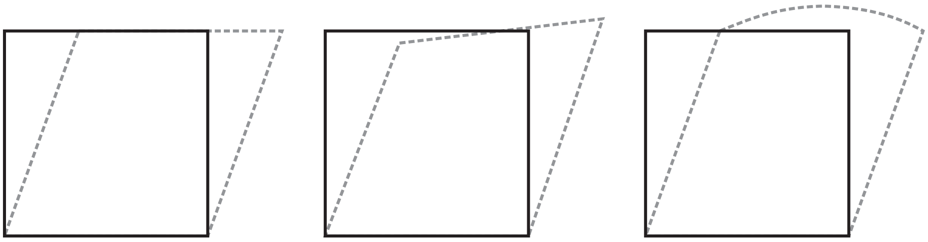

(a) Shear motion (b) Tilting motion (c) Bending motion

Figure 8.7: Possible modes of motion of a piezoelectric actuator.

our actuator is a purely shear one, shown in (a). In this case the motion of any magnetic field source is constrained to lie in the x-y plane, and any signal created by the interferometer is due to translation of the mirror. However, we can envisage other types of motion that may also produce a signal, such as a tilting or bending of the device as shown in (b) and (c). This type of motion could produce a signal in the orthogonal axis. However, in the case at hand one would anticipate that this mechanism would be mitigated by the fact that we are using prisms on top of the actuator; it is likely that the types of motion shown in (b) and (c) would be damped by the bond to the prism.

If the type of non-ideal motion described is a cause for the unexpected signal then this is likely to be exacerbated by our detection method. The Michelson interferometer is a homodyne method, reliant on the spatial positioning of the beams used. Thus the interferometer is also sensitive to misalignments of those beams. There is an interference pattern in a plane orthogonal to the beam direction and if the reflective surface associated with the actuator is tilted then one of the beams will be tilted relative to the other. This will create a change in the interference that takes place, and hence produce signal. To try and minimise this effect, the beams were expanded in the arm sent to the photodiode. This makes the characteristic lengthscale of the interference pattern across the beam larger, and enhances the spatial filtering effect that the photodiode has. This did not result in a significant decrease of the signal. The possibility of steering of the beam was also investigated by observing the signal due to just one arm of the interferometer. If the beam was being diverted significantly the collection efficiency at the photodiode would vary, thus giving a signal. No such evidence was observed.

Due to the unexpected nature of the signal just described, it was deemed that further investigation was necessary. One could, for example, investigate beam deflection over a much larger distance, however an alternative measure of the motion of the actuator was sought. This was found in the form of a laser Doppler vibrometer (LDV), and is discussed in the following section.

8.2.2 Laser Doppler vibrometer

Overview

The laser Doppler vibrometer is an interferometric device, but in contrast to a Michelson interferometer it operates via heterodyne detection. A laser beam is reflected from a moving surface, which imparts a Doppler shift to the frequency of the beam. The reflected beam is then interfered with a reference beam, which has not been Doppler shifted. The result is a beat frequency which is a measure of the velocity of the reflective surface. The heterodyne method has the significant advantage that it is much less sensitive to spatial misalignments, as the interference procedure is based in the frequency domain (although the LDV we used also allowed for better spatial alignment as it was implemented within a microscope setup). If we assume that the motion of the actuator is sinusoidal in form (i.e. described by simple harmonic motion), which we observe to be a very good approximation, then the corresponding amplitude of motion is very easy to calculate, given by $x_0 = v_0/\omega$, where v_0 is the maximum speed observed, and ω is the frequency of motion. As before we can also calculate a phase of the signal relative to the driving voltage. However it is necessary to deduct a $\pi/2$ shift to convert from the phase of the velocity to the phase of the position.

In this manner we also analysed the motion of the actuator through the use of an LDV (Polytec OFV-505 sensor and OFV-5000 controller [221]). This work was carried out in the laboratory of Dr. Hu in the engineering department of Newcastle University.

Results

Example frequency response data (cf. Figure 8.6) are shown in Figure 8.8. We observe behaviour which is qualitatively similar to that derived using the Michelson interferometer; there is a complex structure of resonances, with a general trend that the amplitude of motion decreases as the frequency increases. Also shown is the phase of the displacement of the actuator, relative to the driving voltage applied. We see that this too has a detailed structure. One point to note is that resonant features are often accompanied by a slow variation in the phase. To examine this point in more detail, we will now

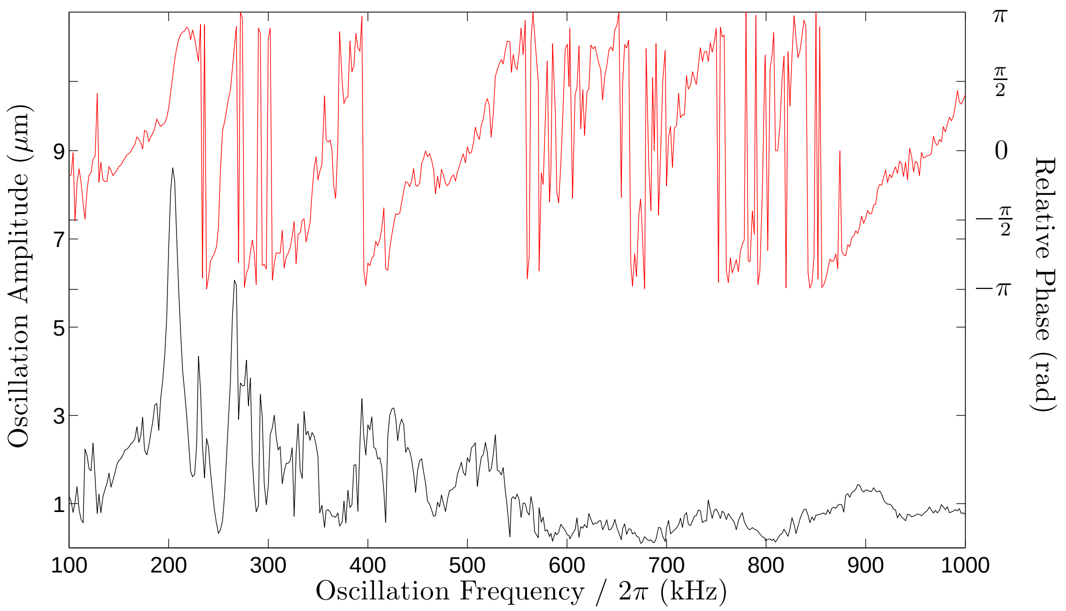

Figure 8.8: Frequency response of an x-y shear actuator, obtained using a laser Doppler vibrometer. The amplitude of motion in one axis is shown in black. Also shown in red is the corresponding phase, relative to the driving voltage. The amplitude of the driving voltage is 75 V. We estimate percentage errors in the oscillation amplitude of less than 5–10%, with the smallest errors evident for large amplitudes. The error in the phase is estimated to be less than 10°. We anticipate significantly lower errors with repeat measurements.

consider one resonant feature in particular. We will study the response of the actuator around the resonance near 290 kHz. This was chosen as it provides a large amplitude of oscillation and seems to be quite a ‘clean’ feature, with a well defined peak. Looking at this resonance in more detail yields Figure 8.9.

We see that the frequency response near the resonance varies quite smoothly. The phase associated with the motion still shows significant variation over the frequency range examined, but also varies more gradually, particularly close to the resonance frequency (around 293 kHz). We also note that the relative phase is approximately 90 degrees at the resonant point, which is as expected when modelling the actuator as a driven harmonic oscillator. The smoothness of the variation in response suggests that effective actuation of the device is fairly insensitive to the frequency used. In practice

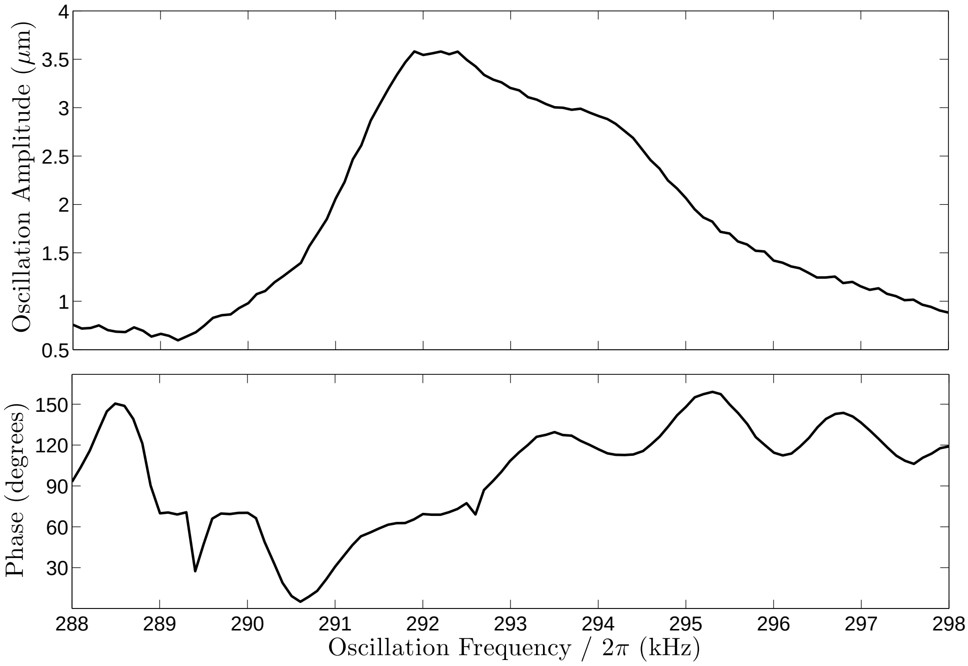

Figure 8.9: Frequency response of one axis of a shear actuator being driven near a resonant frequency. The upper plot shows the amplitude of the resulting oscillation. The lower plot shows the phase of the displacement relative to the driving voltage. The amplitude of the driving voltage is 75 V. Errors are as per Figure 8.8.

the function generators used to produce the driving signal have a precision far greater than that required for effective actuation at a resonant frequency. This will allow for tuning of the amplitude and phase of the motion, which is important for ensuring that the motion is circular in nature, which we shall consider later.

As with the investigation using the Michelson interferometer we also examined the linearity of the device's response. This is shown in Figure 8.10. The dependence on the driving voltage amplitude shows a very similar behaviour to that observed using the Michelson interferometer — the variation is an approximately linear one. With our previous methodology it was difficult to examine this linearity at a resonant frequency as the technique became less appropriate for large amplitudes of motion. Using the LDV we see that on resonance it is possible to achieve significantly larger displacements than have previously been measured. We also note that the observed

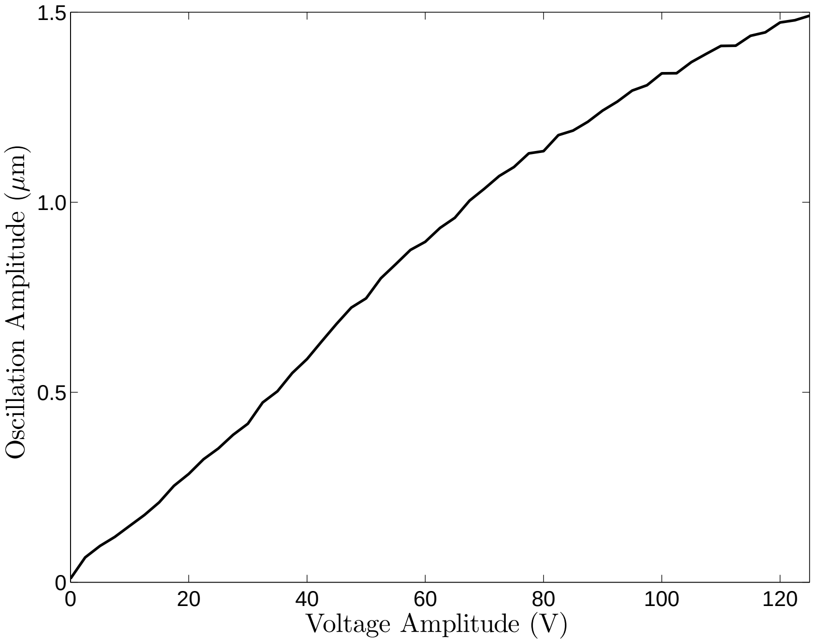

Figure 8.10: Amplitude of oscillation of one axis of an x-y shear actuator as a function of the amplitude of the driving voltage. The frequency of oscillation is 293 kHz. Errors are as per Figure 8.8.

displacements are larger than those quoted for the device; a displacement of around 3 μm is expected for an applied voltage of 250 V. However, this value is based on static operation. Our observations seem to indicate that much larger displacements are possible when the device is oscillating on resonance.

In our previous investigation of the movement of the actuator we observed some rather unexpected behaviour. This was the apparent oscillation along an axis orthogonal to that expected according to the applied voltage. To investigate this further we observed the frequency response of the device along the 'wrong' axis. In fact, all four combinations of measurement were considered, and are shown in Figure 8.11.

As before we note that significant displacement is evident when applying a driving signal which is nominally associated with an axis orthogonal to that being observed. Again, the size of this unexpected signal is comparable to that associated with the correct axis. Examining Figure 8.11 we see that there are similarities between the spectra associated with a common axis being driven, e.g. the 2nd and 3rd traces have very similar structure between 200 and 300 kHz. This seems to suggest that driving one axis (in

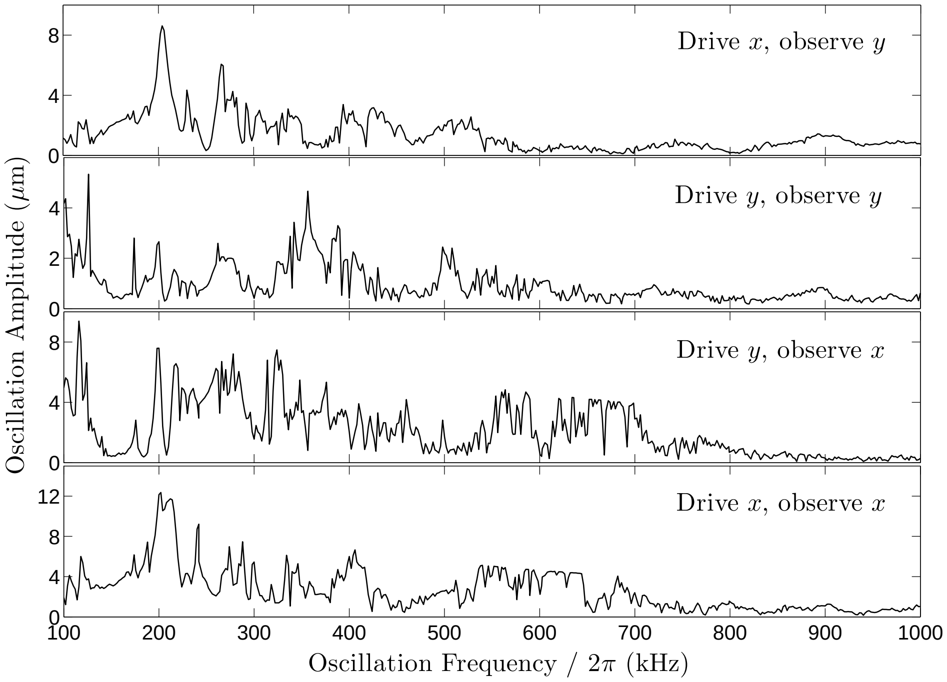

Figure 8.11: Frequency response of both axes of a shear actuator when driven by either axis. Significant displacement is observed in all cases. The amplitude of the driving voltage is 75 V. Errors are as per Figure 8.8.

this example the one we label y) produces motion in both axes, with a degree of commonality in the frequency response. This lends credence to the idea that modes which deviate from the ideal picture of shear motion are being excited, as per Figure 8.7.

Drawing comparisons between the spectra we see that for either axis being driven, a larger displacement is observed in the x-axis than in the y-axis. The reason for this disparity is not known, but we can suggest that the prism associated with the x-axis is located at a position on the actuator which is moving more quickly, and hence produces more signal. We also note when observing a particular axis, greater movement is seen when driving the x-axis. This is perhaps less surprising as one would anticipate that variations between devices created by the manufacturing process would lead to differences in performance. The x-axis actuator is the upper of the two, so one might reason that some damping of the motion is present when the lower actuator is being driven.

From our analysis of the motion of the actuator there are two main points to consider. The first is that the kind of motion which we require in order to realise a PATAP scheme seems very feasible; displacements of the order of several microns at (linear) frequencies of several hundred kHz have been observed. By comparison with Figures 8.1 and 8.2 we see that these parameters are more than adequate to achieve a time-averaged potential based on a nanomagnetic domain wall which is both adiabatic and sufficiently deep. However, the time averaging technique relies on a circular motion. Given the complexity of the response of the device it is likely that realising such motion will require further study of the piezoelectric actuator behaviour, and perhaps a modification of the setup. For example, it is known that the mounting of such actuators can have a dramatic effect on the nature of the motion [222, 223]. This is one aspect that certainly merits further investigation.

Despite the aforementioned complexity of the motion, we shall consider an example showing how it may be possible to create circular motion. We assume a driving frequency of 293 kHz, corresponding to the resonant feature previously considered and examine how the motion varies as the amplitudes of the driving signals are changed. The resulting data are shown in Figure 8.12. We see that there is a relatively smooth variation in the amplitude and phase of the motion when we maintain a constant frequency. However, the variation that is present is not insignificant, and it is this, as well as the fact that a signal in either axis produces motion in both axes, that makes realisation of circular motion challenging. As previously stated, it was not possible to drive both axes at the same time due to technical limitations. Thus we will assume that the contributions to the motion from each axis are independent, i.e. we can simply add together the motion due to each driving voltage. This is of course one aspect of the actuator's behaviour which would benefit from further study.

To ensure circular motion, we have three parameters to choose, given that we work at a set frequency. These are the amplitude of the signal provided to each axis, and the relative phase between each. That is if we drive the two axes with signals of the form

$$V^x(t) = V_0^x \sin(\omega t)\,, \tag{8.13}$$

$$V^y(t) = V_0^y \sin(\omega t + \phi)\,, \tag{8.14}$$

then we must choose V_0^x, V_0^y and ϕ. The easiest way to determine a suitable

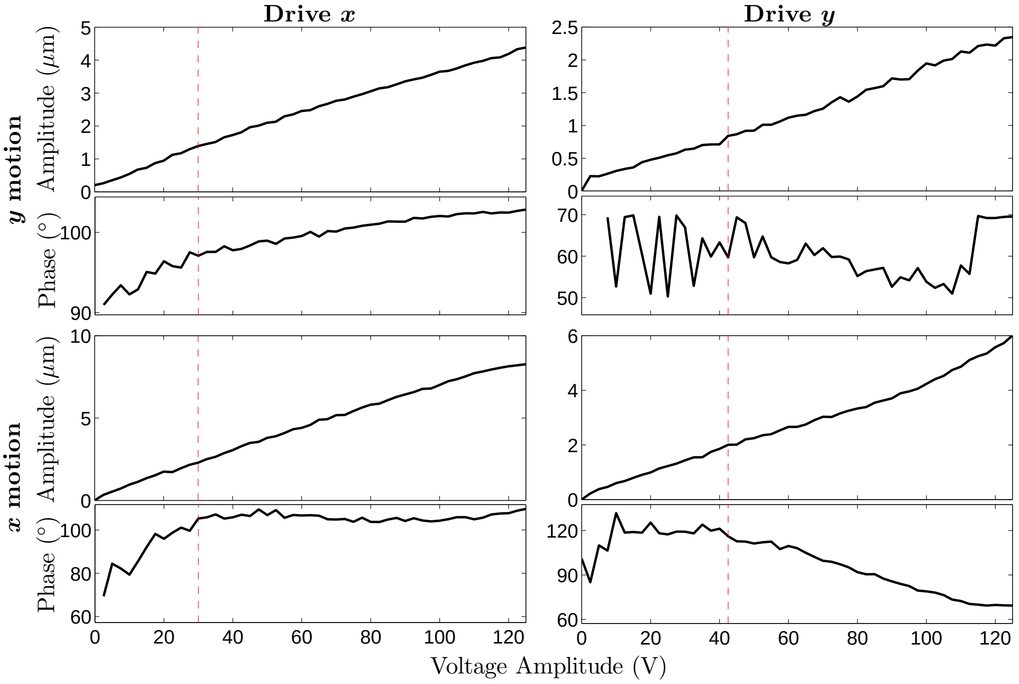

Figure 8.12: Detailed analysis of the motion of a shear actuator at a resonant frequency. The amplitude and relative phase of the motion of the actuator are examined as the amplitude of the driving voltage is varied. In addition, the motion in both axes is considered, in response to voltage applied to either axis. We note that a voltage applied to either axis induces motion in both. The red dashed lines show choices of driving voltage for the two axes, which, along with a relative phase between the applied signals of 188°, produces circular motion. Errors are as per Figure 8.8.

set of parameters is simply to compute the resulting motion over all parameters, and assess how circular the motion is. This was carried out, and we found that we could, under the assumptions stated, produce almost perfect circular motion for a large range of radii, up to around 1.5 µm. The best choice of parameters yields a circle with a radius of approximately 0.8 µm and the corresponding parameters are $V_0^x = 30.0$ V, $V_0^y = 42.5$ V and $\phi = 188°$. This set of parameters is indicated in Figure 8.12 by the red dashed lines.

As we have discussed, additional study is desired to investigate further the nature of the actuator motion, however the data presented here indicate that the method which we wish to employ is technically feasible. Future work should concentrate on deducing the degree to which the motion in the two axes is independent, and demonstrating that circular motion can be achieved. The latter will benefit greatly from the acquisition of a second amplifier in order to apply two independent high-voltage signals simultaneously.

8.3 A ring trap

The calculations and discussions of the previous sections show that a PATAP scheme can offer significant benefits over conventional TAPs, and initial experimental studies into the dynamics of piezoelectric actuators suggest it to be a feasible method. However, we will now consider the possibility of creating more complex trapping potentials using the same method.

The potentials we have considered thus far provide confinement in all three dimensions. This is the simplest type of trap. In contrast a ring trap provides confinement in only one dimension. We label the position around a ring of radius R by some angle, θ. For a given θ the position is then defined by the radial distance from the ring, r, and a second angle, ϕ. Confinement is provided in r, but not in θ or ϕ. This geometry has a number of potential applications within atomic physics, such as the realisation of Josephson junctions [224] or Sagnac interferometers [225] using BECs, or simply to study the dynamics of ultracold atoms in a ring [226, 227, 228, 229, 230]. In some of these applications, the ability to work in arrays of small, tightly confining potentials is desired. Current realisations of ring traps for ultracold atoms are typically limited to single traps and have characteristic sizes which are at least an order of magnitude greater than those which could be created using a PATAP scheme [202, 231, 232, 233, 234].

It is possible to produce a toroidal microtrap geometry by simply increasing the amplitude of motion of the static potential. A sufficiently large circular motion no longer leads to a time-averaged minimum at the centre of the circle of death. Instead there is a set of time-averaged minima which forms a ring within the circle of death. This is a consequence of the finite size of the static potential — as R becomes large the static potential is localised to a small part of the ring at any given time. The transition between these two regimes is illustrated in Figure 8.13.

The manner in which the path of the potential prescribes the shape of

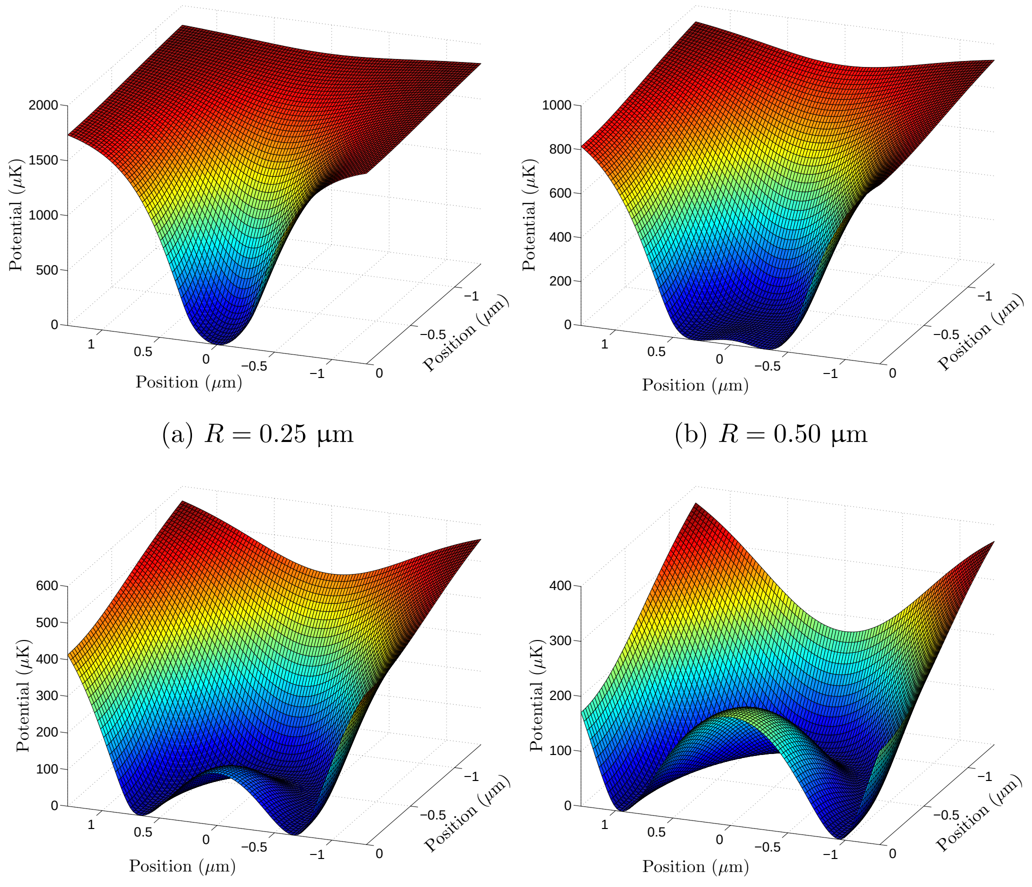

(a) $R = 0.25$ µm

(b) $R = 0.50$ µm

(c) $R = 0.75$ µm

(d) $R = 1.00$ µm

Figure 8.13: The resulting PATAP for a range of oscillation radii, R. According to calculations, the character of the trapping geometry changes from simple 3D confinement to a ring trap with 1D confinement as R increases.

the TAP is analogous to work which has been performed using spatially modulated light fields to create TAPs [233, 235]. A vital difference between the PATAP scheme and a scheme utilising optical potentials is of course the problem of spin flips. Since we are trying to create a ring trap there are now three definitions of the depth: the conventional definition provided by the energy required to move an atom far from the trap; the minimum energy change associated with reaching any point on the circle of death; and the depth given by the central barrier which defines the ring shape. We shall take the trap depth to be defined as the lowest of these three. The first definition of trap depth is in general not of interest as it is much larger than the other two. We shall now consider how the other definitions of trap depth depend on the radius of oscillation as we examine the transition of the trapping potential shown in Figure 8.13. This is illustrated in Figure 8.14.

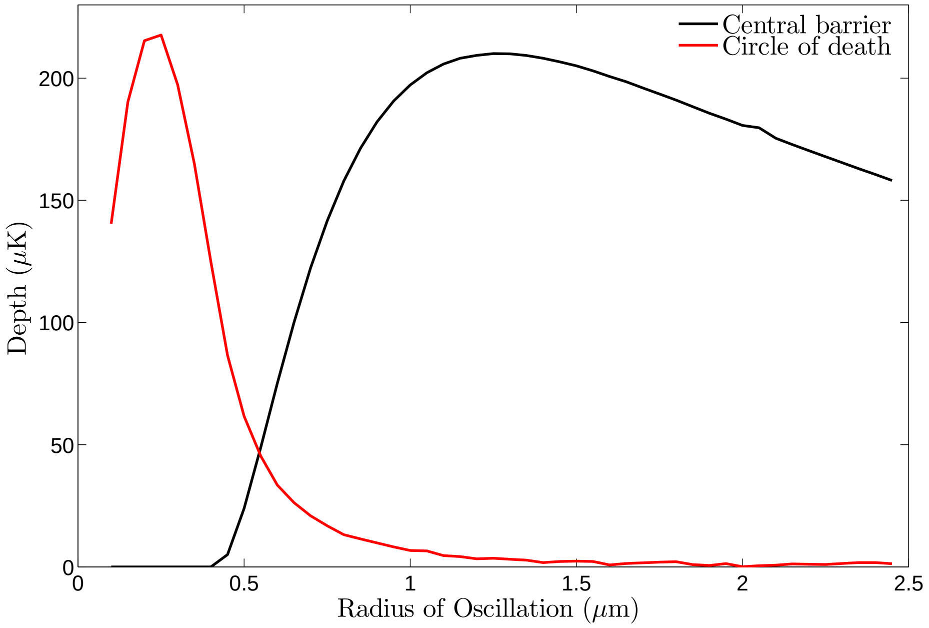

Figure 8.14: The variation in the depth of a PATAP as the radius of oscillation is increased, according to numerical calculations. The depth given by the central barrier that defines the ring shape, and the depth defined as the minimum energy change required to reach the circle of death are both given. A nanowire of cross section 400 nm × 20 nm is assumed, with a trap height of 500 nm.

The trends observed are intuitively as expected. Examining Figure 8.13 we see that the ring shape of the potential develops as the radius of oscillation increases. Thus the depth associated with this ring shape also increases, up to a point, after which it gradually decreases. The depth governed by the circle of death reproduces the trend shown in Figure 8.1, i.e. a larger oscillation produces a larger depth, up to a point, after which the depth decreases as the PATAP changes shape. If we wish to produce a ring trap, the depth is then given by the smaller of these two definitions. The deepest trap, for the fixed parameters chosen, is found at a radius of oscillation of around 550 nm, with a corresponding depth of around 45 μK. In the previous section we found that this amplitude of movement is well within the technical capabilities of piezoelectric actuation. We also note that it should be possible to evolve the shape of the PATAP in a continuous and adiabatic manner, transferring atoms from a potential which is confining in three dimensions to a ring trap. For example if atoms are loaded into a PATAP with an oscillation radius of 250 nm and this radius is increased in a spiral fashion to 550 nm then the potential evolves into a ring trap, just as shown in Figure 8.13. During this transition, forced evaporative cooling will also occur as the depth of the trap is lowered.

The shape of the resulting PATAP is shown in Figure 8.15. By examining this shape we find that a trap frequency of around $2\pi \times 75$ kHz can be achieved, with a minimum Larmor frequency of $2\pi \times 48$ MHz. This results in a value of the adiabaticity criterion, $\xi = \omega_{\mathrm{Larmor}}/\omega_{\mathrm{Trap}}$, of around 600, indicating that this trap is likely to be highly adiabatic. We also note that given these parameters one would probably aim to oscillate the potential at a frequency of around $2\pi \times 500$ kHz, which we note is again well within the technical capabilities of the technique.

There is great freedom afforded through the use of piezoelectric actuators: since they are almost purely capacitive, the motion is defined by the applied voltage, which can in principle be arbitrarily complex. Thanks to this flexibility one might imagine adopting a more complex motion in order to enhance the adiabaticity or depth of the trap. For a conventional TAP one ensures that the circle of death surrounds the time-averaged minimum to avoid spin flips. To completely surround the trap minima for a ring geometry one would need to adopt a helical motion, i.e. of the form:

$$\vec{r}(t) = \begin{pmatrix} \left[R + \tilde{R}\cos(\tilde{\omega}t)\right]\cos(\omega t) \\ \left[R + \tilde{R}\cos(\tilde{\omega}t)\right]\sin(\omega t) \\ \tilde{R}\sin(\tilde{\omega}t) \end{pmatrix}, \tag{8.15}$$

where R defines the radius of a circle which the magnetic zero traverses with a frequency ω. $\tilde{R}$ is the radial displacement from this circle that creates the helix shape, oscillating at a frequency $\tilde{\omega}$. However, we note that this is actually a worse scheme than that already described. The reason for this is that the trap depth is significantly lowered, to around 10 µK. The locus of points which describes the circle of death is greatly expanded, and the minimum energy required to reach one of these points is much less.

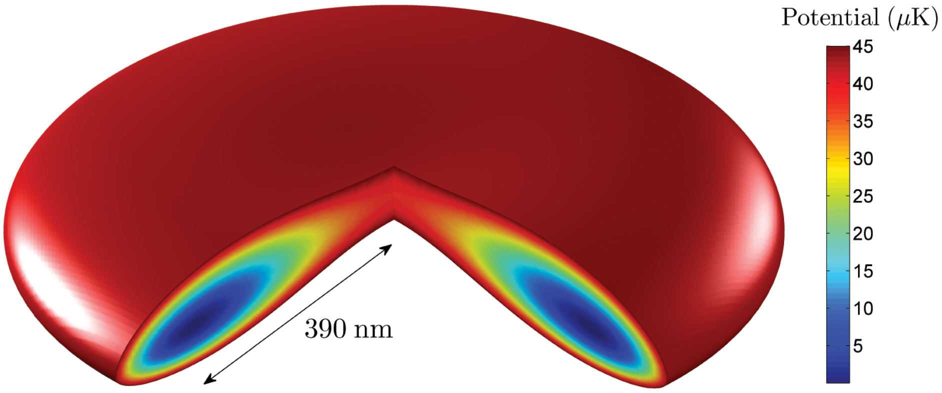

(a) Ring potential created via a PATAP scheme. The isosurface represents a value of 45 µK.

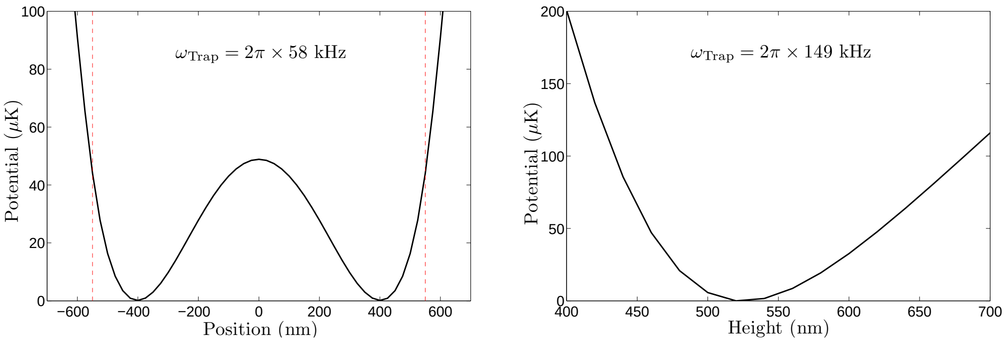

(b) Radial slice through the potential in (a). Red dashed lines indicate the radial location of the circle of death.

(c) A slice through the ring potential shown in (a) along the axial dimension.

Figure 8.15: Illustration of a ring potential created using the PATAP technique. We use a nanowire of cross section 400 nm × 20 nm, a trap height of 500 nm and a radius of oscillation of 550 nm. The depth of the trap is 45 µK and we find $\omega_{\text{Larmor}} = 2\pi \times 48$ MHz, $\omega_{\text{Trap}} = 2\pi \times 75$ kHz and $\xi \approx 600$.

8.4 Conclusions

The results that we have presented are somewhat surprising: a mechanical analogue of the conventional time-averaging procedure is shown to produce harmonic potentials in a very similar manner, but with significant advantages. These are namely that the resulting potentials are significantly more adiabatic, deep, and technically feasible than for a conventional time-averaged potential scheme when working with tight traps.

We have also shown that we can use the same form of motion to produce a ring trap, simply by increasing the amplitude of the motion. This trap is also seen to be exceptionally tight and adiabatic, and has a depth which can easily hold laser cooled atoms. We also note that it is not possible to use a conventional TAP technique to achieve a ring trap; the addition of extra magnetic fields ‘smears’ the ring shape that is defined by the circle of death. Instead, 3D confinement with greater adiabaticity, larger trap depth, and lower trap frequency is yielded.

The PATAP technique is of course not limited to applications using domain walls — it can be applied to any sufficiently small magnetic field source. Future work aimed at applying this technique should focus on three things: the characterisation of the degree of independence between the axes of actuation; the role of the physical mounting of the actuator on its motion; and the simultaneous driving of two axes and observation of the resulting motion. A thorough understanding of these principles will likely permit an easier and more effective realisation of the technique we have presented here.

Chapter 9

Conclusions

In this thesis we have described the first realisation of a hybrid quantum device combining ultracold atoms with spintronics. This was achieved through the design and characterisation of a ferromagnetic planar nanowire array which can host 8 million domain walls of alternating parity. The fringing fields created by this array were employed as a magnetic atom mirror from which we reflected $\sim 10^7$ ^{87}Rb atoms. We also reported the development of an analytic model for the fringing fields based on phenomenological considerations, supported by comparison with micromagnetic simulations. This model showed very good accuracy, particularly in the far-field. Using this model we calculated the nature of the transient atom-nanowire interaction and accurately predicted the resulting diffuse reflection.

We have quantitatively analysed the dynamics of the reflected atom cloud via the use of a resonant sheet of light and observed that the resulting data agreed well with Monte Carlo simulations. We have also demonstrated the reconfigurability of the nanowire array through an observation of the modulation of the atomic reflection. In turn, we have used the atomic cloud as a probe of the micromagnetic state of the array. We have shown that it is possible to tune accurately and reliably the interaction between the atoms and the nanowires. This has revealed that the collective micromagnetic behaviour is generally deterministic but there are also elements of stochasticity exhibited by successive population or annihilation of domain walls.

The technique of moving molasses has been employed as a method to extend the investigation of the interaction between atoms and nanowires. We reported that initial data using this technique showed some agreement with theoretical predictions, however we also observed some unexpected behaviour which requires further study to explain. We have also considered the feasibility of employing this technique to probe the surface interaction arising from our device. We expect that this will be very challenging to achieve due to the complexity and concomitance of the magnetic and electrostatic potentials.

We anticipate that the experimental realisation of a spintronics-based atom-optical element will be a proof-of-principle demonstration that provides a stepping stone to more complex devices. In this regard we have considered using the same technology to produce a tight mobile atom trap based on the fringing field from a single domain wall. We plan to use the large magnetic field gradients provided to give potentials with trap frequencies of the order of MHz. We have investigated a number of different methods for circumventing the problem of Majorana spin-flips within the trapping potentials we hope to create. We found that many popular methods such as Ioffe-type traps or RF-dressing are not appropriate when working in the regime of extremely high field gradients.

To overcome this problem we proposed the use of time-averaging techniques to effectively remove the zero point from the potential. We have found that the conventional method of applying oscillating magnetic fields presents a significant technical challenge when considering the regime in which we work. To remedy this we propose a novel technique for achieving time-averaged potentials based on a mechanical actuation of the magnetic field source using piezoelectric devices. Theoretical considerations have indicated that this methodology offers significant fundamental and technical advantages over existing techniques. Initial work into the characterisation of the movement of piezoelectric actuators suggests that the effective implementation of this scheme is feasible.

The work presented here lays the foundations for future developments of spintronic atom chips. We believe that the successful realisation of a domain-wall based trap will confer significant advantage over alternative methods of manipulating ultracold atoms, providing unprecedented precision and freedom of control.

Appendix A

Fringing field models figures of merit

The table overleaf provides the figures of merit for all six geometries of nanowire considered when analysing the accuracy of the analytic models of nanomagnetic fringing fields in Section 2.3.

Table A.1: A summary of the figures of merit. E_{RMS} is the RMS error over all points, E'_{RMS} is the RMS error with optimal s, E_{M} is the mean percentage error, $E_{\mathrm{RMS}}^{\mathrm{MaxB}}$ is the RMS error in the maximum field for a given height. The labels A-F refer to the wire geometries detailed in Table 2.1.

	Model																				
	Monopole						**1D**						**2D**						**Triangle**		
Quantity	**A**	**B**	**C**	**D**	**E**	**F**	**A**	**B**	**C**	**D**	**E**	**F**	**A**	**B**	**C**	**D**	**E**	**F**	**A**	**B**	**C**
E_{RMS} (%)	11	20	67	6	21	129	11	18	35	5	17	59	10	16	30	4	10	26	7	8	14
E'_{RMS} (%)	–	–	–	–	–	–	–	–	–	–	–	–	10	16	30	3	7	19	6	8	14
E_{M} (%)	7	10	21	2	6	24	7	10	19	2	6	22	7	10	17	1	3	8	4	5	8
$E_{\mathrm{RMS}}^{\mathrm{MaxB}}$ (%)	110	169	355	116	330	720	15	10	14	27	52	85	3	4	10	7	10	15	3	6	12

Appendix B

Nanowire manufacture

In this section we briefly outline the procedure used to produce the nanowire array used in the atom mirror experiment. The process is illustrated in Figure B.1.

The first step of the fabrication process is to deposit a resist layer of poly(methyl methacrylate) (PMMA) onto a silicon substrate. The serpentine pattern is then written into the PMMA layer using an electron beam. To aid the accuracy and speed of the process, each wire shape was written in a single pass by defocussing the electron beam to give a dose corresponding to the desired width of the nanowire, which was chosen to be 125 nm. The exposed regions are then selectively removed by a developer solvent. With the pattern written, a 30 nm layer of permalloy is then thermally evaporated onto the sample with a base pressure of $\sim 10^{-7}$ mbar. The unwanted metal surrounding the written pattern is then removed via lift-off processing using acetone, leaving the serpentine permalloy pattern intact.

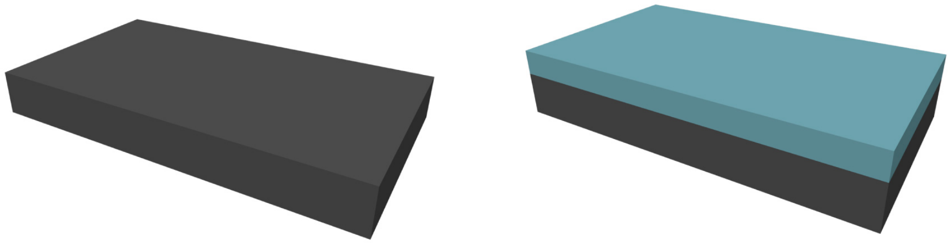

(a) Substrate of Si/SiO_2.

(b) Layer of PMMA resist added.

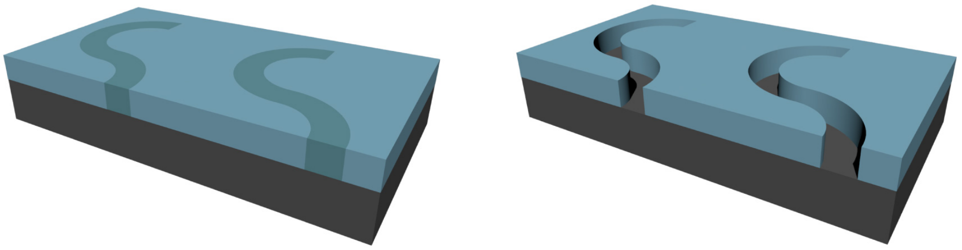

(c) Pattern written into PMMA using a single pixel write of electron beam.

(d) PMMA pattern removed by a developer.

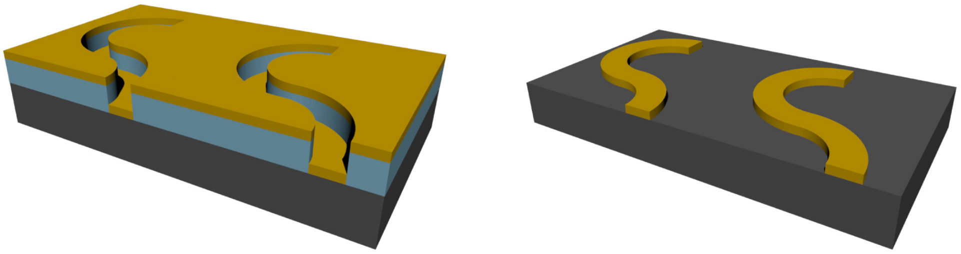

(e) Permalloy thermally evaporated onto the sample.

(f) PMMA removed via lift-off processing to leave the nanowire pattern.

Figure B.1: Schematic of the fabrication procedure for producing the undulating nanowires via electron-beam writing and lift-off processing.

Appendix C

Electronic circuits

C.1 Pulse-generating circuit

The circuit shown in Figure C.1 is used to create the magnetic pulses that reconfigure the nanowire array. It produces a voltage pulse which is sent to a MOSFET which then controls the voltage across the coils (cf. Section 3.4.3). The operation of the circuit can be divided roughly into five stages. The first stage provides electrical isolation between the low voltage, low power computer control circuit and the high power, high voltage circuit which powers the coils. This is achieved via the use of an opto-isolator (IL213AT). A TTL pulse is inputted to the circuit which provides a rising edge which acts as a trigger. This TTL signal is passed through the isolator before passing to the next stage of the circuit.

The signal out of the opto-isolator is then passed to a timing chip (74123) which acts to regulate the length of the pulse created. Pin 1 of the chip detects a falling edge which occurs when the opto-isolator output is high. Pin 2 is always high as this comes directly from the output of the voltage regulator (LM29401). Both 1 and 2 need to be high to create an output from the timing chip. Pin 3 is also kept high and is connected to the 'clear' pin of the chip. This simply prevents the device from resetting, unless the power is removed. Once the pulse signal is received, the timing sequence starts and is controlled by the inputs to Pins 5 and 6. The former is buffered by the presence of a capacitor, C1, and it is this, together with the corresponding variable resistor, R1, that sets the length of the pulse generated.

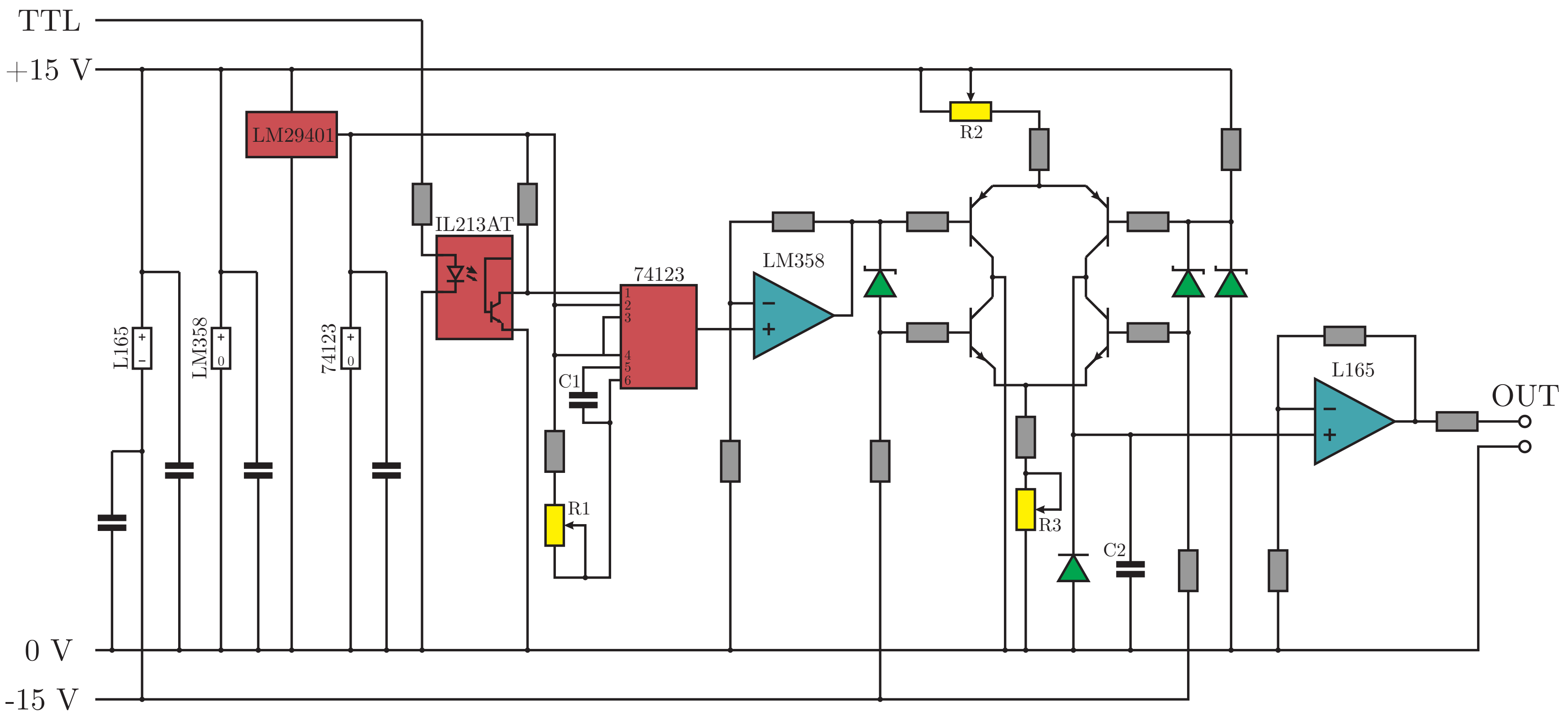

Figure C.1: The circuit used to produce the pulse that controls the current to the switching coils. Grey boxes represent resistors, yellow boxes variable resistors, red boxes represent the labelled chips, and the white boxes represent connections to the labelled components, displayed separately for clarity. All other symbols have their standard meanings.

If the input pulse duration is longer than required the timer output will still switch off appropriately.

The pulse generated by the timing circuit is then passed to an amplifier (LM358) which increases the voltage and current so that it is compatible with the next part of the circuit.

The amplified pulse is then transformed so that it is less square in shape. This ensures that the MOSFETs which we drive switch cleanly, i.e. no oscillation occurs. The rise and fall times of the pulse edges are increased by a circuit analogous to a typical push-pull output stage. Diagonally opposite transistors operate on either the rising or falling edge and are buffered by the capacitor C2, located below. This capacitor, together with variable resistors R2 and R3 control the length of the rising and falling edges, creating a linear ramp to the edges of the signal.

The final phase is simply to pass the modified pulse to a power amplifier. The output is then sent to a high-power MOSFET which controls the current in the coils that produce the magnetic field.

C.2 Light sheet servo

The circuit shown in Figure C.2 is used to stabilise the power in the light sheet used to detect the passage of the atomic cloud (cf. Section 3.4.2). This is achieved by picking off some laser light just before it is focussed into a sheet. This light is then monitored by a fast photodiode, providing the input signal for the circuit shown. This is then compared to a stable voltage, producing a signal proportional to the difference between these two voltages. The output is then fed back to the VCO which controls the AOM associated with the light sheet, thus servoing the power in the beam.

The operation of the circuit is as follows. A stable voltage is produced which is passed through an op amp which smooths the voltage further. A second inverting amplifier of unity gain is then used to revert the voltage to being positive. The signal from the reference photodiode is inverted so that it can be subtracted from the stable voltage. An additional op amp is used to invert the reference photodiode signal again so that it can be monitored. After subtraction of the reference photodiode signal a number of gain stages are used which amplify the signal by a variable amount and also integrate the signal.

The operation of the circuit is thus essentially that of a differential amplifier. The power in the light sheet is easily tuned by changing the stable voltage to which the reference photodiode signal is compared. The servoing behaviour can be tuned by varying the gain of the op amp stages using the potentiometer or by varying other resistor/capacitor values.

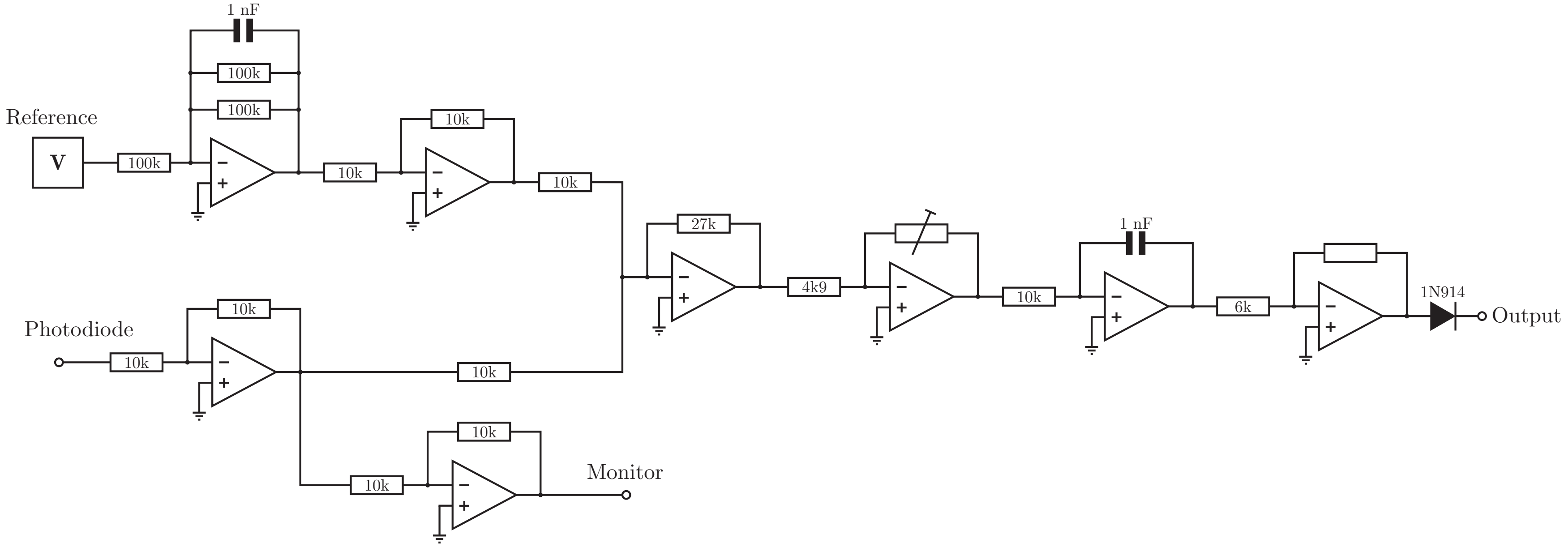

Figure C.2: Circuit diagram of the servo used to stabilise the power in the light sheet. See text for a detailed description. All operational amplifiers use the TL072 integrated chip.

Appendix D

Atom mirror simulation code

Provided below is the Matlab code used to simulate the atom bouncing experiment.

```
%%
tic
clear all
scrsz=get(0,’ScreenSize’);
figure(’outerposition’,[1,1,scrsz(3),scrsz(4)])

% DEFINED CONSTANTS/VARIABLES
angdist=1;                            % Use distribution of angles for given mean isosurface angle?
animate=0;                            % Whether to plot the animation
c=3e8;                                % Speed of light
chipsize=2e-3;                        % Dimension of nanowire chip
d=1000;                               % Wire period (nm)
dropheight=9.75e-3;                   % Initial height of cloud
dt=0.0001;                            % Time increment
g=-9.81;                              % Acceleration due to gravity
G=2*pi*6.07e6;                        % Atomic linewidth
gF=1/2;                               % Gyromagnetic ratio
hp=6.63e-34;                          % Planck’s constant
ig=200;                               % Size of isosurface grid
interval=5;                           % Plot every nth iteration
Isat=16.7;                            % Saturation intensity (W/m^2)
isoang=15;                            % Fixed/mean angle of isosurface (degrees)
isoangr=pi/180*isoang;                % Fixed/mean angle of isosurface (radians)
isoload=1;                            % Whether or not to load the magnetic isosurface from file
kb=1.38e-23;                          % Boltzmann constant
lambda=780e-9;                        % Laser wavelength (m)
lost=0;                               % Number of atoms that fall through the chip
lsheight=4;                           % Height of lightsheet (mm)
lspol=0;                              % Whether or not to consider light sheet pumping
lspower=50e-9;                        % Light sheet beam power (W)
lsthick=0.18;                         % Thickness of lightsheet in mm (1/e^2)
lswidth=7.8;                          % Width of lightsheet in mm (1/e^2)
M=8.6e5;                              % Magnetisation of permalloy
m=87*1.67e-27;                        % Mass of Rubidium atom (kg)
```

```
maniso=0;                          % Whether or not to use an isosurface with fixed angle
mF=2;                              % Zeeman sub level
missed=0;                          % Number of atoms that miss the mirror
motD=2*pi*12e6;                    % MOT beam detuning (Hz)
motR=4e-3;                         % 1/e^2 radius of the MOT beams (m)
mu0=4e-7*pi;                       % Permeability of free space
muB=9.27e-24;                      % Bohr magneton
N=1000;                            % Number of atoms to simulate
Nact=1.06e7;                       % Actual number of atoms in system
nbins=100;                         % Number of bins in position histograms
opduration=1.5e-4;                 % Optical pumping duration (s)
opP=0e-6;                          % Optical pumping beam power (W)
opr=1.43e-3;                       % Optical pumping beam 1/e^2 radius (m)
plotls=1;                          % Whether or not to highlight atoms in light sheet
plotrecap=0;                       % Whether or not to highlight recaptured atoms
Pmot=10e-3;                        % MOT beam power (W)
recaptest=0;                       % Whether or not to discard recaptured atoms to get cumulative number
retro=1;                           % Whether or not we retroreflect the light sheet
s=0.74e-3;                         % Standard deviation of Gaussian position distribution
sigav=20;                          % Number of times over which to average the signal
T=13e-6;                           % Temperature in Kelvin
Tnum=5;                            % Number of temperature increments
toffit=0;                          % Whether or not to do time of flight fitting
Tstep=5e-6;                        % Temperature increment
tnumb=800;                         % Number of time increments
vlaunch=0;                         % Moving molasses launch velocity (m/s)
wt=30e-9;                          % Nanowire thickness (m)
wv=2*pi/lambda;                    % Laser wavevector (m^-1)
ww=125e-9;                         % Nanowire width (m)

% DERIVED VARIABLES
I0=8*lspower/pi/lswidth/lsthick/1e-6; % Peak intensity of light sheet (W/m^2)
Iavg=I0/2;                         % Average light sheet power (W/m^2)
IaIs=Iavg/Isat;                    % I/Isat for light sheet
Ravg=G/2*IaIs/(1+IaIs);            % Average scattering rate of light sheet
Ep=hp*c/lambda;                    % Photon energy (J)
Imot=2*Pmot/pi/motR^2;             % Mot beam peak intensity (W/m^2)
Imotavg=Imot/2;                    % Average mot beam intensity (W/m^2)
Iopa=opP/pi/opr^2;                 % Average intensity in OP beam (W/m^2)
IaIsop=Iopa/Isat;                  % Average intensity / saturation intensity for OP beam
Ropavg=G/2*IaIsop/(1+IaIsop);      % Average scattering rate for OP beam

signal=zeros(sigav,tnumb,Tnum);    % Preallocation
Psig=signal;                       %

xs=[-1e3*chipsize/2,1e3*chipsize/2]; % Define surface to represent nanowire chip
ys=xs;                             %
zs=[0,0;0,0];                      %
xs2=[-1e4*chipsize,1e4*chipsize];  % Define surface to represent light sheet
ys2=[-lswidth,lswidth];            %
zs2=lsheight*ones(2,2);            %
zs3=(lsheight+lsthick)*ones(2,2);  %
```

```

% Optical pumping due to light sheet
if lspol
    t_end=lsthick*1e-3/sqrt(2*-g*(dropheight-lsheight*1e-3));  % Time spent in light sheet
    options=odeset('RelTol',1e-6,'AbsTol',1e-6);               % Options for ODE solver
    % Initial conditions -- atoms in F=2 ground state, zero detuning, intensity
    init=[1/5*ones(1,5) zeros(1,19) 0 IaIs];
    [tt,pop]=ode45(@popfunct87b,[0 t_end],init,options);       % Population solver
    mF12frac=pop(length(pop),5);                               % Weak-field-seeking fraction
    lspol=0;
    clear tt pop
end

for df=1:Tnum              % Range of temperatures

time=0:dt:(tnumb-1)*dt;    % Preallocation
recap=zeros(sigav,tnumb);  %
recapt=zeros(sigav,1);     %
signalb=zeros(1,tnumb);    %
vx=zeros(1,N);             %
vy=vx;                     %
vz=vx;                     %
x=vx;                      %
y=vx;                      %
z=vx;                      %
num=0;                     %
surface=zeros(ig,ig);      %
xiso=zeros(1,ig);          %
yiso=xiso;                 %


%%%%%%%%%%%%%%%%%%%%%%%%%%%%%
% Calculation of isosurface %
%%%%%%%%%%%%%%%%%%%%%%%%%%%%%

if(~maniso)                        % If not using an isosurface of given angle
    if(isoload)                    % If using precalculated isosurface
        load anglex30nm            % Files containing data about isosurface
        anglex=anglex30nm;         %
        angley=anglex';            % By symmetry
    else
        target=(1/2*m*vlaunch^2-g*m*dropheight)/(muB*mF*gF);  % Field required to bounce
        ulim=isofindb(M,wt,ww,0,ww/2,1e-6,target,1e-5)*1.2;   % Upper bound to associated field
        for j=1:ig
            xiso(j)=(j-(ig+1)/2)*1e-8;                        % Isosurface x position
            for k=1:ig
                yiso(k)=(k-(ig+1)/2)*1e-8;                    % Isosurface y position
                surface(j,k)=isofindb(M,wt,ww,xiso(j),...     % Subroutine to find height of
                                 yiso(k),1e-6,target,ulim);  % required field
            end
        end
        surface=surface(57:156,51:150);   % Extract unit cell
```

```
        gradx=diff(surface)/1e-8;         % Take simple gradient
        gradx=[gradx;gradx(1,:)];         % Taking gradient loses a row -- add back in
        anglex=atan(gradx);               % Calculate angle relative to flat
        grady=diff(surface')/1e-8;
        grady=[grady;grady(1,:)];
        angley=atan(grady);
    end
end

%%

%%%%%%%%%%%%%%%%%%%%%%%%%%
% Analysis of isosurface %
%%%%%%%%%%%%%%%%%%%%%%%%%%

if(~maniso)
    % 1D angle distribution
    angle1=180*abs(anglex(:))/pi;                   % Convert angle to degrees
    for i=1:length(angle1)
        if(angle1(i)==0)                            % Zero angle corresponds to hole in isosurface
            angle1(i)=100;                          % Put the 'holes' into a separate bin
        end
    end

    % 3D angle distribution
    xb=linspace(-d/2,d/2,100);                      % Coordinates of unit cell
    yb=xb;                                          % By symmetry
    si=length(xb);                                  % Number of divisions in coordinates

    dotted=zeros(si);                               % Preallocation
    v1x=ones(si,si);                                %
    v1y=zeros(si,si);                               %
    v2x=v1y;                                        %
    v2y=v1x;                                        %

    v1z=tan(anglex);                                % First tangential vector
    v1(:,:,1)=v1x;                                  %
    v1(:,:,2)=v1y;                                  %
    v1(:,:,3)=v1z;                                  %
    v2z=tan(angley);                                % Second tangential vector
    v2(:,:,1)=v2x;                                  %
    v2(:,:,2)=v2y;                                  %
    v2(:,:,3)=v2z;                                  %

    n=cross(v1,v2);                                 % Normal from cross product of tangential vectors
    nabs=sqrt(n(:,:,1).^2+n(:,:,2).^2+n(:,:,3).^2); % Size of normal
    nabsb(:,:,1)=nabs(:,:);                         %
    nabsb(:,:,2)=nabs(:,:);                         %
    nabsb(:,:,3)=nabs(:,:);                         %
    n=n./nabsb;                                     % Unit normal

    zunit(:,:,1)=zeros(si,si);                      % Unit vector in z direction
```

```
    zunit(:,:,2)=zeros(si,si);                      %
    zunit(:,:,3)=ones(si,si);                       %

    for i=1:si;                                     % Take dot product of normal and unit z
        for j=1:si;
            dotted(i,j)=zunit(i,j,1)*n(i,j,1)+zunit(i,j,2)*n(i,j,2)+zunit(i,j,3)*n(i,j,3);
        end
    end

    angle3=180*acos(dotted)/pi;                     % Calculate angle between n and z
    angles=angle3(:);                               % Convert to vector

    for i=1:length(angles)
        if(angles(i)==0)                            % Zero angle corresponds to hole in isosurface
            angles(i)=100;                          % Put 'holes' into separate bin
        end
    end
end

clear angle1 angle3 angles anglex30nm dotted n nabs nabsb surface v1 v1x v1y v1z v2 v2x v2y v2z zunit


%%%%%%%%%%%%
% Bouncing %
%%%%%%%%%%%%

% Randomly populate positions and velocities according to Gaussian distributions
for h=1:sigav
        R=rand(1,N);
        vx=sqrt(2*kb*T/m)*erfinv(2*R-1);
        R=rand(1,N);
        vy=sqrt(2*kb*T/m)*erfinv(2*R-1);
        R=rand(1,N);
        vz=-vlaunch+sqrt(2*kb*T/m)*erfinv(2*R-1);
        R=rand(1,N);
        x=s*sqrt(2)*erfinv(2*R-1);
        R=rand(1,N);
        y=s*sqrt(2)*erfinv(2*R-1);
        R=rand(1,N);
        z=dropheight+s*sqrt(2)*erfinv(2*R-1);

    for t=1:tnumb

%%%%%%%%%%%%%%%%%%%%%%%%%%
% TIME OF FLIGHT FITTING %
%%%%%%%%%%%%%%%%%%%%%%%%%%

        % Transformations to determine light present at atoms and motion relative to beams
        if toffit
            xp1=1/sqrt(2)*(x-(z-dropheight));      % Coordinate rotation through 45 degrees
            zp1=1/sqrt(2)*(x+(z-dropheight));      %
            vxp1=1/sqrt(2)*(vx-vz);                %
```

```
        vzp1=1/sqrt(2)*(vx+vz);                %
        xp2=1/sqrt(2)*((z-dropheight)-x);      % Coordinate rotation through -45 degrees
        zp2=1/sqrt(2)*(-x-(z-dropheight));     %
        vxp2=1/sqrt(2)*(vz-vx);                %
        vzp2=1/sqrt(2)*(-vx-vz);               %

        Itof1=Imot*exp(-2*(y.^2+(zp1-dropheight).^2)./motR^2)/Isat;   % Beam intensities at atoms
        Itof2=Imot*exp(-2*(y.^2+(zp2-dropheight).^2)./motR^2)/Isat;   %
        Itof3=Imot*exp(-2*(x.^2+(z-dropheight).^2)./motR^2)/Isat;     %

        Rmot1=G/2*Itof1./(1+Itof1+(4*wv^2*vxp1.^2+motD^2)/G^2);       % Scattering rates
        Rmot2=G/2*Itof2./(1+Itof2+(4*wv^2*vxp2.^2+motD^2)/G^2);       %
        Rmot3=G/2*Itof3./(1+Itof3+(4*wv^2*vy.^2+motD^2)/G^2);         %
        Rmott=Rmot1+Rmot2+Rmot3;                                      % Total scattering rate

        xphots=[x',Rmot1',Rmot2',Rmot3'];      % Sort photon number spatially
        xphots=sortrows(xphots,1);             %
        yphots=[y',Rmot1',Rmot2',Rmot3'];      %
        yphots=sortrows(yphots,1);             %
        zphots=[z',Rmot1',Rmot2',Rmot3'];      %
        zphots=sortrows(zphots,1);             %
        tphots=xphots+yphots+zphots;           % Total number of photons from all beams

        binnum=200;                                 % Sort atom positions into binnum bins
        binedges=linspace(min(x),max(x),binnum+1);  % Define the bins
        xbincents=linspace(min(x)+(binedges(2)-binedges(1))/2,max(x)-(binedges(2)-binedges(1))/2,binnum);
        [~,whichbin]=histc(x,binedges);             % Label which bin the atoms go into

        for i=1:binnum
            binlabel=(whichbin==i);                 % Label the atoms in a particular bin
            binmems=Rmott(binlabel);                % Get the photons those atoms scatter
            xbinvals(i)=sum(binmems);               % Count the photons
        end

        x0=[0, max(xbinvals), 0, max(xbincents)/2]; % Fit a Gaussian
        options=optimset('MaxFunEvals',1e4,'TolFun',1e-6);
        xparams=fminsearch(@gaussian_fit,x0,options,xbincents,xbinvals);
        xwb(t)=abs(xparams(4));

        binedges=linspace(min(y),max(y),binnum+1);  % Repeat for y
        ybincents=linspace(min(y)+(binedges(2)-binedges(1))/2,max(y)-(binedges(2)-binedges(1))/2,binnum);
        [~,whichbin]=histc(y,binedges);

        for i=1:binnum
            binlabel=(whichbin==i);
            binmems=Rmott(binlabel);
            ybinvals(i)=sum(binmems);
        end

        y0=[0, max(ybinvals), 0, max(ybincents)/2];
        options=optimset('MaxFunEvals',1e4,'TolFun',1e-6);
        yparams=fminsearch(@gaussian_fit,y0,options,ybincents,ybinvals);
```

```
            ywb(t)=abs(yparams(4));

            binedges=linspace(min(z),max(z),binnum+1);  % Repeat for z
            zbincents=linspace(min(z)+(binedges(2)-binedges(1))/2,max(z)-(binedges(2)-binedges(1))/2,binnum);
            [~,whichbin]=histc(z,binedges);

            for i=1:binnum
                binlabel=(whichbin==i);
                binmems=Rmott(binlabel);
                zbinvals(i)=sum(binmems);
            end

            [mm,pp]=max(zbinvals);
            cent=zbincents(pp);
            z0=[0, max(zbinvals), 0, cent];
            options=optimset(’MaxFunEvals’,1e4,’TolFun’,1e-6);
            zparams=fminsearch(@gaussian_fit,z0,options,zbincents,zbinvals);
            zwb(t)=abs(zparams(4));
        end

%%%%%%%%%%%%
% PLOTTING %
%%%%%%%%%%%%

        if(t/interval==floor(t/interval)&&animate)               % Plot every 1 in t steps
            subplot(1,3,1)
            hold off
            fig1=scatter3(1e3*x,1e3*y,1e3*z,’filled’);  % Atoms
            hold on
            colormap bone
            surf(xs,ys,zs);                             % Nanowire chip
            surf(xs2,ys2,zs2);                          % Light sheet
            surf(xs2,ys2,zs3);                          %
            if plotrecap                                % Plotting recaptured atoms in green
                scatter3(1e3*x(recapind),1e3*y(recapind),1e3*z(recapind),’filled’,’g’);
            end
            if plotls                                   % Plotting atoms in light sheet in red
                scatter3(1e3*x(sigcind),1e3*y(sigcind),1e3*z(sigcind),’filled’,’r’);
            end
            alpha(0.8);
            xlabel(’X Position (mm)’,’fontsize’,16,’position’,[18,0,-6],’interpreter’,’latex’)
            ylabel(’Y Position (mm)’,’fontsize’,16,’position’,[-26,-5,0],’interpreter’,’latex’)
            zlabel(’Z Position (mm)’,’fontsize’,16,’interpreter’,’latex’)
            xlim([-chipsize*1e4,chipsize*1e4])
            ylim([-chipsize*1e4,chipsize*1e4])
            zlim([0,1.2*dropheight*1e3])
            text(-25,25,14.5,sprintf(’N=%d’,num),’fontsize’,24,’interpreter’,’latex’);
            text(-25,25,16,sprintf(’t=%0.1f (ms)’,t*dt*1e3),’fontsize’,24,’interpreter’,’latex’);

            subplot(1,3,2)
            hold on
            plot(t*dt*1e3,num*100/N,’-ok’,’MarkerEdgeColor’... % Number of atoms left
```

```
                ,'g','MarkerFaceColor','g','MarkerSize',3)
            xlabel('Time (ms)','fontsize',16)
            ylabel('Percentage of Atoms','fontsize',16)
            xlim([0,tnumb*dt*1e3])
            ylim([0,1e2])

            subplot(1,3,3)
            hold on
            plot(t*dt*1e3,signal(h,t-1)*100/N,'-or',...        % light-sheet signal
                'MarkerEdgeColor','r','MarkerFaceColor','r','MarkerSize',3)
            xlabel('Time (ms)','fontsize',16)
            ylabel('Percentage of Atoms','fontsize',16)
            xlim([0,tnumb*dt*1e3])
            ylim([0,20])
            drawnow
        end

%%%%%%%%%%%%%%%%%
% ATOM DYNAMICS %
%%%%%%%%%%%%%%%%%

        % Incrementally evolve the positions (and vz) of the atoms
        x=x+vx*dt;
        y=y+vy*dt;
        z=z+vz*dt+0.5*g*dt^2;
        vz=vz+g*dt;

        % Reflecting the atoms when z position becomes negative
        for j=1:length(z)
            if(z(j)<0.0)
                if(~(abs(x(j))>chipsize/2||abs(y(j))>chipsize/2))  % Can ignore those outside chip
                    if(~maniso)                                    % If using calculated isosurface
                        Ra=ceil(rand*100);                         % Random points on surface
                        Rb=ceil(rand*100);                         %
                        angx=anglex(Ra,Rb);                        % Corresponding angles
                        angy=angley(Ra,Rb);                        %
                        pumped=rand;                               %
                        mF12frac=1;                                % Weak-field-seeking fraction
                        if(angx==0.0||angy==0.0||pumped>mF12frac)  % Some atoms go through potential
                            x(j)=100;                              % These get moved away
                            lost=lost+1;                           % and counted
                        else
                            x1=[1,0,tan(angx)];                    % Vector in plane
                            x2=[0,1,tan(angy)];                    % Vector in plane
                            n=cross(x1,x2);                        % Normal vector
                            n=n/norm(n);                           % Unit normal vector
                        end
                    else                     % If using manually set isosurface
                        phi=rand*2*pi;       % Randomly set azimuthal angle
                        if(angdist)          % If using precalculated angle distribution
                            if isoang==0;    % Flat isosurface
                                theta=0;
```

```
                            else
                                loop=1;
                                % Precalculated parameters describing the lineshape, A B C D E F G
                                % For x<F: -0.0031+A*exp(B(x-4.246)), for x>F: C+D*exp(E(x-10.88))
                                % G=Mean angle
                                params=[0.2 0.13 0 0.00485 -0.41 0 2.5;
                                        0.17 0.13 0 0.0227 -0.2 0 5;
                                        0.18 0.13 0.0004 0.027 -0.18 2 7.5;
                                        0.116 0.13 0.0008 0.032 -0.17 4 10;
                                        0.088 0.135 0.0014 0.0341 -0.1725 5 12.5;
                                        0.068 0.14 0.002 0.037 -0.175 6 15;
                                        0.044 0.12 0.0022 0.044 -0.14 8 17.5;
                                        0.032 0.125 0.0024 0.054 -0.13 10 20;
                                        0.022 0.125 0.0024 0.061 -0.11 12 22.5;
                                        0.016 0.12 0.0024 0.063 -0.092 14 25;
                                        0.011 0.125 0.0024 0.064 -0.08 16 27.5;
                                        0.0092 0.1229 0.0024 0.062 -0.0706 17 30];
                                [pset,~]=find(params(:,7)==(isoang));  % Pick out correct row

                                % Accept reject method to generate angles
                                % according to the above distributions
                                while(loop)
                                    R=rand*90;
                                    R2=rand;
                                    if(R<params(pset,6))
                                        if(R2<-0.0031+params(pset,1)*exp(params(pset,2)*(R-4.246)))
                                            loop=0;
                                            theta=pi/180*R;
                                        end
                                    else
                                        if(R2<params(pset,3)+params(pset,4)*exp(params(pset,5)*(R-10.88)))
                                            loop=0;
                                            theta=pi/180*R;
                                        end
                                    end
                                end
                            end
                        else            % Else use fixed angle
                            theta=isoangr;  % Set elevation angle -- determines surface flatness
                        end
                        n=[sin(theta)*cos(phi),sin(theta)*sin(phi),cos(theta)]; % Normal vectors
                    end
                    v=[vx(j),vy(j),vz(j)];  % Incoming vector
                    v=v-2*(v*n')*n;         % Outgoing vector
                    vx(j)=v(1);             % Outgoing vector components
                    vy(j)=v(2);             %
                    vz(j)=v(3);             %
                    z(j)=-z(j);             % Simple reflection
                end
            end
        end
```

```
        inds=find(z>0&x~=100);   % Discard atoms that miss the chip or fall through the potential
        x=x(inds);               %
        y=y(inds);               %
        z=z(inds);               %
        vx=vx(inds);             %
        vy=vy(inds);             %
        vz=vz(inds);             %

        % Number of atoms within MOT beam overlap region
        recapind=find(sqrt(x.^2+y.^2)<motR&sqrt(x.^2+(z-0.01).^2)<motR&sqrt(y.^2+(z-0.01).^2)<motR);
        recap(h,t)=length(recapind);
        if t*dt>50e-3&&recaptest              % Only count recaptured after 50 ms
            x(recapind)=100;                  % Discard atoms once recaptured -- only count once
            recapt(h)=recapt(h)+recap(h,t);
        end

        % EFFECT OF LIGHT

        % Number of atoms within 1/e^2 radii of light sheet
        signal(h,t,df)=length(find(z>((lsheight-lsthick/2)*1e-3)&...
            z<((lsheight+lsthick/2)*1e-3)&y<(lswidth*1e-3/2)&y>(-lswidth*1e-3/2)));
        % Atoms within 2 1/e^2 radii of light sheet
        signalb=(z>(lsheight-lsthick)*1e-3)&(z<((lsheight+lsthick)*1e-3))&...
            (y<(lswidth*1e-3))&(y>-(lswidth*1e-3));
        signalc(t)=length(find(signalb));
        [sigcind]=find(z>((lsheight-lsthick)*1e-3)&...
                          z<((lsheight+lsthick)*1e-3)&...
                          y<(lswidth*1e-3/2)&...
                          y>(-lswidth*1e-3/2));
        sigcl=length(sigcind);

        Isig=I0*exp((-8*y.^2/(lswidth*1e-3)^2)).*exp((-8*...   % Light sheet intensity at atoms
            (z-lsheight*1e-3).^2/(lsthick*1e-3)^2)).*signalb;  %
        scattsig=G/2*((Isig/Isat)./...                         % Scattering rates for atoms
            (1+Isig/Isat+4*wv^2*signalb.*vy.^2/G^2));          %
        Pscatt=sum(scattsig)*Ep*Nact/N;                        % Total power scattered
        Psig(h,t,df)=100-(100*(lspower-Pscatt)/lspower);       % Percentage of light sheet absorbed

        if signal(h,t,df)>0
            R1=rand(1,sigcl);                                  % Random numbers for incoming light
            R2=rand(1,sigcl);                                  % Random numbers for retro light
            Pnum1=scattsig(sigcind)*dt+...                     % Poissonian incoming photons absorbed
                sqrt(2*scattsig(sigcind)*dt).*erfinv(2*R1-1);  %
            Pnum2=scattsig(sigcind)*dt+...                     % Poissonian retro photons absorbed
                sqrt(2*scattsig(sigcind)*dt).*erfinv(2*R2-1);  %
            if retro                                           % If light sheet is retroreflected
                Pnum=Pnum1-Pnum2;                              % Net photon kick
            else                                               % If not
                Pnum=Pnum1;                                    % Just from one beam
            end
            vx(sigcind)=vx(sigcind)+hp/lambda/m*Pnum;          % Apply kick
        end
```

```

        % Optical Pumping Beam Push
        if t*dt<=opduration                                     % Push happens at start
            [opatoms]=find((y.^2+(z-dropheight).^2)<opr*1e-3);  % Atoms in OP beam
            opatomnum=length(opatoms);                          % Number of atoms
            Pnumop=1.3;                                         % Precalculated scattering rating
            vx(opatoms)=vx(opatoms)+hp/lambda/m*Pnumop;         % Apply kick
        end

        num=length(inds);  % Number of atoms left
        time(t)=t*dt*1e3;
        if(isempty(inds))  % Stop if no more atoms left
            break
        end
    end
end

if(sigav>1)  % If averaging the signal, take the average
    signalav=mean(signal);
    Psigav(:,df)=mean(Psig(:,:,df));
    recapav=mean(recap);
else
    signalav=squeeze(signal);
    Psigav=squeeze(Psig);
    recapav=squeeze(recap);
end

T=T+Tstep;

end


% Plot resulting light-sheet signal
Temps=5e-6:Tstep:Tnum*Tstep;
figure
waterfall(time’,Temps’,Psigav’)
xlabel(’Time (ms)’,’fontsize’,16,’Interpreter’,’Latex’)
ylabel(’Temperature ($\mu$K)’,’fontsize’,16,’Interpreter’,’Latex’)
zlabel(’$\%$ Absorption of Light Sheet’,’fontsize’,16,’Interpreter’,’Latex’)

toc
```

Appendix E

Light sheet push

An atom falling through the light sheet is travelling at a speed

$$v = \sqrt{2gs_1} \tag{E.1}$$

where g is the acceleration due to gravity and s_1 is the distance from the drop position to the light sheet. Thus the atom spends a time

$$t_1 = w/\sqrt{2gs_1} \tag{E.2}$$

in the light sheet, where w is the light sheet width (we assume that $w \ll s$). The acceleration imparted on the atom whilst in the light sheet is given by $a = \hbar kR/m$ where k is the magnitude of the wavevector associated with the light, R is the scattering rate, given by Equation 5.7 (with $\Delta = v = 0$), and m is the mass of the atom. The displacement produced whilst in the light sheet is then

$$d_1 = \frac{1}{2}at_1^2 = \frac{\hbar kRw^2}{4mgs_1}. \tag{E.3}$$

Assuming there is no initial speed perpendicular to gravity, the speed in this direction after passing through is

$$v_{\mathrm{LS}} = at_1 = \frac{\hbar kRw}{m\sqrt{2gs_1}}. \tag{E.4}$$

The time taken to fall the remainder of the distance to the chip is given by

$$t_2 = \frac{\sqrt{2gh} - \sqrt{2gs_1}}{g}. \tag{E.5}$$

The displacement perpendicular to gravity after the light sheet is then simply given by

$$d_2 = v_{\mathrm{LS}}t_2 = \frac{\hbar kRw}{m\sqrt{2gs_1}} \frac{\sqrt{2gh} - \sqrt{2gs_1}}{g} \tag{E.6}$$

Thus the total displacement produced is given by

$$\begin{aligned} d_{\text{tot}} &= d_1 + d_2 && \text{(E.7)} \\ &= \frac{\hbar k R w^2}{4 m g s_1} + \frac{\hbar k R w}{m\sqrt{2 g s_1}} \frac{\sqrt{2gh} - \sqrt{2 g s_1}}{g}. && \text{(E.8)} \end{aligned}$$

We find that for the parameters used in our experiment that a light sheet power of 50 nW produces a displacement of around 0.4 mm, which is a significant perturbation to the atomic cloud, given that an atom displaced by 1 mm will completely miss the nanowire array. This is in contrast to the case of a retroreflected light sheet where 50 nW is a sufficiently low power to produced a negligible perturbation.

Bibliography

[1] C. S. Adams, M. Sigel, and J. Mlynek, *Atom optics*, Phys. Rep. **240**, 143–210 (1994)

[2] P. Meystre, *Atom Optics* (Springer, 2001)

[3] A. D. Cronin, J. Schmiedmayer, and D. E. Pritchard, *Optics and interferometry with atoms and molecules*, Rev. Mod. Phys. **81**, 1051–1129 (2009)

[4] M. J. Madou, *Fundamentals of microfabrication: The science of miniaturization*, 3rd ed. (CRC Press, 2011)

[5] J. Reichel and V. Vuletic, *Atom chips* (Wiley VCH, 2011)

[6] M. Gierling, P. Schneeweiss, G. Visanescu, P. Federsel, M. Häffner, D. P. Kern, T. E. Judd, A. Günther, and J. Fortágh, *Cold-atom scanning probe microscopy*, Nat. Nanotechnol. **6**, 446–451 (2011)

[7] S. Wildermuth, S. Hofferberth, I. Lesanovsky, E. Haller, L. M. Andersson, S. Groth, I. Bar-Joseph, P. Krüger, and J. Schmiedmayer, *Bose-Einstein condensates: microscopic magnetic-field imaging*, Nature **435**, 440 (2005)

[8] P. Treutlein, D. Hunger, S. Camerer, T. W. Hänsch, and J. Reichel, *Bose-Einstein condensate coupled to a nanomechanical resonator on an atom chip*, Phys. Rev. Lett. **99**, 140403 (2007)

[9] F. Brennecke, T. Donner, S. Ritter, T. Bourdel, M. Köhl, and T. Esslinger, *Cavity QED with a Bose-Einstein condensate*, Nature **450**, 268–271 (2007)

[10] D. Rugar, R. Budakian, H. J. Mamin, and B. W. Chui, *Single spin detection by magnetic resonance force microscopy*, Nature **430**, 329–332 (2004)

[11] M. D. LaHaye, J. Suh, P. M. Echternach, K. C. Schwab, and M. L. Roukes, *Nanomechanical measurements of a superconducting qubit*, Nature **459**, 960–964 (2009)

[12] A. D. O'Connell, M. Hofheinz, M. Ansmann, R. C. Bialczak, M. Lenander, E. Lucero, M. Neeley, D. Sank, H. Wang, M. Weides, J. Wenner, J. M. Martinis, and A. N. Cleland, *Quantum ground state and single-phonon control of a mechanical resonator*, Nature **464**, 697–703 (2010)

[13] M. Kohnen, M. Succo, P. G. Petrov, R. A. Nyman, M. Trupke, and E. A. Hinds, *An array of integrated atom-photon junctions*, Nature Photon. **5**, 35–38 (2011)

[14] C. Monroe, *Quantum information processing with atoms and photons*, Nature **416**, 238–246 (2002)

[15] D. Stick, W. K. Hensinger, S. Olmschenk, M. J. Madsen, K. Schwab, and C. Monroe, *Ion trap in a semiconductor chip*, Nature Phys. **2**, 36–39 (2006)

[16] J. Benhelm, G. Kirchmair, C. F. Roos, and R. Blatt, *Towards fault-tolerant quantum computing with trapped ions*, Nature Phys. **4**, 463–466 (2008)

[17] D. Kielpinski, C. Monroe, and D. Wineland, *Architecture for a large-scale ion-trap quantum computer*, Nature **417**, 709–711 (2002)

[18] M. D. Barrett, J. A. Sauer, and M. S. Chapman, *All-optical formation of an atomic Bose-Einstein condensate*, Phys. Rev. Lett. **87**, 010404 (2001)

[19] C. Weitenberg, M. Endres, J. F. Sherson, M. Cheneau, P. Schauss, T. Fukuhara, I. Bloch, and S. Kuhr, *Single-spin addressing in an atomic mott insulator*, Nature **471**, 319–324 (2011)

[20] E. L. Raab, M. Prentiss, A. Cable, S. Chu, and D. E. Pritchard, *Trapping of neutral sodium atoms with radiation pressure*, Phys. Rev. Lett. **59**, 2631–2634 (1987)

[21] A. L. Migdall, J. V. Prodan, W. D. Phillips, T. H. Bergmann, and H. J. Metcalf, *First observation of magnetically trapped neutral atoms*, Phys. Rev. Lett. **54**, 2596–2599 (1985)

[22] E. A. Hinds and I. G. Hughes, *Magnetic atom optics: mirrors, guides, traps and chips for atoms*, J. Phys. D **32**, R119–R146 (1999)

[23] W. Gerlach and O. Stern, *Der experimentelle Nachweiss der Richtungsquantelung im Magnetfeld*, Z. Phys. **9**, 349–355 (1922)

[24] H. Friedburg and W. Paul, *Optische Abbildung mit neutralen Atomen*, Naturwissenschaften **38**, 159–160 (1951)

[25] J. Schmiedmayer, *Guiding and trapping a neutral atom on a wire*, Phys. Rev. A **52**, R13–R16 (1995)

[26] D. E. Pritchard, *Cooling neutral atoms in a magnetic trap for precision spectroscopy*, Phys. Rev. Lett. **51**, 1336–1339 (1983)

[27] S. Aubin, S. Myrskog, M. H. T. Extavour, L. J. Leblanc, D. McKay, A. Stummer, and J. H. Thywissen, *Rapid sympathetic cooling to Fermi degeneracy on a chip*, Nature Phys. **2**, 384–387 (2006)

[28] K. Brugger, P. Krüger, X. Luo, S. Wildermuth, H. Gimpel, M. W. Klein, S. Groth, R. Folman, I. Bar-Joseph, and J. Schmiedmayer, *Two-wire guides and traps with vertical bias fields on atom chips*, Phys. Rev. A **72**, 023607 (2005)

[29] R. Folman, P. Krüger, J. Schmiedmayer, J. Denschlag, and C. Henkel, *Microscopic atom optics: from wires to an atom chip*, Adv. Atom. Mol. Opt. Phys. **48**, 263–356 (2002)

[30] T. Schumm, S. Hofferberth, L. M. Andersson, S. Wildermuth, S. Groth, I. Bar-Joseph, J. Schmiedmayer, and P. Krüger, *Matter-wave interferometry in a double well on an atom chip*, Nature Phys. **1**, 57–62 (2005)

[31] M. P. A. Jones, C. J. Vale, D. Sahagun, B. V. Hall, and E. A. Hinds, *Spin coupling between cold atoms and the thermal fluctuations of a metal surface*, Phys. Rev. Lett. **91**, 080401 (2003)

[32] J. Fortágh, H. Ott, S. Kraft, A. Günther, and C. Zimmermann, *Surface effects in magnetic microtraps*, Phys. Rev. A **66**, 041604(R) (2002)

[33] A. E. Leanhardt, A. P. Chikkatur, D. Kielpinski, Y. Shin, T. L. Gustavson, W. Ketterle, and D. E. Pritchard, *Propagation of a Bose-Einstein condensate in a magnetic waveguide*, Phys. Rev. Lett. **89**, 040401 (2002)

[34] W. Hänsel, J. Reichel, P. Hommelhoff, and T. W. Hänsch, *Trapped-atom interferometer in a magnetic microtrap*, Phys. Rev. A **64**, 063607 (2001)

[35] A. E. Leanhardt, Y. Shin, A. P. Chikkatur, D. Kielpinski, W. Ketterle, and D. E. Pritchard, *Bose-Einstein condensates near a microfabricated surface*, Phys. Rev. Lett. **90**, 100404 (2003)

[36] C. Henkel, S. Pötting, and M. Wilkens, *Loss and heating of particles in small and noisy traps*, Appl. Phys. B **69**, 379–387 (1999)

[37] J. D. Jackson, *Classical electrodynamics* (Wiley, 1975)

[38] T. M. Roach, H. Abele, M. G. Boshier, H. L. Grossman, K. P. Zetie, and E. A. Hinds, *Realization of a magnetic mirror for cold atoms*, Phys. Rev. Lett. **75**, 629–632 (1995)

[39] I. G. Hughes, P. A. Barton, T. M. Roach, M. G. Boshier, and E. A. Hinds, *Atom optics with magnetic surfaces: I. Storage of cold atoms in a curved 'floppy disk'*, J. Phys. B **30**, 647–658 (1997)

[40] A. D. West, K. J. Weatherill, T. J. Hayward, P. W. Fry, T. Schrefl, M. R. J. Gibbs, C. S. Adams, D. A. Allwood, and I. G. Hughes, *Realization of the manipulation of ultracold atoms with a reconfigurable nanomagnetic system of domain walls*, ArXiv e-prints 1112.0485

[41] Y. T. Xing, I. Barb, R. Gerritsma, R. J. C. Spreeuw, H. Luigjes, Q. F. Xiao, C. Rétif, and J. B. Goedkoop, *Fabrication of magnetic atom chips based on FePt*, J. Magn. Magn. Mat. **313**, 192–197 (2007)

[42] J. Fortágh and C. Zimmerman, *Magnetic microtraps for ultracold atoms*, Reviews of Modern Physics **79**, 235–289 (2007)

[43] S. Whitlock, B. V. Hall, T. Roach, R. Anderson, M. Volk, P. Hannaford, and A. I. Sidorov, *Effect of magnetization inhomogeneity on magnetic microtraps for atoms*, Phys. Rev. A **75**, 043602 (2007)

[44] S. Whitlock, R. Gerritsma, T. Fernholz, and R. J. C. Spreeuw, *Two-dimensional array of microtraps with atomic shift register on a chip*, New Journal of Physics **11**, 023021 (2009)

[45] R. Gerritsma and R. J. C. Spreeuw, *Topological constraints on magnetostatic traps*, Phys. Rev. A **74**, 043405 (2006)

[46] S. Chikazumi, *Physics of Ferromagnetism*, 2nd ed. (Oxford University Press, 1997)

[47] T. Dastagir, W. Xu, S. Sinha, H. Wu, Y. Cao, and H. Yu, *Tuning the permeability of permalloy films for on-chip inductor applications*, Appl. Phys. Lett. **97**, 162506 (2010)

[48] D. Dimitrov, I. Halianov, J. Kassabov, and S. Marinov, *Magnetic permeability of sputtered permalloy thin films*, J. Phys.: Condens. Mat. **5**, 1257–1260 (1993)

[49] *CRC Handbook of Chemistry and Physics*, 92nd ed. (CRC Press, 2011)

[50] M. A. Akhter, D. J. Mapps, Y. Q. Ma Tan, A. Petford-Long, and R. Doole, *Thickness and grain-size dependence of the coercivitiy in permalloy thin films*, J. Appl. Phys. **81**, 4122–4124 (1997)

[51] R. M. Bozorth, *The permalloy problem*, Rev. Mod. Phys. **25**, 42–48 (1953)

[52] L. F. Yin, D. H. Wei, N. Lei, L. H. Zhou, C. S. Tian, G. S. Dong, and X. F. Jin, *Magnetocrystalline anisotropy in permalloy revisited*, Phys. Rev. Lett. **97**, 067203 (2006)

[53] H.-P. Klein and E. Kneller, *Variation of magnetocrystalline anisotropy of iron with field and temperature*, Phys. Rev. **144**, 372–374 (1966)

[54] J. Dean, M. T. Bryan, T. Schrefl, and D. A. Allwood, *Stress-based control of magnetic nanowire domain walls in artificial multiferroic systems*, J. Appl. Phys. **109**, 023915 (2011)

[55] G. Tatara, H. Kohno, and J. Shibata, *Microscopic approach to current-driven domain wall dynamics*, Phys. Rep. **468**, 213–301 (2008)

[56] D. Atkinson, D. Allwood, G. Xiong, M. Cooke, C. C. Faulkner, and R. P. Cowburn, *Magnetic domain-wall dynamics in a submicrometre ferromagnetic structure*, Nature Mater. **2**, 85–87 (2003)

[57] G. S. D. Beach, M. Tsoi, and J. L. Erskine, *Current-induced domain wall motion*, J. Magn. Magn. Mat. **320**, 1272–1281 (2008)

[58] A. Goussev, J. M. Robbins, and V. Slastikov, *Domain-wall motion in ferromagnetic nanowires driven by arbitrary time-dependent fields: An exact result*, Phys. Rev. Lett. **104**, 147202 (2010)

[59] Z. Z. Sun and J. Schliemann, *Fast domain wall propagation under an optimal field pulse in magnetic nanowires*, Phys. Rev. Lett. **104**, 037206 (2010)

[60] X. R. Wang, P. Yan, J. Lu, and C. He, *Magnetic field driven domain-wall propagation in magnetic nanowires*, Ann. Phys. **324**, 1815–1820 (2009)

[61] S. S. P. Parkin, M. Hayashi, and L. Thomas, *Magnetic domain-wall racetrack memory*, Science **320**, 190–194 (2008)

[62] S. A. Wolf, D. D. Awschalom, R. A. Buhrman, J. M. Daughton, S. von Molnár, M. L. Roukes, A. Y. Chtchelkanova, and D. M. Treger, *Spintronics: A spin-based electronics vision for the future*, Science **294**, 1488–1495 (2001)

[63] D. A. Allwood, G. Xiong, C. C. Faulkner, D. Atkinson, D. Petit, and R. P. Cowburn, *Magnetic domain-wall logic*, Science **309**, 1688 (2005)

[64] S. Parkin, X. Jiang, C. Kaiser, A. Panchula, K. Roche, and M. Samant, *Magnetically engineered spintronic sensors and memory*, Proc. IEEE **91**, 661–680 (2003)

[65] T. Schrefl, M. E. Schabes, D. Suess, and M. Stehno, *Dynamic micromagnetic write head fields during magnetic recording in granular media*, IEEE Trans. Magn. **40**, 2341–2343 (2004)

[66] D. A. Allwood, T. Schrefl, G. Hrkac, I. G. Hughes, and C. S. Adams, *Mobile atom traps using magnetic nanowires*, Applied Physics Letters **89**, 014102 (2006)

[67] *Object Oriented MicroMagnetic Framework (OOMMF)*, `http://math.nist.gov/oommf`

[68] *Suessco*, `http://www.suessco.com/`

[69] T. J. Hayward, A. D. West, K. J. Weatherill, T. Schrefl, I. G. Hughes, and D. A. Allwood, *Nanomagnetic engineering of the properties of domain wall atom traps*, J. Appl. Phys. **110**, 123918 (2011)

[70] A. D. West, T. J. Hayward, K. J. Weatherill, T. Schrefl, D. A. Allwood, and I. G. Hughes, *A simple model for calculating magnetic nanowire domain wall fringing fields*, J. Phys. D **45**, 095002 (2012)

[71] T. J. Hayward, M. T. Bryan, P. W. Fry, P. M. Fundi, M. R. J. Gibbs, D. A. Allwood, M.-Y. Im, and P. Fischer, *Direct imaging of domain-wall interactions in* $Ni_{80}Fe_{20}$ *planar nanowires*, Phys. Rev. B **81**, 020410(R) (2010)

[72] C. Castelnovo, R. Moessner, and S. L. Sondhi, *Magnetic monopoles in spin ice*, Nature **451**, 42–45 (2008)

[73] E. Mengotti, L. J. Heyderman, A. F. Rodriguez, F. Nolting, R. V. Hügli, and H.-B. Braun, *Real-space observation of emergent magnetic monopoles and associated Dirac strings in artificial kagome spin ice*, Nature Phys. **7**, 68–74 (2011)

[74] S. T. Bramwell, S. R. Giblin, S. Calder, R. Aldur, D. Prabhakaran, and T. Fennell, *Measurement of the charge and current of magnetic monopoles in spin ice*, Nature **461**, 956–959 (2009)

[75] S. Ladak, D. Read, T. Tyliszczak, W. R. Branford, and L. F. Cohen, *Monopole defects and magnetic Coulomb blockade*, New J. Phys. **13**, 023023 (2011)

[76] T. J. Hayward, M. T. Bryan, P. W. Fry, P. M. Fundi, M. R. J. Gibbs, M.-Y. Im, P. Fischer, and D. A. Allwood, *Pinning induced by inter-domain wall interactions in planar magnetic nanowires*, J. Appl. Phys. **96**, 052502 (2010)

[77] T. J. Hayward, A. D. West, K. J. Weatherill, P. J. Curran, P. W. Fry, P. M. Fundi, M. R. J. Gibbs, T. Schrefl, C. S. Adams, I. G. Hughes, S. J. Bending, and D. A. Allwood, *Design and characterization of a field-switchable nanomagnetic atom mirror*, J. Appl. Phys. **108**, 043906 (2010)

[78] R. D. McMichael and M. J. Donahue, *Head to head domain wall structures in thin magnetic strips*, IEEE Trans. Magn. **33**, 4167–4169 (1997)

[79] *Wolfram Research, Inc., Mathematica, Version 7.0, Champaign, IL (2008)*

[80] I. S. Gradshteyn and I. M. Ryzhik, *Table of integrals, series, and products, corrected and enlarged edition* (Academic Press, San Diego, 1980)

[81] S. J. Wark and G. I. Opat, *An electrostatic mirror for neutral polar molecules*, J. Phys. B **25**, 4229–4240 (1992)

[82] G. I. Opat, S. J. Wark, and A. Cimmino, *Electric and magnetic mirrors and gratings for slowly moving neutral atoms and molecules*, Appl. Phys. B **54**, 396–402 (1992)

[83] A. I. G. Flórez, S. A. Meek, H. Haak, H. Conrad, G. Santambrogio, and G. Meijer, *An electrostatic elliptical mirror for neutral polar molecules*, Phys. Chem. Chem. Phys. **13**, 18830–18834 (2011)

[84] E. Vliegen and F. Merkt, *Normal-incidence electrostatic Rydberg atom mirror*, Phys. Rev. Lett. **97**, 033002 (2006)

[85] E. R. Huson, J. R. Bochinski, H. J. Lewandowski, B. C. Sawyer, and J. Ye, *Efficient Stark deceleration of cold polar molecules*, Eur. Phys. J. D **31**, 351–358 (2004)

[86] S. A. Meek, H. Conrad, and G. Meijer, *A Stark decelerator on a chip*, New J. Phys. **11**, 055024 (2009)

[87] R. Fulton, A. I. Bishop, and P. F. Barker, *Optical Stark decelerator for molecules*, Phys. Rev. Lett. **93**, 243004 (2004)

[88] S. Kallush, B. Segev, and R. Côté, *Evanescent-wave mirror for ultracold diatomic polar molecules*, Phys. Rev. Lett. **95**, 163005 (2005)

[89] N. Westbrook, C. I. Westbrook, A. Landragin, G. Labeyrie, L. Cognet, V. Savalli, G. Horvath, A. Aspect, C. Hendel, K. Moelmer, J.-Y. Courtois, W. D. Phillips, R. Kaiser, and V. Bagnato, *New physics with evanescent wave atomic mirrors: The van der Waals force and atomic diffraction*, Phys. Scripta **178**, 7–12 (1998)

[90] D. Voigt, B. T. Wolschrijn, R. A. Cornelussen, R. Jansen, N. Bhattacharya, H. B. van Linden van den Heuvell, and R. J. C. Spreeuw, *Elastic and inelastic evanscent-wave mirrors for cold atoms*, C. R. Acad. Sci. **2**, 619–624 (2001)

[91] R. Grimm, M. Weidemüller, and Y. B. Ovchinnikov, *Optical dipole traps for neutral atoms*, Adv. At., Mol., Opt. Phys. **42**, 95–170 (2008)

[92] S. Jochim, M. Bartenstein, A. Altmeyer, G. Hendl, C. Chin, J. H. Denschlag, and R. Grimm, *Pure gas of optically trapped molecules created from fermionic atoms*, Phys. Rev. Lett. **91**, 240402 (2003)

[93] J. J. Zirbel, K.-K. Ni, S. Ospelkaus, T. L. Nicholson, M. L. Olsen, P. S. Julienne, C. E. Wieman, J. Ye, and D. S. Jin, *Heteronuclear molecules in an optical dipole trap*, Phys. Rev. A **78**, 013416 (2008)

[94] A. Ashkin, J. M. Dziedzic, J. E. Bjorkholm, and S. Chu, *Observation of a single-beam gradient force optical trap for dielectric particles*, Opt. Lett. **11**, 288–290 (1986)

[95] D. G. Grier, *A revolution in optical manipulation*, Nature **424**, 810–816 (2003)

[96] I. G. Hughes, P. A. Barton, T. M. Roach, and E. A. Hinds, *Atom optics with magnetic surfaces: II. Microscopic analysis of the 'floppy disk' mirror*, J. Phys. B **30**, 2119–2132 (1997)

[97] W. Wernsdorfer, K. Hasselbach, A. Benoit, B. Barbara, B. Doudin, J. Meier, J.-P. Ansermet, and D. Mailly, *Measurements of magnetization switching in individual nickel nanowires*, Phys. Rev. B **55**, 552–559 (1997)

[98] M. T. Bryan, D. Atkinson, and R. P. Cowburn, *Experimental study of the influence of edge roughness on magnetization switching in permalloy nanostructures*, Appl. Phys. Lett. **85**, 3510–3512 (2004)

[99] G. F. Fitzgerald, *On the rotation of the plane of polarization of light by reflection from the pole of a magnet*, Proc. R. Soc. Lond. **25**, 447–450 (1876)

[100] D. A. Allwood, G. Xiong, M. D. Cooke, and R. P. Cowburn, *Magneto-optical Kerr effect analysis of magnetic nanostructures*, J. Phys. D **36**, 2175–2182 (2003)

[101] V. V. Khotkevych, M. V. Milošević, and S. J. Bending, *A scanning Hall probe microscope for high resolution magnetic imaging down to 300 mK*, Rev. Sci. Instr. **79**, 123708 (2008)

[102] A. Oral, S. J. Bending, and M. Henini, *Real-time scanning Hall probe microscopy*, Appl. Phys. Lett. **69**, 1324–1326 (1996)

[103] A. M. Chang, H. D. Hallen, L. Harriott, H. F. Hess, H. L. Kao, J. Kwo, R. E. Miller, R. Wolfe, J. van der Ziel, and T. Y. Chang, *Scanning Hall probe microscopy*, Appl. Phys. Lett. **61**, 1974–1976 (1992)

[104] *Kimball Physics*, `http://www.kimballphysics.com`

[105] *Varian Inc.*, `http://www.varianinc.com`

[106] H. J. Metcalf and P. van der Straten, *Laser cooling and trapping* (Springer, 2002)

[107] *SAES*, `http://www.saesgetters.com`

[108] *Caburn MDC*, `http://www.caburn.com`

[109] M. A. Kasevich, E. Riis, and S. Chu, *RF spectroscopy in an atomic fountain*, Phys. Rev. Lett. **63**, 612–615 (1989)

[110] D. A. Steck, *Rubidium 87 D line data*, `http://steck.us/alkalidata`

[111] *AA Opto-Electronic*, `http://opto.braggcell.com`

[112] *http://www.toptica.com/*

[113] M. L. Harris, C. S. Adams, S. L. Cornish, I. McLeod, E. Tarleton, and I. G. Hughes, *Polarization spectroscopy in rubidium and cesium*, Phys. Rev. A **73**, 062509 (2006)

[114] H. D. Do, G. Moon, and H. Noh, *Polarization spectroscopy of rubidium atoms: Theory and experiment*, Phys. Rev. A **77**, 032513 (2008)

[115] C. P. Pearman, C. S. Adams, S. G. Cox, P. F. Griffin, D. A. Smith, and I. G. Hughes, *Polarization spectroscopy of a closed atomic transition: applications to laser frequency locking*, J. Phys. B **35**, 5141–5151 (2002)

[116] K. L. Corwin, Z. Lu, C. F. Hand, R. J. Epstein, and C. E. Wieman, *Frequency stabilized diode laser with the Zeeman shift in an atomic vapor*, Applied Optics **37**, 3295–3298 (1998)

[117] A. Millett-Sikking, I. G. Hughes, P. Tierny, and S. L. Cornish, *DAVLL lineshapes in atomic rubidium*, J. Phys. B **40**, 187–198 (2007)

[118] W. D. Lett, P. D. Phillips, S. L. Rolston, C. E. Tanner, R. N. Watts, and C. I. Westbrook, *Optical molasses*, J. Opt. Soc. Am. B **6**, 2084–2107 (1989)

[119] *PCO*, `http://www.pco.de`

[120] *Computar*, `http://computarganz.com`

[121] *Thorlabs*, `http://www.thorlabs.com`

[122] G. W. C. Kaye and T. H. Laby, *Tables of physical and chemical constants*, 16th ed. (Kaye & Laby Online. Version 1.0, 2005) `http://www.kayelaby.npl.co.uk`

[123] W. Smythe, *Static and Dynamic Electricity*, 3rd ed. (McGraw-Hill, 1968)

[124] *Honeywell*, `http://honeywell.com`

[125] *Bosch*, `http://www.bosch.com`

[126] *National Instruments*, `http://www.ni.com`

[127] I. Yavin, M. Weel, A. Andreyuk, and A. Kumarakrishnan, *A calculation of time-of-flight distribution of trapped atoms*, Am. J. Phys. **70**, 149–152 (2002)

[128] X. Zhao, D. J. Vieira, and F. Fang, *Precision polarization measurements of atoms in a far-off-resonance optical dipole trap*, Phys. Rev. A **83**, 013416 (2011)

[129] M. Abramowitz and I. A. Stegun, *Handbook of mathematical functions with formulas, graphs and mathematical tables* (Dover, New York, 1964)

[130] J. Kim, M.-H. Jung, and S.-B. Choe, *Stability of magnetic domains with notches in permalloy nanowires*, IEEE Trans. Magn. **45**, 2481–2484 (2009)

[131] J.-E. Wegrowe, J. P. Meier, B. Doudin, J.-P. Ansermet, W. Wernsdorfer, B. Barbara, W. T. Coffey, Y. P. Kalmykov, and J.-L. Déjardin, *Magnetic relaxation of nanowires: beyond the Néel-Brown activation process*, Europhys. Lett. **38**, 329–334 (1997)

[132] N. D. Rizzo, M. DeHerrera, J. Janesky, B. Engel, J. Slaughter, and S. Tehrani, *Thermally activated magnetization reversal in submicron magnetic tunnel junctions for magnetoresistive random access memory*, Appl. Phys. Lett. **80**, 2335–2337 (2002)

[133] M. H. Kalos and P. A. Whitlock, *Monte Carlo methods*, 2nd ed. (Wiley-VCH, 2008)

[134] G. L. Trigg, *Mathematical tools for physicists* (Wiley-VCH, 2005)

[135] C. J. Foot, *Atomic Physics* (Oxford, 2005)

[136] C. Cohen-Tannoudji, J. Dupont-Roc, and G. Grynberg, *Atom-photon interactions: basic processes and applications* (Wiley-VCH, 2004)

[137] N. F. Ramsey, *Molecular beams*, Oxford Classics (Oxford, 2005)

[138] G. Breit and I. I. Rabi, *Measurement of nuclear spin*, Phys. Rev. **38**, 2082–2083 (1931)

[139] D. Raskin and P. Kusch, *Interaction between a neutral atomic or molecular beam and a conducting surface*, Phys. Rev. **179**, 712–721 (1969)

[140] A. Shih and V. A. Parsegian, *Van der Waals forces between heavy alkali atoms and gold surfaces: Comparison of measured and predicted values*, Phys. Rev. A **12**, 835–841 (1975)

[141] A. Anderson, S. Haroche, E. A. Hinds, W. Jhe, and D. Meschede, *Measuring the van der Waals forces between a Rydberg atom and a metallic surface*, Phys. Rev. A **37**, 3594–3597 (1988)

[142] E. S. Sabisky and C. H. Anderson, *Verification of the Lifshitz theory of the van der Waals potential using liquid-helium films*, Phys. Rev. A **7**, 790–806 (1973)

[143] M. Gorlicki, S. Feron, V. Lorent, and M. Ducloy, *Interferometric approaches to atom-surface van der Waals interactions in atomic mirrors*, Phys. Rev. A **61**, 013603 (1999)

[144] M. Oria, M. Chevrollier, D. Bloch, M. Fichet, and M. Ducloy, *Spectral observation of surface-induced van der Waals attraction on atomic vapour*, Europhys. Lett. **14**, 527–532 (1991)

[145] H. Failache, S. Saltiel, M. Fichet, D. Bloch, and M. Ducloy, *Resonant van der Waals repulsion between excited Cs atoms and sapphire surface*, Phys. Rev. Lett. **83**, 5467–5470 (1999)

[146] C. I. Sukenik, M. G. Boshier, D. Cho, V. Sandoghdar, and E. A. Hinds, *Measurement of the Casimir-Polder force*, Phys. Rev. Lett. **70**, 560–563 (1993)

[147] F. Shimizu, *Specular reflection of very slow metastable neon atoms from a solid surface*, Phys. Rev. Lett. **86**, 987–990 (2001)

[148] T. A. Pasquini, Y. Shin, C. Sanner, M. Saba, A. Schirotzek, D. E. Pritchard, and W. Ketterle, *Quantum reflection from a solid surface at normal incidence*, Phys. Rev. Lett. **93**, 223201 (2004)

[149] A. Landragin, J.-Y. Courtois, G. Labeyrie, N. Vansteenkiste, C. I. Westbrook, and A. Aspect, *Measurement of the van der Waals force in an atomic mirror*, Phys. Rev. Lett. **77**, 1464–1467 (1996)

[150] A. K. Mohapatra and C. S. Unnikrishnan, *Measurement of the van der Waals force using reflection of cold atoms from magnetic thin-film atom mirrors*, Europhys. Lett. **73**, 839–845 (2006)

[151] J. L. Hall, M. Zhu, and P. Buch, *Prospects for using laser-prepared atomic fountains for optical frequency standards applications*, J. Opt. Soc. Am. B **6**, 2194–2205 (1989)

[152] E. Riis, D. S. Weiss, K. A. Moler, and S. Chu, *Atom funnel for the production of a slow, high-density atomic beam*, Phys. Rev. Lett. **64**, 1658–1661 (1990)

[153] A. Clarion, C. Salomon, S. Guellati, and W. D. Phillips, *Ramsey resonance in a Zacharias fountain*, Europhys. Lett. **16**, 165–170 (1991)

[154] K. Gibble and S. Chu, *Laser-cooled Cs frequency standard and a measurement of the frequency shift due to ultracold collisions*, Phys. Rev. Lett. **70**, 1771–1774 (1993)

[155] S. Ohshima, T. Kurosu, T. Ikegami, and Y. Nakadan, *Cesium atomic fountain with two-dimensional moving molasses*, Jpn. J. Appl. Phys. **34**, L1170–L1173 (1995)

[156] *Tektronix*, `http://www.tek.com`

[157] *Mini-Circuits*, `http://www.minicircuits.com`

[158] F. London, *The general theory of molecular forces*, Trans. Faraday Soc. **33**, 8b–26 (1937)

[159] H. B. G. Casimir and D. Polder, *The influence of retardation on the London-van der Waals forces*, Phys. Rev. **73**, 360–372 (1948)

[160] A. O. Sushkov, W. J. Kim, D. A. R. Dalvit, and S. K. Lamoreaux, *Observation of the thermal Casimir force*, Nature Phys. **7**, 230–233 (2011)

[161] M. Kardar and R. Golestanian, *The 'friction' of vacuum, and other fluctuation-induced forces*, Rev. Mod. Phys. **71**, 1233–1245 (1999)

[162] M. Bordag, U. Mohideen, and V. M. Mostepanenko, *New developments in the Casimir effect*, Phys. Rep. **353**, 1–205 (2001)

[163] J.-Y. Courtois, J.-M. Courty, and J. C. Mertz, *Internal dynamics of multilevel atoms near a vacuum-dielectric interface*, Phys. Rev. A **53**, 1862–1878 (1996)

[164] W. R. Johnson, V. A. Dzuba, and U. I. Safronova, *Finite-field evaluation of the Lennard-Jones atom-wall interaction constant C_3 for alkali-metal atoms*, Phys. Rev. A **69**, 022508 (2004)

[165] J. Mitroy and M. W. J. Bromley, *Semiempirical calculation of van der Waals coefficients for alkali-metal and alkaline-earth-metal atoms*, Phys. Rev. A **68**, 052714 (2003)

[166] A. O. Caride, G. L. Klimchitskaya, V. M. Mostepanenko, and S. I. Zanette, *Dependences of the van der Waals atom-wall interaction on atomic and material properties*, Phys. Rev. A **71**, 042901 (2005)

[167] M. Fichet, F. Schuller, D. Bloch, and M. Ducloy, *Van der Waals interactions between excited-state atoms and dispersive dielectric surfaces*, Phys. Rev. A **51**, 1553–1564 (1995)

[168] R. Büscher and T. Emig, *Nonperturbative approach to Casimir interactions in periodic geometries*, Phys. Rev. A **69**, 062101 (2004)

[169] P. S. Davids, F. Intravaia, F. S. S. Rosa, and D. A. R. Dalvit, *Modal approach to Casimir forces in periodic structures*, Phys. Rev. A **82**, 062111 (2010)

[170] A. M. Contreras-Reyes, R. Guérout, P. A. Maia Neto, D. A. R. Dalvit, A. Lambrecht, and S. Reynaud, *Casimir-Polder interaction between an atom and a dielectric grating*, Phys. Rev. A **82**, 052517 (2010)

[171] V. Yannopapas and N. V. Vitanov, *Casimir-Polder interaction between an atom and a periodic nanostructure*, Phys. Rev. A **81**, 042506 (2010)

[172] M. N. A. Halif, R. Messina, and T. M. Fromhold, *Calculation of the Casimir-Polder interaction between Bose-Einstein condensates and microengineered surfaces: a pairwise-summation approach*, J. Phys.: Conf. Ser. **286**, 012045 (2011)

[173] V. V. Vladimirsky, *Magnetic mirrors, channels and bottles for cold neutrons*, Sov. Phys. JETP **12**, 740–746 (1961)

[174] C. V. Heer, *Feasibility of confinement of quantum magnetic dipoles*, Rev. Sci. Instr. **34**, 532–537 (1963)

[175] Y. V. Gott, M. S. Ioffe, and V. G. Tel'kovskii, *Some new results on confinement in magnetic traps*, Nuclear Fusion **Suppl. 2**, 1045–1047 (1962)

[176] W. Ertmer, R. Blatt, J. L. Hall, and M. Zhu, *Laser manipulation of atomic beam velocities: Demonstration of stopped atoms and velocity reversal*, Phys. Rev. Lett. **54**, 996–999 (1985)

[177] S. Chu, L. Hollberg, J. E. Bjorkholm, A. Cable, and A. Ashkin, *Three-dimensional viscous confinement and cooling of atoms by resonance radiation pressure*, Phys. Rev. Lett. **55**, 48–51 (1985)

[178] O. J. Luiten, M. W. Reynolds, and J. T. M. Walraven, *Kinetic theory of the evaporative cooling of a trapped gas*, Phys. Rev. A **53**, 381–389 (1996)

[179] R. deCarvalho and J. Doyle, *Evaporative cooling at low trap depth*, Phys. Rev. A **70**, 053409 (2004)

[180] J. Reichel, *Microchip traps and Bose-Einstein condensation*, Appl. Phys. B **75**, 469–487 (2002)

[181] R. Salem, Y. Japha, J. Chabé, B. Hadad, M. Keil, K. A. Milton, and R. Folman, *Nanowire atomchip traps for sub-micron atom-surface distances*, New J. Phys. **12**, 023039 (2010)

[182] E. Majorana, *Atomi orientati in campo magnetico variabile*, Nuovo Cimento **9**, 43–50 (1932)

[183] C. V. Sukumar and D. M. Brink, *Spin-flip transitions in a magnetic trap*, Phys. Rev. A **56**, 2451–2454 (1997)

[184] A. Messiah, *Quantum Mechanics* (North-Holland, 1961)

[185] E. W. Laing and A. E. Robson, *Non-adiabatic magnetic traps*, J. Nucl. Energy C **3**, 146–155 (1961)

[186] T. Bergeman, G. Erez, and H. J. Metcalf, *Magnetostatic trapping fields for neutral atoms*, Phys. Rev. A **35**, 1535–1546 (1987)

[187] T. Esslinger, I. Bloch, and T. W. Hänsch, *Bose-Einstein condensation in a quadrupole-Ioffe-configuration trap*, Phys. Rev. A **58**, R2664–R2667 (1998)

[188] C. Zener, *Non-adiabatic crossing of energy levels*, Proc. R. Soc. Lond. **137**, 696–702 (1932)

[189] Y. Colombe, E. Knyazchyan, O. Morizot, B. Mercier, V. Lorent, and H. Perrin, *Ultracold atoms confined in rf-induced two-dimensional trapping potentials*, Europhys. Lett. **67**, 593–599 (2004)

[190] S. Hofferberth, I. Lesanovsky, B. Fischer, J. Verdu, and J. Schmiedmayer, *Radiofrequency-dressed-state potentials for neutral atoms*, Nature Physics **2**, 710–716 (2006)

[191] P. W. Courteille, B. Deh, J. Fortágh, A. Günther, S. Kraft, C. Marzok, S. Slama, and C. Zimmerman, *Highly versatile atomic micro traps generated by multifrequency magnetic field modulation*, J. Phys. B **39**, 1055–1064 (2006)

[192] I. Lesanovsky, S. Hofferberth, J. Schmiedmayer, and P. Schmelcher, *Manipulation of ultracold atoms in dressed adiabatic radio-frequency potentials*, Phys. Rev. A **74**, 033619 (2006)

[193] W. H. Heathcote, E. Nugent, B. T. Sheard, and C. J. Foot, *A ring trap for ultracold atoms in an RF-dressed state*, New J. Phys. **10**, 043012 (2008)

[194] I. Lesanovsky, T. Schumm, S. Hofferberth, L. M. Andersson, P. Krüger, and J. Schmiedmayer, *Adiabatic radio-frequency potentials for the coherent manipulation of matter waves*, Phy. Rev. A **73**, 033619 (2006)

[195] O. Zobay and B. M. Garraway, *Two-dimensional atom trapping in field-induced adiabatic potentials*, Phys. Rev. Lett. **86**, 1195–1198 (2001)

[196] E. Nugent, *Novel traps for Bose-Einstein condensates*, Ph.D. thesis, University of Oxford (2009)

[197] I. Lesanovsky and W. von Klitzing, *Time-averaged adiabatic potentials: versatile matter-wave guides and atom traps*, Phys. Rev. Lett. **99**, 083001 (2007)

[198] W. Paul, *Electromagnetic traps for charged and neutral particles*, Rev. Mod. Phys. **62**, 531–540 (1990)

[199] M. H. Anderson, J. R. Ensher, M. R. Matthews, C. E. Wieman, and E. A. Cornell, *Observation of Bose-Einstein condensation in a dilute atomic vapor*, Science **269**, 198–201 (1995)

[200] T. G. Tiecke, M. Kemmann, C. Buggle, I. Shvarchuck, W. von Klitzing, and J. T. M. Walraven, *Bose-Einstein condensation in a magnetic double-well potential*, J. Opt. B **5**, S119–S123 (2003)

[201] M. Gildemeister, E. Nugent, B. E. Sherlock, M. Kubasik, B. T. Sheard, and C. J. Foot, *Trapping ultracold atoms in a time-averaged adiabatic potential*, Phys. Rev. A **81**, 031402(R) (2010)

[202] B. E. Sherlock, M. Gildermeister, and O, *Time-averaged adiabatic ring potential for ultracold atoms*, Phys. Rev. A **83**, 043408 (2011)

[203] W. Petrich, M. H. Anderson, J. R. Ensher, and E. A. Cornell, *Stable, tightly confining magnetic trap for evaporative cooling of neutral atoms*, Phys. Rev. Lett. **74**, 3352–3355 (1995)

[204] J. R. Ensher, *The first experiments with Bose-Einstein condensation of ^{87}Rb*, Ph.D. thesis, University of Colorado (1998)

[205] B. E. Sherlock, *Ultracold quantum gases in time-averaged adiabatic potentials*, Ph.D. thesis, University of Oxford (2011)

[206] M. Siercke, *Realization of Bose-Einstein condensation of ^{87}Rb in a time-orbiting potential trap*, Ph.D. thesis, University of Toronto (2011)

[207] J. M. Reeves, O. Garcia, B. Deissler, K. L. Baranowski, K. J. Hughes, and C. A. Sackett, *Time-orbiting potential trap for Bose-Einstein condensate interferometry*, Phys. Rev. A **72**, 051605(R) (2005)

[208] A. Trimeche, M. N. Bera, J.-P. Cromières, J. Robert, and N. Vanhaecke, *Trapping of a supersonic beam in a traveling magnetic wave*, Eur. Phys. J. D **65**, 263–271 (2011)

[209] K. B. Davis, M.-O. Mewes, M. R. Andrews, N. J. van Druten, D. S. Durfee, D. M. Kurn, and W. Ketterle, *Bose-Einstein condensation in a gas of sodium atoms*, Phys. Rev. Lett. **75**, 3969–3973 (1995)

[210] O. Morizot, C. L. Garrido, P. Pottie, V. Lorent, and H. Perrin, *Trapping and cooling of rf-dressed atoms in a quadrupole magnetic field*, J. Phys. B **40**, 4013–4022 (2007)

[211] E. Hodby, G. Hechenblaikner, O. M. Maragoò, J. Arlt, S. Hopkins, and C. J. Foot, *Bose-Einstein condensation in a stiff TOP trap with adjustable geometry*, J. Phys. B **33**, 4087–4094 (2000)

[212] *Physik Instrumente*, `http://www.piceramic.com`

[213] B. Jaffe, W. R. Cook, and H. Jaffe, *Piezoelectric ceramics* (Techbooks, 1989)

[214] *Falco Systems*, `http://www.falco-systems.com`

[215] S. Tadigadapa and K. Mateti, *Piezoelectric mems sensors: state-of-the-art and perspectives*, Meas. Sci. Technol. **20**, 092001 (2009)

[216] *Tower Optical*, `http://www.toweroptical.com`

[217] *Epoxy Technology, Inc.*, `http://www.epotek.com`

[218] *Impedance spectroscopy: theory, experiment and applications*, 2nd ed., edited by E. Barsoukov and J. R. Macdonal (Wiley, 2005)

[219] M. G. Cain and M. Stewart, *Measurement good practice guide: Piezoelectric resonance*, `http://publications.npl.co.uk`

[220] F. Xing, B. Dong, and Z. Li, *Impedance spectroscopic studies of cement-based piezoelectric ceramic composites*, Comp. Sci. Technol. **68**, 2456–2460 (2008)

[221] *Polytec PI*, `http://polytecpi.com`

[222] T. C. Briles, D. C. Yost, A. Cingöz, J. Ye, and T. R. Schibli, *Simple piezoelectric-actuated mirror with 180 kHz servo bandwidth*, Opt. Express **18**, 9739–9746 (2010)

[223] G. Park, C. R. Farrar, A. C. Rutherford, and A. N. Robertson, *Piezo-sensor self-diagnostics using elecrical impedance measurements*, in *Proceedings of the 15th International Conference on Adaptive Structures and Technologies* (2004)

[224] M. Abad, M. Guilleumas, R. Mayol, M. Pi, and D. M. Jezek, *A dipolar self-induced bosonic Josephson junction*, Europhys. Lett. **94**, 10004 (2011)

[225] T. L. Gustavson, A. Landragin, and M. A. Kasevich, *Rotation sensing with a dual atom-interferometer Sagnac gyroscope*, Class. Quantum Grav. **17**, 2385–2398 (2000)

[226] P. L. Halkyard, M. P. A. Jones, and S. A. Gardiner, *Rotational response of two-component Bose-Einstein condensates in ring traps*, Phys. Rev. A **81**, 061602(R) (2010)

[227] P. L. Halkyard, *Dynamics in cold atomic gases: resonant behaviour of the quantum delta-kicked accelerator and Bose-Einstein condensates in ring traps*, Ph.D. thesis, Durham University (2010)

[228] J. Brand and W. P. Reinhardt, *Generating ring currents, solitons and svortices by stirring a Bose-Einstein condensate in a toroidal trap*, J. Phys. B **34**, L113–L119 (2001)

[229] S. T. John, Z. Hadzibabic, and N. R. Cooper, *Spectroscopic method to measure the superfluid fraction of an ultracold atomic gas*, Phys. Rev. A **83**, 023610 (2011)

[230] A. Ramanathan, K. C. Wright, S. R. Muniz, M. Zelan, W. T. Hill III, C. J. Lobb, K. Helmerson, W. D. Phillips, and G. K. Campbell, *Superflow in a toroidal bose-einstein condensate: an atom circuit with a tunable weak link*, Phys. Rev. Lett. **106**, 130401 (2011)

[231] S. Gupta, K. W. Murch, K. L. Moore, T. P. Purdy, and D. M. Stamper-Kurn, *Bose-Einstein condensation in a circular waveguide*, Phys. Rev. Lett. **95**, 143201 (2005)

[232] O. Morizot, Y. Colombe, V. Lorent, H. Perrin, and B. M. Garraway, *Ring trap for ultracold atoms*, Phys. Rev. A **74**, 023617 (2006)

[233] K. Henderson, C. Ryu, C. MacCormick, and M. G. Boshier, *Experimental demonstration of painting arbitrary and dynamic potentials for Bose-Einstein condensates*, New J. Phys. **11**, 043030 (2009)

[234] A. S. Arnold, *Adaptable-radius, time-orbiting magnetic ring trap for Bose-Einstein condensates*, J. Phys. B **37**, L29–L33 (2004)

[235] B. Zimmermann, T. Müller, J. Meineke, T. Esslinger, and H. Moritz, *High-resolution imaging of ultracold fermions in microscopically tailored optical potentials*, New J. Phys. **13**, 043007 (2011)